energies

Biomass Chars

Elaboration, Characterization and Applications II

Edited by
Mejdi Jeguirim and Lionel Limousy
Printed Edition of the Special Issue Published in *Energies*

www.mdpi.com/journal/energies

MDPI

Biomass Chars

Biomass Chars: Elaboration, Characterization and Applications II

Special Issue Editors

Mejdi Jeguirim
Lionel Limousy

MDPI • Basel • Beijing • Wuhan • Barcelona • Belgrade

Special Issue Editors
Mejdi Jeguirim
Institut de Sciences des Matériaux de Mulhouse
France

Lionel Limousy
Institut de Sciences des Matériaux de Mulhouse
France

Editorial Office
MDPI
St. Alban-Anlage 66
4052 Basel, Switzerland

This is a reprint of articles from the Special Issue published online in the open access journal *Energies* (ISSN 1996-1073) from 2017 to 2019 (available at: https://www.mdpi.com/journal/energies/special_issues/biomass_chars_2017).

For citation purposes, cite each article independently as indicated on the article page online and as indicated below:

LastName, A.A.; LastName, B.B.; LastName, C.C. Article Title. *Journal Name* **Year**, *Article Number*, Page Range.

ISBN 978-3-03921-662-8 (Pbk)
ISBN 978-3-03921-663-5 (PDF)

Contents

About the Special Issue Editors

Mejdi Jeguirim has been Associate Professor at the University of Haute Alsace (France) since 2005 in the field of energy and process engineering. Most of his research is dedicated to the study of biomass valorization through thermochemical conversion and char elaboration for energy and syngas production, pollutant removal, and soil amendment. This research has been conducted in the framework of international collaborations and industrial contracts. He has served as PhD advisor for 10 students and co-authored 85 referred publications in international journals. He is on the Editorial Board of numerous international scientific journals (*Energy*, *Energy for Sustainable Development*, *Energies*) and has organized several Special Issues as Guest Editor. He belongs to the scientific committee of numerous international congresses and is involved as a scientific expert for several national and international research programs. He has received the French National Research Excellence Award as a researcher with a high level of scientific activity for the periods 2009–2012, 2013–2016, and 2017–2020.

Lionel Limousy has been Associate Professor at the University of Haute Alsace since 2010. He teaches in chemical and environmental engineering as well as risk management and assessment. He was recruited to the University of South Brittany in 2000 where he was Head of the Chemical Engineering and Process department from 2003 and 2005. He founded the Prodiabio platform in 2005, where he was Director until 2010. In 2013, he joined the Institute of Material Science of Mulhouse where he became responsible for the industrial research partnership. He has experience in the biological and chemical treatment of wastewater, membrane filtration, biomass valorization, and materials characterization. He is involved in several national and international academic and industrial projects. He has 89 scientific publications and collaborated in the organization of Special Issues. He has received the French National Research Excellence Award as a researcher with a high level of scientific activity for the periods 2013–2016 and 2017–2020.

Preface to ”Biomass Chars: Elaboration, Characterization and Applications II”

Biomass Chars: Elaboration, Characterization and Applications II is a continuation of the previous and successful Special Issue “Biomass Chars: Elaboration, Characterization and Applications”. This SI contains 22 original articles that were selected and evaluated for this Special Issue and provide an overview of the properties of biomass chars as well as methods for their production, characterization techniques, as well as suitable recovery processes.

Mejdi Jeguirim, Lionel Limousy
Special Issue Editors

energies

Editorial

Biomass Chars: Elaboration, Characterization and Applications II

Mejdi Jeguirim * and Lionel Limousy

Université de Strasbourg, Université de Haute Alsace, Institut de Science des Matériaux de Mulhouse (IS2M) UMR CNRS 7361, 68093 Mulhouse, France; lionel.limousy@uha.fr
* Correspondence: mejdi.jeguirim@uha.fr

Received: 14 November 2018; Accepted: 23 January 2019; Published: 25 January 2019

This Special Issue of *Energies* contains the successful invited submissions [1–21] on the subject area of "Biomass Chars: Elaboration, Characterization and Applications". After the organization of a first edition, the guest editors have decided to continue focusing on char production from biomass and their applications various applications. In response to our call for papers we received 27 submissions, of which 21 have been published and six rejected during the peer review process. The geographical distribution of the authors of the published papers is as follows:

- China (5)
- UK (1)
- France (4)
- Greece (1)
- Spain (1)
- Korea (6)
- Germany (1)
- Tunisia (1)
- Poland (1)

Published submissions are related to biomass char production methods, including pyrolysis, and hydrothermal carbonization. In addition, various characterization techniques were used to identify the physico-chemical, morphological, textural, surface chemistry and structural properties of the products. The main applied techniques were thermogravimetric analysis (TGA), calorimetry, pH measurements, scanning electron microscopy (SEM)–energy dispersive X-ray (EDX) analyses, X-ray diffraction (XRD), nitrogen gas adsorption, Fourier transform infrared spectroscopy (FTIR), etc. The different recovery routes of biomass-derived chars were also addressed. Particular attention was paid to char gasification and combustion as well as to the applications of chars for gas storage and soil amendment. The main results are described below. New developments are still under progress, encouraging the organization of a third edition of this special issue.

Moulogianni and Bournaris have ranked the agro-energy regions in the Region of Central Macedonia (RCM) according to their biomass production potential [1]. In this context, the authors have developed a Multi-Criteria Analysis (MCDA) model using the ELimination and Et Choix Traduisant la REalite (ELECTRE) III method through the construction of outranking relations. The authors concluded that agro-energy regions with cereals and arable crops will have better results than regions with fruit trees and other crops.

Khiari and Jeguirim have attempted to identify an environmentally friendly valorization method for the huge amounts of grape marc generated in Tunisia by the wine industry [2]. Hence, the authors have determined physico-chemical and energy characteristics of grape marc according to international standards. Based on these characteristics, they proposed a pyrolysis process as a recovery route for the grape marc due to its high minerals content and the ability to create high added value derived products. During the thermogravimetric analysis the biochar yield was about 40%, a value never previously reported in the literature for an agricultural biomass subjected to slow pyrolysis. Such behavior may be attributed to the high lignin and high minerals contents in grape marc, confirming its potential for agricultural applications.

Lee et al. have studied an alternative for the recovery of food waste compost since the amount generated every day is higher than the amount consumed in farms [3]. Hence, authors have suggested producing biochar from food waste compost using pyrolysis processes. In this context, they have analyzed the thermal degradation behavior, calorific value, and char composition (using gas chromatography) during the pyrolysis of food waste compost. The authors showed that biochar from the pyrolysis of food waste compost had a high carbon content of 51% at 300 °C. Hence, it seems that food waste compost can be used as a promising alternative fuel at a low pyrolysis temperature, like other lignocellulosic refuse-derived fuels (RDF)

Liu et al have studied the pyrolysis of rice straw in a horizontal tube reactor at temperatures ranging from 500 to 900 °C [4]. The authors have monitored the gaseous nitrogen components emitted during rice straw pyrolysis in order to identify the release mechanism of fuel-N into NO_x and N_2O precursors. A high dependency between the gaseous products and temperature was found. NH_3 and HNCO were preferentially formed at lower temperatures and HCN tended to form at higher temperatures. The authors have also noted that NO was also an important product and its formation during the pyrolysis of rice straw was due to the direct oxidization reaction of –NH and –OH, the latter being abundant in the raw material.

Hydrothermal carbonization (HTC) is an emerging technology used for bioenergy conversion from bio-wastes such as sewage sludge, livestock manure, and food waste. Oh and Yoon have studied the hydrothermal carbonization of poultry slaughterhouse sludge cake in a pilot-scale HTC reactor at temperatures from 170 to 220 °C [5]. The authors have analyzed the gross energy recovery efficiency based on the calorific value of the HTC-biochar and the ultimate methane potential of the HTC-hydrolysate, indicating that poultry slaughterhouse sludge cake is a useful source for bioenergy conversion with a total gross energy recovery (GER_{total}) of 4318 MJ/kg attained at 180 °C.

Similar analysis were performed by Liu et al. during the hydrothermal carbonization of a major energy crop, reeds [6]. The HTC experiments were performed in a batch reactor at 200–280 °C for 0.5 to 4 h. The authors indicated that the hydrochar mass yield changed from 66.7% to 19.2% and high heating value (HHV) from 20.0 kJ/g to 28.3 kJ/g, respectively, by increasing the carbonization temperature from 200 °C to 280 °C and decreasing the residence time from 2 h to 1 h.

The operating conditions in pyrolysis and hydrothermal carbonization strongly impact the properties of biochars and hydrochars. Dieguez-Alonso et al. have used pine wood (PW) and corn digestate (CD) as feedstocks for biochar and hydrochar production [7]. CD biochars showed lower H/C ratios, thermal recalcitrance and total specific surface area than PW biochars, but higher mesoporosity. CD and PW biochars presented higher naphthalene and phenanthrene contents, respectively, which may indicate different reaction pathways. High temperatures (>500 °C) lead to lower polycyclic aromatic hydrocarbon (PAH) content (<12 mg/kg) and higher specific surface area. In hydrochars the high inorganic content favors decarboxylation over dehydration reactions. Hydrochars showed mainly mesoporosity, with a higher pore volume but generally lower specific surface area than biochars. Biochars presented negligible availability of NO_3^- and NH_4^+, irrespective of the nitrogen content of the feedstock. For hydrochars, a potential increase in availability of NO_3^-, NH_4^+, PO_4^{3-}, and K^+ with respect to the feedstock is possible.

The char characterization is a crucial step to identify the suitable recovery route for biochar. Lee et al. have analyzed the chemical characteristics of biochar produced using food waste containing low- and high-concentration salt and biochar flushed with water to remove the concentrated salt [8]. Peak analysis of XRD confirmed that it is difficult to find salt crystals in flushed char since salt remains in the form of crystals when salty food waste was pyrolyzed was washed away after water flushing.

In addition, the Cl content significantly decreased to 1–2% after flushing, similar to that of Cl content in the standard, non-salted food waste char. On the other hand, a significant amount of Na was found in pyrolyzed char even after flushing resulting from a phenomenon in which salt is dissolved in water while flushing and Na ions are adsorbed. FT-IR analysis showed that salt in waste affects the binding of aromatic carbons to compounds in the pyrolysis process. NMR spectroscopy experiments demonstrated that the aromatic carbon content, which is an indicator of the stability of a biochar, is not influenced by the salt content and increases with increasing pyrolysis temperature.

Lee et al. have followed up on their investigation by analyzing food-waste-derived biochar structures obtained through pyrolysis and with different NaCl concentrations [9]. The authors indicate that increased NaCl concentration in the samples inhibited cellulose and lignin decomposition, ultimately increasing the biochar yield by 2.7% for 20%-NaCl concentration. NaCl added in solution state exhibited templating effects, with maximum increase in the Brunauer–Emmett–Teller (BET) surface area and pore volume of 1.23 to 3.50 $m^2 \cdot g^{-1}$ and 0.002 to 0.007 $cm^3 \cdot g^{-1}$, respectively, after washing. Adding a high concentration (20%) of NaCl reduced the BET surface area. In contrast, the mean pore diameter increased owing to the increased NaCl clustering area.

Different recovery routes for biomass-derived chars were examined in the literature such as combustion, gasification, pollutants adsorption, soil amendments. Boukaous et al. have examined the combustion characteristics of flax shives, beech wood, hemicellulose, cellulose, lignin, and their chars prepared in a fixed-bed reactor at 850 °C [10]. The authors have assessed the thermal behavior based on characteristic temperatures (ignition, maximum, and final temperatures), burnout time and maximum rate. The results revealed that the combustion of pure pseudo-components behaved differently from that of biomass. In contrast, the combustion of the hemicellulose and cellulose chars showed that they have almost the same structure. Their overall thermal and kinetic behavior remained between that of biomass and lignin.

Mami et al. have carried out combustion tests of olive mill solid wastes pellets (olive pomace (OP), and olive pits (OPi)) in an updraft counter-current fixed bed reactor [11]. The authors have found that the exhaust gases were emitted in acceptable concentrations compared to the combustion of standard wood pellets reported in the literature (EN 303-5). Furthermore, it was shown that the bed temperature increased from the ambient value to a maximum value ranging from 750 to 1000 °C as previously reported in the literature. The results demonstrated the interest of using olive mill solid waste pellets as an alternative biofuel for heat and/or electricity production

Kim et al. have examined experimentally the effect of oxygen-enriched air on char combustion [12]. During their investigation, a coal-heating reactor equipped with a platinum wire mesh in the reaction chamber was used to analyze the combustion temperature, reaction time, and reaction kinetics. The authors have found that increasing the oxygen content of the primary combustion air increased the combustion temperature and decreased the reaction time. As the oxygen content increased from 21% to 30%, the average temperature increased by 47.72 K at a setup temperature of 1673 K, and the reaction time decreased by 30.22% at the same temperature. The graphite sample exhibited similar trends in temperature and reaction time, although the degree of change was smaller because the pores produced during char devolatilization expanded the active surface available for oxidation of the char sample. A mathematical model was used to define the intrinsic kinetics of the reaction. As the oxygen content increased from 21% to 30%, the reaction rate of the low-rank coal char increased. These results were also compared with those of the graphite sample

Char gasification is attracting nowadays growing interest. Liu et al. have studied the char gasification of two coals (i.e., Shenfu bituminous coal and Zunyi anthracite) and a petroleum coke under a steam and CO_2 mixture (steam/CO_2 partial pressures, 0.025–0.075 MPa; total pressures, 0.100 MPa) and CO_2/steam chemisorption of char samples using a Thermogravimetric Analyzer (TGA) [13]. As a result a modified model based on Langmuir–Hinshelwood model and assuming that char–CO_2 and char–steam reactions partially shared active sites was proposed and had indicated high accuracy for estimating the interactions in char–steam–CO_2 reaction. Moreover, it was found that two new model parameters (respectively characterized as the amount ratio of shared active sites to total active sites in char–CO_2 and char–steam reactions) in the modified model hardly varied with gasification conditions, and the results of chemisorption indicate that these two new model parameters mainly depended on the carbon active sites in char samples

The char gasification reactivity is strongly affected by the presence of inorganic elements in the raw biomass. Feng et al. have examined the effect of chemical speciation (H_2O/NH_4Ac/HCl-soluble and insoluble) of alkali and alkaline earth metallic species on the steam gasification of sawdust biochar in a lab-scale, fixed-bed reactor, with the method of chemical fractionation analysis [14]. The results indicated that H_2O/NH_4Ac/HCl-soluble AAEMs have a significant effect on biochar gasification rates. The release of K occurs mainly in the form of inorganic salts and hydrated ions, while that of Ca occurs mainly as organic ones. The sp^3-rich or sp^2-sp^3 structures and different chemical-speciation AAEMs function together as the preferred active sites during steam gasification. H_2O/HCl-soluble AAEMs could promote the transformation of biochar surface functional groups, from ether/alkene C-O-C to carboxylate COO− in biochar, while they may both be improved by NH_4Ac-soluble AAEMs. H_2O-soluble AAEMs play a crucial catalytic role in biochar reactivity.

In addition to the inorganic elements, char preparation methods may influence the gasification reactivity. Dahou et al. conducted a study to investigate the parameters that influence the steam gasification kinetics according to the biomass type and char preparation method [15]. Chars were prepared using three different sets of low heating rate (LHR) pyrolysis conditions including different temperatures and biomass bed geometry. The authors have shown by a characteristic time analysis that these pyrolysis conditions were not associated with a chemical regime in a large amount of devices. However, they have shown that conditions used to prepare the char had a much lower influence on steam gasification kinetics than the biomass type.

The presence of heavy metals in waste wood may have negative effects during the gasification process through toxicity emissions and facility damaging. Therefore, Al-Badri et al. have performed thermodynamic equilibrium calculations for the Boudouard reaction (BR) and partial combustion reaction (PCR) to explore the possible interactions and interferences among CCA-elements themselves and with Ca, Na, S, Cl, Fe, and Ni during the gasification of contaminated waste wood [16]. The results revealed that Ni-As interactions generate dominant species As_2Ni_5 and As_8Ni_{11}, which increase the solid–gaseous transformation temperature of As. Moreover, the interactions between Ca and Cr predominantly form C_3Cr_7; whereas the absence of Ca leads to $Cr_2Na_2O_4$ causing instability in the Cr phase transformation.

During the char gasification, an ash layer is accumulated on the char surface. The ash layer increases the mass transfer resistance of O_2 to the gasification surface, which may become the limiting step of whole process. In this context, Lin et al. studied O_2 diffusion in the ash layer formed on cylindrical char samples using a specially designed one-dimension setup in a thermogravimetric apparatus (TGA) [17]. The effective internal diffusion coefficient (D_e) was found to increase with an increase in ash layer thickness, due to an increase in median pore diameter. Methods were established to correlate D_e with operating conditions and to estimate the role of internal diffusion resistance in overall mass transfer resistance.

The effect of ash melting phenomena was also assessed by Kim et al. through the development of a one-dimensional (1-D) entrained-flow gasifier model [18]. The authors have included sensible heat of slag and the fusion heat of ash in the heat balance equation in their model. To consider the melting of ash, they have proposed an algorithm that calculates the energy balance for three scenarios based on temperature. Based on the Texaco pilot plant gasifier, the model was validated. The obtained results showed good agreement with previous experimental data. Kim et al. have concluded that the sensible heat of slag and the fusion heat of ash must be included in the entrained flow gasifier model.

In addition to the thermal conversion, biomass chars could be physically or chemically activated in order to elaborate efficient adsorbents. In this sense, Abdeljaoued et al. have produced an activated carbon from coconut shells with suitable characteristics to separate CO_2 from biogas [19]. The textural characterization of the adsorbent has been determined. Pure component adsorption isotherms of CO_2 and CH_4 at 30–70 °C have been measured. The obtained results revealed that the activated carbon had high CO_2 adsorption capacity. Equilibrium of adsorption of CO_2 and CH_4 adsorption on the produced activated carbon reached 8.36 mmol/g and 4.63 mmol/g, respectively, at 30 °C and 10 bar.

Peredo-Mancilla et al. have compared the performance of different biomass-based activated carbons for CO_2 and CH_4 adsorption [20]. In particular, authors have studied the influence of the activation method on the adsorption uptake using three activated carbons obtained by different activation methods (H_3PO_4 chemical activation and H_2O and CO_2 physical activation) of olive stones. For the three adsorbents, the CO_2 adsorption was more important than that of CH_4. The chemically-activated carbon presented a higher specific surface area and micropore volume, which led to a higher adsorption capacity of both CO_2 and CH_4. For methane adsorption, the presence of mesopores facilitated the diffusion of the gas molecules into the micropores. In the case of carbon dioxide adsorption, the presence of more oxygen groups on the water vapor-activated carbon enhanced its adsorption capacity.

Energy crops such as *Miscanthus* have attracted growing interest during the last decade. Saletnik et al. have assessed the possibility of using biochar and ash from plant biomass to fertilise giant miscanthus (*Miscanthus x giganteus*). Authors have examined the optimisation of the combination of fertiliser applications of the aforementioned materials in the context of the plant yield obtained. There was an increase in yield of 8–68% over the two years of research when compared with the control plots. It was found that the application of biochar, ash from biomass and a combination of the two at appropriate rates as a soil additive can substitute for classic mineral fertilisers and strengthen the ecological aspects of energy crop cultivation.

We found the edition and selections of papers for this Special Issue very inspiring and rewarding. We also thank the editorial staff and reviewers for their efforts and help during the process.

References

1. Moulogianni, C.; Bournaris, T. Biomass Production from Crops Residues: Ranking of Agro-Energy Regions. *Energies* **2017**, *10*, 1061. [CrossRef]
2. Khiari, B.; Jeguirim, M. Pyrolysis of Grape Marc from Tunisian Wine Industry: Feedstock Characterization, Thermal Degradation and Kinetic Analysis. *Energies* **2018**, *11*, 730. [CrossRef]
3. Lee, Y.; Jo, J.; Kim, I.; Yoo, Y. Value-Added Performance and Thermal Decomposition Characteristics of Dumped Food Waste Compost by Pyrolysis. *Energies* **2018**, *11*, 1061. [CrossRef]
4. Liu, X.; Luo, Z.; Yu, C.; Jin, B.; Tu, H. Release Mechanism of Fuel-N into NOx and N_2O Precursors during Pyrolysis of Rice Straw. *Energies* **2018**, *11*, 520. [CrossRef]
5. Oh, S.; Yoon, Y. Energy Recovery Efficiency of Poultry Slaughterhouse Sludge Cake by Hydrothermal Carbonization. *Energies* **2017**, *10*, 1876. [CrossRef]
6. Liu, C.; Huang, X.; Kong, L. Efficient Low Temperature Hydrothermal Carbonization of Chinese Reed for Biochar with High Energy Density. *Energies* **2017**, *10*, 2094. [CrossRef]
7. Dieguez-Alonso, A.; Funke, A.; Anca-Couce, A.; Rombolà, A.; Ojeda, G.; Bachmann, J.; Behrendt, F. Towards Biochar and Hydrochar Engineering—Influence of Process Conditions on Surface Physical and Chemical Properties, Thermal Stability, Nutrient Availability, Toxicity and Wettability. *Energies* **2018**, *11*, 496. [CrossRef]
8. Lee, Y.; Jo, J.; Kim, I.; Yoo, Y. Chemical Characteristics and NaCl Component Behavior of Biochar Derived from the Salty Food Waste by Water Flushing. *Energies* **2017**, *10*, 1555. [CrossRef]
9. Lee, Y.; Jo, J.; Kim, I.; Yoo, Y. Influence of NaCl Concentration on Food-Waste Biochar Structure and Templating Effects. *Energies* **2018**, *11*, 2341. [CrossRef]
10. Boukaous, N.; Abdelouahed, L.; Chikhi, M.; Meniai, A.; Mohabeer, C.; Bechara, T. Combustion of Flax Shives, Beech Wood, Pure Woody Pseudo-Components and Their Chars: A Thermal and Kinetic Study. *Energies* **2018**, *11*, 2146. [CrossRef]
11. Mami, M.; Mätzing, H.; Gehrmann, H.; Stapf, D.; Bolduan, R.; Lajili, M. Investigation of the Olive Mill Solid Wastes Pellets Combustion in a Counter-Current Fixed Bed Reactor. *Energies* **2018**, *11*, 1965. [CrossRef]

12. Kim, G.; Kim, J.; Lisandy, K.; Jeon, C. Experimental Model Development of Oxygen-Enriched Combustion Kinetics on Porous Coal Char and Non-Porous Graphite. *Energies* **2017**, *10*, 1436. [CrossRef]
13. Liu, X.; Wei, J.; Huo, W.; Yu, G. Gasification under CO_2–Steam Mixture: Kinetic Model Study Based on Shared Active Sites. *Energies* **2017**, *10*, 1890. [CrossRef]
14. Feng, D.; Zhao, Y.; Zhang, Y.; Sun, S.; Gao, J. Steam Gasification of Sawdust Biochar Influenced by Chemical Speciation of Alkali and Alkaline Earth Metallic Species. *Energies* **2018**, *11*, 205. [CrossRef]
15. Dahou, T.; Defoort, F.; Thiéry, S.; Grateau, M.; Campargue, M.; Bennici, S.; Jeguirim, M.; Dupont, C. The Influence of Char Preparation and Biomass Type on Char Steam Gasification Kinetics. *Energies* **2018**, *11*, 2126. [CrossRef]
16. Al-Badri, S.; Jiang, Y.; Wagland, S. Possible Interactions and Interferences of Copper, Chromium, and Arsenic during the Gasification of Contaminated Waste Wood. *Energies* **2018**, *11*, 1966. [CrossRef]
17. Lin, X.; Liu, Q.; Liu, Z. Estimation of Effective Diffusion Coefficient of O_2 in Ash Layer in Underground Coal Gasification by Thermogravimetric Apparatus. *Energies* **2018**, *11*, 460. [CrossRef]
18. Kim, J.; Oh, H.; Lee, S.; Yoon, Y. Advanced One-Dimensional Entrained-Flow Gasifier Model Considering Melting Phenomenon of Ash. *Energies* **2018**, *11*, 1015. [CrossRef]
19. Abdeljaoued, A.; Querejeta, N.; Durán, I.; Álvarez-Gutiérrez, N.; Pevida, C.; Chahbani, M. Preparation and Evaluation of a Coconut Shell-Based Activated Carbon for CO_2/CH_4 Separation. *Energies* **2018**, *11*, 1748. [CrossRef]
20. Peredo-Mancilla, D.; Ghouma, I.; Hort, C.; Matei Ghimbeu, C.; Jeguirim, M.; Bessieres, D. CO_2 and CH_4 Adsorption Behavior of Biomass-Based Activated Carbons. *Energies* **2018**, *11*, 3136. [CrossRef]
21. Saletnik, B.; Zagula, G.; Bajcar, M.; Czernicka, M.; Puchalski, C. Biochar and Biomass Ash as a Soil Ameliorant: The Effect on Selected Soil Properties and Yield of Giant Miscanthus (Miscanthus x giganteus). *Energies* **2018**, *11*, 2535. [CrossRef]

energies

Article

CO_2 and CH_4 Adsorption Behavior of Biomass-Based Activated Carbons

Deneb Peredo-Mancilla [1,2,*], Imen Ghouma [3], Cecile Hort [2], Camelia Matei Ghimbeu [3], Mejdi Jeguirim [3] and David Bessieres [1]

[1] CNRS/Total/Univ Pau & Pays Adour/ E2S UPPA, Laboratoire des Fluides Complexes et Leurs Reservoirs-IPRA, UMRS5150, 64000 Pau, France; david.bessieres@univ-pau.fr
[2] Univ Pau & Pays Adour/ E2S UPPA, Laboratoire de Thermique, Energetique et Procedes-IPRA, EA1932, 64000 Pau, France; cecile.hort@univ-pau.fr
[3] Institut de Sciences des Matériaux de Mulhouse, UMR 7661 CNRS, 15 rue Jean Starcky, 68057 Mulhouse, France; imenghouma83@gmail.com (I.G.); camelia.ghimbeu@uha.fr (C.M.G.); mejdi.jeguirim@uha.fr (M.J.)
* Correspondence: peredo-mancilla.jd@univ-pau.fr

Received: 25 July 2018; Accepted: 8 November 2018; Published: 13 November 2018

Abstract: The aim of the present work is to study the effect of different activation methods for the production of a biomass-based activated carbon on the CO_2 and CH_4 adsorption. The influence of the activation method on the adsorption uptake was studied using three activated carbons obtained by different activation methods (H_3PO_4 chemical activation and H_2O and CO_2 physical activation) of olive stones. Methane and carbon dioxide pure gas adsorption experiments were carried out at two working temperatures (303.15 and 323.15 K). The influence of the activation method on the adsorption uptake was studied in terms of both textural properties and surface chemistry. For the three adsorbents, the CO_2 adsorption was more important than that of CH_4. The chemically-activated carbon presented a higher specific surface area and micropore volume, which led to a higher adsorption capacity of both CO_2 and CH_4. For methane adsorption, the presence of mesopores facilitated the diffusion of the gas molecules into the micropores. In the case of carbon dioxide adsorption, the presence of more oxygen groups on the water vapor-activated carbon enhanced its adsorption capacity.

Keywords: CO_2 adsorption; CH_4 adsorption; biomass; activated carbon

---

1. Introduction

As part of the efforts being made to fight climate change, governments of 195 countries signed the Paris Agreement, in which they agreed to keep the increase of the global average temperature well below 2 °C from the preindustrial temperatures [1]. In order to meet this target, the EU set a 20-20-20 goal: 20% increase of energy efficiency, 20% reduction of greenhouse gas (GHG) emissions and 20% of EU energy from renewables by 2020. Furthermore, 10% of transportation fuels have to come from renewable sources such as biofuels [2].

Biogas is a gaseous mixture produced when organic matter is degraded by micro-organisms under anaerobic conditions in a process known as anaerobic digestion (AD); its main components are methane (CH_4) in a concentration of 50–70 vol% and carbon dioxide (CO_2) ranging from 30–45 vol% Collected biogas can be directly burned to produce electricity with an efficiency of roughly 38% [3]. Alternatively, the energy density of biogas can be increased by an upgrading process in which the non-combustible gas (CO_2) and other impurities are separated to produce biomethane, a highly-purified methane stream (around 98% purity), which can function as a vehicle fuel or can also be injected into the natural gas grid.

The use of biogas and biomethane as alternative energy sources has gained attention, because it results in the reduction of greenhouse gases from both the burning of fossil fuels and from the landfill of organic wastes, which accounts for 3.2% of the total GHG emissions of the EU. Consequently, in Europe, more than 90% of the produced biogas is already being used for electricity generation, and the upgrading of biogas is being promoted more and more [4]. EU energy production from biomethane rose from 752 GWh in 2011 to 17.264 GWh in 2016 (+16.512 GWh). Moreover, in 2016, biomethane production in Europe increased by 4.971 GWh (+40%), proving an accelerated development in the sector [5].

Adsorption-based processes have been widely explored for the upgrading of biogas. They present several advantages such as relatively low energy requirements and low capital investment costs, flexibility of design, safety and simplicity of operation, as well as a high separation efficiency [6]. In this type of separation technology, the components of a gas mixture are separated by their molecular characteristics and affinity to an adsorbent material. For this purpose, a variety of materials have been studied including zeolites [7–9], carbon molecular sieves (CMS) [10–12], metal organic frameworks (MOFs) [13–15] and activated carbons (ACs) [16–18]. Among these materials, activated carbons present advantages in terms of: (i) hydrophobicity; thus, there is no need for a drying step before upgrading; (ii) low heat of adsorption, therefore a low energy of regeneration; (iii) the possibility of heteroatoms' functionalization to modify their adsorption behavior; and (iv) high CO_2 adsorption capacity at ambient pressure [19]. Furthermore, activated carbons can be produced with a lower cost than other adsorbents, with a wide range of available precursor materials. In fact, any carbonaceous material can be used as a precursor for activated carbon production as long as it has a low ash content and a high proportion of carbon [20]. In this sense, the use of agro-industrial wastes as an alternative to coal and wood as precursors for activated carbon production has been widely studied [21–23]. This waste-valorization process reduces the environmental and economic costs associated with the precursors while eliminating the need for disposal or incineration of unwanted agricultural by-products [24]. Materials such as corn cobs, palm shells, starch, coconut shells, durian shell, olive stones and bamboo have already been studied for activated carbon production [19,25–32]. In particular, olive stones are seen as suitable precursors, giving activated carbon with high adsorption capacities, important mechanical strength and low ash content [29,33]. A complete review of precursors, activation methods and applications of biomass-based activated carbons is available elsewhere [34].

Depending on the activation conditions, ACs can present surface areas as high as 3000 $m^2\,g^{-1}$. Activated carbons can be produced in two ways: physical activation and chemical activation. Physical activation is a two-step process that begins with the carbonization of the precursor at high temperatures (up to 1073 K), a process in which the volatile compounds present in the precursor are removed under an inert atmosphere (i.e., nitrogen atmosphere) producing a carbon-rich material. Carbonization is followed by the activation step: the material is exposed to an oxidizing gas current (such as air, CO_2 and water vapor) at a temperature between 1073 and 1273 K. On the other hand, chemical activation consists of the immersion of the raw material into a dehydrating agent followed by a heat treatment step. Examples of dehydrating agents are sodium and potassium hydroxide (KOH and NaOH), zinc chloride ($ZnCl_2$) and phosphoric acid (H_3PO_4). Chemical activation with KOH results in activated carbons with a high micropore volume, a key factor for CH_4 and CO_2 adsorption; nevertheless, this activation agent presents the disadvantage of low production yields due to the presence of potassium atoms on the resulting structure, which lowers the activated carbon yield; thus, the carbon content of the obtained activated carbon is lower than that of the precursor material. The use of ZnCl as the activation agent has environmental disadvantages due to zinc chloride's high corrosivity. Therefore, H_3PO_4 has become the most used impregnation agent for AC production [35].

Different activation methods and activation conditions (i.e., temperature and time of activation) result in differences in the textural properties such as surface area, pore size distribution and micropore volume, as well as in the chemical properties of the obtained activated carbons. The textural properties are the most determining factor of the adsorption behavior in a physical adsorption process.

However, specific interactions between the adsorbed gas and the adsorbent may also play a role in the adsorption process, and they are unique for each adsorbent/adsorbate pair [36]. Therefore, it is necessary to establish the best activation method for each particular adsorption process.

Several studies have been published on the CH_4 and CO_2 adsorption capacity of CO_2 physically-activated carbon, as well as KOH chemically-activated carbons, but a less important number of works report H_3PO_4 activation [19,25,31,35,37–42]. The literature review shows that the use of olive stones as precursor materials for activated carbon production is a promising alternative for biogas upgrading with the additional advantage of waste valorization. In this context, the present work provides a novel systematic analysis of the influence of both the textural properties and surface chemistry of olive stone activated carbons on the methane and carbon dioxide adsorption. The effect of the activation method (physical versus chemical activation) on the properties of the obtained activated carbons is also discussed. To this end, the adsorption capacity of both methane and carbon dioxide is determined for three activated carbons produced from olive stones by different activation methods: CO_2 physical activation, H_2O physical activation and H_3PO_4 chemical activation. The factors influencing the gas adsorption capacity are discussed in terms of the effect of the activation method on both the textural and chemical properties of the obtained activated carbon.

2. Materials

2.1. Sample Preparation

Three activated carbons were prepared using olive stones provided by an olive oil factory located in Zarzis (Tunisia); two of them were obtained by physical activation and the other one by chemical activation. Prior to the activation procedures, the raw materials, were thoroughly washed with hot distilled water, dried under ambient conditions for 24 h and crushed to form particles with a diameter between 1 and 3 mm. The activated carbon preparation methods are summarized in this section. A detailed description of the selection procedure of the optimal activation conditions and sample characterization can be found in [43–45].

2.1.1. Physical Activation

Two physical activation methods were carried out: activation with water vapor and activation with carbon dioxide. Both methods followed a two-step scheme in which the first step was the carbonization of the precursor under a continuous flow of purified nitrogen with a flow rate of 10 NL/h. Using a heating velocity of 5 K/min, the precursor was heated from room temperature to a temperature of 873 K and kept at this final temperature for 60 min. Nitrogen flow was used in order to evacuate the residual oxygen from the system. The second step was the activation of the samples consisting of placing the sample under a gas flow of the activation agent at a flow velocity of 10 Nl/h and a temperature of 1023 K for 360 min (temperature ramp of 15 K/min). For the water vapor activated carbon (AC-H_2O), the activation agent was water 70 vol. % in N_2. Meanwhile, for CO_2 activation, a flow of pure carbon dioxide was employed.

2.1.2. Chemical Activation

The olive stones were immersed in an orthophosphoric acid aqueous solution (50% w/w) at a weight ratio of 1:3. The mixture was kept under stirring for 9 h at 383 K. Consecutively, the solution was filtrated, dried and flushed by a stream of nitrogen at a temperature of 443 K for 30 min and an extra 150 min at 683 K. The heating velocity during this whole procedure was 5 K/min. The sample, referred to as AC-H_3PO_4, had a chemical activation yield of 33 wt%.

2.2. Samples Properties

The characterization of the activated carbons was done by means of textural properties (such as surface area and pore volume) and surface chemistry. The specific surface area was calculated by means of the Brunauer–Emmett–Teller (BET) method [46] from the linear plot of the nitrogen adsorption isotherm at 77 K in the relative pressure range of 0.05–0.15 (Figure S1 of the Supplementary Materials). Total pore volume was determined by the amount of nitrogen adsorbed by each material at a relative pressure P/P° = 0.99. The *t*-plot method was used for the calculation of the micropore volume. The mesopore volume was defined as the difference between the total pore volume and the micropore volume. Finally, the pore size distribution (PSD) (Figure S2 of the Supplementary Materials) was obtained by non-local density functional theory (NLDFT) using a model for slit carbon pores. The textural properties of the three activated carbons are summarized in Table 1 and can also be found in the literature [43]. The three activated carbons are mainly microporous. The water vapor activated carbon has a higher total pore volume V_{TOT} due to the presence of an important volume of mesopores (V_{meso} = 0.30 cm^3 g^{-1}). The presence of mesopores on water vapor-activated carbons due to a higher gasification of the carbon source of the precursor has been previously reported [43,47]. On the other hand, the chemically-activated carbon AC-H_3PO_4 has significantly higher specific surface area (SSA) and micropore volume V_μ than the physically-activated ones, in agreement with the literature [48].

Table 1. Textural properties of carbon materials. SSA, specific surface area; AC, activated carbon.

Sample	SSA (m^2 g^{-1})	V_μ (cm^3 g^{-1})	V_{TOT} (cm^3 g^{-1})	V_{meso} (cm^3 g^{-1})
AC-H_3PO_4	1178	0.45	0.49	0.04
AC-CO_2	757	0.30	0.32	0.02
AC-H_2O	754	0.28	0.58	0.30

The surface chemistry of the adsorbent can be of great importance for the adsorption process; for this reason, the type and quantity of surface oxygenated groups were determined by means of a home-made temperature programmed desorption device coupled with a mass spectrometer (TPD-MS). In the TPD-MS experiments, a sample weighting 10 mg of each activated carbon was placed in a quartz tube that was introduced to an oven. The temperature of the oven was then increased at a rate of 5 K per minute under vacuum conditions. The surface properties of the sample were analyzed in the temperature range 298–1173 K. During the heating process, the quantitative evolution of gases was analyzed by mass spectrometry. The total amount of emitted CO and CO_2 during the TPD-MS analysis was obtained by integration of the desorption peaks (see Table 2). With the increase of temperature, oxygenated groups decomposed into CO_2 and CO. The desorption temperature gives information about the nature of oxygenated groups present on the carbon surface. Furthermore, by correlation between diffuse reflectance infrared Fourier transform spectroscopy (DRIFTS) spectra of different activated carbons and their TPD-MS profiles, it has been established that the emission of carbon dioxide results from the decomposition of lactones, carboxylic acids and anhydrides, while carbon monoxide is emitted by the decomposition of groups such as phenols, ethers and quinones [49].

Table 2. Cumulated amounts of the emitted CO and CO_2 during the temperature programmed desorption (TPD-MS) analysis of carbon materials.

Sample	CO (mmol g^{-1})	CO_2 (mmol g^{-1})
AC-H_3PO_4	3.43	0.72
AC-CO_2	1.06	0.38
AC-H_2O	1.25	0.39

In this context, the chemically-activated carbon (AC-H_3PO_4) presented higher amounts of oxygenated groups, mainly carboxylic acids, quinones and anhydrides. Among the physically-activated carbons, the water vapor activation resulted in more surface oxygen in the form of phenol and carboxylic acids. Meanwhile, carbon dioxide activation resulted in the formation of quinones, lactones and carboxylic acids on the activated carbon surface [43].

3. Experimental Methodology

3.1. High Pressure Manometric Adsorption Setup

The instrument used in the present study was a high pressure (HP) manometric device. A schematic view of this "homemade" apparatus is provided in Figure 1. The fundamental elements of this apparatus are the dosing cell (V_{dos}) and the adsorption cell (V_{ads}). The pressure was measured by a MKS pressure transducer Baratron Type 121 A MKS Instruments, München, Deutschland). (0.01% uncertainty in the full scale from vacuum to 3.3 MPa) connected to the dosing cell. The two cells were isolated by spherical valves, thus limiting the "dead space" volume. During the adsorption experiments, the isothermal condition of the system was ensured by a heating wire controlled by a Eurotherm 3208 PID. (Schneider Electric, Worthing, United Kingdom). Thermocouples located at several points of the instrument allowed verifying the non-appearance of temperature gradients within the system. This setup was designed to operate over wide a range of pressure (0–3.3 MPa) and temperature up to 373.15 K [50,51].

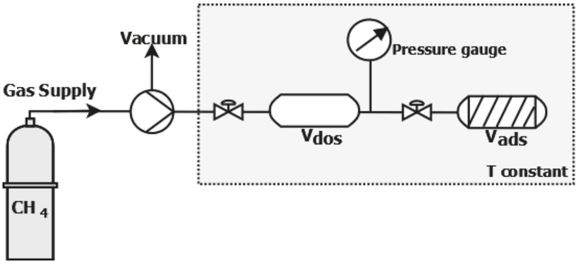

Figure 1. Schematic diagram of the high pressure and high temperature (HP/HT) manometric adsorption setup.

3.2. Determination of Excess Adsorption

Prior to the adsorption experiments, both the dossing cell volume and adsorption cell volume need to be calculated. The volume of the dosing cell was measured by a gravimetric scheme in which the pressure change at a given temperature due to a known quantity of carbon dioxide (CO_2) was recorded, using the NIST isothermal properties of carbon dioxide, the corresponding volume was calculated [52]. The adsorption cell accessible volume, also known as void volume, in the presence of the sample of activated carbon was calculated by helium (He) expansions from the dossing cell to the adsorption cell (helium is considered as a non-sorbing gas). The experimental methodology applied for the adsorption isotherms' measurement was based on a mass balance principle. The uncertainty in the calculations of the void and adsorption cell volume was always less than 0.5%. In all cases, an out-gassing process consisting of keeping the sample under vacuum conditions at 473 K for 10 h was performed before any experiment. The adsorption isotherms were obtained by an accumulative process: successive doses ($\approx$3 bar) of the adsorbate (CH_4 or CO_2) were introduced into the dosing cell and expanded into the adsorption cell. The stability of the pressure was the chosen indicator of equilibrium conditions. The reproducibility of the experiment was tested by repeating one of the adsorption isotherm 3 times, and the absolute standard deviation was found to be less than 1%.

3.3. Parametrization of Excess Adsorption Isotherms

The excess adsorption isotherms were fitted to a modified Langmuir model:

$$n_{exc} = n_L \frac{p}{p + p_L} \left(1 - \frac{\rho_g(p,T)}{\rho_{ads}} \right) \tag{1}$$

In this expression, n_{exc} represents the adsorbed amount of gas (mol kg^{-1}) at a pressure p (MPa); p_L is the pressure at which half of the adsorption sites are occupied (monolayer), also known as the Langmuir pressure; n_L is the maximum Langmuir capacity, which corresponds to the adsorbed amount in which the monolayer is filled; ρ_g is the gas density (kg m^{-3}) at pressure p and temperature T. Meanwhile, ρ_{ads} (kg m^{-3}) stands for the adsorbed phase density; in this work, it was fixed to the inverse of the van der Waals volume of each gas (373 kg m^{-3} for methane and 1027 kg m^{-3} for carbon dioxide) [53]. The Langmuir model has the advantage of taking into account the volume of the adsorbed phase. It has a theoretical basis, whilst other models such as Toth (1995) [54] and Sips (1948) [55] are empirical. This model was initially developed for the low pressure region; nevertheless, it provides a reasonable estimation of the excess adsorption isotherms at higher pressures [17].

The best fit of the Langmuir model for each adsorption isotherm was obtained by minimizing the root mean square error ($RMSE$) provided by Equation (2) [7]:

$$RMSE = \frac{1}{k} \cdot \sqrt{\sum_{1}^{k} (n_{exp} - n_{calc})^2} \tag{2}$$

where n_{exp} and n_{calc} are the experimental and calculated adsorption amounts in mol kg^{-1} at a pressure p for a number k of data points in the adsorption isotherm.

4. Results

CH_4 and CO_2 adsorption isotherms were obtained for the set of three olive stone-based activated carbons (Figures 2 and 3) up to a pressure of 3.2 MPa at two working temperatures: 303.15 and 323.15 K, with a reproducibility superior to 99% (average absolute deviation of less than 1%). All the isotherms were fitted by the Langmuir two-parameter model (see Equation (1)), and the obtained fitting parameters and root mean square error ($RMSE$) are presented in Table 3 (CH_4 adsorption) and Table 4 (CO_2 adsorption). The goodness of the fitting process is depicted by the $RMSE$ values; values under 0.09 were obtained for the fitting of all the isotherms.

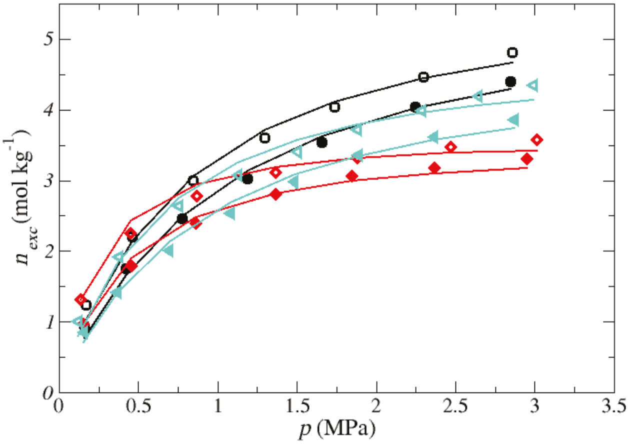

Figure 2. CH_4 adsorption isotherms for the three olive stone-based activated carbons: AC-H_3PO_4 (black circles), AC-CO_2 (red diamonds) and AC-H_2O (turquoise triangles). Open symbols represent the adsorption data at 303.15 K, while the data at 323.15 are shown by the filled symbols. Uncertainties: Δp = 0.01 MPa, ΔT = 0.2 K. The obtained Langmuir fitting isotherms are shown by the solid lines.

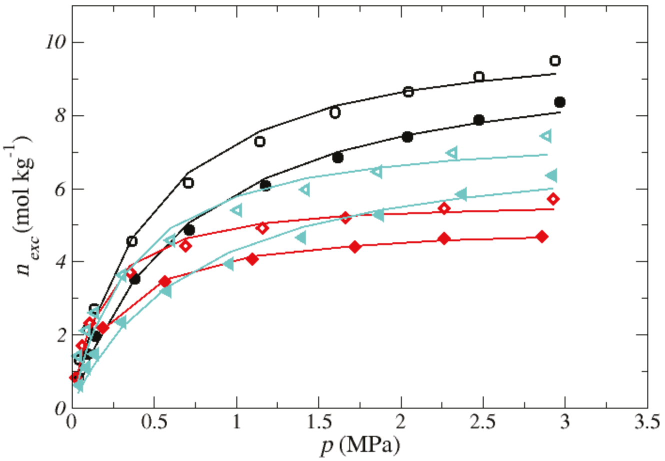

Figure 3. CO_2 adsorption isotherms for the three olive stone-based activated carbons: AC-H_3PO_4 (black circles), AC-CO_2 (red diamonds) and AC-H_2O (turquoise triangles). Open symbols represent the adsorption data at 303.15 K, while the data at 323.15 are shown by the filled symbols. Uncertainties: Δp = 0.01 MPa, ΔT = 0.2 K. The obtained Langmuir fitting isotherms are shown by the solid lines.

A higher adsorption of carbon dioxide than methane can be noticed for the three ACs (Figures 2 and 3). This is a typical behavior of activated carbon adsorption that can be explained by the presence of a quadrupole moment on the molecule of carbon dioxide that leads to stronger adsorptive/adsorbent interactions. Another possible explanation can be given in terms of the critical point of the gases: the critical temperature (190 K) and critical pressure (4.59 MPa) of methane were much lower than those of carbon dioxide (304.45 K and 7.38 MPa), which means that carbon dioxide was in the form of a condensable vapor, while methane acted as a supercritical gas at the adsorption conditions. A lower adsorption and lower maximum Langmuir capacity (n_L) upon an increase in the adsorand Tables 3 and 4, indicating a physical adsorption process. Furthermore, for both adsorptives, the chemically-activated carbon AC-H_3PO_4 showed a higher adsorption capacity; the adsorption tendency varied in the following order: AC-H_3PO_4 > AC-H_2O > AC-CO_2.

Table 3. Langmuir fitting parameters for the CH_4 adsorption isotherms.

CH_4 Adsorption				
Sample	**Temperature (K)**	**n_L (mol kg^{-1})**	**ρ_L (MPa)**	***RMSE***
AC-H_3PO_4	303.15	6.518	0.932	0.042
	323.15	6.369	1.182	0.037
AC-CO_2	303.15	3.913	0.273	0.043
	323.15	3.830	0.076	0.031
AC-H_2O	303.15	5.417	0.714	0.067
	323.15	5.301	1.011	0.056

The superior adsorption of AC-H_3PO_4 can be explained in regards to the textural properties of the samples (see Table 1); the chemically-activated carbon had the highest specific surface area and micropore volume, both adsorption-enhancing factors. A higher surface area means more available physisorption sites, while a linear relationship between the micropore volume and the adsorption of both methane and carbon dioxide has been reported [21,56]. Concerning the difference in the methane adsorption capacity of the two physically-activated carbons, the presence of the mesoporosity of the structure of the water vapor-activated carbon AC-H_2O is thought to be the determining factor. Both physically-activated carbons had similar SSA and micropore volume, with the only difference being the mesopore volume. In fact, it has been shown that activated carbons that combine both micropores and mesopores can adsorb a significantly higher amount of CH_4 than their totally microporous counterparts [57].

Table 4. Langmuir fitting parameters for the CO_2 adsorption isotherms.

CO_2 Adsorption				
Sample	**Temperature (K)**	**n_L (mol kg^{-1})**	**ρ_L (MPa)**	**$RMSE$**
AC-H_3PO_4	303.15	10.873	0.488	0.080
	323.15	10.254	0.733	0.065
AC-CO_2	303.15	5.878	0.181	0.059
	323.15	5.191	0.273	0.020
AC-H_2O	303.15	7.968	0.371	0.073
	323.15	7.721	0.772	0.087

While methane adsorption by activated carbons is only influenced by the textural properties of the adsorbent, the carbon dioxide adsorption is also thought to be related to the surface chemistry. In the present work, the influence of the surface chemistry was depicted by normalizing the CO_2 adsorption isotherms by the surface area (Figure 4). One could expect that by doing this, the adsorption of the chemically-activated carbon would still be the most important due to a higher micropore volume. In reality, the AC-H_2O showed a higher adsorption. Chemical activation with phosphoric acid (H_3PO_4) was reported to produce acid activated carbon surfaces [58], which seems to reduce the interactions between the basic surface groups and the carbon dioxide molecules, explaining its lower adsorption when the textural effect is eliminated by normalizing the adsorption isotherms by the specific surface area. However, the negative influence of acid surface groups on the AC-H_3PO_4 was small compared to the effect of its higher surface area, thus showing a higher adsorption capacity when no normalization of the isotherms was done (Table 4).

Among the two physically-activated carbons, AC-H_2O had the highest quantity of oxygenated surface groups (Table 2), which explains its dominant adsorption when SSA normalized. An increase in the CO_2 adsorption capacity in the presence of oxygen-containing surface functionalities by means of acid-base interactions and hydrogen bond formation between the adsorbate and the activated carbons surface was shown [59,60]. The high electronic density of oxygen on the oxygenated surface groups, due to electron gain from the carbon surface atoms, allowed them to act as electron-donors, in which case the CO_2 adsorbate molecules behaved as basic groups.

Table 5 shows the comparison of the adsorption capacities of the activated carbons studied in this work with other biomass-based activated carbons of the literature. It can be seen that the adsorption values were well in the range reported in the literature for both carbon dioxide and methane. Their competitive adsorption capacities and higher carbon dioxide adsorption capacity over methane made the olive stone activated carbons a suitable material for further studies on the CH_4 and CO_2 storage and separation.

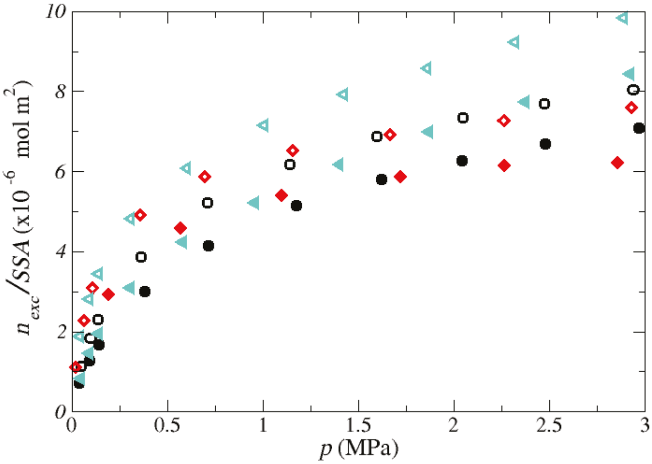

Figure 4. *SSA* normalized CO_2 adsorption isotherms of the activated carbons: AC-H_3PO_4 (black circles), AC-CO_2 (red diamonds) and AC-H_2O (turquoise triangles). Open symbols represent the adsorption data at 303.15 K, while the data at 323.15 are shown by the filled symbols 323.15 K.

Table 5. Adsorption capacities of different biomass-based adsorbents.

CO_2 and CH_4 Adsorption Capacity					
Sample	**Precursor**	**Activation Agent**	**Temperature (K)**	**CH_4 Adsorption Capacity (mol kg^{-1})**	**CO_2 Adsorption Capacity (mol kg^{-1})**
AC-H_3PO_4 *	Olive stones	H_3PO_4	303.15	6.518	10.873
AC-CO_2 *	Olive stones	CO_2	303.15	3.913	5.878
AC-H_2O *	Olive stones	H_2O *	303.15	5.417	7.968
BC [19]	Babassu coconut	CO_2	293	5.343	10.49
CS [19]	Coconut shell	CO_2	293	7.259	14.67
Pinpel20 [61]	Wood pellets	CO_2	303	3.36	6.66
MSS-AC [62]	Mango Seeds	H_3PO_4	303	0.858	8.788
CS-H_2O [39]	Cherry stones	H_2O	303	8.36	14.45

* This work.

5. Conclusions

In this work, the effects of the textural and chemical properties of three activated carbons on the adsorption behavior of carbon dioxide and methane were studied. For this purpose, three activated carbons produced from olive stones by CO_2 physical activation, H_2O physical activation and H_3PO_4 chemical activation were employed. The activated carbons were mainly microporous. The activated carbon obtained by chemical activation with phosphoric acid of the precursor material presents a higher surface area, total pore volume and micropore volume, which led to a higher adsorption capacity for both methane and carbon dioxide. Even though the two physically-activated carbons had similar surface areas and micropore volume, the water vapor-activated carbon had also an important volume of mesopores that facilitated the diffusion of the methane molecules into the micropores; thus, its methane adsorption capacity was higher. In the case of carbon dioxide, adsorption-specific interactions between the adsorptive and adsorbent were also found to participate in the adsorption process. Amongst the two physically-activated carbons, H_2O-activated carbon had the highest content of oxygen surface group and therefore a higher CO_2 adsorption capacity. Nevertheless, even if the surface chemistry of the adsorbents can influence the adsorption of carbon dioxide, textural properties are still the main governing parameters. Finally, the three activated carbons from olive stones had a higher adsorption of carbon dioxide than methane, meaning a higher selectivity towards carbon dioxide than methane. Furthermore, their carbon dioxide and methane adsorption capacities were found to be in the range of other biomass-based activated carbons reported in the literature, making them suitable candidates for the upgrading of biogas.

Supplementary Materials: The following are available online at http://www.mdpi.com/1996-1073/11/11/3136/s1, Figure S1: Adsorption and desorption of nitrogen (N2) at 77 K on the olive stone activated carbons. Figure S2: Pore size distribution (PSD) of the olive stone activated carbons obtained by means of density functional theory (DFT). Figure S3: Emitted CO_2 during temperature programmed desorption-mass spectroscopy (TPD-MS) of the olive stone activated carbons. Figure S4: Emitted CO during temperature programmed desorption-mass spectroscopy (TPD-MS) of the olive stone activated carbons.

Author Contributions: Sample preparation and characterization: I.G., C.M.G. and M.J. Adsorption isotherms: D.P.-M., C.H. and D.B. Writing of the article: D.P.-M. Revision of the article content: All of the authors.

Funding: This research received no external funding

Acknowledgments: Deneb Peredo is grateful to CONACyT for the fellowship 293897 to pursue her PhD degree.

Conflicts of Interest: The authors declare no conflict of interest.

References

1. European Comission. Paris Agreement. Available online: https://ec.europa.eu/clima/policies/international/negotiations/paris_en (accessed on 12 November 2018)
2. European Comission. Renewable Energy. Moving towards a low carbon economy. Available online: https://ec.europa.eu/energy/en/topics/renewable-energy (accessed on 12 November 2018)
3. Starr, K.; Villalba, G.; Gabarrell, X. Upgraded biogas from municipal solid waste for natural gas substitution and CO_2 reduction—A case study of Austria, Italy, and Spain. *Waste Manag.* **2015**, *38*, 105–116, doi:10.1016/j.wasman.2015.01.001. [CrossRef] [PubMed]
4. Sahota, S.; Shah, G.; Ghosh, P.; Kapoor, R.; Sengupta, S.; Singh, P.; Vijay, V.; Sahay, A.; Vijay, V.K.; Thakur, I.S. Review of trends in biogas upgradation technologies and future perspectives. *Bioresour. Technol. Rep.* **2018**, *1*, 79–88, doi:10.1016/j.biteb.2018.01.002. [CrossRef]
5. EBA European Biogas Association. EBA Statictical Report 2017 Published Soon. Available online: http://european-biogas.eu/2017/12/14/eba-statistical-report-2017-published-soon/ (accessed on 12 November 2018)
6. Angelidaki, I.; Treu, L.; Tsapekos, P.; Luo, G.; Campanaro, S.; Wenzel, H.; Kougias, P.G. Biogas upgrading and utilization: Current status and perspectives. *Biotechnol. Adv.* **2018**, *36*, 452–466, doi:10.1016/j.biotechadv.2018.01.011. [CrossRef] [PubMed]
7. Jiang, Y.; Ling, J.; Xiao, P.; He, Y.; Zhao, Q.; Chu, Z.; Liu, Y.; Li, Z.; Webley, P.A. Simultaneous biogas purification and CO_2 capture by vacuum swing adsorption using zeolite NaUSY. *Chem. Eng. J.* **2018**, *334*, 2593–2602, doi:10.1016/j.cej.2017.11.090. [CrossRef]
8. Gong, H.; Lee, S.S.; Bae, T.H. Mixed-matrix membranes containing inorganically surface-modified 5A zeolite for enhanced CO_2/CH_4 separation. *Microporous Mesoporous Mater.* **2017**, *237*, 82–89, doi:10.1016/j.micromeso.2016.09.017. [CrossRef]
9. Kennedy, D.A.; Tezel, F.H. Cation exchange modification of clinoptilolite—Screening analysis for potential equilibrium and kinetic adsorption separations involving methane, nitrogen, and carbon dioxide. *Microporous Mesoporous Mater.* **2018**, *262*, 235–250, doi:10.1016/j.micromeso.2017.11.054. [CrossRef]
10. Son, S.J.; Choi, J.S.; Choo, K.Y.; Song, S.D.; Vijayalakshmi, S.; Kim, T.H. Development of carbon dioxide adsorbents using carbon materials prepared from coconut shell. *Korean J. Chem. Eng.* **2005**, *22*, 291–297, doi:10.1007/BF02701500. [CrossRef]
11. Rocha, L.A.; Andreassen, K.A.; Grande, C.A. Separation of CO_2/CH_4 using carbon molecular sieve (CMS) at low and high pressure. *Chem. Eng. Sci.* **2017**, *164*, 148–157, doi:10.1016/j.ces.2017.01.071. [CrossRef]
12. Arya, A.; Divekar, S.; Rawat, R.; Gupta, P.; Garg, M.O.; Dasgupta, S.; Nanoti, A.; Singh, R.; Xiao, P.; Webley, P.A. Upgrading biogas at low pressure by vacuum swing adsorption. *Ind. Eng. Chem. Res.* **2015**, *54*, 404–413, doi:10.1021/ie503243f. [CrossRef]
13. Samarasinghe, S.A.; Chuah, C.Y.; Yang, Y.; Bae, T.H. Tailoring CO_2/CH_4 separation properties of mixed-matrix membranes via combined use of two- and three-dimensional metal-organic frameworks. *J. Membr. Sci.* **2018**, *557*, 30–37, doi:10.1016/j.memsci.2018.04.025. [CrossRef]

14. Zacharia, R.; Gomez, L.F.; Chahine, R.; Cossement, D.; Benard, P. Thermodynamics and kinetics of CH_4/CO_2 binary mixture separation by metal-organic frameworks from isotope exchange and adsorption break-through. *Microporous Mesoporous Mater.* **2018**, *263*, 165–172, doi:10.1016/j.micromeso.2017.12.011. [CrossRef]
15. Cheng, Y.; Wang, X.; Jia, C.; Wang, Y.; Zhai, L.; Wang, Q.; Zhao, D. Ultrathin mixed matrix membranes containing two-dimensional metal-organic framework nanosheets for efficient CO_2/CH_4 separation. *J. Membr. Sci.* **2017**, *539*, 213–223, doi:10.1016/j.memsci.2017.06.011. [CrossRef]
16. Yao, K.X.; Chen, Y.; Lu, Y.; Zhao, Y.; Ding, Y. Ultramicroporous carbon with extremely narrow pore distribution and very high nitrogen doping for efficient methane mixture gases upgrading. *Carbon* **2017**, *122*, 258–265, doi:10.1016/j.carbon.2017.06.073. [CrossRef]
17. Koonaphapdeelert, S.; Moran, J.; Aggarangsi, P.; Bunkham, A. Low pressure biomethane gas adsorption by activated carbon. *Energy Sustain. Dev.* **2018**, *43*, 196–202, doi:10.1016/j.esd.2018.01.010. [CrossRef]
18. Saha, D.; Nelson, K.; Chen, J.; Lu, Y.; Ozcan, S. Adsorption of CO_2 ,CH_4, and N_2 in Micro-Mesoporous Nanographene: A Comparative Study. *J. Chem. Eng. Data* **2015**, *60*, 2636–2645, doi:10.1021/acs.jced.5b00291. [CrossRef]
19. Vilella, P.C.; Lira, J.A.; Azevedo, D.C.; Bastos-Neto, M.; Stefanutti, R. Preparation of biomass-based activated carbons and their evaluation for biogas upgrading purposes. *Ind. Crops Prod.* **2017**, *109*, 134–140, doi:10.1016/j.indcrop.2017.08.017. [CrossRef]
20. Rashidi, N.A.; Yusup, S. An overview of activated carbons utilization for the post-combustion carbon dioxide capture. *J. CO_2 Util.* **2016**, *13*, 1–16, doi:10.1016/j.jcou.2015.11.002. [CrossRef]
21. Serafin, J.; Narkiewicz, U.; Morawski, A.W.; Wróbel, R.J.; Michalkiewicz, B. Highly microporous activated carbons from biomass for CO_2 capture and effective micropores at different conditions. *J. CO_2 Util.* **2017**, *18*, 73–79, doi:10.1016/j.jcou.2017.01.006. [CrossRef]
22. Yadavalli, G.; Lei, H.; Wei, Y.; Zhu, L.; Zhang, X.; Liu, Y.; Yan, D. Carbon dioxide capture using ammonium sulfate surface modified activated biomass carbon. *Biomass Bioenergy* **2017**, *98*, 53–60, doi:10.1016/j.biombioe.2017.01.015. [CrossRef]
23. Hao, W.; Björkman, E.; Lilliestråle, M.; Hedin, N. Activated carbons prepared from hydrothermally carbonized waste biomass used as adsorbents for CO_2. *Appl. Energy* **2013**, *112*, 526–532, doi:10.1016/j.apenergy.2013.02.028. [CrossRef]
24. Gil, R.R.; Ruiz, B.; Lozano, M.S.; Fuente, E. Influence of the pyrolysis step and the tanning process on KOH-activated carbons from biocollagenic wastes. Prospects as adsorbent for CO_2 capture. *J. Anal. Appl. Pyrolysis* **2014**, *110*, 194–204, doi:10.1016/j.jaap.2014.09.001. [CrossRef]
25. Bagheri, N.; Abedi, J. Adsorption of methane on corn cobs based activated carbon. *Chem. Eng. Res. Des.* **2011**, *89*, 2038–2043, doi:10.1016/j.cherd.2011.02.002. [CrossRef]
26. Arami-Niya, A.; Daud, W.M.A.W.; Mjalli, F.S. Comparative study of the textural characteristics of oil palm shell activated carbon produced by chemical and physical activation for methane adsorption. *Chem. Eng. Res. Des.* **2011**, *89*, 657–664, doi:10.1016/j.cherd.2010.10.003. [CrossRef]
27. Alabadi, A.; Razzaque, S.; Yang, Y.; Chen, S.; Tan, B. Highly porous activated carbon materials from carbonized biomass with high CO_2 capturing capacity. *Chem. Eng. J.* **2015**, *281*, 606–612, doi:10.1016/j.cej.2015.06.032. [CrossRef]
28. Chen, Y.; Zhou, L.j.; Hong, Y.z.; Cao, F.; Li, L.; Li, J.b. Preparation of high-surface-area activated carbon from coconut shell fibers. *Carbon* **2010**, *48*, 3005, doi:10.1016/j.carbon.2010.03.059. [CrossRef]
29. Iley, M.; Marsh, H.; Rodriguez-Reinoso, F. The Adsorptive Properties of Carbonised Olive Stones. *Carbon* **1973**, *11*, 633–636, doi:10.1016/0008-6223(73)90330-8. [CrossRef]
30. Zhao, G.; Zou, G.; Hou, H.; Ge, P.; Cao, X.; Ji, X. Sulfur-doped carbon employing biomass-activated carbon as a carrier with enhanced sodium storage behavior. *J. Mater. Chem. A* **2017**, *5*, 24353–24360, doi:10.1039/C7TA07860A. [CrossRef]
31. Yakout, S.M.; Sharaf El-Deen, G. Characterization of activated carbon prepared by phosphoric acid activation of olive stones. *Arab. J. Chem.* **2016**, *9*, S1155–S1162, doi:10.1016/j.arabjc.2011.12.002. [CrossRef]
32. Wei, H.; Deng, S.; Hu, B.; Chen, Z.; Wang, B.; Huang, J.; Yu, G. Granular Bamboo-Derived Activated Carbon for High CO_{2} Adsorption: The Dominant Role of Narrow Micropores. *ChemSusChem* **2012**, *5*, 2354–2360, doi:10.1002/cssc.201200570. [CrossRef] [PubMed]

33. Álvarez-Gutiérrez, N.; García, S.; Gil, M.V.; Rubiera, F.; Pevida, C. Towards bio-upgrading of biogas: Biomass waste-based adsorbents. *Energy Procedia* **2014**, *63*, 6527–6533, doi:10.1016/j.egypro.2014.11.688. [CrossRef]
34. González-García, P. Activated carbon from lignocellulosics precursors: A review of the synthesis methods, characterization techniques and applications. *Renew. Sust. Energy Rev.* **2018**, *82*, 1393–1414, doi:10.1016/j.rser.2017.04.117. [CrossRef]
35. Gil, M.V.; Martínez, M.; García, S.; Rubiera, F.; Pis, J.J.; Pevida, C. Response surface methodology as an efficient tool for optimizing carbon adsorbents for CO_2 capture. *Fuel Process. Technol.* **2013**, *106*, 55–61, doi:10.1016/j.fuproc.2012.06.018. [CrossRef]
36. Djeridi, W.; Ben Mansour, N.; Ouederni, A.; Llewellyn, P.L.; El Mir, L. Influence of the raw material and nickel oxide on the CH_4 capture capacity behaviors of microporous carbon. *Int. J. Hydrogen Energy* **2015**, *40*, 13690–13701, doi:10.1016/j.ijhydene.2015.05.010. [CrossRef]
37. Soudani, N.; Najar-Souissi, S.; Abderkader-Fernandez, V.; Ouederni, A. Effects of nitrogen plasma treatment on the surface characteristics of olive stone-based activated carbon. *Environ. Technol.* **2017**, *38*, 956–966, doi:10.1080/09593330.2016.1214626. [CrossRef] [PubMed]
38. Balsamo, M.; Tsyntsarski, B.; Erto, A.; Budinova, T.; Petrova, B.; Petrov, N.; Lancia, A. Dynamic studies on carbon dioxide capture using lignocellulosic based activated carbons. *Adsorption* **2015**, *21*, 633–643, doi:10.1007/s10450-015-9711-7. [CrossRef]
39. Álvarez-Gutiérrez, N.; García, S.; Gil, M.V.; Rubiera, F.; Pevida, C. Dynamic Performance of Biomass-Based Carbons for CO_2/CH_4 Separation. Approximation to a Pressure Swing Adsorption Process for Biogas Upgrading. *Energy Fuels* **2016**, *30*, 5005–5015, doi:10.1021/acs.energyfuels.6b00664. [CrossRef]
40. Erto, A.; Tsyntsarski, B.; Balsamo, M.; Budinova, T.; Lancia, A.; Petrova, B.; Petrov, N. Synthesis of Activated Carbons by Thermal Treatments of Agricultural Wastes for CO_2 Capture from Flue Gas. *Combust. Sci. Technol.* **2016**, *188*, 581–593, doi:10.1080/00102202.2016.1138809. [CrossRef]
41. Moussa, M.; Bader, N.; Querejeta, N.; Durán, I.; Pevida, C.; Ouederni, A. Toward sustainable hydrogen storage and carbon dioxide capture in post-combustion conditions. *J. Environ. Chem. Eng.* **2017**, *5*, 1628–1637, doi:10.1016/j.jece.2017.03.003. [CrossRef]
42. Balsamo, M.; Silvestre-Albero, A.; Silvestre-Albero, J.; Erto, A.; Rodríguez-Reinoso, F.; Lancia, A. Assessment of CO_2 adsorption capacity on activated carbons by a combination of batch and dynamic tests. *Langmuir* **2014**, *30*, 5840–5848, doi:10.1021/la500780h. [CrossRef] [PubMed]
43. Ghouma, I.; Jeguirim, M.; Sager, U.; Limousy, L.; Bennici, S.; Däuber, E.; Asbach, C.; Ligotski, R.; Schmidt, F.; Ouederni, A. The potential of activated carbon made of agro-industrial residues in NOx immissions abatement. *Energies* **2017**, *10*, 508, doi:10.3390/en10101508. [CrossRef]
44. Ghouma, I.; Jeguirim, M.; Dorge, S.; Limousy, L.; Matei Ghimbeu, C.; Ouederni, A. Activated carbon prepared by physical activation of olive stones for the removal of NO_2 at ambient temperature. *Comptes Rendus Chimie* **2015**, *18*, 63–74, doi:10.1016/j.crci.2014.05.006. [CrossRef]
45. Limousy, L.; Ghouma, I.; Ouederni, A.; Jeguirim, M. Amoxicillin removal from aqueous solution using activated carbon prepared by chemical activation of olive stone. *Environ. Sci. Pollut. R.* **2017**, *24*, 9993–10004, doi:10.1007/s11356-016-7404-8. [CrossRef] [PubMed]
46. Brunauer, S.; Emmett, P.H.; Teller, E. Adsorption of Gases in Multimolecular Layers. *J. Am. Chem. Soc.* **1938**, *60*, 309–319. [CrossRef]
47. Román, S.; Ledesma, B.; Álvarez-Murillo, A.; Al-Kassir, A.; Yusaf, T. Dependence of the microporosity of activated carbons on the lignocellulosic composition of the precursors. *Energies* **2017**, *10*, 542, doi:10.3390/en10040542. [CrossRef]
48. Song, T.; Liao, J.M.; Xiao, J.; Shen, L.H. Effect of micropore and mesopore structure on CO_2 adsorption by activated carbons from biomass. *Xinxing Tan Cailiao/New Carbon Mater.* **2015**, *30*, 156–166, doi:10.1016/S1872-5805(15)60181-0. [CrossRef]
49. Figueiredo, J.; Pereira, M.; Freitas, M.; Órfão, J. Modification of the surface chemistry of activated carbons. *Carbon* **1999**, *37*, 1379–1389, doi:10.1016/S0008-6223(98)00333-9. [CrossRef]
50. Ortiz Cancino, O.P.; Peredo Mancilla, D.; Pozo, M.; Pérez, E.; Bessieres, D. Effect of Organic Matter and Thermal Maturity on Methane Adsorption Capacity on Shales from the Middle Magdalena Valley Basin in Colombia. *Energy Fuels* **2017**, *31*, 11698–11709, doi:10.1021/acs.energyfuels.7b01849. [CrossRef]

51. Peredo-Mancilla, D.; Hort, C.; Jeguirim, M.; Ghimbeu, C.M.; Limousy, L.; Bessieres, D. Experimental Determination of the CH_4 and CO_2 Pure Gas Adsorption Isotherms on Different Activated Carbons. *J. Chem. Eng. Data* **2018**, doi:10.1021/acs.jced.8b00297. [CrossRef]
52. National Institute of Standards and Technology NIST, U.S. Secretary of Commerce. Isothermal Properties for Carbon Dioxide. Available online: https://webbook.nist.gov/cgi/cbook.cgi?Name=carbon+dioxide&Units=SI (accessed on 12 November 2018).
53. Gensterblum, Y.; Merkel, A.; Busch, A.; Krooss, B.M. High-pressure CH_4 and CO_2 sorption isotherms as a function of coal maturity and the influence of moisture. *Int. J. Coal Geol.* **2013**, *118*, 45–57, doi:10.1016/j.coal.2013.07.024. [CrossRef]
54. Tóth, J. Uniform interpretation of gas/solid adsorption. *Adv. Colloid Interface Sci.* **1995**, *55*, 1–239, doi:10.1016/0001-8686(94)00226-3. [CrossRef]
55. Sips, R. On the Structure of a Catalyst Surface. *J. Chem. Phys.* **1948**, *16*, 490–495, doi:10.1063/1.1746922. [CrossRef]
56. Lozano-Castelló, D.; Cazorla-Amorós, D.; Linares-Solano, A.; Quinn, D.F. Influence of pore size distribution on methane storage at relatively low pressure: Preparation of activated carbon with optimum pore size. *Carbon* **2002**, *40*, 989–1002, doi:10.1016/S0008-6223(01)00235-4. [CrossRef]
57. Casco, M.E.; Martínez-Escandell, M.; Gadea-Ramos, E.; Kaneko, K.; Silvestre-Albero, J.; Rodríguez-Reinoso, F. High-pressure methane storage in porous materials: Are carbon materials in the pole position? *Chem. Mater.* **2015**, *27*, 959–964, doi:10.1021/cm5042524. [CrossRef]
58. Nowicki, P.; Wachowska, H.; Pietrzak, R. Active carbons prepared by chemical activation of plum stones and their application in removal of NO_2. *J. Hazard. Mater.* **2010**, *181*, 1088–1094, doi:10.1016/j.jhazmat.2010.05.126. [CrossRef] [PubMed]
59. Liu, Y.; Wilcox, J. Molecular Simulation Studies of CO_2 Adsorption by Carbon Model Compounds for Carbon Capture and Sequestration Applications. *Environ. Sci. Technol.* **2013**, *47*, 95–101, doi:10.1021/es3012029. [CrossRef] [PubMed]
60. Xing, W.; Liu, C.; Zhou, Z.; Zhou, J.; Wang, G.; Zhuo, S.; Xue, Q.; Song, L.; Yan, Z. Oxygen-containing functional group-facilitated CO_2 capture by carbide-derived carbons. *Nanoscale Res. Lett.* **2014**, *9*, 1–8, doi:10.1186/1556-276X-9-189. [CrossRef] [PubMed]
61. Vivo-Vilches, J.F.; Pérez-Cadenas, A.F.; Maldonado-Hódar, F.J.; Carrasco-Marín, F.; Faria, R.P.V.; Ribeiro, A.M.; Ferreira, A.F.P.; Rodrigues, A.E. Biogas upgrading by selective adsorption onto CO_2 activated carbon from wood pellets. *J. Environ. Chem. Eng.* **2017**, *5*, 1386–1393, doi:10.1016/j.jece.2017.02.015. [CrossRef]
62. Munusamy, K.; Somani, R.S.; Bajaj, H.C. Breakthrough adsorption studies of mixed gases on mango (*Mangifera indica* L.) seed shell derived activated carbon extrudes. *J. Environ. Chem. Eng.* **2015**, *3*, 2750–2759, doi:10.1016/j.jece.2015.05.010. [CrossRef]

energies

MDPI

Article

Biochar and Biomass Ash as a Soil Ameliorant: The Effect on Selected Soil Properties and Yield of Giant Miscanthus (Miscanthus x giganteus)

Bogdan Saletnik *, Grzegorz Zagula, Marcin Bajcar, Maria Czernicka and Czeslaw Puchalski

Department of Bioenergetics and Food Analysis, Faculty of Biology and Agriculture, Rzeszow University, Cwiklinskiej 2D, 35-601 Rzeszow, Poland; g_zagula@ur.edu.pl (G.Z.); mbajcar@ur.edu.pl (M.B.); czernicka.maria@gmail.com (M.C.); cpuchal@ur.edu.pl (C.P.)

* Correspondence: bogdan.saletnik@urz.pl; Tel.: +48-177-854-965

Received: 15 August 2018; Accepted: 20 September 2018; Published: 22 September 2018

Abstract: We assess the possibility of using biochar and ash from plant biomass to fertilise giant miscanthus (*Miscanthus* x *giganteus*). The paper concerns the optimisation of the combination of fertiliser applications of the aforementioned materials in the context of the plant yield obtained. There was an increase in yield of 8–68% over the two years of research when compared with the control plots. It was found that the application of biochar, ash from biomass and a combination of the two at appropriate rates as a soil additive can substitute for classic mineral fertilisers and strengthen the ecological aspects of energy crop cultivation. The interpretation of the results obtained enabled the selection of optimum fertiliser applications, resulting in a significant increase in the yield of plants and an improvement in soil chemical properties. It was found that the highest yield of dry matter of giant miscanthus plants, after both the first and second year of cultivation, was obtained by applying the fertiliser containing ash at a rate of 1.5 t ha^{-1}, together with biocarbon and the combination of biochar and ash at a rate of 1.5 t ha^{-1}.

Keywords: biochar; ash from biomass; giant miscanthus; fertilisation

---

1. Introduction

Plant biomass, due to its specific chemical structure and high calorific value, can be used in numerous conversion processes aimed at the production of solid, liquid and gaseous fuels [1]. The acquisition of energy from biomass is possible through its conversion in the form of direct combustion, co-incineration with coal, gasification, pyrolysis, and fermentation [2].

The factors determining the growth performance of biomass in energy crops are the choice of plant species and production cycle, including the location of the plantation and appropriate fertilisation. In turn, the proper preparation of the material and the optimisation of the technological process, including the management of waste products, i.e., ashes generated during combustion, affect the efficiency of using biomass as an energy source. Both the cultivation of energy crops and the utilisation of the ash from biomass are part of sustainable energy management and have a huge impact on the environment. Agroenergy is also recommended from an environmental protection point of view to carry out agrotechnical sanitation in contaminated areas, especially those with toxic metals [3]. Ash from biomass, according to data available in the literature, can favourably affect the physicochemical properties of soils to a comparable or even greater degree than mineral fertiliser [4]. According to the latest research, the effective improvement of the physicochemical properties of soils and the increase in fertility of less fertile soils can be obtained by using biochar. Biochar is a material formed in the process of thermal conversion of biomass under conditions of limited access of oxygen, which results in the formation of a product with a high carbon content and very good sorption properties [5]. In addition, it was proven that biochar has high chemical reactivity to organic and inorganic compounds present in the soil environment, and therefore its potential use in the reclamation of chemically degraded soils is more and more frequently discussed. From an agricultural point of view, the introduction of biochar into soils provides many benefits by improving physical, chemical and biological properties, which in turn contributes to an increase in crop yield [6,7].

From an agricultural point of view, the introduction of biochars into soils as agents that improve their properties seems to be beneficial due to the possibility of improving the conditions for the growth, development and increased yield of crops [7]. In addition, in view of the rapid effects and relatively low costs of using them, biochar compounds are more and more often used in the remediation and soil protection process [8]. The performance of biochar introduced into the soil environment mainly depends on the raw materials used for its production, as well as the parameters of the pyrolysis process. They determine the contents of macro- and microelements, as well as harmful substances such as heavy metals. The heterogenous chemical composition of biochars allows their interaction with a large group of inorganic and organic compounds present in the soil [9]. Various properties of these materials allow reactions with mineral and organic particles in the soil, as well as the formation of mineral–organic complexes [10]. Biochars introduced into the soil are characterised by high stability and resistance to biological decomposition, which is why they are considered a highly effective agent of carbon dioxide sequestration in the soil [11]. In addition, the application of biochars not only allows the soil to increase its carbon content, but also other biogenic compounds, such as phosphorus, potassium, magnesium and nitrogen [12,14]. The high ion-exchange capacity and the specific surface of biochars contribute to the reduction of leaching of biogenic elements from the soil environment and reduce the emission of nitrogen oxide [14]. Biochars introduced into the soil as fertiliser materials also affect the increase in soil pH [15]. The research conducted so far has shown that biochars contain numerous alkaline substances, such as calcium carbonate, which may affect the soil pH, and the best results in the form of pH increase can be obtained in heavily acidified soils [16,17]. Biochar added to the soil also affects its physical properties by increasing the ability to form soil aggregates and resistance to erosion or improvement in water retention [18]. The improvement of physical properties of soils after the application of the biochar additive mainly depends on its properties, which are predominantly determined by the technology used in its production [19,20]. The highly porous structure of biochars can also create a favourable environment for the existence of microorganisms, which results in increased fertility and soil productivity [21].

Giant miscanthus (*Miscanthus* x *giganteus)* is a long-term energy crop, characterised by high yield potential. This impressive grass originates from tropical, subtropical and more temperate areas of Southeast Asia. In its natural environment it can reach 6 meters in height, and the diameter of stiff sprouts can be 20 mm. It has been known in Europe for about 50 years; it was originally treated as an ornamental plant, and then started to be used for energy purposes. This plant is a natural hybrid that was created by crossing *Miscanthus sinensis* and *Miscanthus sacchariflorus*. This interspecific hybrid belongs to the group of plants with the C-4 photosynthetic cycle, which is an efficient process of photosynthesis. In the first year of cultivation, the miscanthus can reach a height of about 2 meters and the yield is at the level of 2–5 t ha^{-1} dry matter. In the second year of cultivation, the plants can reach a height of more than 3 meters and the obtained yield can be at the level of 8–10 t ha^{-1} dry matter. In order to ensure the correct rate of plant growth, it is important to apply an appropriate fertilizer dose in the initial growing period. The maximum potential harvesting of miscanthus starts from the third year of cultivation. High biomass yields, which can reach over 20 t ha^{-1} of dry matter, can keep to 10 years during harvesting.Biomass from the giant miscanthus is a very high-quality form of 'fuel' intended for direct combustion. It also has high potential as a substrate in bio-oil production, gasification and charring processes [22,23].

The purpose of the paper is to assess the possibility of using biochar and ash formed through the plant biomass combustion process as a fertiliser used in the cultivation of giant miscanthus (*Miscanthus* x *giganteus)* and the optimisation of the combination of fertiliser applications. Prior to the studies, the following research problem was formulated: if biochar and ash from plant biomass can be used as a fertiliser in the cultivation of energy crops, which has a positive effect on soil properties and increases crop yields?

2. Results

2.1. Names of Tests

The tests used for further identification are described by symbols, due to the type and application rate of the fertiliser used:

- B1/P1 (control test—no fertiliser),
- P2 (fertilised with ash at a dose of 1.5 t ha^{-1}),
- P3 (fertilised with ash at a dose of 3.0 t ha^{-1}),
- P4 (fertilised with ash at a dose of 4.5 t ha^{-1}),
- B2/P1 (fertilised with biochar at a dose of 11.5 t ha^{-1}),
- B2/P2 (fertilised with biochar and ash at doses of 11.5 and 1.5 t ha^{-1}, respectively),
- B2/P3 (fertilised with biochar and ash at doses of 11.5 and 3.0 t ha^{-1}, respectively),
- B2/P4 (fertilised with biochar and ash at doses of 11.5 and 4.5 t ha^{-1}, respectively).

2.2. Biochar and Biomass Ash

Tables 1 and 2 present the results of the pH value, total carbon and total nitrogen content, ash and water content, volatile substances and contents of available forms of the chosen minerals in biochar and biomass ash used as fertilisers.

Table 1. pH value, contents of absorbable forms of macroelements and percentage content of carbon and nitrogen in biochar and ash from biomass.

	pH (KCl)	**Carbon**	**Nitrogen**	**P_2O_5**	**K_2O**	**Mg**
		%		**mg kg^{-1}**		
		x ± SD				
Biochar	6.59 ± 0.21	74.35 ± 0.24	0.93 ± 0.07	1382 ± 41	5752 ± 63	645 ± 22
Ash	12.89 ± 0.32	1.22 ± 0.22	0.17 ± 0.01	6394 ± 52	91133 ± 4	31306 ± 74

x—average, SD—standard deviation.

Table 2. Contents of water, ash and volatile substances in biochar and ash from biomass.

	Water	**Ash**	**Volatile Substances**
	%		
	x ± SD		
Biochar	9.11 ± 0.03	11.57 ± 0.21	66.42 ± 0.18
Ash	-	-	94.42 ± 0.27

x—average, SD—standard deviation.

Table 3 presents the contents of selected macro- and microelements in biochar and ash from biomass. Ash from biomass was characterised by a higher content of all the ingredients studied than that found in biochar. Bearing in mind that fertilisers used in agriculture may contain toxic metals, the fertiliser material applied was examined. Aluminium, arsenic, cadmium and lead were not present in the materials analysed.

Table 3. Contents of selected macro- and microelements in biochar and ash from biomass.

	Al	**As**	**Ca**	**Cd**	**Cr**	**Cu**	**Mn**
				mg kg^{-1}			
				x ± SD			
Biochar	< 0.01	< 0.01	18,520 ± 21	< 0.01	< 0.01	10 ± 0.8	240 ± 2.5
Ash	< 0.01	< 0.01	131,220 ± 35	< 0.01	50 ± 0.9	110 ± 0.7	1930 ± 9.5
	Mo	**Na**	**Ni**	**Pb**	**S**	**Sr**	**Zn**
				mg kg^{-1}			
				x ± SD			
Biochar	< 0.01	< 0.01	< 0.01	< 0.01	880 ± 12	< 0.01	130 ± 11.5
Ash	< 0.01	< 0.01	40 ± 2.5	< 0.01	19,710 ± 23	< 0.01	710 ± 8.2

x—average, SD—standard deviation.

2.3. Soil

Figure 1 shows the pH value of the soil before the experiment (2015) and after the first and second year of cultivation, depending on the fertiliser used. The soil taken from the area on which the field experiment was carried out was, as in the previous experiment, characterised by an acid reaction (pH in 1M KCl—4.98). The pH value of the soil determined for the control plots (no fertilisation) was 5.13, after both the first and second year of cultivation. There were no statistically significant differences for this variant when compared to the results obtained prior to the experiment. The addition of biochar, ash and their mixture in the soil influenced the increase in the pH value of the soil to a statistically significant extent when compared to the results obtained in 2015 (in 13 cases out of the 16 analysed). Depending on the type of fertiliser used and its application rate, there was an increase in the study parameter by a value in the range from 0.19 to 1.29 after the first year and from 0.04 to 1.13 after the second year of cultivation when compared to the control group. The highest concentrations of hydrogen ions in the soil, after both the first and second year of cultivation of giant miscanthus were determined in the case of fertilisation with ash at an application rate of 4.5 t ha^{-1} and a combination of biochar and ash at an application rate of 3.0 and 4.5 t ha^{-1}.

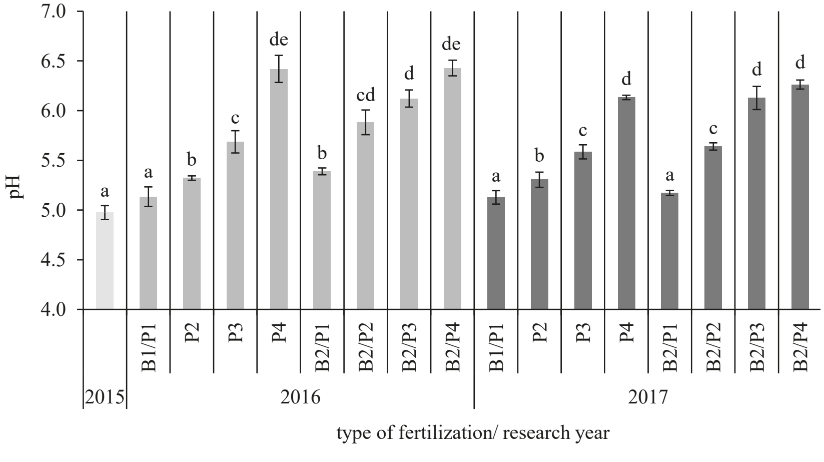

Figure 1. pH value of the soil before the experiment (2015) and after the first and second year of cultivation, depending on the fertiliser used. Differences between average values marked with the same Arabic letters are not statistically significant at the level of $\alpha \leq 0.05$ according to the Bonferroni test.

Figure 2 presents the contents of absorbable forms of phosphorus, potassium and magnesium in the soil before the experiment (2015) and after the first and second year of cultivation, depending on the fertilisers used. The analyses performed before the field experiment showed the contents of absorbable forms of phosphorus, potassium and magnesium in the soil at a level of 48, 90 and 95 mg kg^{-1} respectively. The contents of the study elements in the fertiliser variants showed, in most cases, statistically significant differences in comparison with the control plots and the year 2015 (before the experiment). After the second year of cultivation of giant miscanthus (2017), the contents of the form of phosphorus, potassium and magnesium available to plants in the soil on plots without the use of fertilisers amounted to 58.75, 104.00 and 95.25 mg kg^{-1}, respectively. Thus, a slight decrease in the potassium content and an increase in the content of phosphorus and magnesium was noted in relation to the previous season.

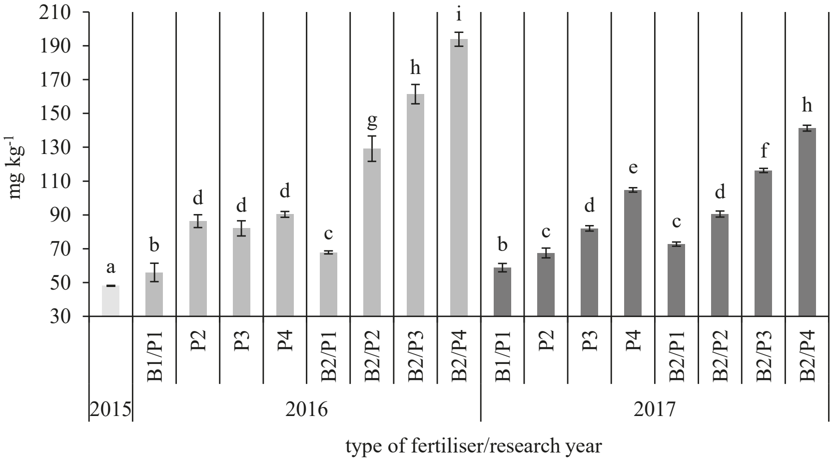

(**a**)

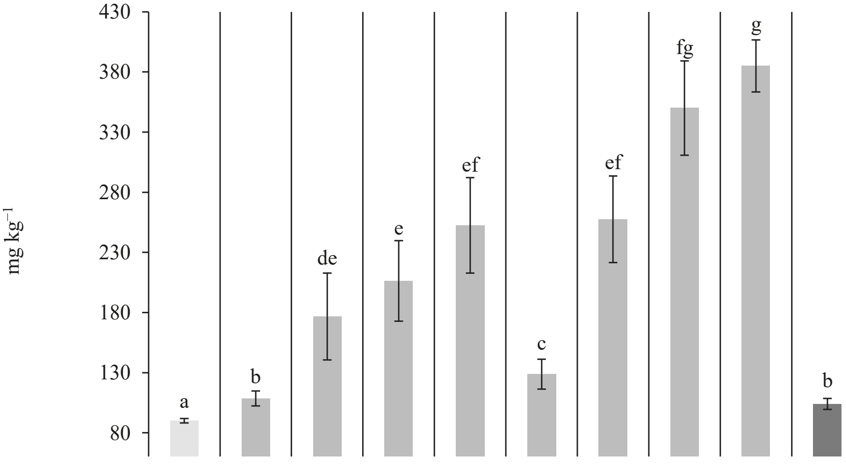

(**b**)

Figure 2. *Cont.*

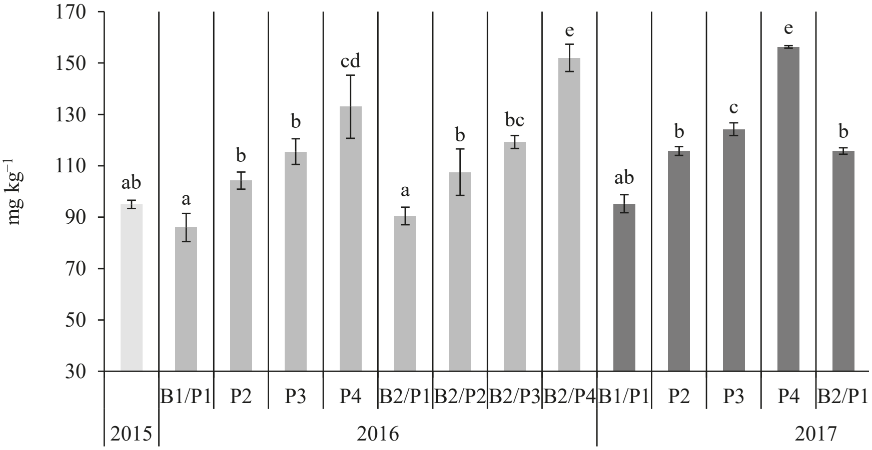

(**c**)

Figure 2. Contents of absorbable forms of phosphorus P_2O_5 (**a**), potassium K_2O (**b**), and magnesium Mg (**c**) in the soil before the experiment (2015) and after the first and second year of cultivation, depending on the fertiliser used. Differences between average values marked with the same Arabic letters are not statistically significant at the level of $\alpha \leq 0.05$ according to the Bonferroni test.

Figure 3 presents the percentage of total carbon and total nitrogen before the experiment (2015) and after the first and second year of cultivation, depending on the fertiliser used. The content of carbon in the soil in the area selected for the field experiment was 0.64%. After the first year of cultivation of giant miscanthus (2016), an increase of 3.13% (control plots) was noted in the carbon content in the soil. In 2017, this content increased to 3.17%; however, it was not a statistically significant change. The experimental factors in the form of fertilisation with ash did not significantly change this parameter in relation to the control plots after the first and second year of cultivation. Only fertilising with biochar and the combination of biochar with ash contributed to an increase in the concentration of total carbon in the soil when compared to the control plots. The highest carbon content determined in the soil samples collected was 4.41% after the first year and 4.34% after the second year of the experiment.

The content of carbon in the soil before the experiment was 0.63% and it increased to 1.16% after the first year of cultivation (control plots). In 2017, there was a statistically insignificant decrease in the content of this parameter to the value of 1.06%. The fertilisers used in the experiment did not have a significant impact on the change in the carbon content when compared to the control plots after the first year of cultivation (carbon content in the range from 1.15 to 1.27%). After the second year, small fluctuations in these parameters were noted; however, in most cases they were not statistically significant. The carbon content in the soil, after the use of fertilisers, was in the range 1.13–1.26%.

The content of nitrogen in the arable land studied was 0.26% before the field experiment. The content of this element in the control plots dropped to 0.02% and 0.07%, respectively, after the first and second year of cultivation. The concentration of nitrogen in the soil, after the use of fertilisers, was in the range 0.002–0.07% after the second year of the experiment. The following was observed.

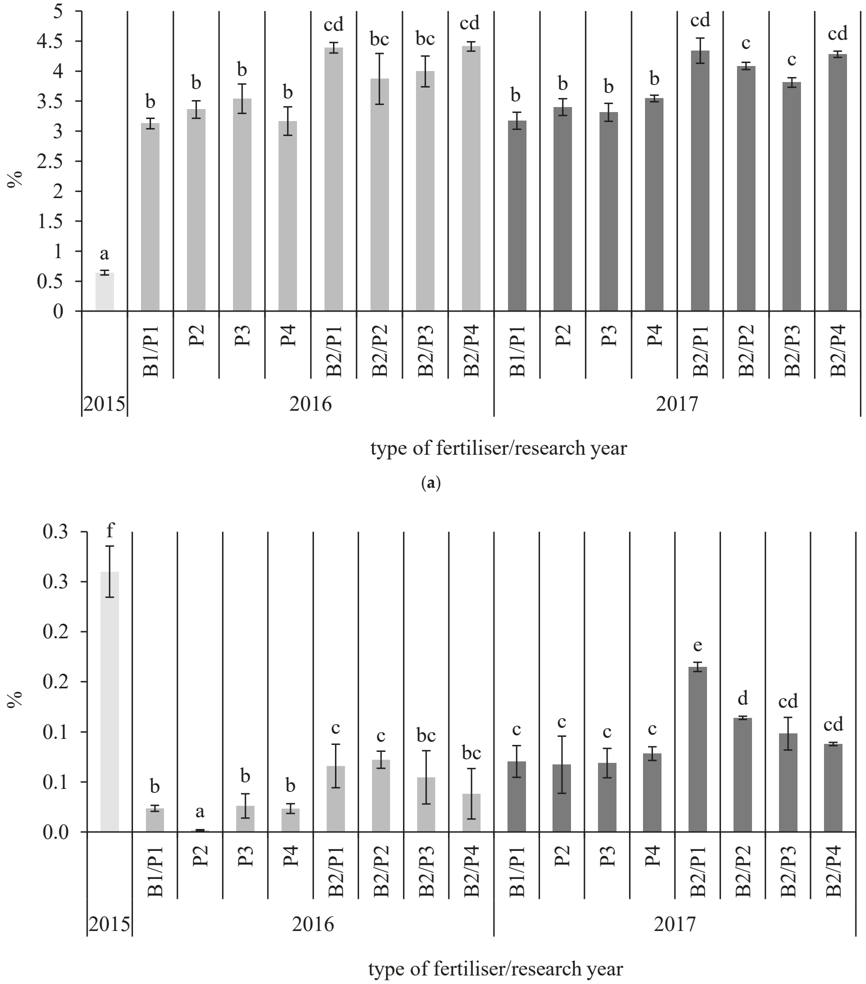

(**a**)

(**b**)

Figure 3. Content of carbon (**a**) and nitrogen (**b**) in the soil before the experiment (2015) and after the first and second year of cultivation, depending on the fertiliser used. Differences between average values marked with the same Arabic letters are not statistically significant at the level of $\alpha \leq 0.05$ according to the Bonferroni test.

Table 4 presents the total contents of selected macro- and microelements and heavy metals in the soil before the experiment (2015) and after the first and second year of cultivation, depending on the fertiliser used. The highest concentration of the macroelements examined (total contents of calcium, sodium and sulphur) in both 2016 and 2017 was recorded after the use of fertiliser in the form of a combination of biochar and ash at an application rate of 1.5 t ha^{-1}. The largest increase in the totals of the soil macroelements examined after the first and second year of the experiment when compared to the year 2015 was 50% and 31%, respectively. The lowest total contents of Ca, Na and S in 2016 and 2017 were recorded in the case of fertilising with ash (all fertiliser application rates).

Table 4. Contents of selected macro- and microelements and heavy metals in the soil before the experiment and after the first and second year of cultivation, depending on the fertiliser used.

Year	Fertiliser Used	Macro- and Microelements									
		As	Ca	Cd	Cu	Mn	Na	Ni	Pb	S	Zn
		mg kg^{-1}									
		x ± SD									
2015	-	<0.01	2 300 ^{b} ± 19	<0.01	20.00 ^{a} ± 0.41	624 ^{c} ± 5	174.75 ^{h} ± 1.50	<0.01	12.40 ^{a} ± 0.41	113 ^{a} ± 0.87	50.03 ^{d} ± 2.41
2016	B1/P1	<0.01	2 646 ^{c} ± 19	<0.01	53.75 ^{c} ± 0.50	520 ^{b} ± 18	91.09 ^{e} ± 26.25	<0.01	13.91 ^{b} ± 0.69	160 ^{c} ± 13	25.95 ^{a} ± 10.70
	P2	<0.01	2 352 ^{b} ± 158	<0.01	50.93 ^{c} ± 1.57	505 ^{b} ± 2	93.88 ^{e} ± 40.23	<0.01	13.65 ^{b} ± 0.82	131 ^{c} ± 18	30.49 ^{ab} ± 12.37
	P3	<0.01	2 338 ^{b} ± 20	<0.01	46.32 ^{b} ± 3.12	507 ^{b} ± 27	19.17 ^{a} ± 8.47	<0.01	13.89 ^{b} ± 0.22	139 ^{c} ± 19	25.49 ^{a} ± 10.24
	P4	<0.01	2 436 ^{bc} ± 93	<0.01	51.54 ^{c} ± 2.44	527 ^{b} ± 12	11.48 ^{a} ± 0.85	<0.01	16.10 ^{e} ± 0.60	125 ^{b} ± 3	33.72 ^{b} ± 4.80
	B2/P1	<0.01	2 848 ^{c} ± 139	<0.01	53.97 ^{c} ± 2.17	505 ^{b} ± 11	109.59 ^{f} ± 18.75	<0.01	13.70 ^{c} ± 0.82	196 ^{e} ± 6	37.07 ^{b} ± 3.30
	B2/P2	<0.01	3 690 ^{f} ± 350	<0.01	54.78 ^{c} ± 0.66	516 ^{b} ± 2	125.25 ^{g} ± 4.70	<0.01	16.97 ^{e} ± 0.73	210 ^{f} ± 6	56.99 ^{d} ± 10.02
	B2/P3	<0.01	2 893 ^{c} ± 150	<0.01	44.89 ^{b} ± 3.40	484 ^{a} ± 3	51.71 ^{c} ± 20.58	<0.01	13.60 ^{c} ± 0.84	197 ^{e} ± 2	26.67 ^{a} ± 10.23
	B2/P4	<0.01	3 038 ^{d} ± 65	<0.01	47.15 ^{b} ± 3.55	521 ^{b} ± 5	79.68 ^{d} ± 25.23	<0.01	15.29 ^{d} ± 0.78	213 ^{f} ± 8	44.69 ^{c} ± 0.81
2017	B1/P1	<0.01	1 959 ^{a} ± 7	<0.01	42.55 ^{b} ± 0.96	460 ^{a} ± 5	33.60 ^{b} ± 1.82	<0.01	13.24 ^{b} ± 0.38	154 ^{c} ± 5	25.51 ^{a} ± 0.76
	P2	<0.01	2 303 ^{b} ± 105	<0.01	47.89 ^{b} ± 1.10	478 ^{a} ± 4	52.93 ^{c} ± 6.01	<0.01	13.26 ^{c} ± 0.15	169 ^{cd} ± 2	27.67 ^{a} ± 0.27
	P3	<0.01	2 137 ^{b} ± 138	<0.01	44.63 ^{b} ± 3.50	453 ^{a} ± 6	52.66 ^{c} ± 37.08	<0.01	13.89 ^{b} ± 0.42	173 ^{d} ± 7	27.26 ^{a} ± 0.21
	P4	<0.01	3 303 ^{e} ± 858	<0.01	57.96 ^{d} ± 3.77	495 ^{ab} ± 12	158.34 ^{g} ± 35.16	<0.01	15.97 ^{d} ± 0.93	189 ^{d} ± 10	34.33 ^{b} ± 1.95
	B2/P1	<0.01	2 306 ^{b} ± 33	<0.01	44.61 ^{b} ± 1.61	481 ^{a} ± 8	55.21 ^{c} ± 1.96	<0.01	15.05 ^{c} ± 0.11	190 ^{d} ± 4	29.27 ^{ab} ± 0.39
	B2/P2	<0.01	3 137^{d} ± 297	<0.01	57.80 ^{d} ± 2.28	511 ^{b} ± 17	184.87 ^{h} ± 37.12	<0.01	13.63 ^{c} ± 0.50	189 ^{d} ± 4	32.23 ^{b} ± 1.47
	B2/P3	<0.01	2 684 ^{c} ± 167	<0.01	51.37 ^{c} ± 2.67	505 ^{b} ± 8	82.10 ^{d} ± 13.84	<0.01	15.29 ^{d} ± 0.74	187 ^{d} ± 5	33.32 ^{b} ± 2.08
	B2/P4	<0.01	2 747 ^{c} ± 48	<0.01	48.65 ^{b} ± 0.20	535 ^{b} ± 17	48.89 ^{c} ± 4.07	<0.01	16.94 ^{e} ± 0.57	199 ^{e} ± 9	35.03 ^{b} ± 1.19

x—average, SD—standard deviation. Differences between average values marked with the same Arabic letters (a–f) are not statistically significant at the level of $\alpha \leq 0.05$ according to the Bonferroni test.

The highest total contents recorded for the microelements examined in soil samples collected after the first and second year of cultivation of giant miscanthus, respectively, were found in plots that were fertilised with biochar and biochar with ash at an application rate of 4.5 t ha^{-1}. The decrease in the totals of the soil microelements after the first and second year of the experiment was determined to be 15% and 13%, respectively, in comparison with the initial values obtained, i.e., before the experiment was carried out for all the aforementioned variants of fertiliser dosage. The lowest total value found during analysis of microelements in the soil in 2016 and 2017 was recorded in the case of fertilising with biochar and ash at an application rate of 3.0 t ha^{-1} and ash alone at this application rate. In the soil samples studied, no arsenic, cadmium or nickel was found in the material collected before the experiment or after the first and second year of the experiment—values were below the detection limit (0.01 mg kg^{-1}) of the analytical method used. The marked concentration of lead changed slightly depending on factors and the year of research, but it should be emphasised that, again, in no case did it exceed the permissible contents for soil used for agricultural purposes.

Principal component analysis of variables (elements) for the soil after the first and second year of cultivation of giant miscanthus identified two factors describing the level of variation in the group with values for the first year for factor 1 (70%) and factor 2 (18.7%), as well as for the second year for factor 1 (46.6%) and factor 2 (24.4%), respectively. The selection of the number of main components was made using the scree test and the Kaiser criterion. The first factor included the following variables: calcium, copper, manganese, sodium, lead, sulphur, zinc (first year) and calcium, sodium, sulphur, zinc (second year). The second factor was represented by the following variables: sodium (first year), and copper and manganese (second year). It was noted that factor 1 is most strongly associated with the variable Ca, while factor 2 with the variable Mn (first year). In the second year of research it was found that factor 1 is mainly associated with the variable Zn, while factor 2 is most strongly associated with the variable Na. The projection of variables on the factor plane is presented in Figure 4.

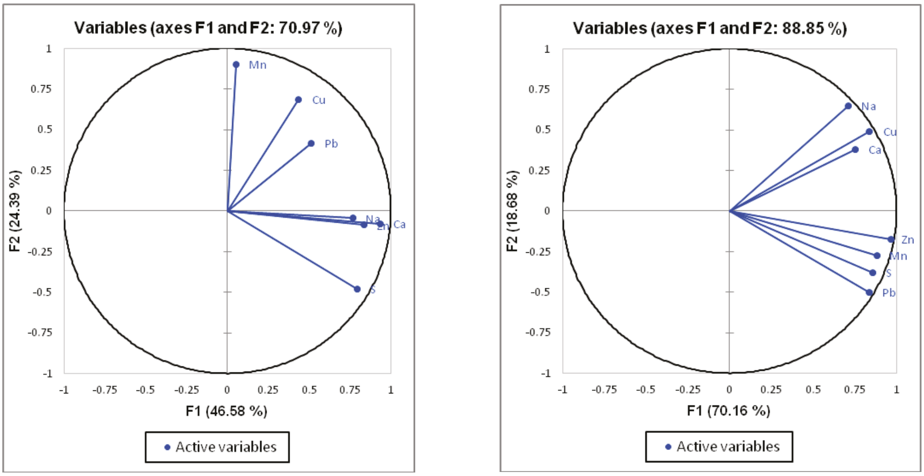

(**a**) (**b**)

Figure 4. Variable plot in the system of the first two factor axes for the soil after the first (**a**) and second (**b**) year of cultivation of giant miscanthus.

2.4. Biomass of Giant Miscanthus

Figure 5 presents the yield of biomass of giant miscanthus (dry matter—d.m.) after the first year of cultivation, depending on the fertiliser used. The average yield of biomass obtained from the control plots (no fertiliser) was 1.04 t ha^{-1} of d.m. The largest values of the parameter studied of 1.22, 1.22 and 1.75 t ha^{-1}, respectively, were recorded in the case of fertilising with ash at an application rate of 1.5 t ha^{-1}, with biochar and with the combination of biochar and ash at an application rate of 1.5 t ha^{-1}. The highest yield of biomass of plants in 2016 was obtained by introducing the fertilisation factor in the form of the combination of biochar and ash at an application rate of 1.5 t ha^{-1}. Fertilisation with ash at doses of 3.0 and 4.5 t ha^{-1} and its combinations with biochar affected yield, with values of 0.75, 0.57, 0.90 and 0.86 t ha^{-1} of d.m., respectively.

After the second year of cultivation of giant miscanthus, the average yield of biomass in the control plots was 8.82 t ha^{-1} of d.m. As in the previous year, the highest values of average yield of dry matter of 9.50, 13.04, and 9.80 t ha^{-1}, respectively, were recorded for the plots fertilised with the lowest application rate of ash, biochar alone, and the combination of biochar and ash at a dose of 1.5 t ha^{-1}. The highest yield of dry matter of plants in 2017 was recorded on plots fertilised only with biochar before the experiment. Fertiliser application rates of ash of 3.0 and 4.5 t ha^{-1} and its combination with biochar negatively influenced crop yield—there was a decrease in the average yield of dry matter of plants when compared with the control plots of 1.43, 2.56, 0.23, and 0.38 t ha^{-1}, respectively (Figure 5).

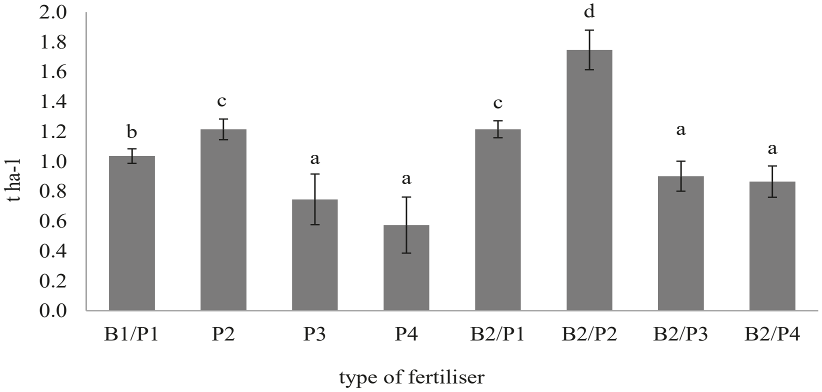

(**a**)

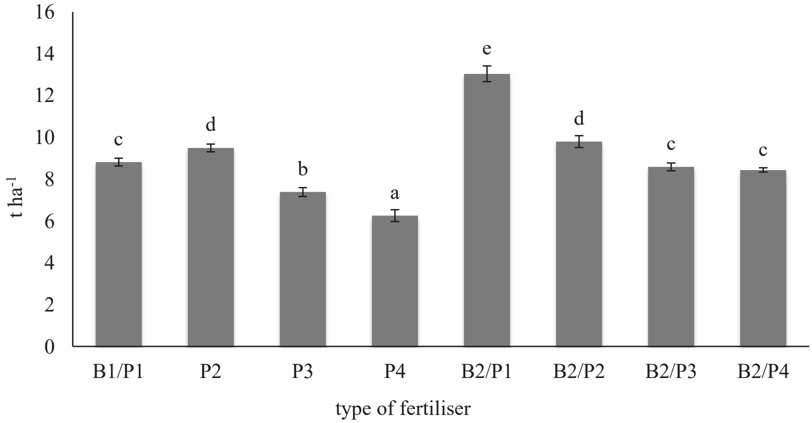

(**b**)

Figure 5. Biomass yield of giant miscanthus after the first (**a**) and second (**b**) year of cultivation, depending on the fertilisation used. Differences between average values marked with the same Arabic letters are not statistically significant at the level of $\alpha \leq 0.05$ according to the Bonferroni test.

Figure 6 presents the calorific value of biomass of giant miscanthus, depending on the fertiliser used and the year of research. The calorific value of biomass after the first year of cultivation ranged from 17.54 to 17.75 MJ kg^{-1} of d.m., while after the second year of cultivation it ranged from 17.65 to 17.72 MJ kg^{-1} of d.m. There were no statistically significant differences between the values measured. When assessing the calorific value of the biomass of giant miscanthus in laboratory tests, both after the first and second year of cultivation, no effects were found on changes in the parameters analysed in relation to the use of fertilisers.

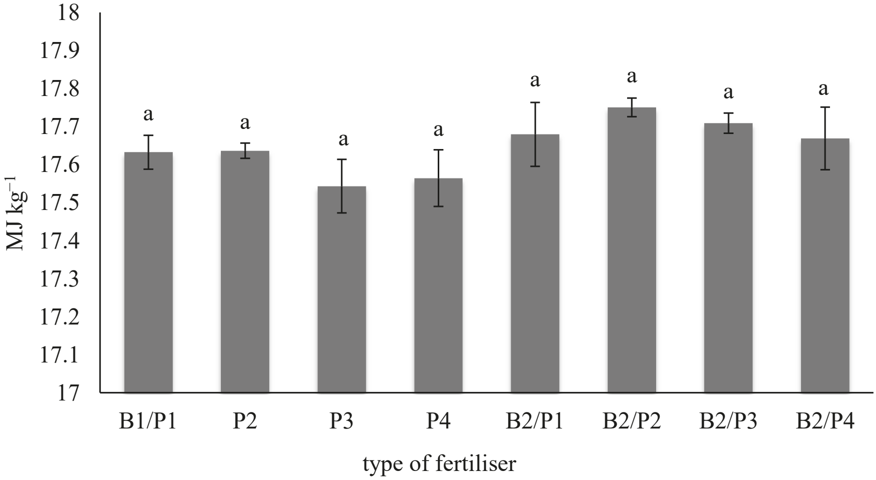

(**a**)

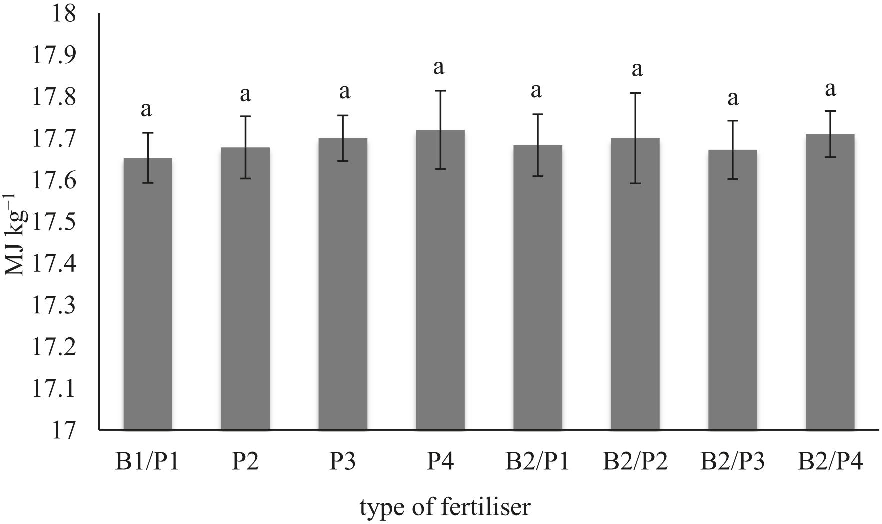

(**b**)

Figure 6. Calorific value of giant miscanthus after the first (**a**) and second (**b**) year of cultivation, depending on the fertiliser used. Differences between average values marked with the same Arabic letters are not statistically significant at the level of $\alpha \leq 0.05$ according to the Bonferroni test.

Table 5 presents the total contents of selected macroelements in the biomass of giant miscanthus, depending on the fertiliser used and year of research. The highest concentration of the macroelements studied in the above ground parts of plants in 2016 and 2017, respectively, was recorded after the use of fertiliser in the form of ash at the lowest application rate and ash at an application rate of 3.0 t ha^{-1}. The greatest increase in the total of the macroelements studied in the biomass of plants was recorded after the first and second year of the experiment in the control plots, with increases of 13% and 7%, respectively. The lowest total content of the elements studied in 2016 and 2017, respectively, was recorded for the fertiliser in the form of biochar and the combination of biochar and ash at a dose of 1.5 t ha^{-1}. Among the ions analysed, the highest concentration in the biomass of giant miscanthus was found for potassium—after both the first and second year of cultivation. There was a change in the content of this element, depending on the combination of factors used in the experiment; however, not all changes were statistically significant. When analysing the results of the total contents of selected macroelements, it was found that aboveground parts of plants of giant miscanthus contained the least sodium and iron. The fertiliser did not produce statistically significant changes in the contents of these elements in the biomass after the first and second year of cultivation when compared to control tests.

Table 6 presents the total contents of selected microelements and heavy metal s in the biomass of giant miscanthus, depending on the fertiliser used and the year of research. In the aboveground parts of the plants analysed after the first year of cultivation, manganese, strontium, zinc and aluminium were found. No strontium was recorded in samples obtained after the second year of cultivation. The concentration of these elements was determined to be at a very low level and did not show statistically significant variability between the experimental plots. Plant biomass obtained after the second year of research was characterised by a lower content of the elements analysed when compared to the previous year. In the plant samples studied, no arsenic, cadmium, chromium, copper, molybdenum, nickel or lead was found after both the first and second year of the experiment—values were below the detection limit (0.01 mg kg^{-1}) in the analytical method used.

Table 5. Contents of selected macroelements in the biomass of giant miscanthus after the first (2016) and second (2017) year of cultivation, depending on the fertiliser used.

Year	Fertiliser Used	Macroelements						
		Ca	Fe	K	Mg	Na	P	S
		mg kg^{-1}						
		x ± SD						
2016	B1/P1	$2.29^{a} \pm 0.16$	$0.20^{a} \pm 0.05$	$6.66^{b} \pm 0.32$	$0.82^{ab} \pm 0.04$	$0.13^{a} \pm 0.02$	$1.28^{b} \pm 0.08$	$0.92^{a} \pm 0.06$
	P2	$2.58^{b} \pm 0.09$	$0.20^{a} \pm 0.03$	$7.71^{c} \pm 0.22$	$0.89^{bc} \pm 0.10$	$0.13^{a} \pm 0.02$	$1.43^{c} \pm 0.11$	$1.00^{a} \pm 0.07$
	P3	$2.23^{a} \pm 0.21$	$0.19^{a} \pm 0.03$	$6.03^{a} \pm 0.19$	$0.74^{a} \pm 0.11$	$0.13^{a} \pm 0.01$	$1.11^{a} \pm 0.04$	$0.96^{a} \pm 0.04$
	P4	$2.38^{a} \pm 0.09$	$0.20^{a} \pm 0.02$	$6.93^{b} \pm 0.29$	$0.91^{b} \pm 0.09$	$0.13^{a} \pm 0.01$	$1.49^{c} \pm 0.03$	$1.06^{a} \pm 0.10$
	B2/P1	$2.31^{a} \pm 0.17$	$0.19^{a} \pm 0.09$	$5.75^{a} \pm 0.23$	$0{,}74^{a} \pm 0.03$	$0.12^{a} \pm 0.01$	$1.25^{b} \pm 0.06$	$0.90^{a} \pm 0.04$
	B2/P2	$2.31^{a} \pm 0.15$	$0.10^{a} \pm 0.05$	$7.13^{b} \pm 0.24$	$0.83^{ab} \pm 0.04$	$0.12^{a} \pm 0.02$	$1.29^{b} \pm 0.10$	$0.99^{a} \pm 0.04$
	B2/P3	$2.23^{a} \pm 0.18$	$0.19^{a} \pm 0.12$	$7.05^{b} \pm 0.34$	$0.99^{c} \pm 0.08$	$0.12^{a} \pm 0.02$	$1.29^{b} \pm 0.09$	$1.03^{a} \pm 0.06$
	B2/P4	$2.33^{a} \pm 0.18$	$0.15^{a} \pm 0.05$	$6.84^{b} \pm 0.42$	$1.03^{c} \pm 0.07$	$0.12^{a} \pm 0.03$	$1.31^{b} \pm 0.11$	$1.06^{a} \pm 0.03$
2017	B1/P1	$1.06^{a} \pm 0.12$	$0.04^{a} \pm 0.01$	$5.59^{c} \pm 0.12$	$0.31^{a} \pm 0.03$	$0.09^{a} \pm 0.00$	$1.13^{c} \pm 0.09$	$0.38^{ab} \pm 0.01$
	P2	$1.13^{a} \pm 0.15$	$0.06^{a} \pm 0.02$	$4.90^{b} \pm 0.07$	$0.34^{b} \pm 0.06$	$0.08^{a} \pm 0.00$	$0.97^{b} \pm 0.07$	$0.34^{a} \pm 0.02$
	P3	$1.60^{c} \pm 0.06$	$0.06^{a} \pm 0.01$	$5.37^{c} \pm 0.09$	$0.37^{b} \pm 0.04$	$0.09^{a} \pm 0.01$	$1.25^{d} \pm 0.07$	$0.47^{c} \pm 0.02$
	P4	$1.26^{a} \pm 0.08$	$0.05^{a} \pm 0.02$	$4.58^{a} \pm 0.12$	$0.36^{b} \pm 0.01$	$0.09^{a} \pm 0.01$	$1.06^{c} \pm 0.04$	$0.37^{ab} \pm 0.02$
	B2/P1	$1.17^{a} \pm 0.12$	$0.05^{a} \pm 0.02$	$4.74^{b} \pm 0.10$	$0.28^{a} \pm 0.03$	$0.08^{a} \pm 0.01$	$0.95^{b} \pm 0.01$	$0.32^{a} \pm 0.01$
	B2/P2	$1.22^{a} \pm 0.19$	$0.05^{a} \pm 0.03$	$4.34^{a} \pm 0.08$	$0.29^{a} \pm 0.05$	$0.07^{a} \pm 0.01$	$0.81^{a} \pm 0.09$	$0.33^{a} \pm 0.03$
	B2/P3	$1.15^{a} \pm 0.03$	$0.04^{a} \pm 0.02$	$4.78^{b} \pm 0.11$	$0.39^{b} \pm 0.10$	$0.07^{a} \pm 0.01$	$0.79^{a} \pm 0.08$	$0.39^{ab} \pm 0.03$
	B2/P4	$1.44^{b} \pm 0.07$	$0.05^{a} \pm 0.01$	$4.66^{a} \pm 0.12$	$0.40^{b} \pm 0.05$	$0.09^{a} \pm 0.00$	$1.09^{c} \pm 0.07$	$0.42^{b} \pm 0.02$

x—average, SD—standard deviation. Differences between average values marked with the same Arabic letters (a–d) are not statistically significant at the level of $\alpha \leq 0.05$ according to the Bonferroni test, for each years.

Table 6. Contents of selected microelements and heavy metals in the biomass of giant miscanthus after the first (2016) and second (2017) year of cultivation, depending on the fertiliser used.

Year	Fertiliser Used	Microelements										
		Al	As	Cd	Cr	Cu	Mo	Ni	Pb	Mn	Sr	Zn
		mg kg^{-1}										
		x ± SD										
2016	B1/P1	0.14 ^{a} ± 0.04	<0.01	<0.01	<0.01	<0.01	<0.01	<0.01	<0.01	0.14 ^{a} ± 0.00	0.01 ^{a} ± 0.00	0.07 ^{a} ± 0.03
	P2	0.18 ^{a} ± 0.06	<0.01	<0.01	<0.01	<0.01	<0.01	<0.01	<0.01	0.14 ^{a} ± 0.02	0.02 ^{a} ± 0.00	0.07 ^{a} ± 0.02
	P3	0.14 ^{a} ± 0.05	<0.01	<0.01	<0.01	<0.01	<0.01	<0.01	<0.01	0.13 ^{a} ± 0.01	0.01 ^{a} ± 0.00	0.06 ^{a} ± 0.02
	P4	0.19 ^{a} ± 0.03	<0.01	<0.01	<0.01	<0.01	<0.01	<0.01	<0.01	0.13 ^{a} ± 0.01	0.01 ^{a} ± 0.00	0.07 ^{a} ± 0.04
	B2/P1	0.16 ^{a} ± 0.03	<0.01	<0.01	<0.01	<0.01	<0.01	<0.01	<0.01	0.12 ^{a} ± 0.01	0.01 ^{a} ± 0.00	0.03 ^{a} ± 0.02
	B2/P2	0.13 ^{a} ± 0.03	<0.01	<0.01	<0.01	<0.01	<0.01	<0.01	<0.01	0.12 ^{a} ± 0.02	0.03 ^{a} ± 0.04	0.06 ^{a} ± 0.05
	B2/P3	0.17 ^{a} ± 0.02	<0.01	<0.01	<0.01	<0.01	<0.01	<0.01	<0.01	0.12 ^{a} ± 0.02	0.01 ^{a} ± 0.00	0.05 ^{a} ± 0.03
	B2/P4	0.16 ^{a} ± 0.03	<0.01	<0.01	<0.01	<0.01	<0.01	<0.01	<0.01	0.12 ^{a} ± 0.01	0.01 ^{a} ± 0.00	0.05 ^{a} ± 0.02
2017	B1/P1	0.02 ^{a} ± 0.00	<0.01	<0.01	<0.01	<0.01	<0.01	<0.01	<0.01	0.09 ^{a} ± 0.02	<0.001	0.03 ^{a} ± 0.01
	P2	0.03 ^{a} ± 0.00	<0.01	<0.01	<0.01	<0.01	<0.01	<0.01	<0.01	0.08 ^{a} ± 0.03	<0.001	0.02 ^{a} ± 0.00
	P3	0.05 ^{a} ± 0.00	<0.01	<0.01	<0.01	<0.01	<0.01	<0.01	<0.01	0.09 ^{a} ± 0.01	<0.001	0.03 ^{a} ± 0.01
	P4	0.04 ^{a} ± 0.02	<0.01	<0.01	<0.01	<0.01	<0.01	<0.01	<0.01	0.09 ^{a} ± 0.01	<0.001	0.02 ^{a} ± 0.01
	B2/P1	0.02^{a} ± 0.01	<0.01	<0.01	<0.01	<0.01	<0.01	<0.01	<0.01	0.08 ^{a} ± 0.03	<0.001	0.02 ^{a} ± 0.00
	B2/P2	0.03 ^{a} ± 0.01	<0.01	<0.01	<0.01	<0.01	<0.01	<0.01	<0.01	0.07 ^{a} ± 0.02	<0.001	0.01 ^{a} ± 0.00
	B2/P3	0.03 ^{a} ± 0.01	<0.01	<0.01	<0.01	<0.01	<0.01	<0.01	<0.01	0.07 ^{a} ± 0.02	<0.001	0.02 ^{a} ± 0.01
	B2/P4	0.03 ^{a} ± 0.00	<0.01	<0.01	<0.01	<0.01	<0.01	<0.01	<0.01	0.09 ^{a} ± 0.01	<0.001	0.02 ^{a} ± 0.01

x—average, SD—standard deviation. Differences between average values marked with the same Arabic letter are not statistically significant at the level of $\alpha \leq 0.05$ according to the Bonferroni test, for each years.

Principal component analysis of variables (elements) for the biomass of giant miscanthus after the first and second year of cultivation selected two factors describing the level of variability in the group with values, respectively, for the first year: factor 1 (27.7%) and factor 2 (21.7%), and for the second year: factor 1 (33.9%) and factor 2 (24.4%). The selection of the number of main components was made using the scree test and the Kaiser criterion. The first factor included variables such as aluminium, potassium, magnesium, sodium, sulphur (first year) and aluminium, manganese, phosphorus, sulphur (second year). The second factor was represented by variables such as iron, manganese, phosphorus (first year) and calcium, potassium, magnesium (second year). It was noted that factor 1 is most strongly associated with variables K and S, while factor 2 is associated with variables Fe and Mn (first year). In the second year of research, it was found that factor 1 is mainly associated with variables S and Sr, while factor 2 is most strongly associated with variable K. The projection of variables on the factor plane is presented in Figure 7.

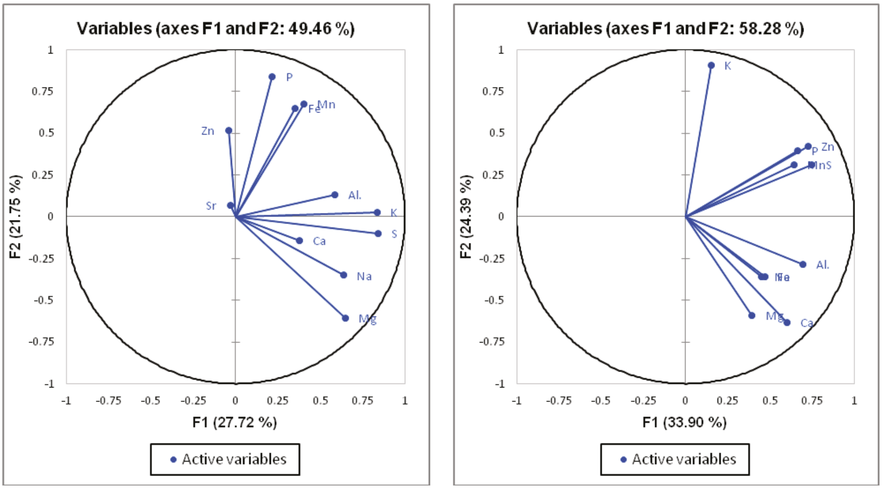

(**a**) (**b**)

Figure 7. Variable plot in the system of the first two factor axes for the biomass of giant miscanthus after the first (**a**) and second (**b**) year of cultivation.

3. Discussion

The cultivation of plants is becoming more and more effective due to the use of numerous means of support, including different types of fertilisers. The agents most commonly used in modern agriculture, which contain easily absorbable mineral components, are fertilisers [24].

Recent years have seen the intensive development of research on the use of unconventional materials as plant fertilisers and for soil reclamation. This research concerns the use of, among other materials, sewage sludge, ash from biomass, brown coal or biochar. In addition, the literature presents only rudimentary information on the use of biochar and ash from biomass as a fertiliser material in the cultivation of perennial energy crops.

The soil reaction plays an important role in many processes occurring in the soil environment. It is important in the uptake of nutrients by plants and affects the mobility of heavy metals, such as cadmium, lead or nickel [5,16]. The alkalizing effect associated with the application of biochar to the soil environment relates to the alkaline compound content and the application rate. The clearest changes can be obtained in the case of heavily acidified soils, where a significant decrease is visible in the share of H^+ and Al^{3+} [17]. Much of the research conducted so far indicates that the addition of biochar produces an increase in soil pH [25–28]. Research conducted by Nigussie et al. [29] showed that biochar produced from corn stalks and applied to soils contaminated with chromium produced an increase in pH and ion exchange in the soils analysed. Clear effects on the soil pH after the application of ashes can be obtained by the application of fertiliser doses at the level of 10–20 t ha^{-1} [30]. However, the use of such high doses of ash could result in the introduction of too large quantities of nutrients or heavy metals into the soil.

According to the analyses performed, the use of fertiliser in the form of a combination of biochar and ash at an application rate of 4.5 t ha^{-1} produced the greatest increase in the content of absorbable forms of phosphorus (P_2O_5), potassium (K_2O) and magnesium (Mg) in the soil on which perennial energy crops were grown.

The high potential of biochars for exchangeable ion sorption affects the increase in the concentration of macro- and microelements in the soil profile, which is why it modulates their effective uptake by plants, as well as reduces the risk of their leaching and being displaced to surface and underground waters [12]. The introduction of biochar into the soil may have a positive effect, including on the increase in the phosphorus content in the soil environment. As emphasised by Chan et al. [14], the use of biochar in the soil at a fertiliser dose of more than 50 t ha^{-1} significantly increases the concentration of phosphorus in the soil. The increase in the phosphorus content in the soil after the application of biochar results from the content of easily absorbable forms of this element in biochars, as well as from its ability to react on the soil reaction, thus producing changes in the solubility of phosphorus forms [31,32]. Numerous authors report that the addition of biochars to the soil affects the intensive growth of soluble forms of potassium in the soil solution [33,34]. Liu et al. [35] note an increase in the contents of macroelements in the soil compared to the control following the application of biochar from the vegetative parts of bamboo and rice straw. In their paper, the authors used biochars obtained from the pyrolysis process with parameters of 500 °C and 600 °C and a process duration of 60 min. Fertiliser doses of biochar from bamboo and rice straw amounted to 5, 18, and 10.5 t ha^{-1}, respectively. According to many authors, ash from plant biomass is characterized by a high amount of the biogenic elements necessary for the proper growth of plants, thanks to which it can supplement deficiencies of macro- and microelements in the soil [36]. Piekarczyk [25] states that the use of ash from wheat straw (1.0 t ha^{-1}) as a fertiliser material produced an increase in absorbable forms of macroelements in the soil, at the same time indicating that these changes were not statistically significant. The author explains this result by the relatively low content of nutrients in the ash used. It should be noted that changes in soil fertility resulting from the introduction of ash depend on the ash source, its elemental composition and the size of the dose applied [37]. In research on the long-term effects of the use of wood ash agents, Klavina et al. [38] note an increase in the concentration of magnesium and phosphorus in peat soils. The authors also inform us about the positive impact of ash on the calcium content and the formation of soil pH.

Biochar and ash from biomass used in field experiments were characterised by total carbon contents of 74.35% and 1.22%, respectively. This was reflected in the results obtained, which indicate the lack of a fertilising effect of ash itself on changes in the total carbon concentration in the soil. Fertilisers in the form of biochar and its combination with ash produced an increase in the concentration of carbon in the soil, in comparison with the control plot (statistically significant changes in most cases). Similar results were obtained by Doan et al. [39], who reported that the use of biochar from cattle manure in the corn cultivation slightly increased the C content of the soil. In research on the impact of biochar and compost on soil properties in a tropical climate, Ghosh et al. [40] determined that the organic carbon content in the soil after the application of biochar was almost twice as high as in the control plot (an increase from 1.18 to 2.13%). It should also be emphasised that stable forms of carbon are characterised by high resistance to biological decomposition, which is why biochar can be treated as an effective agent for carbon sequestration in the soil [11,41,42].

Research conducted as part of the cultivation of giant miscanthus showed that fertilising with a combination of biochar and ash at a dose of 1.5 t ha^{-1} produced the greatest increase in the total calcium, sodium and sulphur contents after the first and second year of cultivation, when compared to 2015.

For the aforementioned fertiliser, a decrease was noted in the total concentration of the microelements in 2016 and 2017 when compared to their concentration before the experiment. Many researchers point to biochar's great potential as a material that can be used to reduce the mobility of heavy metals in the soil [43,44]. According to Bielinska et al. [45], ash from fluidised bed combustion of hard coal used for agricultural purposes did not produce an increase in the amount of zinc, copper and cadmium in the soil. One of the key features of energy crops should be the high level of biomass productivity. On the basis of the research conducted, it was found that the highest yield of dry matter of giant miscanthus plants, both after the first and second year of cultivation, was obtained by fertilising with ash at an application rate of 1.5 t ha^{-1}, with biochar, and the combination of biochar and ash at a dose of 1.5 t ha^{-1}. The aforementioned fertilisers produced an increase in yield in 2016 compared to the control plots by 17%, 17% and 68%, respectively. The dry matter yield of plants recorded in 2017 was several times higher than in the previous year, and the recorded changes for the aforementioned factors in relation to the control plots were 8%, 48% and 11%, respectively. In research on the yield of osier cultivated using the Eko-Salix system (five-year rotation), Szczukowski et al. [46] determined the dry matter yield of plants to be on average 7.46 t ha^{-1} per year. Kwasniewski [47] states that the average yield of fresh biomass of energy willow obtained from 30 selected plantations located in Poland was 7.0 t ha^{-1} (first year of cultivation). Field experiments carried out so far in Poland have shown that the average yield of willow cultivated using the short rotation system ranged from 10 to 15 t ha^{-1} of dry matter [48,49]. Kobylinski and Olszewska [50], conducting research on energy efficiency in the production of giant miscanthus, recorded a dry matter yield of plants of 1.5 t ha^{-1} in the first year of cultivation and 9 t ha^{-1} in the second year of cultivation. These values increased to the level of 15 t ha^{-1} in the third year of cultivation. The authors claim that the slow rate of plant development in the early period of cultivation, environmental conditions and the small doses of mineral fertilisers affected the low biomass yield obtained in the first year. It should also be emphasised that the full yield of perennial energy crops may be obtained after 3–4 years of cultivation.

Research conducted by Puchalski et al. [51] confirms the positive effect of the use of plant biomass ash on the yield of two varieties of topinambour (*Helianthus tuberosus* L.). The fertiliser dose used was 12.8 t ha^{-1}, which produced an increase in the dry matter yield of plants after the first year of cultivation compared to the control plot of 7% for the Albik variety and 21% for the Gigant variety. However, it should be noted that the lower doses of ash used in the experiment did not produce statistically significant changes in the yield. In our own research, a significant increase in the yield of osier and giant miscanthus was obtained after the application of ash at a dose of 1.5 t ha^{-1}. The majority of research conducted so far on the response of giant miscanthus to the fertiliser applied concerned the use of inorganic nitrogen. However, the results obtained were contradictory and did not give a definite answer concerning the positive effect that fertilising with nitrogen has on plants. Many authors state that fertilising with nitrogen did not affect the growth and yield of various types of miscanthus [52–55].

Research conducted so far on the use of biochar in plant production has concentrated in the area of cultivation of such plants as corn, radish, rape, rice and potatoes [14,43,56–58]. According to Liu et al. [59], the use of biochar at doses below 30 t ha^{-1} (field conditions) produced, to varying degrees, an increase in the yield depending on the type of cultivation. The authors note a growth in crop yield of 30%, 29%, 13%, 11%, 8% and 7%, respectively, for legumes, vegetables, grasses, wheat, corn and rice. The literature also states that biochars from sewage sludge can be used for the fertilisation of plants. Hossain et al. [60], following the use of 10 t ha^{-1} of biochar from sewage sludge in the cultivation of cherry tomatoes, obtained a 64% increase in production, compared to the control plot. However, it should be noted that there is an upper limit to the amount of biochar that should be applied with respect to crop productivity. Lehmann et al. [61] note that plants respond positively to the addition of biochar to the soil at doses of up to 55 t ha^{-1}. The authors report that the use of higher doses does not produce a statistically significant impact on the increase in plant yield. Increased plant production due to the use of biochar as a fertiliser material can be observed as changes in plant growth, nutrient uptake and yield [62]. It should be noted that the research conducted so far has been of a short-term character; therefore, the assessment of the long-term impact of biochar on the soil and plants seems to be justified.

The calorific value of the biomass of giant miscanthus harvested after two years of research ranged from 17.54 to 17.75 MJ kg^{-1} of d.m. There were no statistically significant changes in the parameters investigated after the use of fertilisation factors. The results obtained are consistent with the data contained in the available literature [63–65].

The average total contents of the elements studied in the biomass of giant miscanthus after the first and second year of cultivation were determined to be a series of decreasing values of K > Ca > P > S > Mg > Al > F e> Mn > Zn> Na > Sr and K > Ca > P > S > Mg > Mn > Fe> Al > Zn > Na. In 2017, there was a decrease in the average total contents of the macroelements analysed in the biomass obtained from experiments in relation to the previous year. Similar results were obtained by Borkowska and Lipinski [66] in research on the contents of selected elements in the biomass of energy crops. These authors recorded a high concentration of calcium and potassium in comparison with other elements for giant miscanthus, sugar miscanthus and two clones of osier. According to Szyszlak-Barglowicz [67], various levels of mineral fertilisation did not significantly affect the contents of macroelements studied in the biomass of Virginia fanpetals. The analysis of the concentration of N, P, K, Ca and Mg in the stems and leaves of the study plants showed the highest content of potassium and calcium.

No harmful compounds such as arsenic, cadmium, chromium and lead were found in the biomass of the aboveground parts of plants collected from experimental plots. Academic literature states that with the increase in concentration of heavy metals in the substrate, we should expect an increase in the contents of metals in the biomass of miscanthus. Experiments confirm this relationship with respect to cadmium and copper. In the case of the cultivation of miscanthus on a substrate contaminated with lead, there were no significant changes in the content of this element in plants [68]. In research on the impact of fertilisation with sewage sludge on the contents of heavy metals in osier, Kalembasa et al. [69] note the lack of a significant dependence between the lead content in leafless plant shoots as controls and items with fertiliser treatments. However, the authors note that plants from plots on which the highest fertiliser dose was applied contained more heavy metals than those fertilised with a smaller amount of sewage sludge. Bearing in mind the environmental aspects, particular attention should be paid to the potential presence of heavy metals in plant biomass for energy purposes, and one should conduct in-depth qualitative characteristics [70].

4. Materials and Methods

4.1. Site Description

Two-year field trials were conducted in Krasne (Subcarpathian Voivodship, Poland, 50°04′16.1″ N 22°04′37.6″ E) over 2015–2017. They were located on arable land of the IVb land quality class in split-block system in four repetitions. The total number of plots in the field experiment was 32; the area of each was 35 m^2 (7 m length, 5 m width) and to the harvest 24 m^2 (6 m length, 4 m width).

4.2. Experimental Design

The area covered by the research was agricultural fallow left without any intervention for more than 10 years. In order to prepare the soil for cultivation (autumn 2013), mulching was performed with a bush cutter, followed by weeding in the form of a Roundup 360 SL spray (dose: 6 l ha^{-1}); after two weeks, disc ploughs and deep ploughing were performed using a mouldboard plough. In the spring of 2015, treatments for improving the soil (levelling the land surface, breaking up the soil lumps and destroying emerging weeds) were performed in the form of harrowing, with the use of a passive pneumatic seed drill. Based on the results of analyses performed before the experiment and the nutritional needs of plants, recommendations for fertiliser application were developed. Fertiliser treatments with biochar at a dose of 11.5 t ha^{-1}, ash from biomass at doses of 1.5, 3.0, 4.5 t ha^{-1} and a combination of these were used. In April 2015, fertilizers were sown manually, and then mixed with the soil to a depth of approximately 20 cm by means of a rototiller. Seedlings of giant miscanthus were obtained from a private supplier (Lublin Voivodship, Poland). On 16 April 2015, seedlings were manually planted on the experimental plots: planting depth: 10–15 cm; spacing of seedlings: 1 m; spacing of rows: 0.8 m; density: 13,000 plants ha^{-1}. The biomass harvest from the plots was performed in February 2016 and 2017 using a brushcutter with a cutting disc, rejecting extreme rows (height of the cut above the soil surface—10 cm). In the second year of the experiment, no re-application of fertiliser in the form of biochar and ash from biomass was carried out.

4.3. Fertiliser Material

The biochar, in the form of coal scales, originated from the processing of biomass from energy crops (commercially available, Poland). The fertiliser material in the form of ash from the combustion of a mixture of biomass from energy crops and plant biomass of agricultural origin was obtained from the Tauron power station (Stalowa Wola, Poland). Biochar was subjected to a grinding process with the use of the Laarmann CM-1000 high-speed cutting mill. The grinding process was performed using a sieve with a mesh size of 10 mm. Ash generated from the combustion of plant biomass did not require additional treatment before its application.

4.4. Biomass Production

The yield of plants was assessed at the end of each growing season. The plant material collected was dried at 70 °C, weighed and the biomass yield of dry matter in t ha^{-1} was calculated.

4.5. Examination of Samples

Samples of soil, biochar, ash from biomass and the aboveground parts of giant miscanthus plants were subjected to laboratory analyses using current analytical standards (Table 7).

Table 7. Parameters analysed with research methods.

Item	Parameter	Research Method
1	pH w KCl	PN-ISO 10390:1997 [71]
2	Content of absorbable forms of phosphorus (P_2O_5)	PN-R-04023:1996 [72]
3	Content of absorbable forms of potassium (K_2O)	PN-R-04022:1996/Az1:2002 [73]
4	Content of absorbable form of magnesium (Mg)	PN-R-04020:1996/Az1:2004 [74]
5	Content of carbon, nitrogen and hydrogen	PN-EN 15104:2011 [75]
6	Ash content	PN-EN 13775:2010 [76]
7	Content of volatile substances	PN-EN 15138:2011 [77]
8	Calorific value	PN-EN 13918:2010 [78]
9	Total content of selected macro- and microelements	Method using atomic emission spectrometry with excitation in argon plasma (ICP-OES)

The determination of the pH of the study materials was performed by measuring the concentration of hydrogen ions, i.e., the activity of hydrogen ions (H^+) with the use of the potentiometric method. The analysis was performed in KCl solution with a concentration of 1 mol dm^{-3}, assuming a mass ratio of the study sample to solution volume of 1:2.5. Measurements were performed using the Nahita pH meter, model 907 (AUXILAB, Beriáin, Spain).

Analyses of the contents of ash and volatile substances in the study materials using thermogravimetric methods were performed using the TGA 701 apparatus by LECO (LECO Corporation, Saint Joseph, MI, USA). The content of total carbon and nitrogen was tested using the TrueSpec CHN analyser by LECO (LECO Corporation, Saint Joseph, MI, USA).The AC500 calorimeter by LECO (LECO Corporation, Saint Joseph, MI, USA) was used to determine the calorific value of the materials analysed.

The mineralisation of the study material was performed in three repetitions. Contents of elements in samples were determined using a method based on inductively coupled plasma atomic emission spectroscopy (ICP-OES), with the use of the iCAP Dual 6500 analyser (Thermo Fisher Scientific, Schaumburg, IL, USA). The mineralisation of the study samples was performed in Teflon containers using a mixture of acids under specific conditions (Table 8). In each case, a 0.2-g sample was mineralised. The sample obtained in this way was supplemented with mineralised water to make a volume of 50 mL. In the calibration step, standard solutions for all elements were prepared from the spectroscopic grade reagent (Thermo) with a three-step curve. The curve fit factor for all elements was over 0.99. Selection of a measuring line of appropriate length was validated by the method of standard additions. The recovery on selected lines was above 98.5% for each of the elements. Each time, the CRM 1515 (Certified Reference Material) was used and the selection of appropriate lines was implemented using the standard addition method. Each time we also used internal standards for matrix curve correction; these were Yttrium (Y) and Ytterbium (Yb), two elements not detected in the samples. The detection limit of the analytical method used for the elements studied was no worse than 0.01 mg kg^{-1} [79].

Table 8. Parameters of the mineralisation process.

Material	Acid	Temperature and Time	Power	Application Note
Soil	8 mL HNO_3 65% 5 mL HCl 37% 1 mL HF 40% 5 mL H_3BO_3 5%	-temperature increase to 200 °C, time: 15 min; - maintaining at temperature of 200 °C, time: 15 min	1500 W	HPR-EN-13 [80]
Biochar	7 mL HNO_3 65% 1 mL H_2O_2 30%			HPR-PE-19 [81]
Plant biomass	6 mL HNO_3 65% 2 mL H_2O_2 30%			HPR-AG-02 [82]
Ash from biomass	7 mL HNO_3 65% 1 mL HCl 37% 1.5 mL HF 40%	- temperature increase to 220 °C, time: 20 min; - maintaining at temperature of 220 °C, time: 15 min		HPR-EN-04 [83]

4.6. Statistical Analyses

The verification of the influence of the experimental factors used on the parameters analysed and existing dependencies was performed using ANOVA statistical analysis by means of the Bonferroni post hoc test. A materiality level of $\alpha \leq 0.05$ was applied. Principal component analysis (PCA) was also applied. This indirect ordination technique allows one to analyse a large number of variables to detect structure and regularity in relationships between them. Statistical analyses were performed using Statistica 12 software (StatSoft Polska, Krakow, Poland).

5. Conclusions

While verifying the research hypothesis, it should be stated that biochar and ash from plant biomass can be used as a fertiliser in the cultivation of energy crops. The results of research presented in this paper confirm that biochar and ash from biomass used at an appropriate dose have a positive effect on the chemical properties of the soil and increase the yield of giant miscanthus. The result of the research indicates that biochar is a better fertiliser than biomass ash due to the wider spectrum of activity. However, the research conducted needs to be continued in order to monitor soil properties and assess the crop yield to be obtained in the following years. Deepening knowledge in this area is an attempt to direct the circulation of inorganic matter in the environment, and at the same time forms an important support for environmental protection, with particular emphasis on phytoremediation and the utilitarian dimension of sustainable energy management. The introduction of biochar into the soil in combination with ash from biomass may be an alternative to traditional forms of mineral fertiliser, as well as a means to strengthen the ecological aspect of agro-energy.

Author Contributions: Conceptualization, B.S.; Data curation, B.S. and G.Z.; Formal analysis, B.S., G.Z., M.B. and M.C.; Methodology, B.S., G.Z., M.B. and M.C.; Project administration, C.P.; Supervision, C.P.; Writing—original draft, B.S. and G.Z.; Writing—review & editing, C.P.

Funding: This research received no external funding.

Conflicts of Interest: The authors declare no conflict of interest.

References

1. Kumar, P.; Barret, D.M.; Delwiche, M.J.; Stroeve, P. Methods for pretreatment of lignocellulosic biomass for efficient hydrolysis and biofuel production. *Ind. Eng. Chem. Res.* **2009**, *48*, 3713–3729. [CrossRef]
2. Tripathi, M.; Sahu, J.N.; Ganesan, P. Effect of process parameters on production of biochar from biomass waste through pyrolysis: A review. *Renew. Sustain. Energy Rev.* **2016**, *55*, 467–481. [CrossRef]
3. Kalembasa, D. Amount and chemical composition of ash from biomass of energy crops. *Acta Agrophys.* **2006**, *7*, 909–913.
4. Pels, J.R.; Nie, D.S.; Kiel, J.H.A. Utilization of ashes from biomass combustion and gasification. In Proceedings of the 13th European Biomass Conference & Exhibition, Paris, France, 17–21 October 2005.
5. Medyńska-Juraszek, A. Biochar as an addition to soils. *Soil Sci. Annu.* **2016**, *67*, 151–157. [CrossRef]
6. Laird, D.; Fleming, P.; Davis, D.; Horton, R.; Wang, B.; Karlen, D. Impact of biochar amendments on the quality of a typical Midwestern agricultural soil. *Geoderma* **2010**, *158*, 443–449. [CrossRef]
7. Macdonald, L.; Farrell, M.; Van Zwieten, L.; Krull, E. Plant growth responses to biochar addition: An Australian soils perspective. *Biol. Fertil. Soils* **2013**, *50*, 1035–1045. [CrossRef]
8. Beesley, L.; Moreno-Jiménez, E.; Gomez-Eyles, J.; Harris, E.; Robinson, B.; Sizmur, T. A review of biochars' potential role in the remediation, revegetation and restoration of contaminated soils. *Environ. Pollut.* **2011**, *159*, 3269–3282. [CrossRef] [PubMed]
9. Cross, A.; Sohi, S. The priming potential of biochar products in relation to labile carbon contents and soil organic matter status. *Soil Biol. Biochem.* **2011**, *43*, 2127–2134. [CrossRef]
10. Zhang, Q.; Du, Z.; Lou, Y.; He, X. A one-year short-term biochar application improved carbon accumulation in large macro aggregate fractions. *Catena* **2015**, *127*, 26–31. [CrossRef]
11. Lehmann, J.; Rilling, M.C.; Thies, J.; Masiello, C.A.; Hockaday, W.C.; Crowley, D. Biochar effects on soil biota—A review. *Soil Biol. Biochem.* **2011**, *43*, 1812–1836. [CrossRef]
12. Laird, D.A. The charcoal vision: A win-win-win scenario for simultaneously producing bioenergy, permanently sequestering carbon, while improving soil and water quality. *Agron. J.* **2008**, *100*, 178–181. [CrossRef]
13. Chan, K.Y.; Van Zwieten, L.; Meszaros, I.; Downie, A.; Joseph, S. Agronomic values of green waste biochar as a soil amendment. *Aust. J. Soil Res.* **2007**, *45*, 629–634. [CrossRef]
14. Woolf, D.; Amonette, J.E.; Street-Perrott, F.A.; Lehmann, J.; Joseph, S. Sustainable biochar to mitigate global climate change. *Nat. Commun.* **2010**, *1*, 56. [CrossRef] [PubMed]
15. Yuan, J.; Xu, R.; Zhang, H. The forms of alkalis in the biochar produced from crop residues at different temperatures. *Bioresour. Technol.* **2011**, *102*, 3488–3497. [CrossRef] [PubMed]
16. Novak, J.M.; Busscher, W.J.; Laird, D.L.; Ahmedna, M.; Watts, D.W.; Niandou, M.A.S. Impact of biochar amendment on fertility of a Southeastern coastal plain soil. *Soil Sci.* **2009**, *174*, 105–112. [CrossRef]
17. Zong, Y.; Xiao, Q.; Lu, S. Acidity, water retention, and mechanical physical quality of a strongly acidic Ultisol amended with biochars derived from different feedstocks. *J. Soil Sediment* **2006**, *16*, 177–190. [CrossRef]
18. Jien, S.; Wang, C. Effects of biochar on soil properties and erosion potential in a highly weathered soil. *Catena* **2013**, *110*, 225–233. [CrossRef]
19. Agegnehu, G.; Bass, A.; Nelson, P.; Bird, M. Benefits of biochar, compost and biochar-compost for soil quality, maize yield and greenhouse gas emissions in a tropical agricultural soil. *Sci. Total Environ.* **2016**, *543*, 295–306. [CrossRef] [PubMed]
20. Das, O.; Sarmah, A. The love-hate relationship of pyrolysis biochar and water: A perspective. *Sci. Total Environ.* **2015**, *512/513*, 682–685. [CrossRef] [PubMed]

21. Cayuela, M.; Van Zwieten, L.; Singh, B.; Jeffery, S.; Roig, A.; Sanchez-Monedero, M.A. Biochar's role in mitigating soil nitrous oxide emissions: A review and meta-analysis. *Agric. Ecosyst. Environ.* **2013**, *191*, 5–16. [CrossRef]
22. Cadoux, S.; Riche, A.B.; Yates, N.E.; Machet, J.M. Nutrient requirements of *Miscanthus* x *giganteus*: Conclusions from a review of published studies. *Biomass Bioenergy* **2012**, *38*, 13–22. [CrossRef]
23. Lewandowski, I.; Scurlock, J.M.O.; Lindvall, E.; Christou, M. The development and current status of perennial rhizomatous grasses as energy crops in the US and Europe. *Biomass Bioenergy* **2003**, *25*, 335–361. [CrossRef]
24. Landrat, M.; Waluda, T. Possibilities of fertilizer using of rabbit manure. *Arch. Waste Manag. Environ. Prot.* **2016**, *18*, 25–32.
25. Piekarczyk, M. Content of absorbable forms of some macro- and microelements in light soil fertilized with ash from winter wheat straw. *Fragm. Agron.* **2013**, *30*, 92–98.
26. Butnan, S.; Deenik, J.L.; Toomsan, B.; Antal, M.J.; Vityakon, P. Biochar characteristics and application rates affecting corn growth and properties of soils contrasting in texture and mineralogy. *Geoderma* **2015**, *237*, 105–116. [CrossRef]
27. Case, S.D.C.; McNamara, N.P.; Reay, D.S.; Whitaker, J. The effect of biochar addition on N_2O and CO_2 emissions from a sandy loam soil—The role of soil aeration. *Soil Biol. Biochem.* **2012**, *51*, 125–134. [CrossRef]
28. Lai, W.Y.; Lai, C.M.; Ke, G.R.; Chung, R.S.; Chen, C.T.; Cheng, C.H.; Pai, C.W.; Chen, S.Y.; Chen, C. The effects of woodchip biochar application on crop yield, carbon sequestration and greenhouse gas emissions from soils planted with rice or leaf beet. *J. Taiwan Inst. Chem. Eng.* **2013**, *44*, 1039–1044. [CrossRef]
29. Nigussie, A.; Kissi, E.; Misganaw, M.; Ambaw, G. Effect of biochar application on soil properties and nutrient uptake of lettuces (*Lactuca sativa*) grown in chromium polluted soils. *Am.-Eurasian. J. Agric. Environ. Sci.* **2012**, *12*, 369–376.
30. Park, B.B.; Yanai, R.D.; Sahm, J.M.; Lee, D.K.; Abrahamson, L.P. Wood ash effects on plant and soil in a willow bioenergy plantation. *Biomass Bioenergy* **2005**, *28*, 355–365. [CrossRef]
31. Turner, B.L.; Frossard, E.; Oberson, A. *Biological Approaches to Sustainable Soil Systems*; Enhancing phosphorus availability in low-fertility soils; Taylor & Francis: Abingdon, UK, 2006; pp. 191–205.
32. Chintala, R.; Schumacher, T.; McDonald, L.; Clay, D.; Malo, D.; Papiernik, S.; Clay, S.; Julson, J. Phosphorus sorption and availability from biochars and soil/biochar mixtures. *Clean-Soil Air Water* **2013**, *42*, 626–634. [CrossRef]
33. Oram, N.; van de Voorde, T.; Ouwehand, G.; Bezemer, T.; Mommer, L.; Jeffery, S.; van Groenigen, J. Soil amendment with biochar increases the competitive ability of legumes via increased potassium availability. *Agric. Ecosyst. Environ.* **2013**, *191*, 92–98. [CrossRef]
34. Widowati, W.; Asnah, A. Biochar can enhance potassium fertilization efficiency and economic feasibility of maize cultivation. *J. Agric. Sci.* **2013**, *6*, 24–32. [CrossRef]
35. Liu, Y.; Lu, H.; Yang, S.; Wang, Y. Impacts of biochar addition on rice yield and soil properties in a cold waterlogged paddy for two crop seasons. *Field Crops Res.* **2016**, *191*, 161–167. [CrossRef]
36. James, A.K.; Thring, R.W.; Helle, S.; Ghuman, H.S. Ash management review—Applications of biomass bottom ash. *Energies* **2012**, *5*, 3856–3873. [CrossRef]
37. Bakisgan, C.; Dumanli, A.G.; Yürüm, Y. Trace elements in Turkish biomass fuels: Ashes of wheat straw, olive bagasse and hazelnut shell. *Fuel* **2009**, *88*, 1842–1851. [CrossRef]
38. Klavina, D.; Pennanen, T.; Gaitnieks, T.; Velmala, S.; Lazdins, A.; Lazdina, D.; Menkis, A. The ectomycorrhizal community of conifer stands on peat soils 12 years after fertilization with wood ash. *Mycorrhiza* **2016**, *26*, 153–160. [CrossRef] [PubMed]
39. Doan, T.T.; Henry-des-Tureaux, T.; Rumpel, C.; Janeau, J.L.; Jouquet, P. Impact of compost, vermicompost and biochar on soil fertility, maize yield and soil erosion in northern Vietnam: A three-year mesocosm experiment. *Sci. Total Environ.* **2015**, *513*, 137–154. [CrossRef] [PubMed]
40. Ghosh, S.; Ow, L.F.; Wilson, B. Influence of biochar and compost on soil properties and tree growth in a tropical urban environment. *Int. J. Environ. Sci. Technol.* **2015**, *12*, 1303–1310. [CrossRef]
41. Spokas, K.A.; Cantrell, K.B.; Novak, J.M.; Archer, D.A.; Ippolito, J.A.; Collins, H.P.; Boateng, A.A.; Lima, I.M.; Lamb, M.C.; McAloon, A.J.; et al. Biochar: A synthesis of its agronomic impact beyond carbon sequestration. *J. Environ. Qual.* **2012**, *41*, 973–989. [CrossRef] [PubMed]
42. Kuzyakov, Y.; Subbotina, I.; Chen, H.; Bogomolova, I.; Xu, X. Black carbon decomposition and incorporation into soil microbial biomass estimated by 13C labeling. *Soil Biol. Biochem.* **2009**, *41*, 210–219. [CrossRef]

43. Liu, Z.; Chen, X.; Jing, Y.; Li, Q.; Zhang, J.; Huang, Q. Effects of biochar amendment on rapeseed and sweet potato yields and water stable aggregate in upland red soil. *Catena* **2013**, *123*, 45–51. [CrossRef]
44. Puga, A.P.; Abreu, C.A.; Melo, L.C.A.; Paz-Ferreiro, J.; Beesley, L. Cadmium, lead and zinc mobility and plant uptake in a mine soil amended with sugarcane straw biochar. *Environ. Sci. Pollut. Res.* **2015**, *22*, 17606–17613. [CrossRef] [PubMed]
45. Bielińska, E.J.; Baran, S.; Stankowski, S. Assessment of the suitability of fluidized ashes from hard coal for agricultural purposes. *Agric. Eng.* **2009**, *6*, 7–13.
46. Szczukowski, S.; Stolarski, M.; Tworkowski, J. Yielf of willow biomass manufactured with the eco-salix system. *Fragm. Agron.* **2011**, *28*, 104–115.
47. Kwaśniewski, D. Energy efficiency of biomass production from the annual willow. *Agric. Eng.* **2010**, *1*, 289–295.
48. Szczukowski, S.; Stolarski, M.; Tworkowski, J.; Rutkowski, P.; Goliński, P.; Mleczek, M.; Szentner, K. Yield and quality of biomass of selected willow species in the four-year harvest rotation. *Fragm. Agron.* **2013**, *31*, 107–113.
49. Jeżowski, S.; Głowacka, K.; Kaczmarek, Z.; Szczukowski, S. Field traits of eight common osier clones in the first three years following planting in Poland. *Biomass Bioenergy* **2011**, *35*, 1205–1210.
50. Kobyliński, A.; Olszewska, M. Energy efficiency of biomass production *Miscanthus giganteus*. *Grassl. Sci. Pol.* **2013**, *16*, 19–28.
51. Puchalski, C.; Zapałowska, A.; Hury, G. The impact of sewage sludge and biomass ash fertilization on the yield, including biometric features and physiological parameters of plants of two jerusalem artichoke (*Helianthus tuberosus* L.) cultivars. *Folia Pomer. Univ. Technol. Stetin. Agric. Aliment Pisc. Zootech.* **2017**, *332*, 37–52.
52. Boehmel, C.; Claupein, W. Contribution to bioenergy production by different annual and perennial cropping systems. In Proceedings of the 15th European Biomass Conference, Berlin, Germany, 7–11 May 2007.
53. Christou, M.; Mardikis, M.; Alexopoulou, E. Research on the effect of irrigation and nitrogen upon growth and yields of *Arundo donax* L. in Greece. *Asp. Appl. Biol.* **2001**, *65*, 47–55.
54. Danalatos, N.; Archontoulis, S.; Mitsios, I. Potential growth and biomass productivity of *Miscanthus* x *giganteus* as affected by plant density and N–fertilization in central Greece. *Biomass Bioenergy* **2007**, *31*, 31–152. [CrossRef]
55. Smith, R.; Slater, F.M. The effects of organic and inorganic fertilizer applications to *Miscanthus* x *giganteus*, *Arundo donax* and *Phalaris arundinacea*, when grown as energy crops in Wales, UK. *GCB. Bioenergy* **2010**, *2*, 169–179. [CrossRef]
56. Chan, K.Y.; Van Zwieten, L.; Meszaros, I.; Downie, A.; Joseph, S. Using poultry litter biochars as soil amendments. *Aust. J. Soil Res.* **2008**, *46*, 437–444. [CrossRef]
57. Glaser, B.; Lehmann, J.; Zech, W. Ameliorating physical and chemical properties of highly weathered soils in the tropics with charcoal—Review. *Biol. Fertil Soils* **2002**, *35*, 1719–1730. [CrossRef]
58. Uzoma, K.C.; Inoue, M.; Andry, H.; Fujimaki, H.; Zahoor, A.; Nishihara, E. Effect of cow manure biochar on maize productivity under sandy soil condition. *Soil Use Manag.* **2011**, *27*, 205–212. [CrossRef]
59. Liu, X.; Zhang, A.; Ji, C.; Joseph, S.; Bian, R.; Li, L.; Pan, G.; Paz-Ferreiro, J. Biochar's effect on crop productivity and the dependence on experimental conditions—A meta-analysis of literature data. *Plant Soil* **2013**, *373*, 583–594. [CrossRef]
60. Hossain, M.K.; Strezov, V.; Chan, K.Y.; Nelson, P.F. Agronomic properties of wastewater sludge biochar and bioavailability of metals in production of cherry tomato (*Lycopersicon esculentum*). *Chemosphere* **2010**, *78*, 1167–1171. [CrossRef] [PubMed]
61. Lehmann, J.; Gaunt, J.; Rondon, M. Biochar sequestration in terrestrial ecosystems—A review. *Mitig. Adapt. Strateg. Glob. Chang.* **2006**, *11*, 395–419. [CrossRef]
62. Gao, S.; DeLuca, T.H. Influence of biochar on soil nutrient transformations, nutrient leaching and crop yield. *Adv. Plants Agric. Res.* **2016**, *4*, 00150.
63. Klašnja, B.; Orlović, S.; Galić, Z. Comparison of different wood species as raw materials for bioenergy. *South-East Eur. For.* **2013**, *4*, 81–88. [CrossRef]
64. Kołodziej, B.; Antonkiewicz, J.; Sugier, D. *Miscanthus* x *giganteus* as a biomass feedstock grown on municipal sewage sludge. *Ind. Crops Prod.* **2016**, *81*, 72–82. [CrossRef]

65. Szyszlak-Bargłowicz, J.; Zając, G.; Piekarski, W. Energy biomass characteristics of chosen plants. *Int. Agrophys.* **2012**, *26*, 175–179. [CrossRef]
66. Borkowska, H.; Lipiński, W. Content of selected elements in biomass of several species of energy crops. *Acta Agrophys.* **2007**, *10*, 287–292.
67. Szyszlak-Bargłowicz, J. Content of chosen macroelements in biomass of Virginia mallow (*Sida hermaphrodita* Rusby). *J. Cent. Eur. Agric.* **2013**, *15*, 263–271. [CrossRef]
68. Kalembasa, D.; Malinowska, E. Follow-up activities of sewage sludge applied to the soil in the pot experiment on the content of heavy metals in grass *Miscanthus sacchariflorus*. *Acta Agrophys.* **2009**, *13*, 377–384.
69. Kalembasa, S.; Wysokiński, A.; Cichuta, R. Content of heavy metals in willow (*Salix viminalis*) wth different nitrogen fertilization. *Acta Agrophys.* **2009**, *13*, 385–392.
70. Szwalec, A.; Mundała, P.; Kędzior, R.; Telk, M.; Gawroński, P. Differentiation of Cd, Pb, Zn and Cu contents in biomass used for energy production. *Acta Sci. Pol. Formatio Circumiectus* **2016**, *15*, 343–351.
71. Polish Committee for Standardization. *Soil Quality—Determination of Ph*; Polish Committee for Standardization: Warsaw, Poland, 1997.
72. Polish Committee for Standardization. *Chemical and Agricultural Analysis of the Soil—Determination of the Content of Absorbable Phosphorus in Mineral Soils*; Polish Committee for Standardization: Warsaw, Poland, 1996.
73. Polish Committee for Standardization. *Chemical and Agricultural Analysis of the Soil—Determination of the Content of Potassium in Mineral Soils*; Polish Committee for Standardization: Warsaw, Poland, 2002.
74. Polish Committee for Standardization. *Chemical and Agricultural Analysis of the Soil— Determination of the Content of Potassium in Mineral Soils*; Polish Committee for Standardization: Warsaw, Poland, 2004.
75. British Standards Institution. *Solid Biofuels—Determination of Total Carbon, Hydrogen and Nitrogen Content—Instrumental Methods*; British Standards Institution: London, UK, 2011.
76. British Standards Institution. *Solid Biofuels—Determination of Volatile Part Content*; British Standards Institution: London, UK, 2010.
77. British Standards Institution. *Solid Biofuels—Determination of Calorific Value*; British Standards Institution: London, UK, 2011.
78. British Standards Institution. *Solid Biofuels—Determination of Calorific Value*; British Standards Institution: London, UK, 2010.
79. Saletnik, B.; Zaguła, G.; Grabek-Lejko, D.; Kasprzyk, I.; Bajcar, M.; Czernicka, M.; Puchalski, Cz. Biosorption of cadmium (II), lead (II) and cobalt (II) from aqueous solution by biochar from cones of larch (*Larix decidua* Mill. *subsp. decidua*) and spruce (*Picea abies* L. H. Karst). *Environ. Earth Sci.* **2017**, *76*, 574. [CrossRef]
80. Milestone. *SK-10 High Pressure Rotor*; HPR-EN-13 Soil Total Digestion; Milestone: Shelton, CT, USA; Available online: http://subitam.sinop.edu.tr/fileman/Uploads/Subitam/Mikrodalga.pdf (accessed on 16 January 2018).
81. Milestone. *SK-10 High Pressure Rotor*; HPR-PE-19 Carbon Black; Milestone: Shelton, CT, USA; Available online: http://subitam.sinop.edu.tr/fileman/Uploads/Subitam/Mikrodalga.pdf (accessed on 16 January 2018).
82. Milestone. *SK-10 High Pressure Rotor*; HPR-AG-02 Dried Plant Tissue; Milestone: Shelton, CT, USA; Available online: http://subitam.sinop.edu.tr/fileman/Uploads/Subitam/Mikrodalga.pdf (accessed on 16 January 2018).
83. Milestone. *SK-10 High Pressure Rotor*; HPR-EN-04 Fly Ash; Milestone: Shelton, CT, USA; Available online: http://subitam.sinop.edu.tr/fileman/Uploads/Subitam/Mikrodalga.pdf (accessed on 16 January 2018).

energies

MDPI

Article

Influence of NaCl Concentration on Food-Waste Biochar Structure and Templating Effects

Ye-Eun Lee [1,2], Jun-Ho Jo [1], I-Tae Kim [1] and Yeong-Seok Yoo [1,2,*]

[1] Division of Environment and Plant Engineering, Korea Institute of Civil Engineering and Building Technology, 283 Goyang- daero, Ilsanseo-gu Goyang-si, Gyeonggi-do 10223, Korea; yeeunlee@kict.re.kr (Y.-E.L.); junkr@kict.re.kr (J.-H.J.); itkim@kict.re.kr (I.-T.K.)

[2] Department of Construction Environment Engineering, University of Science and Technology, 217 Gajeong-ro, Yuseong-gu, Daejeon 34113, Korea

* Correspondence: ysyoo@kict.re.kr; Tel.: +82-31-910-0298; Fax: +82-31-910-0288

Received: 3 August 2018; Accepted: 31 August 2018; Published: 5 September 2018

Abstract: Food-waste-derived biochar structures obtained through pyrolysis and with different NaCl concentrations were investigated. Increased NaCl concentration in the samples inhibited cellulose and lignin decomposition, ultimately increasing the biochar yield by 2.7% for 20%-NaCl concentration. NaCl added in solution state exhibited templating effects, with maximum increases in the Brunauer–Emmett–Teller (BET) surface area and pore volume of 1.23 to 3.50 $m^2 \cdot g^{-1}$ and 0.002 to 0.007 $cm^3 \cdot g^{-1}$, respectively, after washing. Adding a high concentration (20%) of NaCl reduced the BET surface area. In contrast, the mean pore diameter increased owing to the increased NaCl clustering area. Increased NaCl clustering with increased added NaCl was shown to have positive effects on NaCl removal by washing. Furthermore, as the NaCl adhered to the KCl scattered in the food waste, a high NaCl concentration also had positive effects on KCl removal. This study reports on an investigation on the effects of varying NaCl concentrations injected in solution form on the structure of food-waste biochar during pyrolysis. The templating effect was considered using both added NaCl and NaCl already contained in the food waste, with implementation of a desalination process essential for food-waste treatment for recycling.

Keywords: food waste; food-waste biochar; pyrolysis; NaCl template; desalination

---

1. Introduction

Carbon-negative biochar can be obtained from biomass via pyrolysis in an oxygen-limited environment [1]. Following the recent 2015 Paris Agreement, which expanded responsibility for greenhouse gas emissions mitigation to both developing and advanced countries, biochar production based on biowaste pyrolysis has become a novel alternative for biomass treatment [2–4].

The two main factors determining biochar characteristics are the physical properties of the raw material and the pyrolytic conditions (e.g., temperature, heating rate, and retention time) [5]. Pyrolysis methods can be broadly categorized into fast or slow techniques, respectively featuring a high heating rate of 100–1000 $°C \cdot s^{-1}$ to produce gas or oil or a low heating rate of 20–100 $°C \cdot min^{-1}$, which is more effective for biochar production [6,7].

The feedstocks most commonly used in commercial-scale or academic research are green waste materials, such as wood chips, crop residue, switch grass, and sugarcane, and organic wastes, such as sewage sludge and dairy manure [8]. For example, Van Zwieten et al. [9] reported the characteristics of biochar produced from papermill waste via slow pyrolysis at 550 °C, and Kloss et al. [10] analyzed the characteristics of slow pyrolysis for different sources (wheat straw, poplar wood, and spruce wood) at different temperatures (400, 460, and 525 °C). Furthermore, Ronsse et al. [11] compared different feedstocks, including pine wood, wheat straw, green waste, and dried algae, to analyze the corresponding characteristics of the resultant biochar obtained via slow pyrolysis. However, although various feedstocks were comparatively analyzed in previous studies, the feedstocks themselves were mostly limited to the waste of a single organic crop.

Food is the largest waste source containing a blend of various organics and can be a good energy source with high energy content [12]. However, establishing an appropriate recycling method is challenging, as the NaCl content of food waste necessitates specific treatments. At present, composting is the main treatment method for food waste. However, the presence of NaCl continues to affect the compost quality. According to a recent review on food-waste usage by Pham et al. [13], conversion into biochar may be a promising alternative for food-waste treatment, but there is a lack of research on pyrolysis compared to anaerobic digestion and hydrothermal carbonization. Lee et al. [14] verified the potential application of food-waste pyrolysis at 300–500 °C and desalination to biochar production. Nonetheless, the biochar characteristic dependence on the different food source must be investigated.

In Korea, despite seasonal and source differences due to unique food cultures, the average NaCl content of dried food-waste biomass is 3.45% [15]. This implies that desalination is a prerequisite to food-waste recycling, which may increase the value of biochar. Recently, studies using molten NaCl as a template for increasing porosity have been reported. Among them, Fechler et al. [16] generated a porous material by mixing eutectic NaCl with C material and washing the resulting substance with water, and Liu and Antonietti [17] used molten NaCl and glucose to generate a porous C structure. These reports suggest the possibility of a desalination technique that removes the NaCl already present in the food waste, similar to the activation process for activated carbon.

In this context, the present study investigated whether the same activation effects as those obtained for molten NaCl can be achieved by adding NaCl in solution form to food waste. The corresponding changes in biochar structure, Brunauer–Emmett–Teller (BET) surface area, and pore size were examined for varying NaCl concentrations.

2. Materials and Methods

2.1. Materials

Food-waste samples were prepared using data from the Korean Ministry of the Environment (Table 1) [18]. The food waste was broadly classified into grains, vegetables, fruits, and meat, consisting of 10 ingredients with weight percent (wt %) values of 16, 51, 14, and 19, respectively. Whole ingredients of food waste sample were raw except the cooked rice. And the weight measurements were made at room temperature (25 °C). The prepared samples were dried at 105 °C for 24 h and ground into powder.

Table 1. Standard Food-Waste Samples.

Classification	Composition Ratio (wt %)	Food-Ingredient Processing Methods	
		Food Ingredients	Processing Method
Grains	16	Rice (16)	
Vegetables	51	Napa cabbage (9)	Cutting width: <100 mm
		Potato (20)	Chopped into 5 mm pieces
		Onion (20)	
		Daikon (2)	
Fruits	14	Apple (7)	Split lengthwise into 8 pieces
		Mandarin/orange (7)	
Meat	19	Meat (19)	Cutting width: ~3 cm.
Total	100	100	

2.2. Experimental Methods

The experiment had four steps: sample preparation, NaCl injection and drying, pyrolysis, and washing. Each independent experiment was repeated twice, and the results were presented as mean values. Solutions of 5, 10, and 20% NaCl were added to 120 g dried food-waste samples, corresponding to 6.32, 13.34, and 15.00 g of NaCl dissolved in distilled water, respectively. The NaCl-free and 5, 10, and 20% NaCl-containing samples are referred to as the 0, 5, 10, and 20%-NaCl samples hereafter. The resulting mixtures were dried at 105 °C for 24 h. Next, the 0%-NaCl dried food samples and those impregnated with NaCl were placed in an electric furnace. The temperature was increased to 500 °C at 20 °C/min (the lowest speed of slow pyrolysis), and the pyrolysis was maintained for 1 h. To prevent sample oxidation, 99.99% N_2 gas (SJGAS, Incheon, Korea) was continuously injected into the furnace at 10 L/min through the flowmeter. The samples were subsequently removed from the furnace and cooled at room temperature until the ambient temperature was reached, after which the produced char was weighed. Figure 1 is a schematic of the pyrolysis reactor used in the experiment.

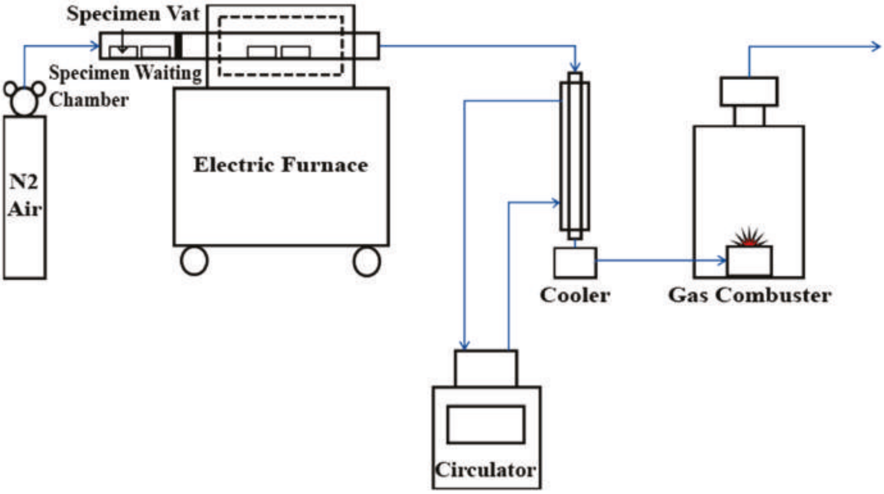

Figure 1. Schematic of the pyrolysis reactor used in this study.

To analyze and compare the differences in BET surface area among the samples, activated C was prepared as follows to be used as a control: For activation, 1 M sodium hydroxide (NaOH) solution was injected into a 0%-NaCl dried food sample at a 1:2 ratio. The sample was then dried at 105 °C before being subjected to pyrolysis under identical conditions as described above. Then, it was washed until the washing water reached pH 7 and dried.

2.3. Analysis Methods

2.3.1. Characterization Analysis Methods

When pyrolysis was complete, a CHNS analyzer (2400SeriesIICHNS/O, Perkin Elmer, Boston, MA, USA) was used to estimate the biochar elemental composition. Under the assumption that C + nitrogen (N) + O + sulfur (S) + hydrogen (H) + sodium (Na) + chlorine (Cl) = 100%, the O content was calculated using the equation $100\ (\%) - (C + N + S + H + Na + Cl) = O$. To estimate the Cl content of the food-waste biochar, combustion ion chromatography (CIC; AQF-2100H, Mitsubishi Chemical Analytech, Chigasaki, Japan) was used. Note that, although CIC was found to be suitable for quantifying the 0%-NaCl biochar and the washed biochar from which the NaCl had been removed, the unwashed 5, 10, and 20%-NaCl biochar samples exceeded the CIC quantifiable range. This was because the NaCl concentrated during pyrolysis. Thus, the following Equation (1) was used, based on the quantified Na content:

$$\frac{(\text{Na content of sample }(\%) - \text{Na content of 0\% biochar }(\%)) \times 35.45\ (\text{Atomic mass of Cl})}{22.98\ (\text{Atomic mass of Na})} = \text{Cl content of sample }(\%) \quad (1)$$

To quantify the Na content of the biochar, atomic absorption spectroscopy (AAnalyst400, Perkin Elmer, Boston, MA, USA) was used.

2.3.2. Structural Analysis

BET and scanning electron microscopy (SEM)–energy dispersive X-ray (EDX) analyses were conducted to study the influence of the NaCl in the food waste on the biochar. The biochar microstructures were observed using SEM (Hitachi Ltd. S-4800 Ibaraki, Japan) with EDX (Oxford, EDX S-10, Abingdon, UK), and the BET surface areas were measured to check the templating effect before and after washing. The BET surface area was estimated based on N_2 gas sorption analysis at 77 K using a specific surface analyzer (BELSORP-MAX, BEL Japan Inc, Osaka, Japan).

To investigate the structural changes in the food-waste-derived biochar according to NaCl concentration, X-ray diffraction (XRD; DMAX 2500, Rigaku, Tokyo, Japan; 18 kW, 60 kV/300 mA) was employed. The 2θ range recorded for the samples was 10–90 °C. To investigate the presence of NaCl in the biochar as well as its influence, the value for 99%-NaCl powder was estimated, which was compared with the Joint Committee on Powder Diffraction and Standards (JCPDS) entry for NaCl (5–628) to establish the standard value. Fourier transform infrared spectroscopy (FT-IR; VERTEX 80V, Bruker Optics, Billerica, MA, USA) was performed and the KBr pellet method was used, in which a 1 mg sample was mixed with KBr powder and pressurized into a thin film. The structure was analyzed by transmitting 400–4000 nm infrared waves. All biochar samples used in the experiment were analyzed without prior treatment.

3. Results and Discussion

3.1. Biochar Characterization

Table 2 lists the chemical compositions of the food-waste-derived biochar for each NaCl concentration. As the NaCl in biochar can be removed by washing, the biochar samples before and after washing were analyzed to study the changes. The biochars before washing were compared with the 0%-NaCl food-waste-derived biochar as a control. Increased NaCl content was found to be accompanied by decreased C, H, and N contents, whereas the Na and Cl were condensed to crystal form. This indicates that the NaCl injected in an ionized state in the solution formed NaCl crystals during the drying and pyrolysis processes, thereby concentrating the NaCl in the biochar and preventing evaporation during pyrolysis. Regarding the post-wash compositions, the C, H, and N contents increased again in a trend similar to that in the control, whereas the Na and Cl contents decreased. This indicates that, although the increased NaCl content per unit weight made it seem as if the relative C, H, and N contents had decreased, the atomic content per unit weight of these materials was recovered as the washing removed the NaCl.

Table 2. Chemical composition of food-waste-derived biochar with different NaCl contents. (A: washed biochar; B: unwashed biochar; –: Not detected.).

(wt %)	C	H	N	S	O	Na	Cl
B_0%	76.29 ± 0.05	2.94 ± 0.02	6.04 ± 0.15	–	14.13 ± 0.10	0.24 ± 0.03	0.38 ± 0.01
B_5%	62.47 ± 0.23	2.39 ± 0.10	5.05 ± 0.01	–	12.62 ± 0.15	7.02 ± 0.01	10.47 ± 0.02
A_5%	75.90 ± 0.13	2.90 ± 0.07	6.03 ± 0.09	–	12.16 ± 0.04	2.20 ± 0.10	0.82 ± 0.10
B_10%	52.43 ± 0.54	2.06 ± 0.05	4.04 ± 0.02	–	10.59 ± 0.35	12.29 ± 0.09	18.60 ± 0.14
A_10%	76.21 ± 0.11	3.00 ± 0.01	5.91 ± 0.19	–	12.04 ± 0.01	2.09 ± 0.14	0.77 ± 0.16
B_20%	38.95 ± 0.89	1.98 ± 0.50	3.41 ± 0.05	–	8.63 ± 1.08	18.64 ± 0.99	28.40 ± 1.53
A_20%	74.92 ± 1.36	3.97 ± 0.72	6.21 ± 0.01	–	12.30 ± 1.09	2.27 ± 0.30	0.34 ± 0.15

Comparison of the Na and Cl contents before and after washing showed that the washing removed most of the NaCl. The post-wash Na content in the 5, 10, and 20%-NaCl biochar was higher than that in the 0%-NaCl control. This may be attributed to the influence of the biochar cation exchange capacity, under which a proportion of the Na^+ ions generated during washing adsorbed to the biochar [14]. Higher Cl content values were obtained for the 5 and 10%-NaCl biochar samples after washing compared to those of the 0%-NaCl biochar. However, the 20%-NaCl biochar exhibited similar contents to that of the control as the content decreased following washing. This similarity was due to the increased NaCl content of that specimen, which caused the NaCl to cluster rather than disperse. The SEM analysis (Section 3.2.2.) also confirmed that clustered NaCl crystals were scattered throughout the biochar for the 20%-NaCl biochar, whereas relatively small, scattered crystals were observed in the 5 and 10%-NaCl biochar samples. In other words, for 5 and 10%-NaCl content, the crystals were bound to the biochar in a scattered state, and complete NaCl removal through washing was difficult. However, for 20%-NaCl content, a large number of clustered NaCl crystals was obtained. Thus, complete removal is possible.The biochar yield, calculated as follows Equation (2):

$$\frac{\text{Weight after pyrolysis (g)} - \text{Impregnated NaCl content (g)}}{\text{Amount of Food waste (g)}} \times 100 = \text{Char Yield (\%)} \quad (2)$$

As Table 3 indicates, the food-waste biochar yield after NaCl injection was higher than that for NaCl-free food waste in general. Further, as the impregnated NaCl content increased, the char yield increased. In other words, the NaCl injection influenced the pyrolysis, thereby affecting the char yield.

Table 3. Effect of NaCl Concentrations on Food Waste Biochar Yield.

Added NaCl	Food Waste (g)	NaCl Content (g)	Weight after Pyrolysis (g)	Char Yield (wt %)
0%	120.00	-	27.29 ± 0.18	22.77 ± 0.15
5%	120.00	6.32	34.79 ± 0.28	23.73 ± 0.23
10%	120.00	13.34	42.04 ± 0.41	23.92 ± 0.34
20%	120.00	30.00	60.59 ± 2.40	25.49 ± 2.01

3.2. Structural Analysis

3.2.1. Brunauer–Emmett–Teller Analysis and Pore Size Distribution

Table 4 lists the BET surface area and pore analysis results for the biochar. For the NaCl-free (0%) biochar, the BET surface area was 1.226 $m^2 \cdot g^{-1}$. For the NaCl-containing biochar, increases in both BET surface area and pore volume after washing were observed, with differences according to NaCl content. This phenomenon was due to the empty spaces following NaCl removal by washing. Note that the SEM results discussed below (Section 3.2.2.) provide additional support for these findings.

When the total pore and mesopore volumes were compared, almost identical values were obtained; thus, most pores were mesopores. The approximately two-fold increase in mesopore volume after washing also indicated that the mesopores were likely to have been caused by NaCl. The average pore diameter of washed sample is lower than unwashed sample. The average pore dimeter before washing is not induced by NaCl but generated by the volatilization of organic matter. On the other hand, the pore diameter after washing is contained the pore induced by NaCl templating effect. In Section 3.2.2. showed that a single NaCl crystal size is about 2 nm. Therefore the average pore diameter is decreased after washing since the relatively small pore created by NaCl templating effect.

In contrast to the increase in total pore and mesopore volumes with increased NaCl content, the BET surface area exhibited a decreasing trend. An initial increase accompanied the NaCl content increase from 5 to 10%, but this was followed by a decrease when 20%-NaCl content was reached. This is thought to have been due to the excess NaCl allowing the clustered NaCl to exceed the large dispersion of NaCl. In other words, the higher the NaCl content was, the larger the NaCl crystals were; this yielded pores with a larger diameter and volume when the NaCl was removed. In contrast, the BET surface area decreased because of the growth of large mesopores instead of the even dispersion of relatively small mesopores.

There are other studies using NaCl as a template and washing as an activation process. Liu and Antonietti [17] used molten NaCl injected into a single source type, and Lu et al. [19] injected small-particle NaCl powder. But, these approaches differ from that of the present study. The findings of this study suggest that NaCl in solution form can have templating effects, and that the washing process induced activation effects.

In terms of competence, the BET surface areas and pore volumes observed in this study are not comparable to those of activated carbon. To explain this difference, the same sources were used in an experiment in which the activation method was implemented; the results are listed in the bottom row of Table 4. NaOH samples were prepared for activation by NaOH injection, followed by drying and pyrolysis at 500 °C, as in the main experiment. Washing was subsequently performed for neutralization. Between the biochar samples activated using 10%-NaCl and NaOH, the NaOH-treated biochar had a larger pore diameter. However, the difference in BET surface area was not substantial (0.414 $m^2 \cdot g^{-1}$). Despite the increased pore diameter, the small increase in BET surface area for NaOH activation may indicate increased pore depth compared to activation based on NaCl crystals.

Studies investigating NaOH activation have reported high BET values for a single organic crop waste source, e.g., fir wood (380 (m^2/g)) [20], coconut shell (1842 (m^2/g)) [21], and flamboyant pods (1076 (m^2/g)) [22]. However, Dai et al. [23] obtained low BET surface area values (12.73 and 12.99 ($m^2 \cdot g^{-1}$)) for livestock excretion as a source. This indicates that the BET surface area deviates significantly according to the source, and a lower BET surface area is generally produced when a mixed source is employed. The results of NaCl activation in this study indicate lower BET values than those of the abovementioned studies. However, the overall BET surface area reduction is likely to have resulted from the raw material and not the activation method, based on the comparison with NaOH activation.

Table 4. Brunauer–Emmett–Teller (BET) Surface Area and Pore Volume Analysis of Food-Waste-Derived Biochar with Different NaCl Contents.

Sample	BET Specific Surface Area ($m^2 \cdot g^{-1}$)	Total Pore Volume (p/p_0 = 0.990) ($cm^3 \cdot g^{-1}$)	Average Pore Diameter (nm)	Mesopore Surface Area ($m^2 \cdot g^{-1}$)	Mesopore Volume ($cm^3 \cdot g^{-1}$)
B_0%	1.226	0.00201	6.552	0.672	0.00176
B_5%	0.824	0.00193	9.475	0.465	0.00177
A_5%	2.946	0.00458	7.556	1.158	0.00377
B_10%	1.184	0.00341	11.505	0.902	0.00329
A_10%	3.500	0.00623	8.501	1.686	0.00537
B_20%	0.795	0.00256	14.119	0.651	0.00248
A_20%	2.485	0.00653	12.610	1.623	0.00613
NaOH	3.914	0.01746	17.845	2.452	0.01675

3.2.2. Scanning Electron Microscopy Analysis

Figure 2 presents images at different magnifications taken before and after biochar washing according to NaCl content. The NaCl crystals are embedded in the biochar surface. In the pre-wash images, the NaCl crystals are clustered together, except for the 20%-NaCl case, in which they are scattered. When crystals cluster, larger pores remain when they are removed through washing. The post-wash images show square-shaped pores identical to the NaCl crystals on the biochar surface. The pore diameter increased from 1.4 to 1.77 and then to 2.3 nm for NaCl contents of 5, 10, and 20%, respectively. In other words, the NaCl injected into the food waste occupied the interparticle spaces, thereby exerting a templating effect that created pores as it left the spaces upon washing. Higher NaCl content corresponded to larger crystals; hence, larger pores were created. The results also suggest that templating effects can be produced using NaCl in solution in addition to molten NaCl.

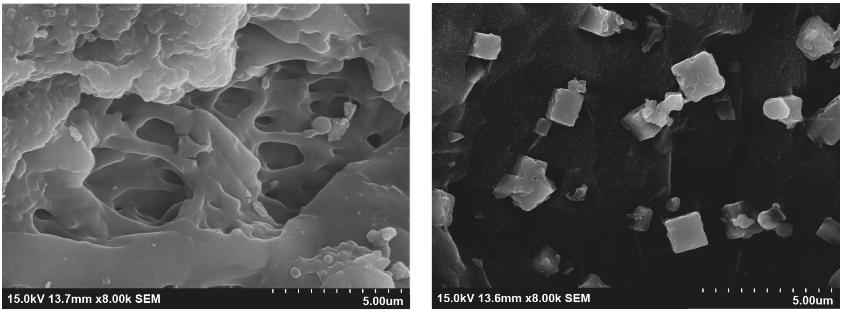

(**a**) 0%-NaCl-x8000 (**b**) 5%-NaCl-x8000 (pre-wash)

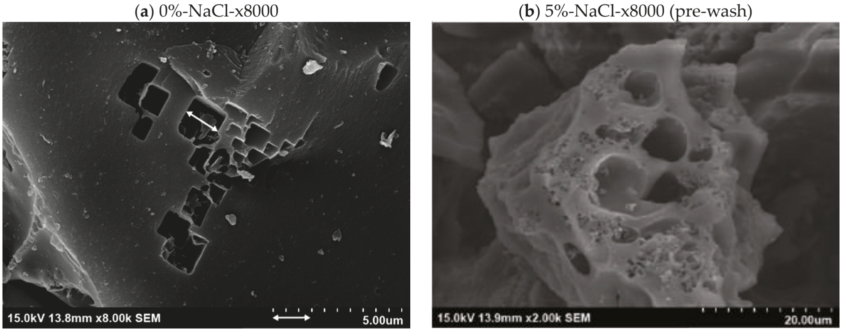

(**c**) 5%-NaCl-x8000 (post-wash) (**d**) 5%-NaCl-x2000 (post-wash)

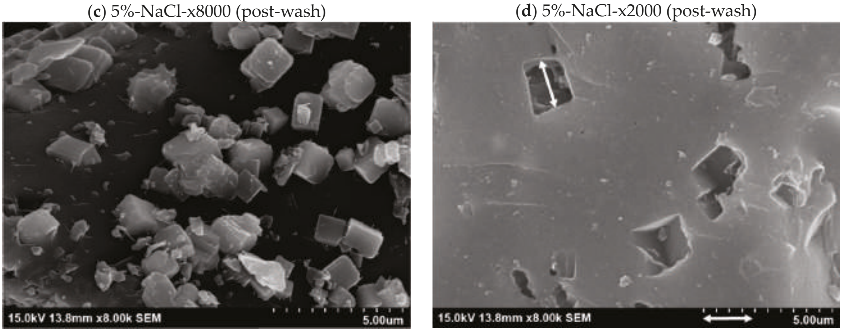

(**e**) 10%-NaCl-x8000 (pre-wash) (**f**) 10%-NaCl-x8000 (post-wash)

Figure 2. *Cont.*

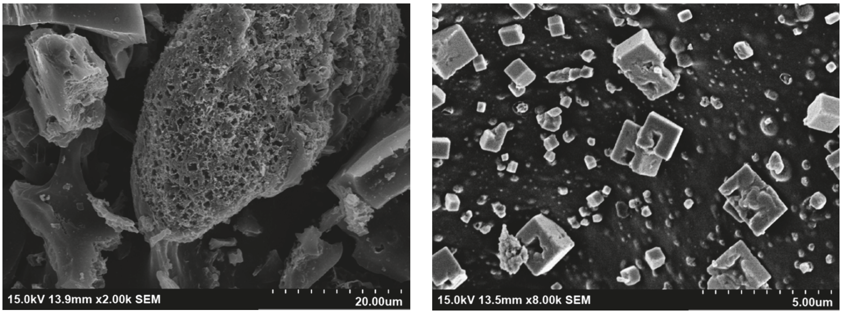

(**g**) 10%-NaCl-x2000 (post-wash) (**h**) 20%-NaCl-x8000 (pre-wash)

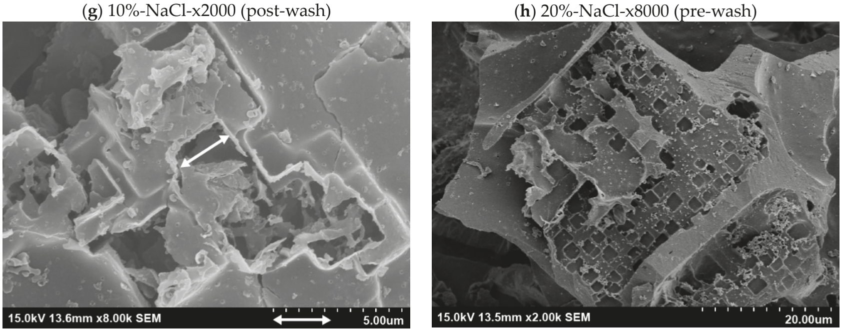

(**i**) 20%-NaCl-x8000 (post-wash) (**j**) 20%-NaCl-x2000 (post-wash)

Figure 2. (**a**–**j**) scanning electron microscopy (SEM) images of biochar samples with different NaCl contents before and after washing: (**a**) 0%-NaCl-x8000; (**b**) 5%-NaCl-x8000 (pre-wash); (**c**) 5%-NaCl-x8000 (post-wash); (**d**) 5%-NaCl-x2000 (post-wash); (**e**) 10%-NaCl-x8000 (pre-wash); (**f**) 10%-NaCl-x8000 (post-wash); (**g**) 10%-NaCl-x2000 (post-wash); (**h**) 20%-NaCl-x8000 (pre-wash); (**i**) 20%-NaCl-x8000 (post-wash); (**j**) 20%-NaCl-x2000 (post-wash).

The EDX results of a marked range of figures (a), (c), and (e) in Figure 3 are shown in (b), (d), and (f) in Figure 3, respectively. The EDX results in Figure 3 indicate the places where intercrystal fusion or binding occurred; peaks corresponding to Na, K, and Cl can be seen together. One possible explanation for this phenomenon is the formation of a novel crystal shape upon binding. This may occur through the reformation of some crystals during sintering, as the melting point decreases when sylvite (KCl) and NaCl coexist [24] or through fusion of the injected NaCl and KCl already present in the food sample.

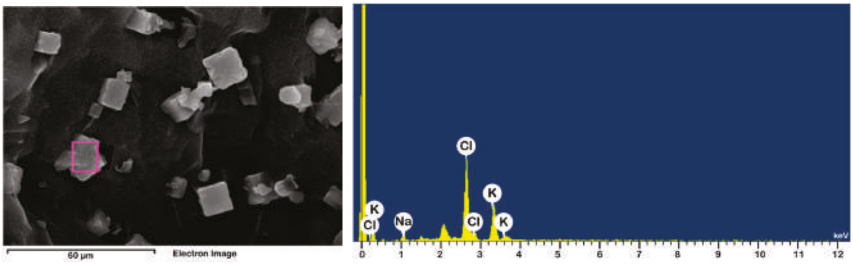

(**a**) 5% biochar (**b**) 5% biochar EDX result

Figure 3. *Cont.*

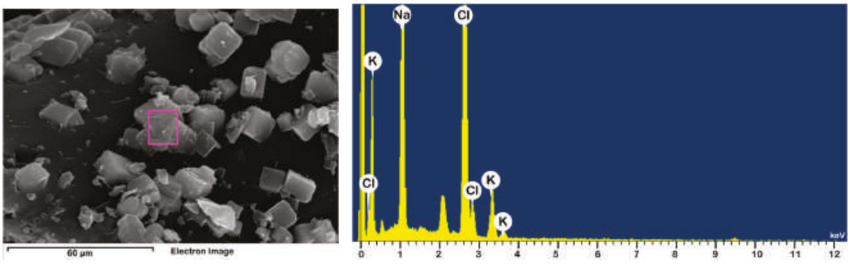

(**c**) 10% biochar

(**d**) 10% biochar EDX result

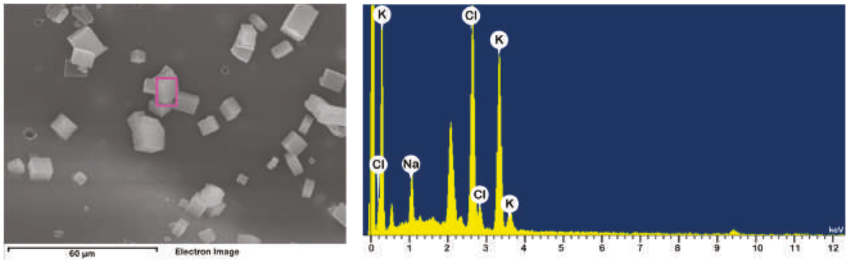

(**e**) 20% biochar

(**f**) 20% biochar EDX result

Figure 3. (**a**–**f**) NaCl crystal shape deformations and EDX results for biochar samples with different NaCl contents. (**a**) 5% biochar; (**b**) 5% biochar EDX result; (**c**) 10% biochar; (**d**) 10% biochar EDX result; (**e**) 20% biochar; (**f**) 20% biochar EDX result.

3.2.3. Fourier Transform Infrared Analysis

The results of the FT-IR analysis of the biochar according to NaCl content are presented in Figure 4. For the 0%-NaCl biochar sample, a peak appeared at 550 cm^{-1}. For the biochar samples containing NaCl that underwent pyrolysis, a peak appeared at 570 cm^{-1}, as if the peak at 550 cm^{-1} had shifted to the right. Vandecandelaere et al. [25] reported that peaks at 550 cm^{-1} indicate the presence of HPO_4^{2-} ions, whereas peaks at 575 cm^{-1} are related to PO_4^{3-} ions. Furthermore, Bekiaris et al. [26] showed that P=O stretching in hydroxyl apatite, apatite, and amorphous calcium phosphate dibasic in biochar yields 570-cm^{-1} peaks. In other words, if NaCl is present in the biomass during pyrolysis, phosphorus-compound decomposition to PO_4^{3-} rather than HPO_4^{2-} is induced. The peak at 520 cm^{-1} representing C-Cl bonding [27] and that at 646 cm^{-1} corresponding to C-Cl bending vibration [28] were not detected in the samples examined in this study. Therefore, the NaCl injection did not induce bonding with C.

The broad peak over the 700–1600 cm^{-1} range in Figure 4 indicates the presence of cellulosic and ligneous constituents. For the NaCl-free (0%) biochar, peaks appeared at 1030, 1070, and 1120 cm^{-1}. With increased NaCl content, the peak at 1030 cm^{-1} shifted to the right, whereas that at 1120 cm^{-1} moved to 1130–1150 cm^{-1}. The peaks at 1030 and 1120 cm^{-1} represent symmetric C-O stretching (cellulose, hemicellulose, and methoxy groups of lignin) and the symmetric C-O stretching characteristic of aliphatic C-O-C in the cellulose group, respectively [29,30]. The shifting of these peaks to the right indicated changes in cellulose from aliphatic C-O-C to alcohol C-O stretching or antisymmetric stretching of C-O-C (glycosyl), as the NaCl in the biochar induces hemolytic cleavage in cellulose [31]. During pyrolysis, cellulose generates levoglucosan production due to heterocyclic cleavage of the glycosidic linkage [31]. However, when NaCl is present, the glycosidic bond breaking is inhibited [31]. Thus, a peak representing the glycosidic linkage appears at 1130–1150 cm^{-1} for the NaCl-containing biochar.

Although the 0, 5, and 10%-NaCl biochar samples mostly displayed similar peaks, the 20%-NaCl biochar exhibited a phase that could be clearly distinguished. These peaks appeared more prominent at 1230 and 1370–1430 cm^{-1}, positions respectively corresponding to the C-H and O-H bending frequencies in lignin [28,32,33]. The peaks at 2918 and 2850 cm^{-1} and 3000-3100 cm^{-1} became more distinct, respectively representing alkanes/aliphatic C-H stretching [34–37] and C-H stretching in aromatic compounds [38,39]. The peaks at 2918 and 2850 cm^{-1} are caused by alkyl adsorption and are strongest in the FT-IR spectra of lignin [40]. The peak at 3000–3100 cm^{-1}, which corresponds to aromatic C-H stretching, is another peak appearing in the spectra of macromolecule units such as lignin [38]. In the present study, the finding that food-waste biochar with 20%-NaCl content produced more distinct peaks for lignin than biochar containing 5 or 10%-NaCl did can be taken to indicate that high NaCl content inhibits lignin degradation during pyrolysis. This is further supported by the fact that the peak at 1700 cm^{-1} corresponding to the carbonyl C=O stretching vibration in cellulose and lignin showed a minor increase for the 5 and 10%-NaCl biochar, whereas a marked increase was detected for the 20%-NaCl biochar. The high NaCl content of the latter probably inhibited the lignin degradation.

The presence of Na during pyrolysis acts as an inhibitor to the conversion of cellulose and lignin into levoglucosan [31,41]. As mentioned above, hemolytic cleavage is induced for cellulose, so that conversion into glycoladehyde and formic acid, rather than levoglucosan, occurs [31]. For lignin, degradation producing a guaiacol group is induced [41]. Thus, for food waste with high NaCl content, a competitive pathway is induced to replace the original degradation pathway, thereby inhibiting fast degradation of lignin and cellulose, and a proportion of these materials is left behind in the biochar. This increase in the residual lignin and cellulose may be interpreted as the cause of the increase in biochar yield reported in Section 3.1 and the increase in H content that accompanied the increase in NaCl content.

The peak at approximately 1560 cm^{-1} indicates C-N stretching and N-H bending [35,42,43]. The peaks in this region are especially strong for 20%-NaCl biochar, suggesting that high NaCl content may enhance N capture during pyrolysis. The peak representing a nitrile group at 2350 cm^{-1} is also absent from the 0%-NaCl biochar [28], but gains intensity as the NaCl content increases. This provides additional support for the positive effect of NaCl content on N capture. A possible explanation may lie in the protein coagulation caused by inorganic NaCl, although further research is required to determine the precise cause [44].

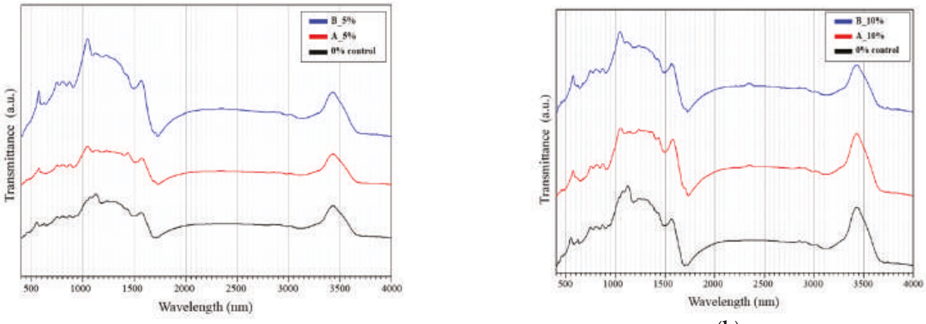

(**a**) (**b**)

Figure 4. *Cont.*

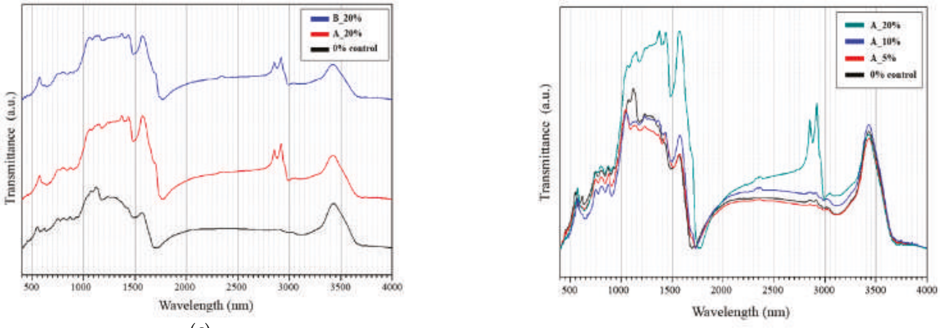

(**c**)

(**d**)

Figure 4. FT-IR results for (**a**) 5%, (**b**) 10%, and (**c**) 20%-NaCl biochar after and before washing, with the results for 0%-NaCl biochar. (**d**) FT-IR results for 0%, 5%, 10%, and 20%-NaCl biochar after washing.

3.2.4. X-ray Diffraction Analysis

The results of the XRD analysis of the NaCl powder are presented in Figure 5e. The NaCl peaks appear at 27.4, 31.5, 45.5, 56.5, 65.5, 75.5, and 84°. In Figure 5, the XRD result for the 0%-NaCl food-waste biochar indicates peaks at 18.5, 28.4, 30.1, 40.5, 50.3, 66.5, and 74°, with a broad peak in the vicinity of 25°. To analyze the influence of the NaCl content on the biochar structure, the results shown in Figure 5a–d for the biochar samples with varying NaCl concentrations before and after washing were compared with those for the control 0%-NaCl biochar shown in Figure 5e.

Table 5 summarizes the XRD peaks for each sample. The pre-wash biochar samples clearly display NaCl peaks. For the post-wash biochar samples, the NaCl peaks either disappear or lose intensity, indicating that the washing removed most of the NaCl content. The pre-wash results indicate that increased NaCl content in the samples generally shifted the NaCl peak from 31.2 to 31.4 and 31.7°, i.e., from left to right, for 5, 10, and 20%-NaCl content, respectively. This shifting of the peak to a lower angle indicates expansion of the space lattice [45,46]. In the BET surface area analysis discussed above (Section 3.2.1.), the average post-wash pore diameter was found to increase with the NaCl content. The increased pore diameter following the NaCl removal indicates that the increase in NaCl content in turn increased the NaCl crystal size. In other words, the peak shifting from left to right may have been due to the increased crystal size reducing the expansion when the imparted energy was the same, so that a larger expansion occurred in the biochar with lower NaCl content because of the small crystal size.

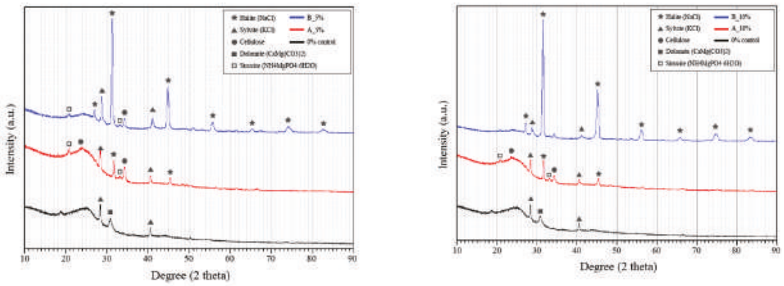

(**a**)

(**b**)

Figure 5. *Cont.*

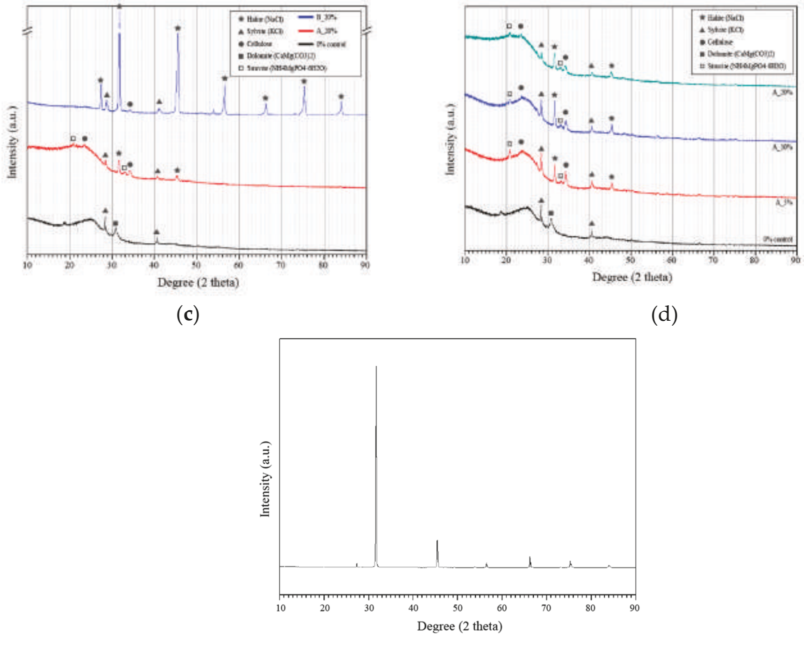

(**c**) (d)

(**e**)

Figure 5. XRD results for (**a**) 5%, (**b**), 10%, and (**c**) 20%-NaCl biochar samples after and before washing, with 0%-NaCl biochar result. (**d**) XRD results for 0%, 5%, 10%, and 20%-NaCl samples after washing. (**e**) XRD result for NaCl powder.

The peaks at 3.14, 2.22, and 1.81 Å correspond to KCl (JCPDS #41–1476) [34,47]. Regardless of NaCl concentration, the peaks for the pre-wash biochar shifted to the right and then shifted back to the left after washing, being detected at 28.4° and 40.5°, i.e., the same positions as the KCl in the control. The peaks detected in the pre-wash biochar appeared in the position between standard KCl and halite. Note that, when KCl and NaCl are present together, the melting point decreases and reformation occurs during sintering [24]. As shown in Figure 3, the crystal cube shape was deformed for the K, Na, and Cl bindings.

According to Broström et al. [24], XRD analysis of a mixture of NaCl and KCl showed the KCl peaks shifting to the right compared to the standard, i.e., to 29 and 41°. This could be explained by partial binding between the NaCl injected into the food waste during pyrolysis and the KCl already present in the food waste, which caused the KCl peak to shift to the right (to 28.8 and 41°). This was followed by the emergence of peaks at 28.4 and 40.5° due to the independent KCl content remaining after washing, which removed only the KCl bound to NaCl. As Figure 5d shows, the larger the NaCl injection volume was, the smaller the KCl peak intensity was. The peak intensities at 28.4 and 40.5° were 3872 and 1827, 3831 and 1849, 3582 and 1741, and 3248 and 1560 for the 0, 5, 10, and 20%-NaCl samples, respectively. This indicates a decrease in peak intensity with increased NaCl content. As the NaCl content was increased, a higher proportion of the KCl dispersed in the food waste could combine with the injected NaCl. Thus, the amount of residual KCl decreased as the larger amount of KCl bound to the NaCl was removed by washing.

Peaks at 3.78 and 2.61 Å were not detected in the 0%-NaCl biochar but did appear in the NaCl-containing biochar. The peaks at these positions indicate the presence of cellulose [48,49]. As mentioned in Section 3.2.3., when NaCl is added to cellulose undergoing pyrolysis, decomposition of the cellulose into levoglucosan is inhibited [31]. For NaCl-free food waste, the cellulose decomposes to produce levoglucosan during pyrolysis. However, cellulose degradation is inhibited for food waste containing NaCl. Thus, the residual cellulose produced the above peaks. In the pre-wash biochar, the peaks appeared indefinite around 3.78 Å. This can be explained by the strong intensity of the NaCl crystal peak comparatively weakening the cellulose peaks. Therefore, although it was difficult to detect both peaks together in the 20%-NaCl biochar, which had the strongest NaCl peaks, they became discernible after washing, which reduced the NaCl peak intensity.

Table 5. X-ray diffraction analysis peaks for NaCl and food-waste-derived biochar with different NaCl contents.

NaCl	0%	B_5%	A_5%	B_10%	A_10%	B_20%	A_20%
	18.7 (4.74)						
		20.8 (4.27)	20.8 (4.27)	20.8 (4.27)	20.8 (4.27)		20.8 (4.27)
			23.5 (3.78)		23.5 (3.78)		23.5 (3.78)
27.4 (3.25)		27 (3.30)	27.2 (3.26)	27.2 (3.27)	27.2 (3.27)	27.4 (3.25)	27.2 (3.27)
	28.4 (3.14)	28.8 (3.10)	28.4 (3.14)	28.8 (3.10)	28.4 (3.14)	28.8 (3.10)	28.4 (3.14)
	30.8 (2.90)						
31.5 (2.84)		31.2 (2.86)	31.6 (2.83)	31.4 (2.85)	31.6 (2.83)	31.7 (2.82)	31.6 (2.83)
		33 (2.71)	33 (2.71)		33 (2.71)		33 (2.71)
		34.3 (2.61)	34.3 (2.61)	34.3 (2.61)	34.3 (2.61)	34.3 (2.61)	34.3 (2.61)
	40.5 (2.22)	41 (2.20)	40.5 (2.22)	41 (2.20)	40.5 (2.22)	41 (2.20)	40.5 (2.22)
45.5 (1.99)		45 (2.01)	45.5 (1.99)	45 (2.01)	45.5 (1.99)	45.5 (1.99)	45.2 (2.00)
	50.3 (1.81)	51 (1.79)	50.3 (1.81)		50.3 (1.81)		50.3 (1.81)
				53.5 (1.71)		53.8 (1.70)	
56.5 (1.63)		55.5 (1.65)	56.5 (1.63)	56 (1.64)	56.4 (1.63)	56.5 (1.63)	56.2 (1.63)
		61.5 (1.51)	61.5 (1.51)				
65.5 (1.42)		65.2 (1.43)		65.7 (1.42)		66.2 (1.41)	
	66.5 (1.40)	67.5 (1.39)	66.5 (1.40)		66.5 (1.40)		
75.5 (1.26)		74 (1.28)		74.7 (1.27)		75.2 (1.26)	
84 (1.15)		82.5 (1.17)		83.5 (1.16)		84 (1.15)	

Finally, the 0%-NaCl biochar had a peak at 30.8°, which indicates the presence of dolomite ($CaMg(CO_3)_2$) [34]. On the other hand, biochar samples with added NaCl had peaks at 20.8° and 33°, which indicates the presence of struvite ($NH_4MgPO_4 \cdot 6H_2O$) [50], and there is no peak at 30.8°. As mentioned in Section 3.2.3, when NaCl is present during pyrolysis, phosphorus compound decomposes to the form of PO_4^{3-} not the form of HPO_4^{2-}. These XRD results support those of the FT-IR. A magnesium (Mg) component contained in the food waste became dolomite during pyrolysis. When NaCl is present during pyrolysis, Mg combined with PO_4^{3-} and crystallized.

4. Conclusions

Food waste is difficult to recycle due to the innate NaCl content. It is essential to remove NaCl in order to utilize food waste biochar. The use of NaCl in food waste and desalination process as a template and activation process, respectively, could be a way to improve the value of the biochar. Therefore, this study investigated changes in biochar structure according to varying NaCl solution concentrations added to food waste and desalination. As the NaCl concentration increased from 0% to 20%, cellulose and lignin decomposition inhibited during pyrolysis, ultimately increasing the biochar yield by 2.7% for 20%-NaCl concentration. Furthermore, the added NaCl formed crystals exerting a templating effect, inducing an increase in BET surface area and pore volume in the biochar when it was washed. In comparison to the NaOH-based activation method, the NaCl templating method yielded a minor difference BET surface area, while the pore depth was found to be shallower. Adding 20% NaCl reduced the BET surface area while the mean pore diameter increased, owing to the increased NaCl clusters. The phenomenon in which the NaCl clustering increases as a NaCl concentration increases was shown to have positive effects on NaCl removal through washing. Further, as the NaCl adhered to the KCl scattered among the food waste, the high concentration of NaCl also had positive effects on the KCl removal. Finally, a NaCl induced form of struvite and yielded a valuable biochar that can be used as a soil fertilizer.

Author Contributions: Conceptualization, Y.-E.L. and Y.-S.Y.; Validation, Y.-E.L., J.-H.J., Y.-S.Y.; Formal Analysis, Y.-E.L.; Investigation, Y.-E.L.; Resources, Y.-E.L. and J.-H.J.; Writing-Original Draft Preparation, Y.-E.L.; Writing-Review & Editing, Y.-E.L., J.-H.J., Y.-E.L., and I.-T.K.; Supervision, Y.-S.Y.; Project Administration, I.-T.K.

Acknowledgments: This work was supported by the Major Project of the Korea Institute of Civil Engineering and Building Technology (KICT) [grant number 2018-0063].

Conflicts of Interest: The authors declare no conflict of interest.

References

1. Glaser, B.; Parr, M.; Braun, C.; Kopolo, G. Biochar is carbon negative. *Nat. Geosci.* **2009**, 2. [CrossRef]
2. Mathews, J.A. Carbon-negative biofuels. *Energy Policy* **2008**, *36*, 940–945. [CrossRef]
3. Guizani, C.; Jeguirim, M.; Valin, S.; Limousy, L.; Salvador, S. Biomass chars: The effects of pyrolysis conditions on their morphology, structure, chemical properties and reactivity. *Energies* **2017**, *10*. [CrossRef]
4. Brassard, P.; Godbout, S.; Raghavan, V.; Palacios, J.H.; Grenier, M.; Zegan, D. The production of engineered biochars in a vertical auger pyrolysis reactor for carbon sequestration. *Energies* **2017**, *10*. [CrossRef]
5. Ghorbel, L.; Rouissi, T.; Brar, S.K.; López-González, D.; Amarillo Ramirez, A.; Godbout, S. Value-added performance of processed cardboard and farm breeding compost by pyrolysis. *Waste Manag.* **2015**, *38*, 164–173. [CrossRef] [PubMed]
6. Ryu, C.; Sharifi, V.N.; Swithenbank, J. Waste pyrolysis and generation of storable char. *Int. J. Energy Res.* **2007**, *31*, 177–191. [CrossRef]
7. Basu, P. *Biomass Gasification, Pyrolysis and Torrefaction: Practical Design and Theory*, 2nd ed.; Academic Press: Cambridge, MA, USA, 2013.
8. Sohi, S.; Lopez-Capel, E.; Krull, E.; Bol, R. Biochar, climate change and soil: A review to guide future research. *CSIRO Land Water Sci. Rep.* **2009**, *5*, 17–31.
9. Van Zwieten, L.; Kimber, S.; Morris, S.; Chan, K.Y.; Downie, A.; Rust, J.; Joseph, S.; Cowie, A. Effects of biochar from slow pyrolysis of papermill waste on agronomic performance and soil fertility. *Plant Soil* **2010**, *327*, 235–246. [CrossRef]

10. Kloss, S.; Zehetner, F.; Dellantonio, A.; Hamid, R.; Ottner, F.; Liedtke, V.; Schwanninger, M.; Gerzabek, M.H.; Soja, G. Characterization of slow pyrolysis biochars:Effects of feedstocks and pyrolysis temperature on biochar properties. *J. Environ. Qual.* **2012**, *41*, 990–1000. [CrossRef] [PubMed]
11. Ronsse, F.; Van Hecke, S.; Dickinson, D.; Prins, W. Production and characterization of slow pyrolysis biochar:Influence of feedstock type and pyrolysis conditions. *Gcb Bioenergy* **2013**, *5*, 104–115. [CrossRef]
12. Lin, C.S.K.; Pfaltzgraff, L.A.; Herrero-Davila, L.; Mubofu, E.B.; Solhy, A.; Clark, J.H.; Koutinas, A.A.; Kopsahelis, N.; Stamatelatou, K.; Dickson, F.; et al. Food waste as a valuable resource for the production of chemicals, materials and fuels. Current situation and global perspective. *Energy Environ. Sci.* **2013**, *6*, 426–464. [CrossRef]
13. Pham, T.P.T.; Kaushik, R.; Parshetti, G.K.; Mahmood, R.; Balasubramanian, R. Food waste-to-energy conversion technologies:Current status and future directions. *Waste Manag.* **2015**, *38*, 399–408. [CrossRef] [PubMed]
14. Lee, Y.-E.; Jo, J.-H.; Kim, I.-T.; Yoo, Y.-S. Chemical Characteristics and NaCl Component Behavior of Biochar Derived from the Salty Food Waste by Water Flushing. *Energies* **2017**, 10. [CrossRef]
15. Kim, N.C.; Jang, B.M. Sodium chloride decomposting method in food waste compost using triple salt. *J. Korra* **2004**, *12*, 86–94.
16. Fechler, N.; Fellinger, T.-P.; Antonietti, M. "Salt templating": A simple and sustainable pathway toward highly porous functional carbons from ionic liquids. *Adv. Mater.* **2013**, *25*, 75–79. [CrossRef] [PubMed]
17. Liu, X.; Antonietti, M. Molten salt activation for synthesis of porous carbon nanostructures and carbon sheets. *Carbon* **2014**, *69*, 460–466. [CrossRef]
18. Ministry of Environment (MOE). *A Study on Food Waste Reduction Equipment Guidelines and Quality Standard*; Ministry of Environment: Sejong City, Korea, 2009.
19. Lu, A.-H.; Li, W.C.; Schmidt, W.; Schüth, F. Fabrication of hierarchically structured carbon monoliths via self-binding and salt templating. *Microporous Mesoporous Mater.* **2006**, *95*, 187–192. [CrossRef]
20. Wu, F.-C.; Tseng, R.-L. High adsorption capacity NaOH-activated carbon for dye removal from aqueous solution. *J. Hazard. Mater.* **2008**, *152*, 1256–1267. [CrossRef] [PubMed]
21. Cazetta, A.L.; Vargas, A.M.A.; Nogami, E.M.; Kunita, M.H.; Martins, A.C.; Silva, T.L.; Moraes, J.C.G.; Almeida, V.C.; Guilherme, M.R. NaOH-activated carbon of high surface area produced from coconut shell: Kinetics and equilibrium studies from the methylene blue adsorption. *Chem. Eng. J.* **2011**, *174*, 117–125. [CrossRef]
22. Vargas, A.M.M.; Garcia, C.A.; Reis, E.M.; Lenzi, E.; Costa, W.F.; Almeida, V.C. NaOH-activated carbon from flamboyant (Delonix regia) pods:Optimization of preparation conditions using central composite rotatable design. *Chem. Eng. J.* **2010**, *162*, 43–50. [CrossRef]
23. Dai, Z.; Meng, J.; Muhammad, N.; Muhammad, L.; Wang, H.; He, Y.; Brookes, P.C.; Xu, J. The potential feasibility for soil improvement, based on the properties of biochars pyrolyzed from different feedstocks. *J. Soils Sedim.* **2013**, *13*, 989–1000. [CrossRef]
24. Broström, M.; Enestam, S.; Backman, R.; Mäkelä, K. Condensation in the KCl–NaCl system. *Fuel Process. Technol.* **2013**, *105*, 142–148. [CrossRef]
25. Vandecandelaere, N.; Rey, C.; Drouet, C. Biomimetic apatite-based biomaterials:On the critical impact of synthesis and post-synthesis parameters. *J. Mater. Sci. Mater. Med.* **2012**, *23*, 2593–2606. [CrossRef] [PubMed]
26. Bekiaris, G.; Bruun, S.; Peltre, C.; Houot, S.; Jensen, L.S. FTIR–PAS: A powerful tool for characterising the chemical composition and predicting the labile C fraction of various organic waste products. *Waste Manag.* **2015**, *39*, 45–56. [CrossRef] [PubMed]
27. Porchelvi, E.; Muthu, S. The spectroscopic (FT-IR, FT-Raman and NMR), NCA, Fukui function analysis first order hyperpolarizability, TGA of 6-chloro-3, 4dihydro-2H-1, 2, 4-benzothiazine-7-sulphonamide1, 1-dioxide by ab initio HF and Density Functional method. *Spectrochim. Acta Part A Mol. Biomol. Spectrosc.* **2014**, *123*, 230–240. [CrossRef] [PubMed]
28. Mohanty, P.; Nanda, S.; Pant, K.K.; Naik, S.; Kozinski, J.A.; Dalai, A.K. Evaluation of the physiochemical development of biochars obtained from pyrolysis of wheat straw, timothy grass and pinewood: Effects of heating rate. *J. Anal. Appl. Pyrolysis* **2013**, *104*, 485–493. [CrossRef]
29. Zhao, S.-X.; Ta, N.; Wang, X.-D. Effect of Temperature on the Structural and Physicochemical Properties of Biochar with Apple Tree Branches as Feedstock Material. *Energies* **2017**, *10*. [CrossRef]

30. Ahmad, M.; Lee, S.S.; Dou, X.; Mohan, D.; Sung, J.K.; Yang, J.E.; Ok, Y.S. Effects of pyrolysis temperature on soybean stover- and peanut shell-derived biochar properties and TCE adsorption in water. *Bioresour. Technol.* **2012**, *118*, 536–544. [CrossRef] [PubMed]
31. Patwardhan, P.R.; Satrio, J.A.; Brown, R.C.; Shanks, R.H. Influence of inorganic salts on the primary pyrolysis products of cellulose. *Bioresour. Technol.* **2010**, *101*, 4646–4655. [CrossRef] [PubMed]
32. Nanda, S.; Mohanty, P.; Pant, K.K.; Naik, S.; Kozinski, J.A.; Dalai, A.K. Characterization of North American lignocellulosic biomass and biochars in terms of their candidacy for alternate renewable fuels. *Bioenergy Res.* **2013**, *6*, 663–677. [CrossRef]
33. Silverstein, R.M.; Webster, F.X.; Kiemle, D.J.; Bryce, D.L. *Spectrometric Identification of Organic Compounds*, 8th ed.; John Wiley & Sons: Hoboken, NJ, USA, 2014.
34. Yuan, J.-H.; Xu, R.-K.; Zhang, H. The forms of alkalis in the biochar produced from crop residues at different temperatures. *Bioresour. Technol.* **2011**, *102*, 3488–3497. [CrossRef] [PubMed]
35. Cantrell, K.B.; Hunt, P.G.; Uchimiya, M.; Novak, J.M.; Ro, K.S. Impact of pyrolysis temperature and manure source on physicochemical characteristics of biochar. *Bioresour. Technol.* **2012**, *107*, 419–428. [CrossRef] [PubMed]
36. Jin, J.; Li, Y.; Zhang, J.; Wu, S.W.; Cao, Y.; Liang, P.; Zhang, J.; Wong, M.H.; Wang, M.; Shan, S.; et al. Influence of pyrolysis temperature on properties and environmental safety of heavy metals in biochars derived from municipal sewage sludge. *J. Hazard. Mater.* **2016**, *320*, 417–426. [CrossRef] [PubMed]
37. Hossain, M.K.; Strezov, V.; Chan, V.S.; Ziolkowski, A.; Nelson, P.F. Influence of pyrolysis temperature on production and nutrient properties of wastewater sludge biochar. *J. Environ. Manag.* **2011**, *92*, 223–228. [CrossRef] [PubMed]
38. Lammers, K.; Arbuckle-keil, G.; Dighton, J. FT-IR study of the changes in carbohydrate chemistry of three New Jersey pine barrens leaf litters during simulated control burning. *Soil Biol. Biochem.* **2009**, *41*, 340–347. [CrossRef]
39. Socrates, G. *Infrared and Raman Characteristic Group Frequencies: Tables and Charts*, 3rd ed.; John Wiley & Sons: Hoboken, NJ, USA, 2004.
40. Zhang, M.; Resende, F.L.P.; Moutsoglou, A.; Raynie, D.E. Pyrolysis of lignin extracted from prairie cordgrass, aspen, and Kraft lignin by Py-GC/MS and TGA/FTIR. *J. Anal. Appl. Pyrolysis* **2012**, *98*, 65–71. [CrossRef]
41. Kleen, M.; Gellerstedt, G. Influence of inorganic species on the formation of polysaccharide and lignin degradation products in the analytical pyrolysis of pulps. *J. Anal. Appl. Pyrolysis* **1995**, *35*, 15–41. [CrossRef]
42. Jiang, W.; Saxena, A.; Song, B.; Ward, B.B.; Beveridge, T.J.; Myneni, S.C. Elucidation of functional groups on gram-positive and gram-negative bacterial surfaces using infrared spectroscopy. *Langmuir* **2004**, *20*, 11433–11442. [CrossRef] [PubMed]
43. Zhang, B.; Xiong, S.; Xiao, B.; Yu, D.; Jia, X. Mechanism of wet sewage sludge pyrolysis in a tubular furnace. *Int. J. Hydrog. Energy* **2011**, *36*, 355–363. [CrossRef]
44. Robertson, T.B. Contributions to the theory of the mode of action of inorganic salts upon proteins in solution. *J. Biol. Chem.* **1911**, *9*, 303–326.
45. Sawabe, T.; Akiyoshi, M.; Yoshida, K.; Yano, T. Estimation of neutron-irradiation-induced defect in 3C–SiC from change in XRD peak shift and DFT study. *J. Nucl. Mater.* **2011**, *417*, 430–434. [CrossRef]
46. Parra, M.R.; Haque, F.Z. Aqueous chemical route synthesis and the effect of calcination temperature on the structural and optical properties of ZnO nanoparticles. *J. Mater. Res. Technol.* **2014**, *3*, 363–369. [CrossRef]
47. Ewais, E.M.M.; Ahmed, Y.M.Z.; El-Amir, A.A.M.; El-didamony, H. Cement kiln dust/rice husk ash as a low temperature route for wollastonite processing. *Epitoany-J. Silicate Based Composite Mater.* **2014**. [CrossRef]
48. Ciolacu, D.; Ciolacu, F.; Popa, V.I. Amorphous cellulose—Structure and characterization. *Cell. Chem. Technol.* **2011**, *45*, 13.
49. Wei, L.; Agarwal, U.P.; Hirth, K.C.; Matuana, L.M.; Sabo, R.C.; Stark, N.M. Chemical modification of nanocellulose with canola oil fatty acid methyl ester. *Carbohydr. Polym.* **2017**, *169*, 108–116. [CrossRef] [PubMed]
50. Lu, X.; Shih, K.; Li, X.Y.; Liu, G.; Zeng, E.Y.; Wang, F. Accuracy and application of quantitative X-ray diffraction on the precipitation of struvite product. *Water Res.* **2016**, *90*, 9–14. [CrossRef] [PubMed]

energies

MDPI

Article

Combustion of Flax Shives, Beech Wood, Pure Woody Pseudo-Components and Their Chars: A Thermal and Kinetic Study

Nourelhouda Boukaous [1,2], Lokmane Abdelouahed [1,*], Mustapha Chikhi [2], Abdeslam-Hassen Meniai [2], Chetna Mohabeer [1] and Taouk Bechara [1]

[1] Laboratoire de Sécurité des Procédés Chimiques LSPC-4704, INSA Rouen, UNIROUEN, Normandie Univ., 76000 Rouen, France; boukaous.nourelhouda@insa-rouen.fr (N.B.); chikirsha.mohabeer@insa-rouen.fr (C.M.); bechara.taouk@insa-rouen.fr (T.B.)

[2] Faculté de Génie des Procédés Université de Constantine 3, 25000 Constantine, Algeria; chikhi_mustapha@yahoo.fr (M.C.); meniai@yahoo.fr (A.-H.M.)

* Correspondence: lokmane.abdelouahed@insa-rouen.fr; Tel.: +33-232-956-655

Received: 30 June 2018; Accepted: 15 August 2018; Published: 17 August 2018

Abstract: Thermogravimetric analysis was employed to investigate the combustion characteristics of flax shives, beech wood, hemicellulose, cellulose, lignin, and their chars. The chars were prepared from raw materials in a fixed-bed reactor at 850 °C. In this study, the thermal behavior based on characteristic temperatures (ignition, maximum, and final temperatures), burnout time and maximum rate was investigated. The kinetic parameters for the combustion of different materials were determined based on the Coats-Redfern approach. The results of our study revealed that the combustion of pure pseudo-components behaved differently from that of biomass. Indeed, principal component analysis showed that the thermal behavior of both biomasses was generally similar to that of pure hemicellulose. However, pure cellulose and lignin showed different behaviors compared to flax shives, beech wood, and hemicellulose. Hemicellulose and cellulose chars had almost the same behaviors, while being different from biomass and lignin chars. Despite the difference between flax shives and beech wood, they showed almost the same thermal characteristics and apparent activation energies. Also, the combustion of the hemicellulose and cellulose chars showed that they have almost the same structure. Their overall thermal and kinetic behavior remained between that of biomass and lignin.

Keywords: biomass; combustion; thermogravimetric analysis; kinetic parameters; thermal characteristics

---

1. Introduction

Biomass is one of the most environment-friendly renewable sources of energy being used for human needs. Usually, its conversion is considered to be a carbon-free process, because the resulting CO_2 was previously captured by plants. Based on life-cycle assessment comparisons, net carbon emissions from biomass per unit of electricity are below 10% of those from the emissions from fossil fuels [1]. Furthermore, the use of biomass and char as alternative energy carriers in the industry is growing as a result of the depletion of fossil energy. Biomass can be converted into heat and electrical power through several methods, where the easiest one is the direct combustion via a steam turbine dedicated to power production. At present, biomass is already used in several processes for heat and power production [2]. Different criteria have been used in the literature to compare the performance of biomass combustion power generation. Among these criteria, the more important are: The capacity of power production [3], the technology used [4], and the composition of biomass [2].

Also, other classifications can be addressed when comparing pollution generated by the combustion of biomass. Indeed, this last one is becoming more important due to global warming [5].

The contribution of biomass sources in global electricity generation from renewable energy in 2014 was about 7.24% [1]. This contribution can be made directly by the combustion of biomass or one of its derivatives. There are three main pseudo-components that constitute biomass, namely hemicellulose, cellulose, and lignin. Hemicellulose constitutes 16 to 23 wt%, cellulose between 42 and 49 wt%, while lignin represents 21 to 39 wt% of the biomass [6]. These last three can be thermochemically valorized in several ways. Indeed, the pyrolysis of pseudo-components has already been studied in the literature [7], and the interaction between these three polymers during pyrolysis has also been investigated [8]. Moreover, the gasification of these pseudo-components has been examined at different temperatures [9] and using supercritical water conditions [10]. The effect of cellulose and lignin content on the combustion has also been highlighted in the literature [11].

Lignin, which is generally considered as a chemically non-recoverable residue, is usually burned to generate the power and heat required for biomass treatment operations in simultaneous saccharification and co-fermentation processes [12]. According to life-cycle assessments conducted by Daylan and Ciliz [13], the heat generated by the combustion of the residual lignin satisfied and ensured the necessary heat and power needed during the process of ethanol production from lignocellulosic biomass. On the other hand, in the gasification process of biomass, it is the char produced by the process which is burned to provide the heat needed by the pyrolysis and the gasification processes [14]. In the fast internally circulating fluidized bed used for biomass gasification, the residual char from the pyrolysis and gasification processes is burnt in a separate reactor to ensure a major part of the heat required for the pyrolysis and the gasification reactions [15].

Now, the design and the scale-up of combustors require several details concerning the reactivity of the solid fuel to be used [16]. Guizani et al. [17] showed that the pyrolysis temperature of biomass, during the production of char, affected the structure and the reactivity of produced char in a considerable manner. Also, the behavior of biomass cannot be condensed to that of one single pseudo-component because of the chemical and physical alterations caused by the use of acids and bases during the separation of the different pseudo-components [18]. Indeed, the knowledge of the reaction kinetics of the solid fuel is essential to correctly design the reactor for the combustion reaction. Also, the more the solid fuel is burnt at a low temperature and a high conversion rate, the shorter the burnout time is; in other words, the reactivity of the substance is higher [19]. Hence, the most reactive substance is the one which shows the highest rate of consumption at the lowest temperature on one hand, and the lowest activation energy on the other. In literature, several authors evaluated the reactivity of substances from thermogravimetric (TG) curves based on; (i) the ignition temperature [20]; (ii) the maximum rate of mass loss [21]; (iii) the activation energy [22]; or (iv) a combination of different parameters from the TG curves [19]. Indeed, El may et al. [19] estimated the reactivity of different substances as the ratio of the maximum rate of mass loss to maximum temperature. In their case, they did not distinguish between the different stages of the reaction. Haykırı-Açma et al. [23] reported that the most important characteristic temperatures of the combustion reaction were the ignition temperature and the maximum temperature, which corresponded to the maximum consumption rate. Other researchers have compared the TG combustion profiles of different chars obtained from biomass pyrolysis and coal [22] and found that biomass chars, based essentially on the maximum temperature, were more reactive than coal and lignite. According to the latter paper, it seemed that the activation energy had less influence on the reactivity compared to the maximum temperature. In this context, a deeper analysis appears to be necessary to better understand the relationship between the different parameters cited above.

Solid fuel combustion has widely been studied in the literature. However, to the best of our knowledge, the combustion characteristics of cellulose, hemicellulose, lignin, and their chars have not been deeply examined. In addition, the synergistic effect of the pseudo-components during the combustion reaction has not been previously discussed. Consequently, the effect of the heating rates and the sample structure may affect not only the rate of combustion, but also important characteristics such as ignition and final temperatures.

The aim of this work is to determine various parameters associated with the combustion reaction (kinetic parameters, burnout time, ignition temperature, final temperature, and maximum rate of consumption) using thermogravimetric analysis (TGA). The raw materials considered in this study are beech wood, flax shives, cellulose, hemicellulose, lignin, and their respective chars. Also, in this paper, the relationship between the different determined parameters of the combustion reaction of biomasses and the pure pseudo-components has been discussed in order to better compare the reactivity of the substances with each other. The availability of such data for kinetic and thermal parameters allows an appropriate design of biomass and char combustor.

2. Materials and Methods

2.1. Raw Materials

"ETS Lignex" and "La Coopérative Terre de Lin" companies provided respectively the beech wood and the flax shives used for this study. Beechwood has been chosen in order to compare our results with the literature, while flax shives have been chosen due to their availability in Europe which represents about 85% of the world's production of scutched flax fibers [24]. The pseudo-components employed were used in their pure form: Microcrystalline cellulose was provided from Merck (Kenilworth, NJ, USA, Ref. 1.02330.0500-500G), hemicellulose was provided from Tokyo Chemical Company Co. Ltd. (Tokyo, Japan, Ref: X0078-100G) and lignin was provided from Sigma-Aldrich (St. Louis, MO, USA, Ref: 471003-100G). All samples were sieved with a diameter of less than 40 micrometers (µm) in order to limit the effects of heat and mass transfer as recommended in [25].

2.2. Char

A fixed-bed reactor was used to prepare the char of the five raw materials by pyrolysis. The pyrolysis was ensured at 850 °C during 2 h under a pure nitrogen flow of 500 $\text{mL}\cdot\text{min}^{-1}$. Afterward, the samples were cooled down under nitrogen to room temperature. The device was already described in a previous work [26]. Experiments were carried out at atmospheric pressure. The proximate and ultimate analyses of the raw material before and after pyrolysis are given in Tables 1 and 2, respectively. The ultimate composition of different raw materials was performed using the CHN elemental analyzer, while the proximate composition was determined based on TG analysis [27]. Low heating value (LHV) of different raw materials were calculated according to Channiwala's correlation [28].

Table 1. Ultimate and proximate characterization of raw materials.

Component	C (%)	H (%)	O (%)	N (%)	VM * (%)	FC ** (%)	Ash (%)	LHV ($\text{MJ}\cdot\text{kg}^{-1}$)
Flax shives	45.7	5.77	48.12	0.41	75.47	21.77	2.76	17.71
Beech wood	47.38	6.11	46.51	0	80.15	18.92	0.92	18.91
Cellulose	41.74	6.08	52.18	0	96.26	3.74	0	16.34
Hemicellulose	41.47	6.48	52.05	0	80.18	19.57	0.25	16.72
Lignin	57.04	4.76	38.21	0	68.42	24.86	6.72	21.42

* Volatile matter, ** Fixed carbon.

Table 2. Ultimate and proximate characterization of char samples.

Component	C (%)	H (%)	O (%)	N (%)	VM * (%)	FC ** (%)	Ash (%)	LHV ($\text{MJ}\cdot\text{kg}^{-1}$)
Flax shives char	75.87	3.2	19.73	1.21	1.67	81.61	16.72	27.84
Beech wood char	78.24	3.13	18.63	0	1.59	93.83	4.58	28.97
Cellulose char	81.4	3.25	15.35	0	0.39	99.25	0.37	30.64
Hemicellulose char	71.19	3.2	25.61	0	0.74	98.83	0.43	25.96
Lignin char	58.04	2.65	39.3	0	2.75	71.67	25.58	18.78

* Volatile matter, ** Fixed carbon.

2.3. Thermogravimetric Experiments

TGA is one of the most frequently used techniques for solid characterization in an inert or oxidative atmosphere [29,30]. In this work, experiments were performed using a TG SDT Q600-TA instruments analyzer (TA Instruments, New Castle, DE, USA). Pure synthesized air constituting of 21 vol% of oxygen and 79 vol% of nitrogen was used as oxidative gas with a flow rate of 50 mL·min^{-1}. The mass of the sample used in the crucible was 6.5 ± 0.2 mg for all samples. The sample was introduced at room temperature and atmospheric pressure. In this work, experiments were performed under non-isothermal conditions at different heating rates: 10, 20, 30 and 40 °C·min^{-1}. TG experiments were repeated three times for each heating rate to improve the accuracy of the results.

2.4. Kinetic Modelling

Several non-isothermal methods have been reported in the literature to determine the apparent kinetics of the biomass and char combustion reactions from the TG mass loss profiles. The kinetic parameters determined by thermogravimetric measurements are very sensitive to the calculation methods used [19,31]. Therefore, their determination in this study was carried out using the Coats-Redfern method by taking into consideration two different models proposed in the literature [32,33]. Indeed, the Coats-Redfern method is considered the best approach for the determination of kinetic parameters for a combustion reaction [21,34–36]. On the other hand and in contrast to other isoconversional methods, the Coats-Redfern method may integrate some particular models that take into account the effect of boundary and diffusion control [21,37].

The conversion rate, X, was calculated based on the variation of the mass loss of the sample, as follows:

$$X = 1 - \frac{m_t - m_f}{m_i - m_f} \tag{1}$$

where m_i and m_f are the initial and the final masses, respectively.

The reaction rate can be expressed by the following relation:

$$\frac{dX}{dt} = k(T)f(X) \tag{2}$$

where $k(T)$ is the rate constant and is defined as:

$$k(T) = A \cdot \exp\left(-\frac{E_a}{RT}\right) \tag{3}$$

where A is the pre-exponential factor, E_a the apparent activation energy, R the ideal gas constant and $f(X)$ is the kinetic model used for solids conversion.

The final form of the decomposition kinetics of biomass was written as follows:

$$\frac{dX}{dt} = A \cdot \exp\left(-\frac{E_a}{RT}\right)f(X) \tag{4}$$

The rearrangement of the relation (4) gave rise to the Equation (5), as follows:

$$\frac{dX}{f(X)} = \frac{k}{\beta}dT \tag{5}$$

where β is the heating rate and is defined as:

$$\beta = \frac{dT}{dt} \tag{6}$$

The integration of the relation (5) gave the following relation:

$$g(X) = \int_0^X \frac{dX}{f(X)} = \frac{A}{\beta} \int_{T_0}^T \exp\left(-\frac{E_a}{RT}\right) dT \tag{7}$$

where g is the integral function of conversion [21,37]. By using the Coats-Redfern method [38], the relation (7) became:

$$ln\left|\frac{g(X)}{T^2}\right| = ln\left[\frac{AR}{\beta E_a}\left(1 - \frac{2RT}{E_a}\right)\right] - \frac{E_a}{RT} \tag{8}$$

The analytic integration of this relation is essentially governed by the form of the function "g" and the order of the reaction considered, as already detailed in articles of interest in the literature [21,39].

3. Results and Discussion

3.1. Thermogravimetric and Differential Thermogravimetic (DTG) Characteristic Curves

The combustion of cellulose, hemicellulose, lignin, beech wood, flax shives, and their chars was studied under the same experimental conditions and for different heating rates. Figures 1 and 2 show the evolution of TG and DTG curves for the combustion reaction with temperature. This study was carried out over temperatures ranging from 25 °C to 1000 °C. The mean deviation was calculated based on the reproducibility of the experiments and was found to be between 2.68 and 5.53%. The deviation was more pronounced at high temperatures, probably due to the very low mass in the crucible. Humidity evaporation was observed between ambient temperature and 150 °C, as already mentioned in previous works [19,31].

3.1.1. Raw Materials Combustion

Figure 1 shows the TG and DTG curves of the combustion of flax shives, beech wood, hemicellulose, cellulose, and lignin. As illustrated in this figure, the raw materials were completely consumed at 550 °C, except for lignin, which required a temperature in the vicinity of 850 °C. Based on the curves of Figure 1, it can be seen that the raw materials exhibited more than one stage, unlike char, which showed a unique stage in Figure 2. Despite the difference in the composition of beech wood and flax shives, see Table 1 for details, the two biomasses typically had the same behavior, with only a slightly higher reactivity for beech wood. Indeed, the biomass DTG showed the existence of two peaks—the first peak appeared in the interval from 225 to 375 °C, and the second peak from 375 to 450 °C. This indicated the existence of at least two steps, depending on the combustion mechanism.

The combustion of hemicellulose showed the presence of three peaks, two of them were completely overlapping as seen in Figure 1c. This could be explained by the heterogeneity of hemicellulose, which is majorly constituted of xylose along with a small part of glucuronic acid and other sugars.

As seen in Figure 1d, the combustion of pure cellulose showed only one peak. Indeed, this can be explained by the occurrence of only the combustion of the volatile fraction of cellulose; note the low fixed carbon content (about 3.74%) of cellulose may be the reason the peak of combustion for the latter was not detected.

The lignin combustion showed a different behavior compared to those previously, as shown in Figure 1e. Indeed, the combustion of lignin showed the existence of two independent stages. The first stage was located at low temperature, between 200 and 450 °C, while the second was located at high temperature, between 800 and 900 °C. Also, the second stage of the combustion reaction might be accompanied by the decomposition of calcium carbonates, which happens at high temperature [22,40]. Zhou et al. [41] observed the same behavior for the pyrolysis of lignin. Surprisingly, we did not see this behavior with both biomasses, although some experiments have been carried out up to 1200 °C. Indeed, after 500 °C, the mass loss of the sample was almost negligible. This could probably be explained by the fact that the combustion of char (the second stage in Figure 1e) from pure lignin was different from the behavior of char from biomass. Pure lignin has a complex and branched structure compared to cellulose and hemicellulose. Also, significant interactions have been reported in the literature between cellulose and lignin during their pyrolysis [8,9], which can modify the global structure of char.

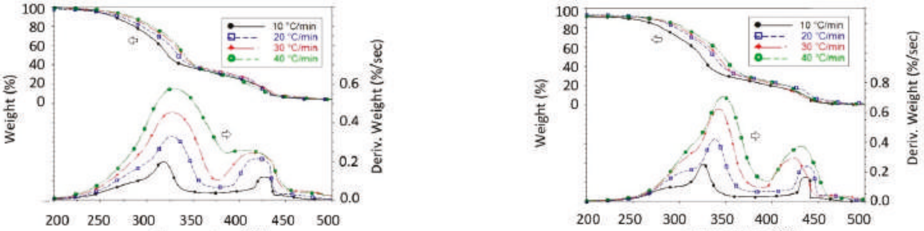

a) Flax shives b) Beechwood

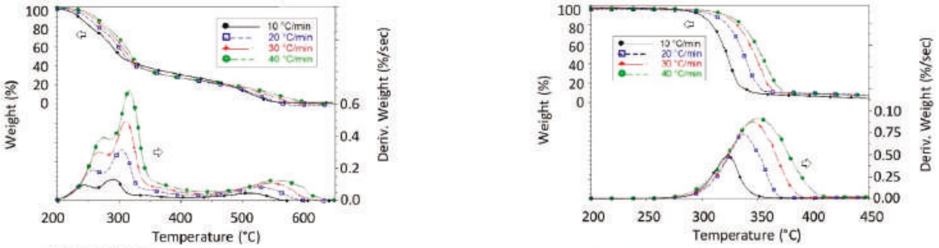

c) Hemicellulose d) Cellulose

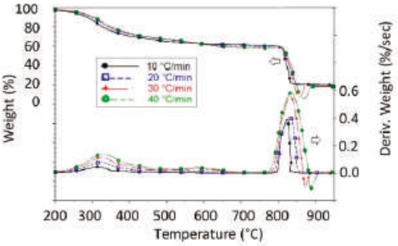

e) Lignin

Figure 1. Mass loss and conversion rate of different raw materials combustion.

3.1.2. Char Combustion

DTG curves of the different bio-char samples demonstrated only one single stage, as shown in Figure 2. This was explained by the existence of only one uniform structure in each char used. However, every char (from cellulose, hemicellulose, lignin, and biomasses) showed different behaviors when compared to one another, as shown in Figure 2. Indeed, the chars produced from pure pseudo-components did not have the same properties as the ones produced from biomass. This has already been observed in the literature, where some DTG curves of biomass samples showed one or two stages [22]. Probably, this can be explained by the importance of lignin in the biomass samples.

In some works in the literature, two DTG peaks can be observed during the combustion of char from biomass, more particularly in cases where the pyrolysis temperature of the biomass is less than 600 °C. This can be explained by the combustion of residual unconverted biomass [17].

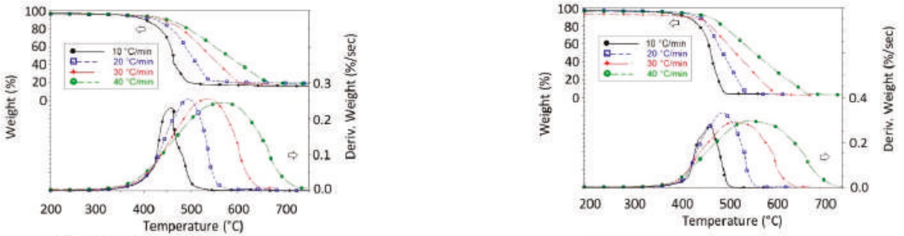

a) Flax shives char

b) Beechwood char

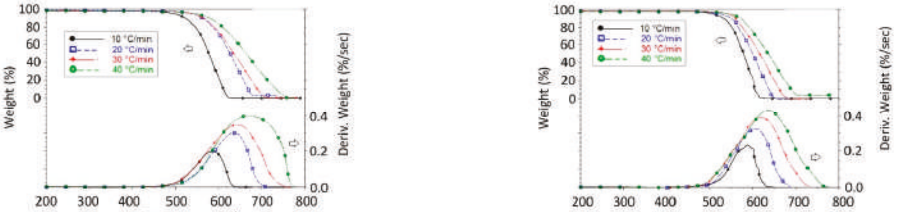

c) Hemicellulose char

d) Cellulose char

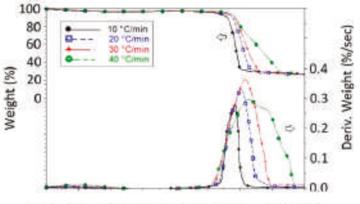

e) Lignin char

Figure 2. Mass loss and conversion rate of different char samples.

3.2. Thermal Analysis

The DTG curves allowed the determination of various parameters related to the combustion reaction, as shown in Figure 3. These parameters were determined and are discussed in the following sections. The evolution of these parameters with the heating rate obtained from the DTG curves has been summarized in Tables S1 and S2 of the supplementary materials.

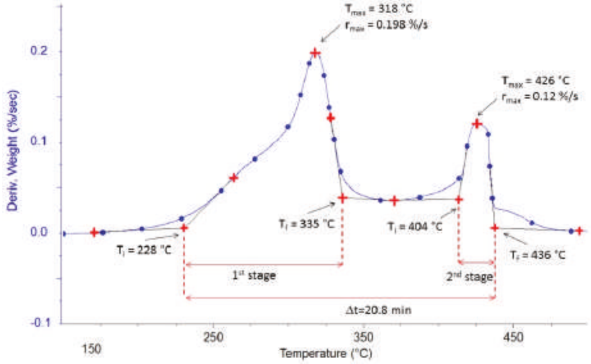

Figure 3. Example of the graphical determination of thermal parameters (for Flax shives with $\beta = 10\ ^\circ\mathrm{C{\cdot}min^{-1}}$).

3.2.1. Ignition and Final Temperatures of Combustion Reaction

The ignition temperature (T_i) is the temperature at which the combustion reaction begins, while the final temperature (T_f) indicates the end of the combustion reaction. These temperatures are essential to ensure the perfect design of the combustor and avoid unburned solid fuel at the outlet of the reactor [22]. It should be noted that $\mathrm{T_i}$ is also used to compare the reactivity of several substances [19–23,42–44]. Several methods have been reported and used in the literature to determine T_i and T_f [32,45–48]. In this work, T_i and T_f have been determined according to the work of Grønli et al. [46], which was based on the use of the second derivative of the mass loss curves. Tables 3 and 4 show the evolution of T_i and T_f during the combustion reaction for different raw materials over a heating rate of 10 °C·min^{-1}. Hemicellulose presented the lowest T_i, followed by lignin and biomasses, while cellulose demonstrated the highest T_i. At the end of the first stage, hemicellulose displayed the lowest T_f, while biomasses and cellulose presented almost the same T_f. Furthermore, the T_f of lignin was the highest. In the second stage of combustion, the T_i of the biomasses and hemicellulose remained close to each other. However, the T_i of lignin remained higher.

The T_i of the char from raw materials had approximately the same behavior. These temperatures remained higher compared to the biomasses and the pure pseudo-components. Also, hemicellulose and cellulose chars showed almost the same T_i and T_f. As for lignin combustion, the char from lignin showed the highest T_i and T_f.

Table 3. Characteristics of the combustion stages of raw materials (β = 10 °C·min^{-1}).

Raw Materials	First Stage				Second Stage				Δt (min)
	T_i (°C)	T_f (°C)	$T_{\max}$ (°C)	$r_{\max}$ (%·s^{-1})	T_i (°C)	T_f (°C)	$T_{\max}$ (°C)	$r_{\max}$ (%·s^{-1})	
Flax shives	228	335	318	0.198	404	436	426	0.12	20.80
Beech wood	245	339	325	0.25	431	444	437	0.164	19.90
Hemicellulose	207	314	291	0.132	448	561	515	0.046	35.40
Cellulose	297	335	323	0.491	-	-	-	-	3.80
Lignin	227	346	314	0.043	806	837	823	0.389	61.00

Table 4. Characteristics of the combustion of char samples (β = 10 °C·min^{-1}).

Chars	T_i (°C)	T_f (°C)	$T_{\max}$ (°C)	$r_{\max}$ (%·s^{-1})	Δt (min)
Flax shives char	441	479	458	0.234	3.8
Beech wood char	441	501	468	0.282	6
Hemicellulose char	532	620	587	0.208	8.8
Cellulose char	513	627	587	0.235	11.4
Lignin char	748	801	784	0.279	5.3

3.2.2. Burnout Time

The burnout time (t_R) is defined as the time between the T_i and the T_f. In this work, the t_R has been calculated taking into account the entire reaction interval through the two stages. Overall, t_R of the combustion of beech wood and flax shives was almost the same. Hemicellulose was the first to burn, and it took more time than the biomasses. The lignin t_R was the longest, since the second stage of its combustion needed a higher temperature. The cellulose t_R was not significant, since the second stage was not visible. The t_R of char samples has been shown in Table 4. The same trend as for the t_R of the raw materials was not obtained. Indeed, it seems that the char produced by holocellulose compounds required more time than chars from beech wood, flax shives, and lignin.

3.2.3. Maximum Temperature

The maximum temperature ($T_{\max}$) is defined as the temperature where the maximum reaction rate (dX/dt) occurs. This temperature is a very important criterion for evaluating the reactivity of substances [19–23,42–44]. Indeed, the lower the $T_{\max}$, the higher the reactivity of the substance.

According to Table 3, hemicellulose was the most reactive substance. The $T_{\max}$ for flax shives, beech wood, hemicellulose, and cellulose were very similar. As for the char samples, the ones produced from biomass pyrolysis remained the most reactive, while the lignin char proved to be the least reactive, as shown in Table 4. Also, the chars of cellulose and hemicellulose showed almost the same behavior.

3.2.4. Maximum Rate

Maximum rate ($r_{\max}$) is also usually considered as a criterion to classify the reactivity of substances [19,22]. Indeed, the higher the $r_{\max}$ and the lower the $T_{\max}$, the more reactive the substance. The maximum reactivity of the different raw materials and char samples are shown in Tables 3 and 4, respectively. In the first stage, the most reactive raw material was cellulose. However, for the second stage, lignin appeared to be the most reactive at high temperatures.

As shown in Figure 1, these parameters, cited above, evolved by increasing the heating rate, more particularly in the first stage of the combustion of raw materials and char. However, the effect of heating rate was more pronounced on $r_{\max}$ than on other parameters.

3.3. Principal Component Analysis

As shown above, the reactivity classification of different substances varied from one criterion to the other. The results were examined using the principal component analysis (PCA), which checks the global behavior of the different raw materials, taking into account the different criteria discussed above. Figure 4 shows the PCA for the first and the second stage of combustion of the raw materials.

PCA is a multivariate technique used in data processing usually presented in a table containing variables and observations. PCA has the goal to detect the existence of similarities or inter-correlation between variables, based on the treatment of observations. PCA is represented by only one orthogonal variable called principal components F1 and F2. In this study, PCA was used to analyze the behavior of raw materials and char based on the different thermal parameters discussed above [49,50].

PCA is a graphical representation of a cloud of points initially drawn in a multidimensional space. The number of dimensions in our case represents the number of axes or variables in this space, and it corresponds to six (T_i, $T_{\max}$, T_f, β, Δt, and $r_{\max}$). In order to facilitate the analysis of the existence of any correlation between each of two variables separately, a projection of this cloud in an orthogonal space (F1 and F2) is created, as previously specified. Often, these two axes have no physical meaning, however, they ensure the maximum recovery of information from the projection of the cloud of points. Obviously, a bad projection of a variable on this new space may not be representative, and therefore, the information about this variable is deformed. The conclusions drawn in this case may not have a physical meaning. The closer the segment representing this variable is to the radius of the circle in Figure 4a (segment in red), the better the parameter is represented in this new space. In this study, overall, all parameters were well represented, as shown in Figures 4 and 5.

Figure 4a analyses the existence of a possible linear correlation between the different parameters considered in this study. The correlation coefficient between each two parameters is calculated from the cosine of the angle formed between these two parameters shown by segments in Figure 4a. Tables S3, S4, and S5 detail the values of these correlation coefficients. For example, Figure 4a shows that the cosine of the angle formed by T_i and $T_{\max}$ was about 0.798. Also, T_i and $T_{\max}$ showed a positive correlation given that they were in the same direction (the same remark can be made for T_f and β in Figure 4a). This means that an increase in T_i implies an increase in $T_{\max}$. A negative correlation can be shown when the correlation coefficient tends to negative values; this means that the two variables show an opposite trend. Δt and $T_{\max}$ in Figure 4a illustrate a negative trend.

The set of four points delimited in Figure 4b for each sample represents the evolution of the different parameters (T_i, T_f, $T_{\max}$, $r_{\max}$, and Δt) with the heating rate (10, 20, 30, and 40 $^{\circ}\mathrm{C}\cdot\mathrm{min}^{-1}$) (the evolution of the temperature T_f with the heating rate is shown in Figure 4b, as an example).

According to PCA, some qualitative conclusions can be addressed, as follows:

Regarding the first stage of raw materials combustion:

- A strong positive dependence between T_i, $T_{\max}$, and $r_{\max}$.
- A strong positive dependence between β and T_f.
- Opposite evolution between Δt and the rest of the parameters.
- Overall, there is no dependence between T_i, $T_{\max}$, and $r_{\max}$.

Regarding the second stage of raw materials combustion:

- A clear opposite trend between Δt and β.
- Δt and β seemed to be unrelated to T_i, T_f, $T_{\max}$, and $r_{\max}$ during this stage.
- A strong positive dependence between T_i, $T_{\max}$, and T_f.

Regarding the combustion of chars:

- A strong positive dependence between T_i, $T_{\max}$, and T_f.
- A strong positive dependence between β and $r_{\max}$.
- Surprisingly, no characteristic temperature seemed dependent on β.

As shown in Figure 4b, flax shives and beech wood exhibited behavior closest to the hemicellulose (overlapped segments), out of the three pseudo-components. Lignin was less reactive and took more time to be completely consumed. The Figure 5b shows that the chars produced from beech wood and flax shives were more reactive than the chars from pseudo-components. Also, the char from holocellulose was more reactive than that from lignin. This analysis also showed that the cellulose, hemicellulose, and lignin contents can modify the co-combustion of pseudo-component/biomass or pseudo-component/char blend. Indeed, in the case of a cellulose/biomass blend, an increase in $T_{\max}$ and $r_{\max}$ can be expected; while increasing the lignin content can reduce $T_{\max}$ and r_m.

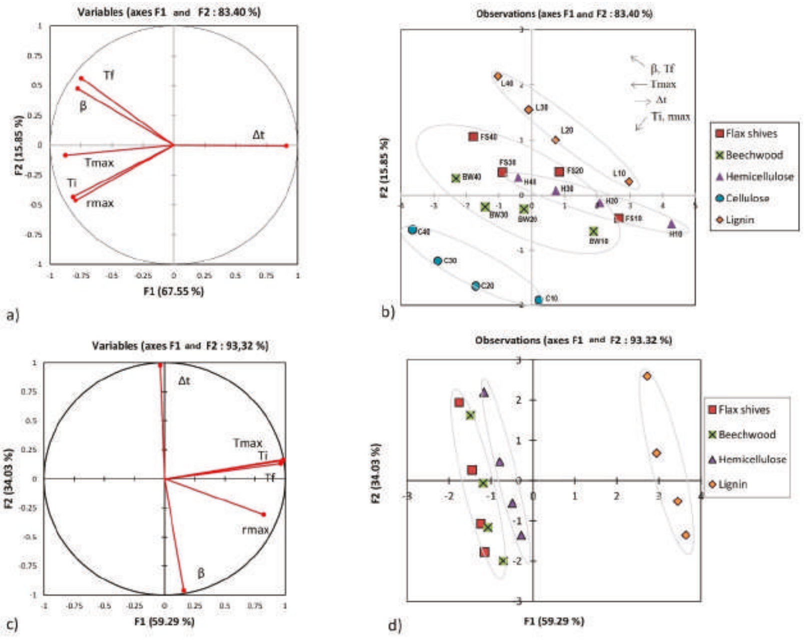

Figure 4. Principal component analysis (PCA) for raw materials: (**a**,**b**) represent the first stage combustion; (**c**,**d**) represent the second stage combustion.

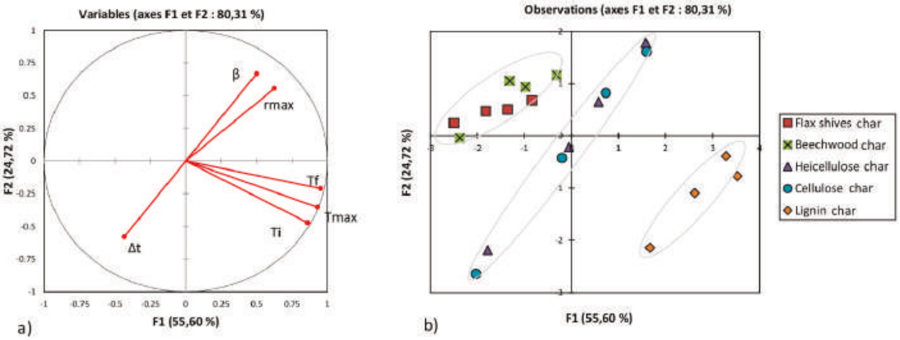

Figure 5. Principal component analysis (PCA) for char samples: (**a**) Correlation between variables; (**b**) Effect of heating rate on different variables.

3.4. Mechanism and Kinetic Parameters of Combustion

3.4.1. Mechanism

Usually, the mechanism of biomass combustion is composed of two stages, as shown in Figure 1. Some authors reported that the first stage illustrated the combustion of the holocellulose component, while the second stage concerned the combustion of lignin according to mechanism 1 [20,34].

Mechanism 1

$$\text{Holocellulose} + O_2 \rightarrow \text{Ash} + CO_2 + H_2O$$

$$\text{Lignin} + O_2 \rightarrow \text{Ash} + CO_2 + H_2O$$

Other authors reported that the mechanism of combustion followed the combustion of volatile matter (1st stage) and then fixed carbon (2nd stage), according to mechanism 2 [21,51,52].

Mechanism 2

$$\text{Volatiles} + O_2 \rightarrow \text{Ash} + CO_2 + H_2O$$

$$\text{Char} + O_2 \rightarrow \text{Ash} + CO_2 + H_2O$$

In light of the results shown above, it seems that both hemicellulose and lignin showed two independent stages. Therefore, the first stage is explained by the combustion of volatile matter derived from the pyrolysis of biomass, while the second stage can be explained by the combustion of residual char produced in the first stage. Cellulose showed only one stage given its low fixed carbon content, as shown in Table 1 (3.75 wt%). Moreover, the second stage of combustion of hemicellulose and lignin corresponded approximately to the same stage of combustion of char produced by hemicellulose and lignin pyrolyzed in the fixed-bed reactor. This observation favored the plausibility of the second mechanism.

In some works in the literature, the reactivity of substances was classified according to the activation energy of their combustion reaction [20]. Therefore, in our case, the activation energy for the combustion reaction was determined for different materials. The combustion of different raw materials was successfully modeled by using two independent reactions (Mechanism 2), with the exception of cellulose (which was modeled using one single reaction, given its low fixed carbon content, as discussed above). The combustion of char samples was modeled assuming one single reaction, according to the DTG curves, see Figure 2.

3.4.2. Kinetic Parameters

The plot of $\ln|g(X)/T^2|$ of relation (8) versus $1/T$ gave a straight line with a slope of $-E_a/R$. Relation (8) was applied in the range of temperatures between T_i and T_f of each combustion stage for different heating rates. The term $2RT/E_a$ can be neglected (compared to 1 in this case) [37]. The E_a was calculated from the slope of relation (8), while A was calculated from the y-intercept. Since this relation was supposed to be independent of the heating rate, the E_a and A were calculated as average values based on the four heating rates.

Several models that take into account the effect of boundary and diffusion control have been tested in order to establish the linearity of relation (8) [21,53,54]. Indeed, flax shives, beech wood, cellulose, lignin, and their char samples followed the first-order kinetics model according to model 1 (relation (9)). The first order is usually considered for combustion reactions [55–58]. The latter model has been the most frequently used in literature and takes into account only the chemical reaction. However, the best fit for hemicellulose combustion was model 2 (relation (10)). In this model, the kinetics of the combustion reaction were fully controlled by the diffusion of oxygen inside the hemicellulose particles. The diffusion limitation has already been observed in the combustion of the pine samples as reported by [52].

Kinetic model function 1:

$$g(X) = (1 - X) \tag{9}$$

Kinetic model function 2:

$$g(X) = \left[1 - (1 - X)^{1/3}\right]^2 \tag{10}$$

The activation energy and the pre-exponential factor for different raw materials are shown in Table 5. A detailed table of kinetic parameters for the raw materials and the char samples has also been provided in Table S6 of the supplementary materials. The deviation of the regression on E_a and A reported in Table 5 has been calculated with respect to the different heating rates. Therefore, the variation in the value of E_a with the different heating rates can be explained by the experimental error on one hand, and, on the other, by the limitations of heat transfer, which tended to increase with high heating rates, as shown in Table S6.

The values of the activation energies shown in Table 5 were globally close to those found in the literature, see Table S7. However, some authors have found much lower values of activation energies for biomass combustion reactions, such as Senneca [59], Sahu et al. [60], and Kumar et al. [61]. For the activation energy of the char combustion, they were globally close to those found in the literature, as shown in Table S8.

Despite the different nature of flax shives and beech wood, their E_a remained similar to each other in the first stage (82.54 ± 2.49 and 99.26 ± 3.10 kJ·mol^{-1}, respectively). Also, hemicellulose and cellulose showed E_a in the same range, with a slight elevation for cellulose (172.33 ± 15.14 and 212.21 ± 8.23 kJ·mol^{-1}, respectively). However, cellulose and hemicellulose showed high E_a compared to the biomasses. Lignin had the lowest E_a in this stage (45.97 ± 0.82 kJ·mol^{-1}). In the second stage, the E_a of both biomasses and those of the holocellulose components were mostly the same (between 66.08 ± 3.00 and 79.51 ± 1.90 kJ·mol^{-1}); unlike lignin, which showed a high E_a in this stage (348.43 ± 15.57 kJ·mol^{-1}) and reacted only at high temperatures.

Table 5. Kinetic parameters of the combustion reaction of different raw materials.

Samples	Raw Materials				Char Samples	
	First Stage		Second Stage		Only One Stage	
	E_a (kJ·mol^{-1})	**log$A$**	**E_a (kJ·mol^{-1})**	**log$A$**	**E_a (kJ·mol^{-1})**	**log$A$**
Flax shives	82.54 ± 2.49	9.06 ± 0.51	66.89 ± 2.73	5.26 ± 0.32	134.90 ± 22.32	17.33 ± 0.63
Beech wood	99.26 ± 3.10	11.53 ± 0.32	79.51 ± 1.90	10.17 ± 0.67	151.68 ± 26.3	14.86 ± 6.21
Hemicellulose	172.33 ± 15.14	24.55 ± 2.08	66.08 ± 3.00	1.67 ± 0.08	180.32 ± 15.26	30.19 ± 1.14
Cellulose	212.21 ± 8.23	33.43 ± 2.30	-	-	218.37 ± 7.11	20.54 ± 2.61
Lignin	45.97 ± 0.82	1.36 ± 0.11	348.43 ± 15.57	25.09 ± 7.72	263.91 ± 32.49	20.54 ± 3.92

The flax shives and beech wood char samples showed almost the same range of E_a (134.90 ± 22.32 and 151.68 ± 26.3 kJ·mol^{-1}, respectively). The same remark for hemicellulose and cellulose can be made with respect to their E_a (180.32 ± 15.26 and 218.37 ± 7.11 kJ·mol^{-1}, respectively). Lignin char showed the highest E_a (263.91 ± 32.49 kJ·mol^{-1}) compared to other chars. This observation coincides with the PCA, shown in Figure 5. As reported by several authors, this can be explained by a porous and highly disordered carbon structure of lignin [22,62].

4. Conclusions

In this study, the combustion of flax shives, beech wood, pure pseudo-components, and their chars has been investigated based on TGA. During the combustion reaction, biomass (despite being essentially comprised of cellulose, hemicellulose, and lignin) exhibited a different behavior compared to its pure pseudo-components. This means that the physical interactions between the pure pseudo-components present in biomass cannot be neglected. It also demonstrated that biomass with a higher cellulose content showed faster conversion rates, higher hemicellulose contents in the biomass led to a lower T_i, and higher lignin content implied a higher E_a and a higher T_f. This study also confirmed that the combustion reaction of biomass could be modeled as two independent reactions. Indeed, the first reaction concerned the combustion of the volatile content, while the second corresponded to the combustion of the fixed carbon component. It is therefore important for the design of the combustor to take into account the substance limiting the process.

As this study showed, char produced from flax shives and beech wood had the same behavior both thermally and kinetically. Also, the same remark can be made for char produced from hemicellulose and cellulose. However, the char from lignin behaved differently from those from biomass and the holocellulosic pseudo-components.

Supplementary Materials: The following are available online at http://www.mdpi.com/1996-1073/11/8/2146/s1.

Author Contributions: The authors equally contributed to the work reported.

Acknowledgments: This work was supported by the European Union with the European regional development fund (ERDF) and by the Normandie Regional Council.

Conflicts of Interest: The authors declare no conflict of interest.

Nomenclature

A	Pre-exponential factor (s^{-1})
dX/dt	The first derivative of conversion rate with respect to time
DTG	Differential thermogravimetry
E_a	Activation energy (kJ·mol^{-1})
m_f	Final mass (kg)
m_i	Initial mass (kg)
m_t	Mass at temperature T (kg)
n	Reaction order (-)
R	Gas constant (8.314 J·K^{-1}·mol^{-1})
R^2	Correlation coefficient (-)
T	Temperature (K)
T_f	Final temperature (K)
TG	Thermogravimetry
TGA	Thermogravimetry analysis
T_i	Ignition temperature (K)
X	Conversion degree (-)
Greek symbols	
β	Heating rate (K·min^{-1})

References

1. International Energy Agency. Available online: http://www.iea.org/ (accessed on 23 March 2017).
2. Nunes, L.J.R.; Matias, J.C.O.; Catalão, J.P.S. Biomass in the generation of electricity in Portugal: A review. *Renew. Sustain. Energy Rev.* **2017**, *71*, 373–378. [CrossRef]
3. Jones, J.M.; Lea-Langton, A.R.; Ma, L.; Pourkashanian, M.; Williams, A. *Combustion of Solid Biomass: Classification of Fuels. Pollutants Generated by the Combustion of Solid Biomass Fuels*; Springer: London, UK, 2014; pp. 9–24. Available online: https://link.springer.com/chapter/10.1007/978-1-4471-6437-1_2 (accessed on 29 July 2018).
4. van den Broek, R.; Faaij, A.; van Wijk, A. Biomass combustion for power generation. *Biomass Bioenergy* **1996**, *11*, 271–281. [CrossRef]
5. Jones, J.M.; Lea-Langton, A.R.; Ma, L.; Pourkashanian, M.; Williams, A. *Pollutants Generated by the Combustion of Solid Biomass Fuels*; Springer: London, UK, 2014; Available online: https://www.springer.com/gb/book/9781447164364 (accessed on 29 July 2018).
6. Sannigrahi, P.; Ragauskas, A.J.; Tuskan, G.A. Poplar as a feedstock for biofuels: A review of compositional characteristics. *Biofuels Bioprod. Biorefin.* **2010**, *4*, 209–226. [CrossRef]
7. Scheer, A. Thermal Decomposition Mechanisms of Lignin Model Compounds: From Phenol to Vanillin. Physics Graduate Thesis & Dissertations. 2011. Available online: https://scholar.colorado.edu/phys_gradetds/55 (accessed on 15 August 2018).
8. Yu, J.; Paterson, N.; Blamey, J.; Millan, M. Cellulose, xylan and lignin interactions during pyrolysis of lignocellulosic biomass. *Fuel* **2017**, *191*, 140–149. [CrossRef]
9. Hosoya, T.; Kawamoto, H.; Saka, S. Cellulose–hemicellulose and cellulose–lignin interactions in wood pyrolysis at gasification temperature. *J. Anal. Appl. Pyrolysis* **2007**, *80*, 118–125. [CrossRef]
10. Yoshida, T.; Matsumura, Y. Gasification of Cellulose, Xylan, and Lignin Mixtures in Supercritical Water. *Ind. Eng. Chem. Res.* **2001**, *40*, 5469–5474. [CrossRef]
11. Gani, A.; Naruse, I. Effect of cellulose and lignin content on pyrolysis and combustion characteristics for several types of biomass. *Renew. Energy* **2007**, *32*, 649–661. [CrossRef]
12. González-García, S.; Luo, L.; Moreira, M.T.; Feijoo, G.; Huppes, G. Life cycle assessment of flax shives derived second generation ethanol fueled automobiles in Spain. *Renew. Sustain. Energy Rev.* **2009**, *13*, 1922–1933. [CrossRef]
13. Daylan, B.; Ciliz, N. Life cycle assessment and environmental life cycle costing analysis of lignocellulosic bioethanol as an alternative transportation fuel. *Renew. Energy* **2016**, *89*, 578–587. [CrossRef]
14. Rajabi Hamedani, S.; Villarini, M.; Colantoni, A.; Moretti, M.; Bocci, E. Life Cycle Performance of Hydrogen Production via Agro-Industrial Residue Gasification—A Small Scale Power Plant Study. *Energies* **2018**, *11*, 675. [CrossRef]
15. Gassner, M.; Maréchal, F. Thermodynamic comparison of the FICFB and Viking gasification concepts. *Energy* **2009**, *34*, 1744–1753. [CrossRef]
16. Qian, K.; Kumar, A.; Patil, K.; Bellmer, D.; Wang, D.; Yuan, W.; Huhnke, R.L. Effects of Biomass Feedstocks and Gasification Conditions on the Physiochemical Properties of Char. *Energies* **2013**, *6*, 3972–3986. [CrossRef]
17. Guizani, C.; Jeguirim, M.; Valin, S.; Limousy, L.; Salvador, S. Biomass Chars: The Effects of Pyrolysis Conditions on Their Morphology, Structure, Chemical Properties and Reactivity. *Energies* **2017**, *10*, 796.
18. Di Blasi, C. Modeling chemical and physical processes of wood and biomass pyrolysis. *Prog. Energy Combust. Sci.* **2008**, *34*, 47–90. [CrossRef]
19. El may, Y.; Jeguirim, M.; Dorge, S.; Trouvé, G.; Said, R. Study on the thermal behavior of different date palm residues: Characterization and devolatilization kinetics under inert and oxidative atmospheres. *Energy* **2012**, *44*, 702–709. [CrossRef]
20. Garcia Torrent, J.; Fernandez Anez, N.; Medic Pejic, L.; Montenegro Mateos, L. Assessment of self-ignition risks of solid biofuels by thermal analysis. *Fuel* **2015**, *143*, 484–491. [CrossRef]
21. Gil, M.V.; Casal, D.; Pevida, C.; Pis, J.J.; Rubiera, F. Thermal behaviour and kinetics of coal/biomass blends during co-combustion. *Bioresour. Technol.* **2010**, *101*, 5601–5608. [CrossRef] [PubMed]
22. Kastanaki, E.; Vamvuka, D. A comparative reactivity and kinetic study on the combustion of coal–biomass char blends. *Fuel* **2006**, *85*, 1186–1193. [CrossRef]

23. Haykırı-Açma, H. Combustion characteristics of different biomass materials. *Energy Convers. Manag.* **2003**, *44*, 155–162. [CrossRef]
24. Le Lin et le Chanvre Européen. Available online: http://www.europeanflax.com/ (accessed on 18 July 2018).
25. Van de Velden, M.; Baeyens, J.; Brems, A.; Janssens, B.; Dewil, R. Fundamentals, kinetics and endothermicity of the biomass pyrolysis reaction. *Renew. Energy* **2010**, *35*, 232–242. [CrossRef]
26. Mohabeer, C.; Abdelouahed, L.; Marcotte, S.; Taouk, B. Comparative analysis of pyrolytic liquid products of beech wood, flax shives and woody biomass components. *J. Anal. Appl. Pyrolysis* **2017**, *127*, 269–277. [CrossRef]
27. García, R.; Pizarro, C.; Lavín, A.G.; Bueno, J.L. Biomass proximate analysis using thermogravimetry. *Bioresour. Technol.* **2013**, *139*, 1–4. [CrossRef] [PubMed]
28. Channiwala, S.A.; Parikh, P.P. A unified correlation for estimating HHV of solid, liquid and gaseous fuels. *Fuel* **2002**, *81*, 1051–1063. [CrossRef]
29. Magdziarz, A.; Wilk, M.; Straka, R. Combustion process of torrefied wood biomass. *J. Therm. Anal. Calorim.* **2017**, *127*, 1339–1349. [CrossRef]
30. Nowak, B.; Karlström, O.; Backman, P.; Brink, A.; Zevenhoven, M.; Voglsam, S.; Winter, F.; Hupa, M. Mass transfer limitation in thermogravimetry of biomass gasification. *J. Therm. Anal. Calorim.* **2012**, *111*, 183–192. [CrossRef]
31. Abdelouahed, L.; Leveneur, S.; Vernieres-Hassimi, L.; Balland, L.; Taouk, B. Comparative investigation for the determination of kinetic parameters for biomass pyrolysis by thermogravimetric analysis. *J. Therm. Anal. Calorim.* **2017**, *129*, 1201–1213. [CrossRef]
32. Wang, Z.; Lin, W.; Song, W.; Wu, X. Pyrolysis of the lignocellulose fermentation residue by fixed-bed micro reactor. *Energy* **2012**, *43*, 301–305. [CrossRef]
33. White, J.E.; Catallo, W.J.; Legendre, B.L. Biomass pyrolysis kinetics: A comparative critical review with relevant agricultural residue case studies. *J. Anal. Appl. Pyrolysis* **2011**, *91*, 1–33. [CrossRef]
34. Álvarez, A.; Pizarro, C.; García, R.; Bueno, J.L.; Lavín, A.G. Determination of kinetic parameters for biomass combustion. *Bioresour. Technol.* **2016**, *216*, 36–43. [CrossRef] [PubMed]
35. Garcia-Maraver, A.; Perez-Jimenez, J.A.; Serrano-Bernardo, F.; Zamorano, M. Determination and comparison of combustion kinetics parameters of agricultural biomass from olive trees. *Renew. Energy* **2015**, *83*, 897–904. [CrossRef]
36. Yorulmaz, S.Y.; Atimtay, A. Investigation of Combustion Kinetics of Five Waste Wood Samples with Thermogravimetric Analysis. In *Survival and Sustainability*; Springer: Berlin/Heidelberg, Germany, 2010; p. 511. Available online: https://link.springer.com/chapter/10.1007/978-3-540-95991-5_46 (accessed on 5 July 2017).
37. Islam, M.A.; Auta, M.; Kabir, G.; Hameed, B.H. A thermogravimetric analysis of the combustion kinetics of karanja (*Pongamia pinnata*) fruit hulls char. *Bioresour. Technol.* **2016**, *200*, 335–341. [CrossRef] [PubMed]
38. Coats, A.W.; Redfern, J.P. Kinetic Parameters from Thermogravimetric Data. *Nature* **1964**, *201*, 68–69. [CrossRef]
39. Damartzis, T.; Vamvuka, D.; Sfakiotakis, S.; Zabaniotou, A. Thermal degradation studies and kinetic modeling of cardoon (*Cynara cardunculus*) pyrolysis using thermogravimetric analysis (TGA). *Bioresour. Technol.* **2011**, *102*, 6230–6238. [CrossRef] [PubMed]
40. Vamvuka, D.; Kastanaki, E.; Lasithiotakis, M. Devolatilization and Combustion Kinetics of Low-Rank Coal Blends from Dynamic Measurements. *Ind. Eng. Chem. Res.* **2003**, *42*, 4732–4740. [CrossRef]
41. Zhou, H.; Long, Y.; Meng, A.; Chen, S.; Li, Q.; Zhang, Y. A novel method for kinetics analysis of pyrolysis of hemicellulose, cellulose, and lignin in TGA and macro-TGA. *RSC Adv.* **2015**, *5*, 26509–26516. [CrossRef]
42. Jiang, L.; Yuan, X.; Li, H.; Xiao, Z.; Liang, J.; Wang, H.; Wu, Z.; Chen, X.; Zeng, G. Pyrolysis and combustion kinetics of sludge–camphor pellet thermal decomposition using thermogravimetric analysis. *Energy Convers. Manag.* **2015**, *106*, 282–289. [CrossRef]
43. Munir, S.; Daood, S.S.; Nimmo, W.; Cunliffe, A.M.; Gibbs, B.M. Thermal analysis and devolatilization kinetics of cotton stalk, sugar cane bagasse and shea meal under nitrogen and air atmospheres. *Bioresour Technol.* **2009**, *100*, 1413–1418. [CrossRef] [PubMed]
44. Sait, H.H.; Hussain, A.; Salema, A.A.; Ani, F.N. Pyrolysis and combustion kinetics of date palm biomass using thermogravimetric analysis. *Bioresour. Technol.* **2012**, *118*, 382–389. [CrossRef] [PubMed]

45. Gai, C.; Liu, Z.; Han, G.; Peng, N.; Fan, A. Combustion behavior and kinetics of low-lipid microalgae via thermogravimetric analysis. *Bioresour. Technol.* **2015**, *181*, 148–154. [CrossRef] [PubMed]
46. Grønli, M.G.; Varhegyi, G.; Di Blasi, C. Thermogravimetric analysis and devolatilization kinetics of wood. *Ind. Eng. Chem. Res.* **2002**, *41*, 4201–4208. [CrossRef]
47. Li, Q.; Zhao, C.; Chen, X.; Wu, W.; Li, Y. Comparison of pulverized coal combustion in air and in O_2/CO_2 mixtures by thermo-gravimetric analysis. *J. Anal. Appl. Pyrolysis* **2009**, *85*, 521–528. [CrossRef]
48. Meng, F.; Yu, J.; Tahmasebi, A.; Han, Y. Pyrolysis and Combustion Behavior of Coal Gangue in O_2/CO_2 and O_2/N_2 Mixtures Using Thermogravimetric Analysis and a Drop Tube Furnace. *Energy Fuels* **2013**, *27*, 2923–2932. [CrossRef]
49. Principal Component Analysis–Abdi–2010–Wiley Interdisciplinary Reviews: Computational Statistics–Wiley Online Library. Available online: https://onlinelibrary.wiley.com/doi/abs/10.1002/wics.101 (accessed on 19 July 2018).
50. Dunteman, G.H. *Principal Components Analysis*; SAGE: Newcastle upon Tyne, UK, 1989.
51. Liu, N.A.; Fan, W.; Dobashi, R.; Huang, L. Kinetic modeling of thermal decomposition of natural cellulosic materials in air atmosphere. *J. Anal. Appl. Pyrolysis* **2002**, *63*, 303–325. [CrossRef]
52. Yorulmaz, S.Y.; Atimtay, A.T. Investigation of combustion kinetics of treated and untreated waste wood samples with thermogravimetric analysis. *Fuel Process. Technol.* **2009**, *90*, 939–946. [CrossRef]
53. Capart, R.; Khezami, L.; Burnham, A.K. Assessment of various kinetic models for the pyrolysis of a microgranular cellulose. *Thermochim. Acta* **2004**, *417*, 79–89. [CrossRef]
54. Vyazovkin, S.; Burnham, A.K.; Criado, J.M.; Pérez-Maqueda, L.A.; Popescu, C.; Sbirrazzuoli, N. ICTAC Kinetics Committee recommendations for performing kinetic computations on thermal analysis data. *Thermochim. Acta* **2011**, *520*, 1–19. [CrossRef]
55. Biagini, E.; Lippi, F.; Petarca, L.; Tognotti, L. Devolatilization rate of biomasses and coal–biomass blends: An experimental investigation. *Fuel* **2002**, *81*, 1041–1050. [CrossRef]
56. Cai, J.; Wang, Y.; Zhou, L.; Huang, Q. Thermogravimetric analysis and kinetics of coal/plastic blends during co-pyrolysis in nitrogen atmosphere. *Fuel Process. Technol.* **2008**, *89*, 21–27. [CrossRef]
57. Jayaraman, K.; Gökalp, I. Pyrolysis, combustion and gasification characteristics of miscanthus and sewage sludge. *Energy Convers. Manag.* **2015**, *89*, 83–91. [CrossRef]
58. Su, W.; Ma, H.; Wang, Q.; Li, J.; Ma, J. Thermal behavior and gaseous emission analysis during co-combustion of ethanol fermentation residue from food waste and coal using TG–FTIR. *J. Anal. Appl. Pyrolysis* **2013**, *99*, 79–84. [CrossRef]
59. Senneca, O. Kinetics of pyrolysis, combustion and gasification of three biomass fuels. *Fuel Process. Technol.* **2007**, *88*, 87–97. [CrossRef]
60. Sahu, S.G.; Sarkar, P.; Chakraborty, N.; Adak, A.K. Thermogravimetric assessment of combustion characteristics of blends of a coal with different biomass chars. *Fuel Process. Technol.* **2010**, *91*, 369–378. [CrossRef]
61. Kumar, A.; Wang, L.; Dzenis, Y.A.; Jones, D.D.; Hanna, M.A. Thermogravimetric characterization of corn stover as gasification and pyrolysis feedstock. *Biomass Bioenergy* **2008**, *32*, 460–467. [CrossRef]
62. Hurt, R.; Sun, J.-K.; Lunden, M. A Kinetic Model of Carbon Burnout in Pulverized Coal Combustion. *Combust. Flame* **1998**, *113*, 181–197. [CrossRef]

energies

Article

The Influence of Char Preparation and Biomass Type on Char Steam Gasification Kinetics

Tilia Dahou [1,2,3,*], Françoise Defoort [1], Sébastien Thiéry [1], Maguelone Grateau [1], Matthieu Campargue [4], Simona Bennici [2], Mejdi Jeguirim [2] and Capucine Dupont [5]

[1] Université Grenoble Alpes, CEA, LITEN, DTBH, 17 avenue des Martyrs, 38054 Grenoble CEDEX 09, France; francoise.defoort@cea.fr (F.D.); sebastien.thiery@cea.fr (S.T.); maguelone.grateau@cea.fr (M.G.)
[2] Institut de Sciences des Matériaux de Mulhouse, UMR 7661 CNRS, 15 rue Jean-Starcky, 68057 Mulhouse CEDEX, France; simona.bennici@uha.fr (S.B.); mejdi.jeguirim@uha.fr (M.J.)
[3] Agence de l'Environnement et de la Maîtrise de l'Energie (ADEME), 20 avenue du Grésillé, BP 90406, 49004 Angers CEDEX 01, France
[4] RAGT Energie, Zone Innoprod, Chemin de la Teulière, 81012 Albi CEDEX 9, France; mcampargue@ragt.fr
[5] IHE Delft Institute for Water Education, Westvest 7, 2611 AX Delft, The Netherlands; c.dupont@un-ihe.org
* Correspondence: tilia.dahou@cea.fr; Tel.: +33-4-38-78-54-69

Received: 23 July 2018; Accepted: 14 August 2018; Published: 15 August 2018

Abstract: A study was conducted to investigate the parameter that has influence on steam gasification kinetics between the biomass type and char preparation. Thermogravimetric analysis (TGA) was carried out on steam gasification of seven biomass samples as well as chars from three of these samples. Chars were prepared using three different sets of low heating rate (LHR) pyrolysis conditions including temperature and biomass bed geometry. It was shown by a characteristic time analysis that these pyrolysis conditions were not associated with a chemical regime in a large amount of devices. However, it has been shown experimentally that conditions used to prepare the char had a much lower influence on steam gasification kinetics than the biomass type.

Keywords: biomass; steam gasification; kinetics; pyrolysis conditions; thermogravimetric analysis; characteristic time analysis

---

1. Introduction

Today, there is a consensus about the increasing need of biomass use for energy applications. Given the limited availability of wood, it seems essential to identify and to convert other biomass resources such as agricultural co-products. Among the various techniques for biomass conversion to energy, the gasification process is a promising one [1] such as in the case of hydrogen production [2–4] or liquid fuel synthesis [5–7]. This process includes two main steps that can overlap: biomass pyrolysis leading to char formation and gasification of the char producing syngas, i.e., a gas mixture of mainly CO and H_2. It has been shown that, with steam as a gasifying agent, the char gasification reaction has the slowest reaction under typical operating conditions [8]. Therefore, the design of industrial gasifiers requires the understanding and control of the steam gasification kinetics.

Since char is the starting material for gasification, it is important to identify the main parameter affecting char gasification kinetics.

In literature, two charring parameters are identified as having a potential influence on the steam gasification kinetics including pyrolysis operating conditions and biomass type [9]. The influence of pyrolysis conditions is largely related to the heating rate. Differences are especially noted between slow pyrolysis—low heating rate (LHR), <50 °C·min^{-1}—and fast pyrolysis—high heating rate (HHR), 500 °C·min^{-1} [10]. The steam gasification rate increases when the heating rate increases, which is linked to char morphology differences. During LHR pyrolysis, the char keeps its natural porosity while, in HHR pyrolysis, larger cavities are formed [9]. This larger surface area in the case of HHR pyrolysis along with the higher content in oxygen and hydrogen results in more available active sites [11]. The influence of the biomass type is basically related to the inorganic elements content of the biomass [12], which can attain high values for some resources such as agricultural residues [13]. In particular, alkali and alkaline earth metals (AAEMs) have a catalytic effect on gasification [14–17]. In contrast, elements such as silicon or phosphorus have an inhibiting effect [18,19].

To explain the origin of the influence of these two parameters, the first step is to determine the regime of the transformation, i.e., the phenomenon—chemical reaction or transfer—limiting its kinetics. Char preparation in conditions outside the chemical regime could result in variations in the properties of the chars. Differences between the chars obtained could lead to differences between their gasification behaviors. The regime of the transformation can be assessed through an analysis of the characteristic times of the phenomena involved. In literature, such an analysis has already been conducted by several authors. For instance, this can include pyrolysis [20–24], pyrogasification [8], and torrefaction [25] at the particle scale. However, most of these studies were performed for fast pyrolysis (HHR) and not slow pyrolysis (LHR). Moreover, time scale analysis is usually applied to a particle (for micrometric to centimetric scale particles), but more rarely to a bed of fine particles. One example can be found for torrefaction for which Gonzalez Martinez et al. [25] performed such an analysis at particle as well as at bed scale.

The present work combines the analysis of these characteristic times both at a particle scale and at a bed scale and an experimental study through thermogravimetric analysis (TGA). It focuses on slow pyrolysis (LHR) conditions (10 to 24 $^{\circ}\mathrm{C}\cdot\mathrm{min}^{-1}$) and parameters as the amount of biomass treated, i.e., geometry (height and surface) of the crucible and the working temperature (450 °C or 800 °C in one or two steps). Gasification was carried out on seven biomass samples as well as on chars prepared from three of these samples in four different sets of conditions. It aims to assess the relative influence of the two parameters previously discussed including char preparation conditions and biomass type on steam gasification kinetics.

2. Materials and Methods

2.1. Biomass Samples

Seven biomass samples covering a variety of compositions were selected for this study. The selection mainly includes agricultural residues. Samples were ground below 200 μm in a rotor mill. The ash content and inorganic element composition of the samples was measured, according to solid fuel standards NF EN 14775 [26] and NF EN ISO 16967 [27], respectively. Values obtained for each biomass sample can be found in Table 1. From these values, the three main inorganic elements in mass were identified.

The main inorganic elements contained in all biomasses are Ca and K. The third main element is Si, Mg, or P. Rice husk and wheat straw can be classified as silica-rich. Sunflower seed shells and alfalfa have a high potassium content. The others are rich in calcium.

Table 1. Ash and inorganic element content of the biomass samples (on dry basis).

Biomass Sample	Rice Husk	Wheat Straw [28]	Apple Orchard Residue [28]	Apricot Orchard Residue [28]	Vineyard Residue [28]	Sunflower Seed Shells	Alfalfa
Ash at 550 °C (wt %)	14.1	6.8	3.8	3.7	2.6	3.3	7.8
Si ($mg\cdot kg^{-1}$)	60,750	20,757	820	990	1012	258	510
K ($mg\cdot kg^{-1}$)	5363	13,063	3771	7254	5045	12,926	25,695
Ca ($mg\cdot kg^{-1}$)	1718	5627	9472	10,927	7808	6392	9694
Mg ($mg\cdot kg^{-1}$)	538	693	872	1374	1604	2812	1123
P ($mg\cdot kg^{-1}$)	630	1373	1325	1161	1011	1323	2997
Na ($mg\cdot kg^{-1}$)	270	164	25	41	37	20	289
Al ($mg\cdot kg^{-1}$)	166	429	71	104	151	257	83
Fe ($mg\cdot kg^{-1}$)	163	299	58	88	113	233	109
Mn ($mg\cdot kg^{-1}$)	183	50	11	20	42	12	<11
Main Inorganic Elements	Si K Ca	Si K Ca	Ca K P	Ca K Mg	Ca K Mg	K Ca Mg	K Ca P

2.2. Char Preparation

LHR pyrolysis in 1 $L\cdot min^{-1}$ N_2 was carried out in three different sets of conditions in order to prepare large amounts of char from the different biomass feedstocks. Two devices were used to carry out the pyrolysis. They are illustrated in Figure 1.

(**a**) (**b**)

Figure 1. (**a**) Device M used for pyrolysis; (**b**) Device P used for pyrolysis.

Device M consists of a sample holder swept by nitrogen and placed in an oven. It can be used for large quantities of sample (30 g to 50 g depending on biomass) but only operates at moderate temperatures (450 °C). Device P consists of a mesh basket sample holder placed in a tube swept by nitrogen and heated by induction. It can reach higher temperatures (800 °C), but a lower amount of sample (approximately 5 g) can be converted at once.

Each set of conditions for char preparation from the biomass samples is described in Table 2. The first set of conditions (char M) is at a low temperature (450 °C) while the two other sets of conditions (char M-P and char P-P) have two temperature steps (450 °C and 800 °C) in the same or different devices.

In addition, char was produced from in-situ pyrolysis of the biomass before gasification in the thermo-balance (see following section), which pyrolysis conditions (char TGA) are listed in Table 2.

Table 2. Pyrolysis conditions for char preparation from the biomass samples.

	Char TGA	**Char M**	**Char M-P**	**Char P-P**
Device for treatment at 450 °C	TGA	Device M	Device M	Device P
Sample holder dimension at 450 °C height × diameter (mm × mm)	2.5 × 7	40 × 70	40 × 70	48 × 32
Heating rate to 450 °C (°C·min^{-1})	24	10	10	24
Holding time at 450 °C (min)	60	60	60	60
Cooling between treatment at 450 °C and 800 °C	No	–	Yes	No
Device for treatment at 800 °C	TGA	–	Device P	Device P
Heating rate to 800 °C (°C·min^{-1})	24	–	24	24
Holding time at 800 °C (min)	30	–	30	30

TGA: thermogravimetric analysis.

2.3. Steam Gasification Reactivity

Steam gasification reactivities of the four types of char (Table 2) were obtained through thermogravimetric analysis (TGA). Experiments were carried out at an atmospheric pressure using a Setsys thermobalance (SETARAM, Caluire, France) coupled with a Wetsys steam generator. For chars M, M-P, and P-P, which is a mass of 3 mg to 4 mg—i.e., the mass experimentally determined to be independent from heat and mass transfer influence—was placed in a cylindrical crucible of 2.5 mm height and 7 mm diameter. Samples were heated at 24 °C·min^{-1} until 800 °C under 0.05 L·min^{-1} N_2 except for char TGA, which starting material was biomass and for which an intermediate step at 450 °C was performed, which is shown in Table 2. In this last case, a mass of 14 mg of biomass was placed in the crucible. Samples were swept by N_2 for 45 min after the final temperature was reached to ensure pyrolysis completion and mass stability. Gas was then switched to a mixture of 20 vol % H_2O in N_2.

Steam gasification reactivities of the biomass samples were also measured. It corresponds to the preparation of char TGA described in the previous section, which is directly followed by steam gasification. The experimental procedure was similar to the one used for chars.

A solid conversion was then defined from mass loss measured as a function of time during TGA by using the following expression.

$$X = \frac{m_i - m(t)}{m_i - m_f}, \quad (1)$$

where m_i, $m(t)$, and m_f are the masses of char before gasification (at the time of steam injection) at the time t and at the end of gasification (remaining ash), respectively.

The gasification rate could then be defined as the variation of conversion versus the equation below.

$$r = X\frac{dX}{dt}. \quad (2)$$

An average reactivity between two values of conversion X_1 and X_2 was also defined below.

$$r_{X_1-X_2} = \frac{\int_{t_{X_1}}^{t_{X_2}} \frac{r(t)dt}{1-X(t)}}{t_{X_2} - t_{X_1}}. \quad (3)$$

2.4. Characteristic Time Calculation

The characteristic time of a phenomenon is the theoretical time needed for a process to occur when it is only controlled by this phenomenon [29]. It depends on the operating conditions. Phenomena to consider can be chemical reactions, heat transfers, mass transport, or other phenomena. From comparing characteristic times, the limiting phenomenon can be identified and the regime of the process can be defined.

In this study, characteristic times were calculated for char preparation through pyrolysis and for steam gasification of the char to represent the chosen experimental procedure as closely as possible in which the two reactions occur one after the other. Analysis of the characteristic times of the pyrolysis step is important since, if other phenomena than the chemical reaction occur, it could result in the production of different chars in the different conditions. Since char is the starting material to gasification, it could mean that these chars would behave differently during gasification. Analysis of the characteristic times of the gasification step is meant to validate the results from steam gasification TGA since reactivities are meaningful only in a chemical regime, i.e., when the chemical reaction is the leading phenomenon.

Phenomena involved in each process are illustrated in Figure 2.

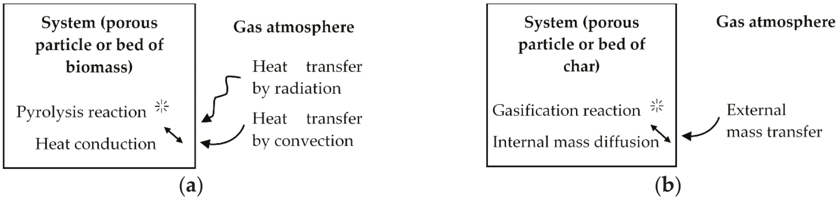

Figure 2. (**a**) Phenomena involved in pyrolysis; (**b**) Phenomena involved in gasification.

In the case of pyrolysis, the process is not led under isothermal conditions. Therefore, the characteristic times of the phenomena were compared to the heating time.

Characteristic times of each phenomenon as well as heating time are defined in Tables 3 and 4 for pyrolysis and gasification, respectively.

Table 3. Characteristic time definition for the pyrolysis of biomass.

Phenomenon	Definition of Characteristic Time
Pyrolysis chemical reaction	$t_{pyro} = \frac{1}{k_{pyro}}$
External heat transfer by convection	$t_{conv} = \frac{\rho_{solid} c_{p\ solid} L_c}{h_t}$
External heat transfer by radiation	$t_{rad} = \frac{\rho_{solid} c_{p\ solid} L_c}{\omega_{solid} \sigma \left(T_{gas} + T_{solid}\right)\left(T_{gas}^2 + T_{solid}^2\right)}$
Internal heat transfer by conduction	$t_{cond} = \frac{\rho_{solid} c_{p\ solid} {L_c}^2}{\lambda_{solid}}$
Heating	$t_{heating} = \frac{T_{gas} - T_{solid}}{r_{heating}}$

Table 4. Characteristic time definition for the gasification of biomass.

Phenomenon	Definition of Characteristic Time
Gasification chemical reaction	$t_{gasif} = \frac{1}{k_{gasif}}$
External mass transfer	$t_{mass\ ext} = \frac{\rho_{solid} R T_{gas} L_c}{h_m P_{H_2O} M_{H_2O}}$
Internal mass diffusion	$t_{diff\ int} = \frac{L_c^2}{D_{eff}}$

Pyrolysis and gasification chemical reactions of kinetic parameters were taken from literature. Pyrolysis kinetic parameters were taken from Di Blasi’s review [30]: results were calculated both for the fastest [31] and the slowest [32] laws. For gasification, a law taking into account biomass composition was chosen [18]. Among a fast-reacting biomass, alfalfa, and a slow reacting one, barley straw were chosen for comparison. All kinetic constants and their parameters values are gathered in Table 5.

Table 5. Kinetic constants for pyrolysis and gasification reactions.

Reaction	Kinetic Constant Expression	Biomass	k_0 (s^{-1})	E_a (kJ·mol^{-1})	$\frac{m_K}{m_{Si}}$	a	b
Pyrolysis	$k_{pyro\ 0}exp\left(-\frac{E_{a\ pyro}}{RT_{gas}}\right)$	Rice husk	5.8×10^{14}	200	-	-	-
		Sunflower shells	1.0×10^{3}	78.15	-	-	-
Gasification	$k_{gasif\ 0}exp\left(-\frac{E_{a\ gasif}}{RT_{gas}}\right)P_{H_2O}^{0.6}\left(a\frac{m_K}{m_{Si}}+b\right)$	Barley straw	8.8×10^{4}	167	0.1	0.18	0.59
		Alfalfa	8.8×10^{4}	167	50	0.18	0.59

Characteristic lengths used in characteristic time calculations are defined in Table 6.

Table 6. Characteristic lengths used for characteristic time calculations with d_p the particle diameter, D_c the bed diameter, and H_c the bed height.

System Considered	Characteristic Length L_c Definition	Device	Characteristic Length L_c Value (m)
Particle scale	$\frac{d_p}{6}$	All devices	3.3×10^{-5}
		TGA	6.3×10^{-4}
Bed scale	$\frac{D_c H_c}{2D_c + 4H_c}$	Device M	1.6×10^{-3}
		Device P	5.3×10^{-3}

Properties of the solids—biomass and char—were estimated from literature data or from our own measurements. They are gathered in Table 7.

Table 7. Physical properties of biomass and char particles and beds.

Property	Biomass Particle	Biomass Bed	Char Particle	Char Bed
Porosity ε_{solid} (-)	-	0.5 (estimated)	0.7 [33]	0.5 (estimated)
Tortuosity τ_{solid} (-)	-	-	3 [34]	1.57 [35]
Density ρ_{solid} (kg·m^{-3})	860	430 (measured)	400 (estimated)	200
Specific heat $c_{p\ solid}$ (J·kg^{-1}·K^{-1})	1266 [36]	1266	-	-
Thermal conductivity λ_{solid} (W·m^{-1}·K^{-1})	0.18 [37]	0.09	-	-
Emissivity ω_{solid} (-)	0.9 [37]	0.9	-	-

Lastly, transfer coefficients were obtained from correlations from literature. They use gas properties from literature [37] and are defined in Table 8.

Table 8. Definition of transfer coefficients.

Transfer Coefficient	Coefficient Definition	Correlation	
Heat transfer coefficient h_t (W·m^{-2}·K^{-1})	$\frac{\lambda_{gas}Nu}{L_c}$	$Nu = 2 + \left(0.4Re^{\frac{1}{2}} + 0.06\,Re^{\frac{2}{3}}\right)Pr^{0.4}$	[38]
Effective diffusion coefficient D_{eff} (m^2·s^{-1})	$\frac{\varepsilon_{solid}}{\tau_{solid}}D_{H_2O-N_2}$	$D_{H_2O-N_2} = \frac{0.001T_{gas}^{1.75}\left(\frac{1}{M_{H_2O}}+\frac{1}{M_{N_2}}\right)^{\frac{1}{2}}}{P_{gas}\left((\Sigma v)_{H_2O}^{\frac{1}{3}}+(\Sigma v)_{N_2}^{\frac{1}{3}}\right)^2}$	[39]
Mass transfer coefficient h_m (m·s^{-1})	$\frac{D_{H_2O-N_2}Sh}{L_c}$	$Sh = 2 + \left(0.4Re^{\frac{1}{2}} + 0.06Re^{\frac{2}{3}}\right)Sc^{0.4}$	[38]

Gas properties have a satisfactory accuracy while biomass and char properties as well as heat and mass transfer coefficients and kinetic parameters are estimated or calculated from empirical equations. Therefore, this low accuracy on the values used for calculations must be taken into account when analyzing the results obtained for characteristic times.

3. Results and Discussion

The experimental method used to demonstrate the influence of char preparation and biomass type involves various experimental devices at different scales. Therefore, it is necessary to look at the time scales of the phenomena involved in the process to determine its regime, i.e., chemical regime or regime led by heat or mass transfer. The analysis was conducted separately on pyrolysis and on gasification since these two steps were experimentally separated.

3.1. Characteristic Time Analysis

3.1.1. Analysis of Characteristic Times of the Pyrolysis Step

Characteristic times of the pyrolysis step are represented in Figure 3 for particle scale and for bed scale in the conditions of TGA, device M, and device P for a particle size below 200 µm. Results are shown as a function of temperature between 200 °C and 450 °C, i.e., in the range of temperature corresponding to biomass degradation, according to the literature [40].

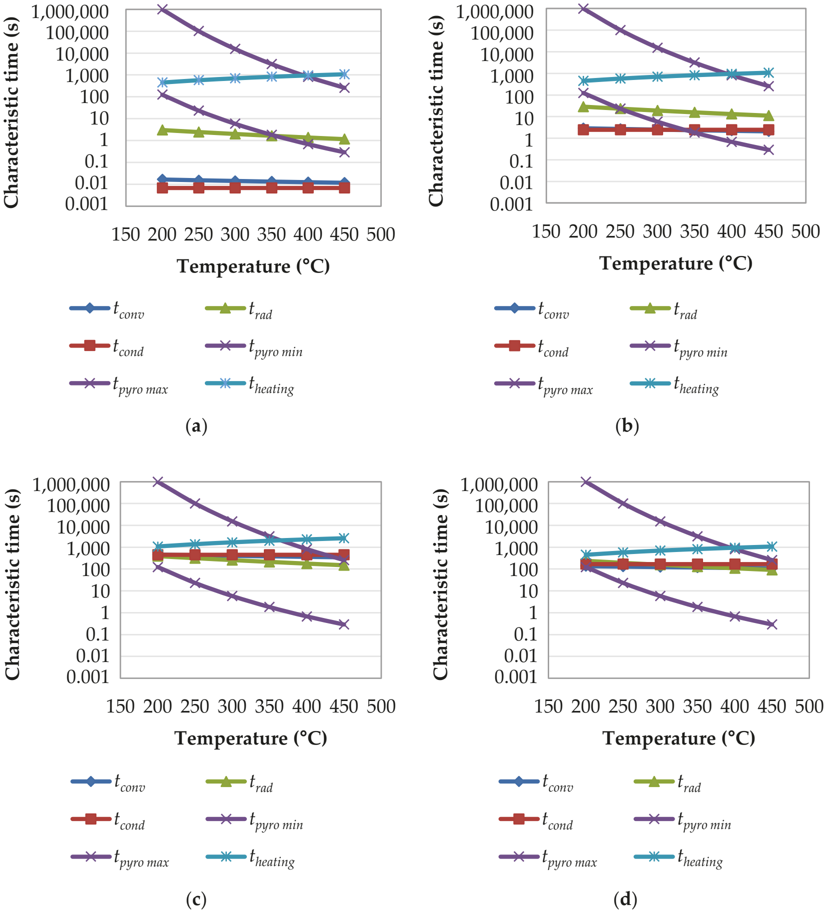

(**a**)

(**b**)

(**c**)

(**d**)

Figure 3. Characteristic times of the pyrolysis step as a function of temperature for: (**a**) particle scale in TGA conditions; (**b**) bed scale in TGA conditions; (**c**) bed scale in device M conditions; and (**d**) bed scale in device P condition. TGA: thermogravimetric analysis.

Calculations at particle scale were carried out for each of the three device conditions but results showed very negligible differences that were not noticeable through graphical representation. Therefore, only results obtained from TGA conditions are presented in this paper.

In all four cases, heating time and pyrolysis reaction times are the same except for heating time in device M conditions, but its variation is negligible. Only the three heat transfer characteristic times vary since they depend on the geometry of the system. Clearly, these characteristic times increase when the scale of the system—particle and beds of different sizes—increases.

When comparing heat transfers to the pyrolysis chemical reaction, it can be seen that their characteristic times are of the same order magnitude at least in part of the temperature range. This indicates that these phenomena occur simultaneously and none can be neglected.

Moreover, since pyrolysis was experimentally carried out in a dynamic mode, these times need to be compared with the heating time. For the phenomena to have enough time to occur, heating time should be higher than the phenomena characteristic times. In this study, heating times chosen for preparing the chars are of the same order of magnitude as the characteristic times of the phenomena involved.

In conclusion, characteristic time analysis shows that the pyrolysis step does not occur in a chemical regime. All phenomena occur simultaneously—none of them is negligible—and heating is too fast for the phenomena to occur.

Not being in a chemical regime during pyrolysis could result in chars that have different properties. Having different starting materials for gasification could, therefore, induce different kinetic behaviors. This is why it is important to check experimentally that chars produced under various conditions give the same gasification kinetics.

3.1.2. Analysis of Characteristic Times of the Gasification Step

Characteristic times of the gasification step are represented in Figure 4 for particle scale and bed scale under TGA conditions. Results are shown as a function of temperature between 500 °C and 1000 °C with the experimental study carried out at 800 °C in our study.

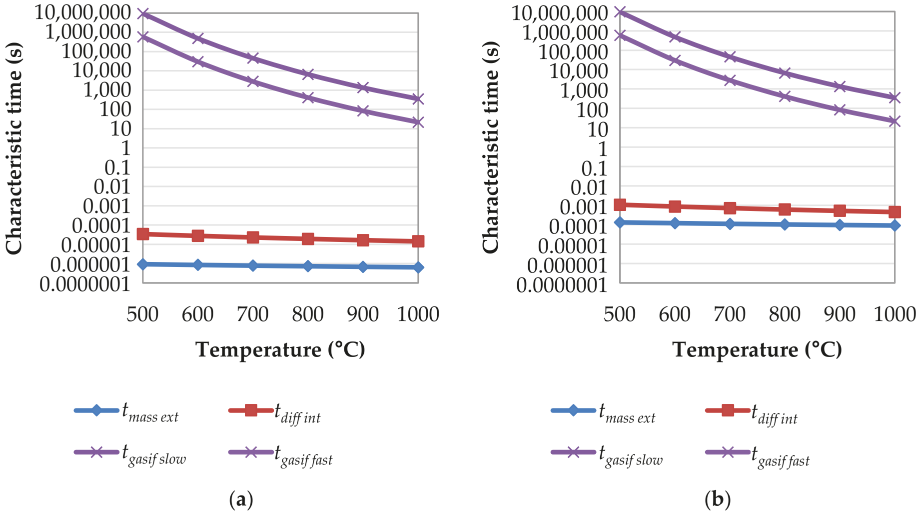

Figure 4. Characteristic times of the gasification step as a function of temperature for TGA conditions at: (**a**) particle scale and (**b**) bed scale.

At both scales, gasification chemical reactions with characteristic times remain the same. Mass transfer times slightly increase when the scale increases. However, at both scales and for both gasification kinetic laws, the gasification chemical reaction times are significantly higher—five to eight orders of magnitude—than mass transfer times. Therefore, according to time scales analysis, the gasification chemical reaction is the limiting phenomenon and mass transfers are negligible in comparison. The process occurs in the chemical regime.

This result is important since it means that kinetics obtained through TGA in these conditions should be intrinsic. According to this analysis, they exclusively represent the gasification chemical reaction without any bias from mass transfers.

However, Di Blasi's review [9] states that, even in TGA, typical operating condition mass transfers can have a non-negligible effect on char gasification. To verify this result experimentally for the conditions of the work presented in this study, gasification was carried out on different masses of the same char sample ranging from the full crucible (14 mg) to 3 mg. Only gasification of 4 mg or below showed the same kinetics. Higher masses of samples reacted more slowly, which indicated mass transfer limitations. These observations were close to previous results obtained on the same apparatus under similar conditions [12]. It shows the limits of characteristic time analysis, which relies on parameters known with limited accuracy.

3.2. Influence of Biomass Type

The influence of the biomass type on gasification kinetics was investigated through TGA of the biomass samples, i.e., preparation of char TGA and gasification of this char. Results from the mass loss as a function of time in these experiments are presented in Figure 5. Replicates are not shown in this paper but were carried out to ensure repeatability of the process, which was validated—variability can be seen in Figure 6 through error bars.

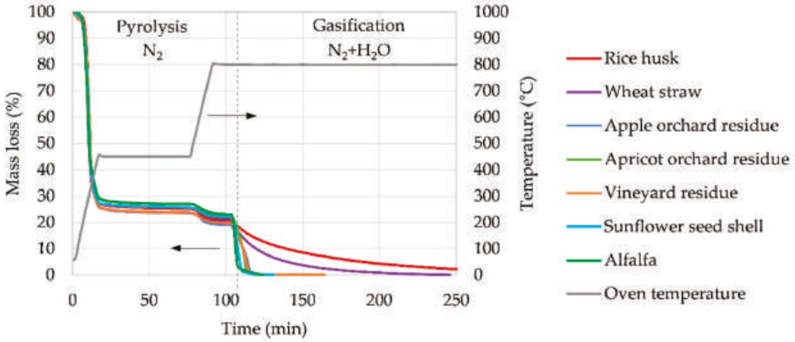

Figure 5. TGA of biomass samples presented as a mass loss and as a function of time. Pyrolysis: 0.05 L·min^{-1} N_2, 24 °C/minutes, 1 h hold at 450 °C, 15-min hold at 800 °C. Gasification: 0.05 L·min^{-1} mixture 80 vol % N_2/20 vol % H_2O, 800 °C.

It can be noted that mass loss profiles obtained during the pyrolysis of biomass samples are very similar.

The highest mass loss is observed for temperatures below 450 °C with approximately 75% of the mass volatilized. Subsequently, around 5% of the mass is lost between 450 °C and 800 °C. These yields align with results from literature [41]. They can be compared with char yields obtained after pyrolysis in other devices used for char preparation, which are gathered in Figure 6.

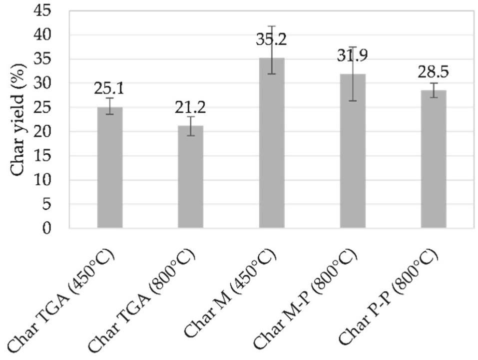

Figure 6. Char yield obtained in each char preparation condition (see Table 2).

There is a visible difference between values obtained at the thermo-balance scale and values obtained on devices M and P. This observation might be due to heat transfer limitations that are higher in the devices M and P, which are seen with characteristic times and can result in a lower solid conversion, i.e., a higher char yield. However, large scale values are close to what is expected for slow pyrolysis at pilot or industrial scale—35% char, 30% condensable products, and 35% non-condensable products [40,42].

The focus is made on the gasification step in Figure 7 and presented as a solid conversion and as a function of time.

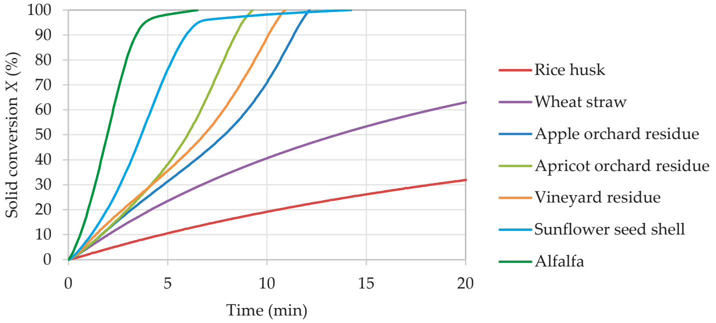

Figure 7. Solid conversion of biomass samples as a function of time during the gasification step (char TGA, 0.05 L·min^{-1} mixture 80 vol % N_2/20 vol % H_2O, 800 °C). Including data from Dupont et al. [28].

Three families of behavior can be identified, which is identified in literature [18]:

- Family 1 and its conversion rate is the highest and is constant and then increases such as in apple orchard residue, apricot orchard residue, and vineyard residue.
- Family 2 and its conversion rate is the slowest and is continuously decreasing such as in a rice husk and wheat straw.
- Family 3 and its conversion rate is intermediate and is constant and then decreases such as in sunflower seed shells and in alfalfa.

In addition, average reactivities of these biomass samples can be compared. Values of average reactivities between 1% and 80% conversion rates are gathered in Figure 8.

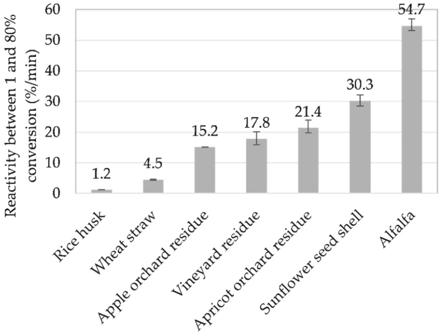

Figure 8. Gasification average reactivity between 1% and 80% conversion of biomass samples (char TGA, 0.05 L·min^{-1} mixture 80 vol % N_2/20 vol % H_2O, 800 °C).

Substantial variation between biomasses is noted due to a factor of almost 50 between average reactivities of rice husk—slowest sample to be gasified at 1.2%·min^{-1}—and alfalfa—fastest sample to be gasified at 54.7%·min^{-1}.

These results could be related to inorganic composition of biomass samples. Silica-rich samples tended to have lower reaction rates than silica-poor samples. Among the latter, the reaction rate tends to increase with increasing content of potassium, which is in accordance with literature [18,43]. Other physicochemical characterizations such as a surface area measurement or H and O quantification have not been performed in the present study and may bring a better understanding of the results.

3.3. Influence of Char Preparation

To investigate the influence of char preparation, steam gasification kinetics of chars prepared in different conditions were compared. To carry out this comparison, samples with extreme behaviors were selected from the study of biomass samples. Sunflower seed shells and alfalfa were chosen for their high reactivity, high potassium content, and low silicon content. The rice husk was chosen for its low reactivity, low potassium content, and high silicon content.

TGA of the gasification step was conducted on this chars selection. Results expressed in the form of solid conversion as a function of time are presented in Figure 9. Reactivities between 1% and 80% were derived from these results and are given in Figure 10.

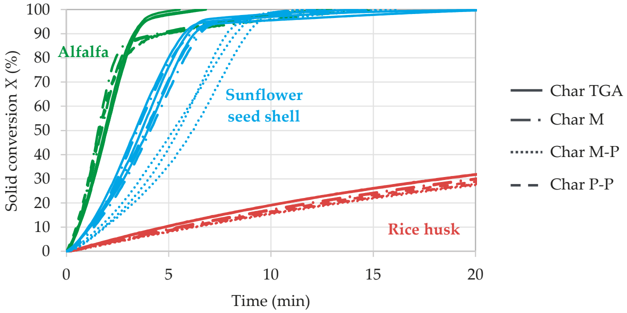

Figure 9. Solid conversion of chars as a function of time during gasification (0.05 L·min^{-1} mixture 80 vol % N_2/20 vol % H_2O, 800 °C).

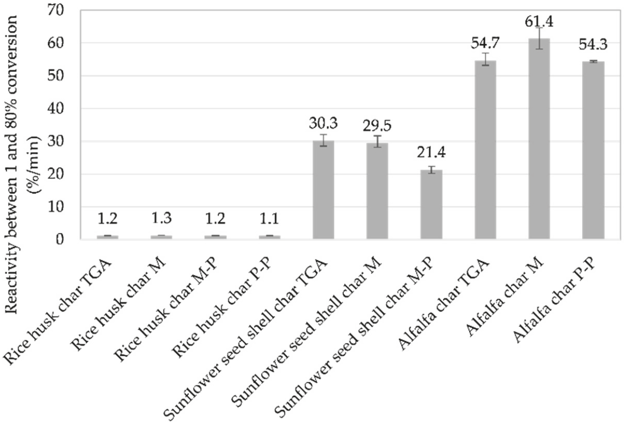

Figure 10. Gasification average reactivity between 1% and 80% conversion of biomass and char samples (see Table 2).

For each biomass, chars prepared in different conditions—in particular LHR pyrolysis conditions and not in a chemical regime—have the same reactivity during gasification. One exception for char M-P comes from the sunflower seed shells. No explanation was found regarding this result but it may be found by characterizing the chars. However, variations are negligible compared to differences that are observed between fast-reacting and slow-reacting biomass types. There is a factor of 1.2 in average between reactivities of the various char samples from each biomass, which is very low when compared to the factor of almost 50 calculated between reactivities of rice husk and alfalfa.

4. Conclusions

Thermogravimetric analysis (TGA) of biomass samples and of chars prepared from these biomasses in different LHR pyrolysis conditions outside the chemical regime showed that the biomass type has a significantly higher influence on steam gasification kinetics than char preparation conditions. In the range of the seven studied biomass samples, a factor of almost 50 was measured between average reactivities of the two samples with extreme behavior (rice husk with 1.2%·min^{-1} and alfalfa with 54.7%·min^{-1}). In comparison, chars prepared in conditions outside the chemical regime from various amounts of biomass depending on the crucible geometry (height and surface) and several working temperatures (450 °C or 800 °C in one or two steps) showed a much lower difference with an average factor of 1.2 for a given biomass type.

The influence of biomass type could be assumed to be related to inorganic content of the biomass as opposed to its molecular constituents—lignin, hemicellulose, cellulose. This assumption is supported by literature data. However, further investigations are in progress and consist of physicochemical characterization of chars from different biomass samples. It will confirm if inorganic composition is the main influential parameter or if it should rather be explained by structural or textural properties of the char.

Author Contributions: Conceptualization, F.D., M.C., S.B., M.J. and C.D. Investigation, T.D., S.T. and M.G. Formal Analysis, T.D. Resources, M.C. Writing-Original Draft Preparation, T.D. Writing-Review & Editing, F.D., M.J. and C.D. Supervision, F.D., M.J. and C.D.

Funding: This research was funded by the Agence de l'Environnement et de la Maîtrise de l'Energie.

Conflicts of Interest: The authors declare no conflict of interest.

Nomenclature

$c_{p\ solid}$	(J·kg^{-1}·K^{-1})	Specific heat of the solid phase (bed or particle)
d_p	(m)	Particle diameter
D_c	(m)	Diameter of the cylindrical bed
D_{eff}	(m^2·s^{-1})	Effective diffusion coefficient
$D_{H2O\text{-}N2}$	(m^2·s^{-1})	Diffusion coefficient of the mixture N_2-H_2O
h_m	(m·s^{-1})	External mass transfer coefficient
h_t	(W·m^{-2}·K^{-1})	Heat transfer coefficient
H_c	(m)	Height of the cylindrical bed
k_{gasif}	(s^{-1})	Kinetic constant of the gasification reaction
k_{pyro}	(s^{-1})	Kinetic constant of the pyrolysis reaction
M_{H2O}	(kg·mol^{-1})	Molecular weight of water
M_{N2}	(kg·mol^{-1})	Molecular weight of nitrogen
Nu	(–)	Nusselt number
P_{H2O}	(Pa)	Partial pressure of steam
P_{gas}	(Pa)	Pressure of the gas
Pr	(–)	Prandtl number
r	(s^{-1})	Gasification rate
$r_{heating}$	(K·s^{-1})	Heating rate
R	(J·mol^{-1}·K^{-1})	Universal gas constant
Re	(–)	Reynolds number
Sc	(–)	Schmidt number
Sh	(–)	Sherwood number
t_{cond}	(s)	Internal heat conduction time
t_{conv}	(s)	External heat convection time
$t_{diff\ int}$	(s)	Characteristic time of internal mass diffusion
t_{gasif}	(s)	Characteristic time of the gasification chemical reaction
$t_{heating}$	(s)	Heating time
$t_{mass\ ext}$	(s)	Characteristic time of external mass transfer
t_{pyro}	(s)	Characteristic time of the pyrolysis chemical reaction
t_{rad}	(s)	External radiation time
T_{gas}	(K)	Gas temperature
T_{solid}	(K)	Solid (bed or particle) temperature
X	(–)	Solid conversion
ε_{solid}	(–)	Porosity of the solid phase (bed or particle)
λ_{gas}	(W·m^{-1}·K^{-1})	Thermal conductivity of the gas phase
λ_{solid}	(W·m^{-1}·K^{-1})	Thermal conductivity of the solid phase (bed or particle)
ρ_{solid}	(kg·m^{-3})	Density of the solid phase (bed or particle)
σ	(W·m^{-2}·K^{-4})	Boltzmann constant
$(\Sigma v)_{H2O}$	(m^3·mol^{-1})	Diffusion volume of H_2O
$(\Sigma v)_{N2}$	(m^3·mol^{-1})	Diffusion volume of N_2
τ_{solid}	(–)	Tortuosity of the solid phase (bed or particle)
ω_{solid}	(–)	Emissivity of the biomass

References

1. Kumar, A.; Jones, D.D.; Hanna, M.A. Thermochemical Biomass Gasification: A Review of the Current Status of the Technology. *Energies* **2009**, *2*, 556–581. [CrossRef]
2. Bartocci, P.; Zampilli, M.; Bidini, G.; Fantozzi, F. Hydrogen-rich gas production through steam gasification of charcoal pellet. *Appl. Therm. Eng.* **2018**, *132*, 817–823. [CrossRef]
3. Luo, S.; Xiao, B.; Guo, X.; Hu, Z.; Liu, S.; He, M. Hydrogen-rich gas from catalytic steam gasification of biomass in a fixed bed reactor: Influence of particle size on gasification performance. *Int. J. Hydrog. Energy* **2009**, *34*, 1260–1264. [CrossRef]

4. Yan, F.; Luo, S.; Hu, Z.; Xiao, B.; Cheng, G. Hydrogen-rich gas production by steam gasification of char from biomass fast pyrolysis in a fixed-bed reactor: Influence of temperature and steam on hydrogen yield and syngas composition. *Bioresour. Technol.* **2010**, *101*, 5633–5637. [CrossRef] [PubMed]
5. Rafati, M.; Wang, L.; Dayton, D.C.; Schimmel, K.; Kabadi, V.; Shahbazi, A. Techno-economic analysis of production of Fischer-Tropsch liquids via biomass gasification: The effects of Fischer-Tropsch catalysts and natural gas co-feeding. *Energy Convers. Manag.* **2017**, *133*, 153–166. [CrossRef]
6. Snehesh, A.S.; Mukunda, H.S.; Mahapatra, S.; Dasappa, S. Fischer-Tropsch route for the conversion of biomass to liquid fuels—Technical and economic analysis. *Energy* **2017**, *130*, 182–191. [CrossRef]
7. Chiodini, A.; Bua, L.; Carnelli, L.; Zwart, R.; Vreugdenhil, B.; Vocciante, M. Enhancements in Biomass-to-Liquid processes: Gasification aiming at high hydrogen/carbon monoxide ratios for direct Fischer-Tropsch synthesis applications. *Biomass Bioenergy* **2017**, *106*, 104–114. [CrossRef]
8. Dupont, C.; Boissonnet, G.; Seiler, J.-M.; Gauthier, P.; Schweich, D. Study about the kinetic processes of biomass steam gasification. *Fuel* **2007**, *86*, 32–40. [CrossRef]
9. Di Blasi, C. Combustion and gasification rates of lignocellulosic chars. *Prog. Energy Combust. Sci.* **2009**, *35*, 121–140. [CrossRef]
10. Ballerini, D.; Alazard-Toux, N. *Les Biocarburants*; Editions Technip: Paris, France, 2006; ISBN 978-2-7108-0969-2.
11. Guerrero, M.; Ruiz, M.P.; Millera, Á.; Alzueta, M.U.; Bilbao, R. Oxidation Kinetics of Eucalyptus Chars Produced at Low and High Heating Rates. *Energy Fuels* **2008**, *22*, 2084–2090. [CrossRef]
12. Dupont, C.; Nocquet, T.; Da Costa, J.A.; Verne-Tournon, C. Kinetic modelling of steam gasification of various woody biomass chars: Influence of inorganic elements. *Bioresour. Technol.* **2011**, *102*, 9743–9748. [CrossRef] [PubMed]
13. Vassilev, S.V.; Baxter, D.; Andersen, L.K.; Vassileva, C.G. An overview of the chemical composition of biomass. *Fuel* **2010**, *89*, 913–933. [CrossRef]
14. Feng, D.; Zhao, Y.; Zhang, Y.; Xu, H.; Zhang, L.; Sun, S. Catalytic mechanism of ion-exchanging alkali and alkaline earth metallic species on biochar reactivity during CO_2/H_2O gasification. *Fuel* **2018**, *212*, 523–532. [CrossRef]
15. Jiang, L.; Hu, S.; Wang, Y.; Su, S.; Sun, L.; Xu, B.; He, L.; Xiang, J. Catalytic effects of inherent alkali and alkaline earth metallic species on steam gasification of biomass. *Int. J. Hydrog. Energy* **2015**, *40*, 15460–15469. [CrossRef]
16. Kajita, M.; Kimura, T.; Norinaga, K.; Li, C.Z.; Hayashi, J.I. Catalytic and noncatalytic mechanisms in steam gasification of char from the pyrolysis of biomass. *Energy Fuels* **2009**, *24*, 108–116. [CrossRef]
17. Lahijani, P.; Zainal, Z.A.; Mohamed, A.R.; Mohammadi, M. CO_2 gasification reactivity of biomass char: Catalytic influence of alkali, alkaline earth and transition metal salts. *Bioresour. Technol.* **2013**, *144*, 288–295. [CrossRef] [PubMed]
18. Dupont, C.; Jacob, S.; Marrakchy, K.O.; Hognon, C.; Grateau, M.; Labalette, F.; Da Silva Perez, D. How inorganic elements of biomass influence char steam gasification kinetics. *Energy* **2016**, *109*, 430–435. [CrossRef]
19. Kannan, M.P.; Richards, G.N. Gasification of biomass chars in carbon dioxide: dependence of gasification rate on the indigenous metal content. *Fuel* **1990**, *69*, 747–753. [CrossRef]
20. Cuervo, N.; Dufaud, O.; Torrado, D.; Bardin-Monnier, N.; Perrin, L.; Laurent, A. Experimental study and modeling of the pyrolysis of organic dusts: application to dust explosions. *Chem. Eng. Trans.* **2013**, 931–936. [CrossRef]
21. Dufour, A.; Ouartassi, B.; Bounaceur, R.; Zoulalian, A. Modelling intra-particle phenomena of biomass pyrolysis. *Chem. Eng. Res. Des.* **2011**, *89*, 2136–2146. [CrossRef]
22. Gómez-Barea, A.; Leckner, B. Modeling of biomass gasification in fluidized bed. *Prog. Energy Combust. Sci.* **2010**, *36*, 444–509. [CrossRef]
23. Palumbo, A.W.; Weimer, A.W. Heat transfer-limited flash pyrolysis of woody biomass: Overall reaction rate and time analysis using an integral model with experimental support. *J. Anal. Appl. Pyrolysis* **2015**, *113*, 474–482. [CrossRef]
24. Septien, S.; Valin, S.; Dupont, C.; Peyrot, M.; Salvador, S. Effect of particle size and temperature on woody biomass fast pyrolysis at high temperature (1000–1400 °C). *Fuel* **2012**, *97*, 202–210. [CrossRef]

25. Martinez, M.G.; Dupont, C.; Thiery, S.; Meyer, X.M.; Gourdon, C. Characteristic time analysis of biomass torrefaction phenomena—Application to thermogravimetric analysis device. *Chem. Eng. Trans.* **2016**, *50*, 61–66. [CrossRef]
26. European Standards. Solid Biofuels—Determination of Ash Content (EN 14775). Available online: https://www.google.com.tw/url?sa=t&rct=j&q=&esrc=s&source=web&cd=1&ved=2ahUKEwjPrM-E1t_cAhVWfd4KHUe6BNIQFjAAegQIABAC&url=https%3A%2F%2Fwww.researchgate.net%2Fprofile%2FAlain_Celzard%2Fpost%2FWhich_ASTM_standard_should_I_refer_to_in_order_to_determine_the_moisture_and_volatiles_content_in_biomass%2Fattachment%2F59d62117c49f478072e9848e%2FAS%253A271759398375424%25401441803897376%2Fdownload%2FSolid%2Bbiofuels%2B-%2BDetermination%2Bof%2Bash%2Bcontent.pdf&usg=AOvVaw0FjluSmH5RWZsNzKmNjEL_ (accessed on 11 June 2018).
27. International Organization for Standardization. Solid Biofuels—Determination of Major Elements—Al, Ca, Fe, Mg, P, K, Si, Na and Ti (ISO 16967: 2015). Available online: https://www.iso.org/standard/58065.html (accessed on 11 June 2018).
28. Dupont, C.; Karakashov, B.; Dahou, T.; Martinez, M.G.; Saavedra, C.; Da Silva Perez, D.; Karakasova, L. Quality of agricultural waste from orchards and vineyards as feedstock for thermal processes with focus on torrefaction and gasification. *Biomass Bioenergy* **2018**. submitted.
29. Villermaux, J.; Antoine, B. Pyrolyse éclair de solides divisés dans un réacteur continu: 1. Un nouveau modèle de volatilisation thermique de particules solides. *Rev. Générale Therm.* **1980**, *227*, 851–860.
30. Di Blasi, C. Modeling chemical and physical processes of wood and biomass pyrolysis. *Prog. Energy Combust. Sci.* **2008**, *34*, 47–90. [CrossRef]
31. Nunn, T.R.; Howard, J.B.; Longwell, J.P.; Peters, W.A. Product compositions and kinetics in the rapid pyrolysis of sweet gum hardwood. *Ind. Eng. Chem. Process Des. Dev.* **1985**, *24*, 3. [CrossRef]
32. Samolada, M.C.; Vasalos, I.A. A kinetic approach to the flash pyrolysis of biomass in a fluidized bed reactor. *Fuel* **1991**, *70*, 883–889. [CrossRef]
33. Brewer, C.E.; Chuang, V.J.; Masiello, C.A.; Gonnermann, H.; Gao, X.; Dugan, B.; Driver, L.E.; Panzacchi, P.; Zygourakis, K.; Davies, C.A. New approaches to measuring biochar density and porosity. *Biomass Bioenergy* **2014**, *66*, 176–185. [CrossRef]
34. Johnsson, J.E.; Jensen, A. Effective diffusion coefficients in coal chars. *Proc. Combust. Inst.* **2000**, *28*, 2353–2359. [CrossRef]
35. Dalloz-Dubrujeaud, B.; Faure, R.; Tadrist, L.; Giraud, G. Perte de pression et vitesse minimum de fluidisation dans un lit de particules 2D. *Comptes Rendus l'Académie Sci.-Ser. IIB-Mech. Phys. Astron.* **2000**, *328*, 231–236. [CrossRef]
36. Dupont, C.; Chiriac, R.; Gauthier, G.; Toche, F. Heat capacity measurements of various biomass types and pyrolysis residues. *Fuel* **2014**, *115*, 644–651. [CrossRef]
37. Perry, R.H.; Green, D.W. *Perry's Chemical Engineers' Handbook*; McGraw-Hill: London, UK, 1998; ISBN 978-0-07-115982-1.
38. Whitaker, S. Forced convection heat transfer correlations for flow in pipes, past flat plates, single cylinders, single spheres, and for flow in packed beds and tube bundles. *AIChE J.* **1972**, *18*, 361–371. [CrossRef]
39. Fuller, E.N.; Schettler, P.D.; Giddings, J.C. New method for prediction of binary gas-phase diffusion coefficients. *Ind. Eng. Chem.* **1966**, *58*, 18–27. [CrossRef]
40. Kan, T.; Strezov, V.; Evans, T.J. Lignocellulosic biomass pyrolysis: A review of product properties and effects of pyrolysis parameters. *Renew. Sustain. Energy Rev.* **2016**, *57*, 1126–1140. [CrossRef]
41. Anca-Couce, A. Reaction mechanisms and multi-scale modelling of lignocellulosic biomass pyrolysis. *Prog. Energy Combust. Sci.* **2016**, *53*, 41–79. [CrossRef]
42. Deglise, X.; Donnot, A. Bois énergie—Propriétés et voies de valorisation. *Tech. Ing. Énerg. Renouvelables* **2017**. Available online: https://www.techniques-ingenieur.fr/base-documentaire/energies-th4/energies-renouvelables-42594210/bois-energie-be8535/ (accessed on 11 June 2018).
43. Zhang, Y.; Ashizawa, M.; Kajitani, S.; Miura, K. Proposal of a semi-empirical kinetic model to reconcile with gasification reactivity profiles of biomass chars. *Fuel* **2008**, *87*, 475–481. [CrossRef]

energies

MDPI

Article

Possible Interactions and Interferences of Copper, Chromium, and Arsenic during the Gasification of Contaminated Waste Wood †

Shurooq Badri Al-Badri [1,2], Ying Jiang [1] and Stuart Thomas Wagland [1,*]

[1] School of Water, Energy, and Environment, Cranfield University, Cranfield MK43 0AL, UK; s.b.albadri@cranfield.ac.uk (S.B.A.-B.); y.jiang@cranfield.ac.uk (Y.J.)
[2] Department of Chemistry, College of Science, University of Baghdad, Baghdad 10071, Iraq
* Correspondence: s.t.wagland@cranfield.ac.uk; Tel.: +44(0)-1234-750-111

† This paper is an extended version of our paper published in the 9th International Renewable Energy Congress (IREC), Hammamet, Tunisia, 20–22 March 2018.

Received: 3 July 2018; Accepted: 25 July 2018; Published: 28 July 2018

Abstract: A considerable proportion (about 64%) of biomass energy is produced from woody biomass (wood and its wastes). However, waste wood (WW) is very often contaminated with metal(loid) elements at concentrations leading to toxicity emissions and damages to facilities during thermal conversion. Therefore, procedures for preventing and/or alleviating the negative impacts of these elements require further development, particularly by providing informative and supportive information regarding the phase transformations of the metal(loid)s during thermal conversion processes. Although it is well known that phase transformation depends on different factors such as elements' vaporization characteristics, operational conditions, and process configuration; however, the influences of reaction atmosphere composition in terms of interactions and interferences are rarely addressed. In response, since Cu, Cr, and As (CCA-elements) are the most regulated elements in woody biomass, this paper aims to explore the possible interactions and interferences among CCA-elements themselves and with Ca, Na, S, Cl, Fe, and Ni from reaction atmosphere composition perspectives during the gasification of contaminated WW. To do so, thermodynamic equilibrium calculations were performed for Boudouard reaction (BR) and partial combustion reaction (PCR) with temperature ranges of 0–1300 °C and 0–1800 °C, respectively, and both reactions were simulated under pressure conditions of 1, 20, and 40 atm. Refinement of the occurred interactions and interferences reveals that Ni-As interactions generate dominant species As_2Ni_5 and As_8Ni_{11}, which increase the solid–gaseous transformation temperature of As. Moreover, the interactions between Ca and Cr predominantly form C_3Cr_7; whereas the absence of Ca leads to $Cr_2Na_2O_4$ causing instability in the Cr phase transformation.

Keywords: waste wood; interactions; interferences; partial combustion reaction in gasification; Boudouard reaction in gasification; MTDATA

1. Introduction

Waste wood (WW) is the term used for wood material that has previously been used for various purposes and is now being treated as a waste material; in the context of this study the waste wood is being utilized for energy production [1]. It comprises a wide variety of wood materials primarily from industrial and commercial activities and from construction and demolition operations [2,3]. Since it is collected from diverse sources, WW may contain both physical and chemical contaminants [1,4]. Physical contaminates can simply be separated by sorting or using mechanical techniques. However, the majority of chemical contaminants are usually linked to the metal(loid) elements contained in wood that has been treated with preservatives, paintings, coatings, and other related activities, and, of course, mechanical separation is not applicable.

Essentially, gasification process involves the conversion of solid carbonaceous fuels into combustible gases composed of a mixture of N_2, H_2O, CH_4, H_2, CO_2, CO, and very small quantities of low molecular weight hydrocarbons and contaminants including ash, tar, and carbon particles [5,6]. In general, biomass gasification consists of four processing steps: drying, pyrolysis of dried biomass particles (de-volatilization), partial oxidation of pyrolysis gases and/or char, and char gasification (reduction) [7], as depicted in Figure 1 [8]. Technically, gasification is an exothermic partial oxidation of biomass operating at high temperatures between 800 and 1300 °C with the presence of gasifying mediums such as carbon dioxide, steam, and air (or a mixture of air and steam) [7,9–11]. Further, the compositions and properties of the gasification products vary according to the operational conditions, gasifier type, and biomass materials.

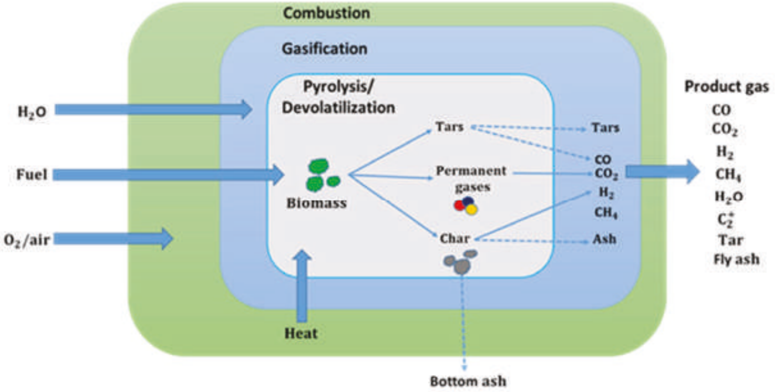

Figure 1. Schematic of the processes in a typical gasifier.

Currently, because of its efficiency and flexibility [12], gasification is vastly employed for generating renewable energy and waste disposal. However, when conducting gasification, metal(loid)s in biomass can cause severe human health and environmental problems as well as significant technical damages when they present at high concentrations. Hence, to avoid and/or limit the risks of metal(loid) elements, the transformation behaviours of these elements across the different phases require further investigating.

A range of studies [13–17] have focused on the distribution of the metal(loid)s between gaseous and solid phases during gasification. These studies report that the partitioning of metal(loid) elements can be directly influenced by a combination of several factors such as feedstock characteristics, operational conditions, and process agents. In fact, phase transformation temperatures of metal(loid)s cannot be accurately determined using traditional analytical tools/instruments because the generated species cannot be easily identified, and hence measured. As such, the mass distribution of metal(loid) elements during gasification is a quite complex problem. Fortunately, thermodynamic equilibrium modelling based on Gibbs energy minimization has effectively been used for yielding the best predictions of the behaviours of metal(loid) elements, and in turn allowing for precise evaluation of the speciation during the thermochemical processes [18–25].

Jiang et al. [18] studied the solid–gaseous transition of Zn, Pb, Ni, Mn, Mg, Fe, Cu, Cr, Co, Cd, As, and Al in five biomass samples during typical gasification scenarios. This study reports that the most volatilized elements are As, Cd, Pb, and Zn, whereas Cu, Co, Ni, and Mn are moderately volatilized, and the phase transformation temperatures of Mg, Fe, Cr, and Al are > 1200 °C. Froment et al. [19] assessed the volatilization and condensation of certain elements in woody biomass during gasification with temperatures ranging from 500 to 1500 °C, and pressure conditions from 1 to 10 bar. The calculation results showed that Zn, Pb, Se, Sb, S, N, Hg, F, Cd, and Cl completely volatilized as either elemental or species, whereas, Ca, Si, Al, P, Cu, Mn, Ti, Fe, Cr, Mg, and Ba remained as oxides in the condensed phase, except copper which condensed as Cu_3As. Kramb et al. [20] modelled the behavior of As during the gasification of CCA-treated wood, and reported that about 99.6% of As can be captured. Thompson and Argent [21] categorized the trace elements in a PRENLFO gasifier into "virtually immobile (Cr, Ba, Ni, V), somewhat mobile (Mo, Be, Cu), mobile (Sb, B) and almost totally mobilized (As, Cd, Pb, Sn, Zn)". Kilgallon et al. [22] investigated the impacts of both pressure conditions and chlorine/sulphur on element phase transitions. Reed et al. [23] reported the speciation prediction of Cd, As, B, Co, Be, Pb, Cu, Sb, V, Sn, and Zn in fuel gas from a gasifier. They explicitly partitioned these elements into three groups: condensed phase (Cu, Be, V, Zn and Co; at $T_{50} \gg 900$ K), gas phase (As without Ni, B without Ca, Sb, and Sn), and condensed phase (As with Ni, B with Ca, Cd, and Pb; at $T_{50} < 900$ K). Liu et al. [24] also reported the speciation of Ni, As, Pb, Cd, Se, and Sb during underground coal gasification with specific agent injection and pressure. A study by Bradshaw et al. [25] showed that the elements Hg, As, Pb, Sb, Cd, Sn, Se, and Te, and alkali metals remained in fuel gas, and the species of Pb, Sb, and Cd can pass through the path of fuel gas forming surface deposits.

Although the modelling of phase transformation yields beneficial information (e.g., elemental vaporization and condensation, optimized operational conditions) about the distribution of metal(loid) elements, factors including the interactions and interferences among these elements cannot be ignored. In particular, metal(loid)s can interact and/or interfere, leading to the generation of new species, which may induce remarkable influence on the volatilization of metal(loid)s. At present, to the best of the authors' knowledge, there has been no single study towards the assessment of occurred interferences between metal(loid)s during thermochemical processes. In fact, only a study by K. Svoboda [26] investigated the instantaneous interferences of both HF and HCl on H_2S sorption. Also, two studies evaluated the effect of interactions on elemental behaviour during coal combustion. Contreras et al. [27] evaluated the interactions between Cd, As, Sb, and Hg, and pointed out that some species can be dominant under specific conditions. For example, As-Cd interaction forms $Cd_3(AsO_4)_2$, which reduces the concentration of gaseous oxides. Yan et al. [28] showed that interactions among Se, Hg, and As lead to the generation of HgSe (g) and AsSe (g) as dominant species under reduced conditions.

In this paper, thermodynamic equilibrium calculations were carried out to explore the possible interactions and interferences between Cu, Cr, and As (CCA-elements) themselves and with Ca, Na, S, Cl, Fe, and Ni in contaminated WW during two reactions of gasification: Boudouard reaction (BR) and partial combustion reaction (PCR). The calculations were performed using MTDATA software (Version 5.10, NPL, London, UK) to predict the phase transformation temperatures and speciation of the considered metal(loid)s. Moreover, contaminated WW samples with complete composition data were selected from the ECN PHYLLIS2 database [29] for the modelling.

2. Thermodynamic Equilibrium Modelling

Thermodynamic equilibrium modellings for Boudouard reaction (BR) and partial combustion reaction (PCR) were carried out using the multiphase module of the MTDATA software coupled with the Scientific Group Thermodata Europe (SGTE) database. With each modelling, the calculations were conducted to study the effects of the occurred interactions and interferences on the fate of the

CCA-elements as consequence of different contents of CCA-elements and of Ca, Na, S, Cl, Fe, and Ni in WW samples.

For model simulations, a primary search of the SGTE database was carried out to reveal the relevant species of CCA-elements. A complete list of the adopted species are given in Table 1. The best fit probability distributions of the composition data of the selected WW samples (#2712, #679, #1779, #1364, #871, #1448, #3498, #2901, #2900) [29] are estimated through the @Risk analysis simulation package (Version 6.1, Palisade Corp., Ithaca, NY, USA), and the estimation results are exhibited in Table 2. As an illustrative example, the statistical analysis of the moisture content is demonstrated in Figure 2. The elements to be introduced to the MTDATA were grouped into major elements (Ar, C, N, O, and H) and minor elements (As, Cr, Cu, Co, Cl, Ca, Ni, S, Na, and Fe). Note that the mass ranges of the minor elements, Table 3, were assumed inconsistent with the information provided by the ECN PHYLLIS2 database [29] concerning the contaminated woody biomass.

Table 1. The selected Cu, Cr, and As (CCA-elements) species.

Species	As	Cr	Cu
Gaseous	As_4O_{10}, AsS, $As_4S_4AsH_2$, AsH_3, As_4O_8, As, As_2, AsN, AsO, AsO_2, $AsCl_3$, AsH, As_4O_6, As_4O_7, As_3, As_4O_9.	ClCr, CrHO, $CrHO_2CrHO_3$, CrH_2O_2, CrH_2O_3, Cl_4Cr, Cl_5Cr, Cl_6Cr, ClCrO, CrH_2O_4, CrH_3O_3, Cl_4CrO, Cr, Cr_2, CrH, CrH_3O_4, CrH_4O_4, Cl_2Cr, Cl_3Cr, CrO_2, CrO_3, Cr_2O, $ClCrO_2$, Cl_2CrO, Cl_2CrO_2, Cl_3CrO, CrS_2, CrH_4O_5, CrN, CrO, Cr_2O_2, Cr_2O_3, CrS.	Cl_5Cu_5, Cu, Cl_3Cu_3, Cl_4Cu_2, CuO, CuS, ClCu, Cu_2S, Cu_2, CuH, CuHO, Cl_2Cu, Cl_2Cu_2, Cl_4Cu_4.
Liquid	$AsCL_3$, As_4S_4.	-	-
Solid	As, $As_2Cu_3O_8$, As_2Fe_3O, As_2S_2, $AsNa_3$, $AsCu_3$, $As_2Ca_3O_8$, $As_2Co_3O_8$, $AsNa_3O_4$, AsNi, As_2Ni_5, As_8Ni_{11}, $AsCrO_4$, $As_2Cr_3O_8$, AsS, $AsCu_3O_4$, $As_2Ni_3O_8$, As_2O_5, As_2S_3, $AsFeO_4$.	$AsCrO_4$, Cl_3Cr, $CoCr_2O_4$, Cr, $Cr_2O_{12}S_3$, CrS, $CaCrO_3$, $CaCr_2O_4$, Cl_2Cr, Cr_2O_3, Cr_5O_{12}, Cr_8O_{21}, $CrNa_2O_4$, $Cr_2Na_2O_4$, $As_2Cr_3O_8$, C_2Cr_3, C_3Cr_7, C_6Cr_{23}, C_6CrO_6, Cr_2FeO_4, CrN, Cr_2N, Cr_2NiO_4, CrO_2, CrO_3.	CuH_6O_7S, $CuH_{10}O_9S$, CuO, Cu_2O, CuO_4S, Cu_2O_4S, Cu_2O_5S, CuS, Cu_2S, $AsCu_3$, $AsCu_3O_4$, $As_2Cu_3O_8$, CCuN, $CCuO_3$, CaCu, Ca_2CuO_3, ClCu, Cl_2Cu, Cu, $CuFeO_2$, $CuFe_2O_4$, $Cu_2Fe_2O_4$, $CuFeS_2$, Cu_5FeS_4, $CaCu_5$, Ca_2Cu, $CaCu_2O_3$, CuH_2O_2, CuH_2O_5S.

Table 2. Statistical analysis results of the composition data.

Composition	Min	Mean	Max	5%	95%
Moisture content (Ar) (%)	4.68	14.86	33	3.82	27.31
Ash content (Ar) (%)	0.79	12.09	70.41	0.843	48.54
Carbon (C) (Dry) (%)	43.31	46.55	49.8	42.84	50.24
Hydrogen (H) (Dry) (%)	5.26	5.69	5.93	5.26	5.95
Nitrogen (N) (Dry) (%)	0.19	1.06	1.93	0.069	2.04
Oxygen (O) (Dry) (%)	37.13	40.57	55.79	37.3	47.34
Sulphur (S) (Dry) (%)	0.03	0.09	0.18	0.02489	0.176
Chlorine (Cl) (Dry) (mg/kg)	113	556.49	1000	48.19	1077.8
Copper (Cu) (Dry) (mg/kg)	4.8	63.64	385	5.04	286.8
Nickel (Ni) (Dry) (mg/kg)	2.8	15.69	46	2.19	43.99
Arsenic (As) (Dry) (mg/kg)	1.3	5.5	13	1.35	35.45
Cobalt (Co) (Dry) (mg/kg)	0.8	4.88	25	84%	21.92
Chromium (Cr) (Dry) (mg/kg)	21	30.2	37	21.73	36.87
Sodium (Na) (Dry) (mg/kg)	210	703.92	1613	162.0	1645.5
Calcium (Ca) (Dry) (mg/kg)	2200	4061.41	6537	2247.0	8959.29
Iron (Fe) (Dry) (mg/kg)	340.3	655.96	1082	348.16	2037.09

Table 3. Mass ranges of minor elements.

Element	Concentration (mole/h)	Element	Concentration (mole/h)	Element	Concentration (mole/h)
As	0, 0.7, 1.4, 5	Ca	0, 100, 250, 500, 1000	Ni	0, 5, 10, 20
Cu	0, 4, 6, 8	Cl	0, 10, 50, 100	Na	0, 100, 200, 500
Cr	0, 5, 10, 21	Fe	0, 50, 100, 500	S	0, 0.05, 0.1, 0.2

Moreover, the operational conditions and process agents for each reaction are presented in Table 4, in which the required oxygen for PCR and the required carbon dioxide for BR are determined using Equation (1) [30] and Equation (2) [7], respectively, as follows:

$$C + 0.5O_2 \rightarrow CO, \tag{1}$$

$$C + CO_2 \rightleftarrows 2CO. \tag{2}$$

Note that the air composition (under standard dry at atmospheric pressure) consists of 1.28% Ar, 23.2% O_2, 0.046% CO_2, and 75.47% N_2. Biomass feed rates for both reactions were calculated by means of the higher heating value (HHV_d) from Equation (3) [30].

$$HHV_d = 0.3491C + 1.1783H + 0.1005S - 0.015N - 0.1034O - 0.0211Ash. \tag{3}$$

Table 4. Operational parameters and gasification agents for partial combustion reaction (PCR) and Boudouard reaction (BR).

Parameter	PCR	BR
Temperature range (°C)	0–1800	0–1300
Pressure (atm)	1	1
Equivalence ratio (kg/h)	0.2	0
Biomass rate (m^3/h)	3.59	3.59
Air rate (m^3/h)	0.72	-
Steam rate	1.44	-
Steam/Air	2:1	-
CO_2	-	1.19
CO_2/Biomass	-	1:3

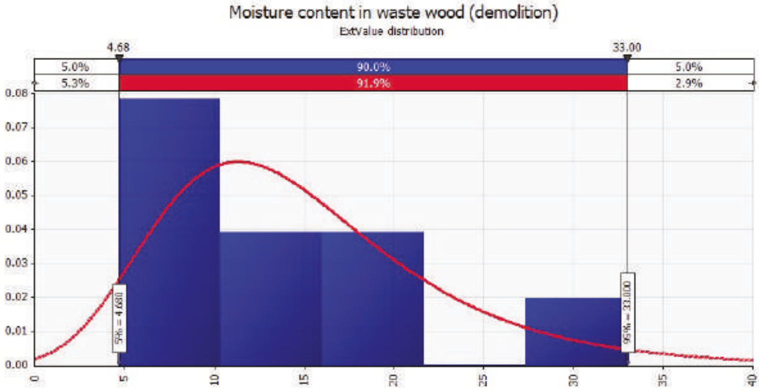

(**a**)

Figure 2. *Cont.*

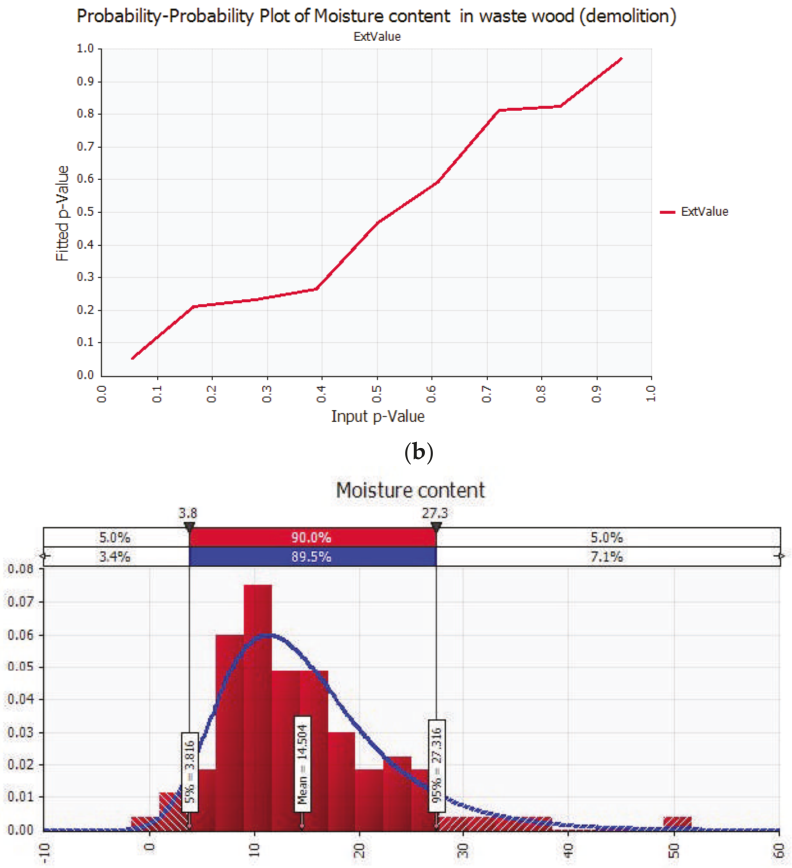

(**b**)

(**c**)

Figure 2. (**a**) Probability distribution of moisture content; (**b**) *p*-value; and (**c**) interval confidence of probability distribution.

3. Results and Discussion

3.1. Under Partial Combustion Reaction (PCR)

3.1.1. Equilibrium Composition of CCA-Elements

Initially, the modelling of PCR was based on composition data in Table 2 (the mean values) and process parameters of PCR in Table 4 in order to predict the equilibrium partitioning of the CCA-elements. The simulation results show that, at temperatures $\leq$1350 °C, about 100% of Cu remained in solid phase as a dominant species of CaCu resulting from Ca-Cu interaction (Figure 3). When the temperature increases from 1350 to 1800 °C, new gaseous species CuH (0.47–4.49%), Cu_2 (0.02–0.43%), and CuCl (5.5×10^{-3}–5.544×10^{-1}%) are formed due to Cu-Cl and Cu-H interactions. At temperatures between 1450 and 1600 °C, Cu is proportionally distributed as elemental between gaseous phase (4.29–94.52%) and solid phase (88.84–33.57%).

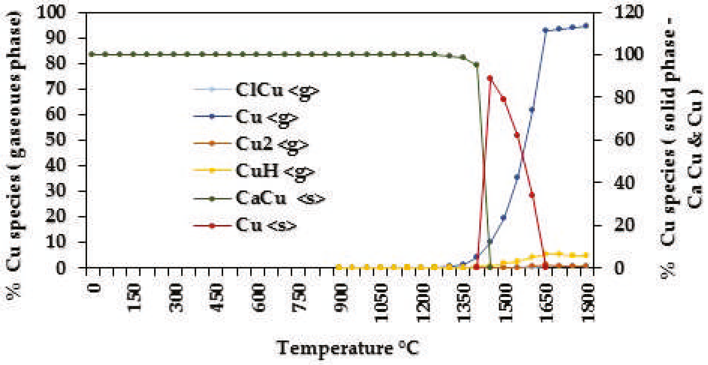

Figure 3. Speciation of copper.

The predicated distribution of Cr is shown in Figure 4. Obviously, at temperatures ≤1550 °C, Cr remained in solid phase as C_3Cr_7 (100%), and this was mainly due to C-Cr interaction. Additionally, at temperatures between 1550 and 1800 °C, the mass percentage of C_3Cr_7 decreased from 100% to 67.34%, while at the same time it was released as elemental Cr (3.16–32.48%) and as a new set of gaseous species generated by Cr-Cl, Cr- H, Cr- N, and Cr-O interactions; the total mass percentage of these gaseous species was less than 0.2%.

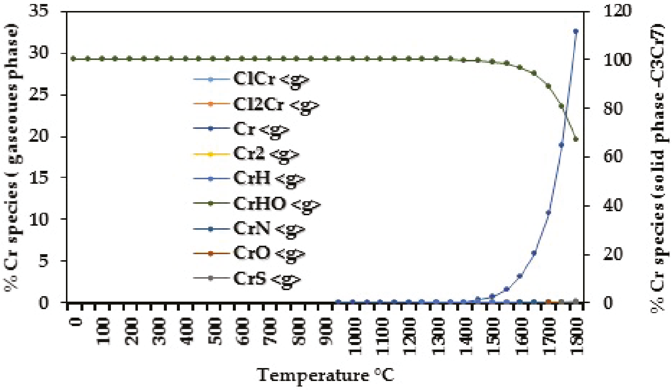

Figure 4. Speciation of chromium.

Figure 5 shows the equilibrium distribution of As. It is clear that at temperatures ≤1400 °C, As is predicated as stable solid species $AsNa_3$ (100%) and As_2Ni_5 (99.99–99.15%) as consequence of As-Na interaction and As-Ni interaction, respectively. As the temperature increases from 1400 to 1800 °C, the mass percentage of As decreases rapidly in solid phase, and it reforms as new gaseous species predominately by interactions. Among them, the dominant ones are As_2 (1.90–46.00%), AsH (0.24–7.13%), and As (5–46.55%). Indeed, AsH is generated by As-H interaction.

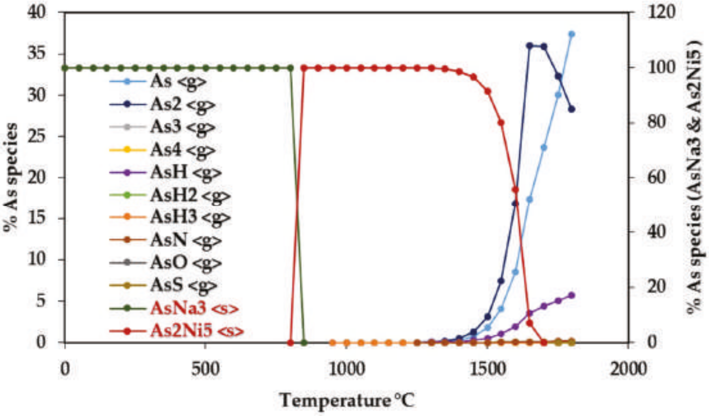

Figure 5. Speciation of arsenic.

To highlight the influence of increased pressure conditions on phase transition temperatures of CCA-elements, the reaction pressure was set to 20 atm and to 40 atm. Not surprisingly, Cr remained completely in condensed phase under both pressures, as shown in Figure 6a. Whereas, under 20 atm, the phase transformation temperatures of Cu and As increased by 300 and 250 °C, respectively, compared to those under 1 atm. Also, under 40 atm, the phase transformation temperatures of Cu and As, respectively, increased by 350 and 300 °C compared to those predicated under 1 atm, as depicted in Figure 6b,c.

3.1.2. Influence of Elemental Contents

Since the elemental content is one of the most important factors that directly affects species formation, different element content in WW samples were simulated to identify the possible interactions and interferences in terms of speciation during PCR, such that the element concentration were introduced to the model as presented in Table 3. Note here that the interactions and interferences that lead to appreciable effects on elemental phase transformation temperature and species formation were ranked as significant.

Influences on CCA-elements

In this case, the concentrations of each CCA-elements were individually changed. The simulation results show that the CCA-elements contents exhibit almost no influence on their phase transformation temperatures, but only concentration shifts are observed as shown in Figure 7a–c. Nevertheless, an exception is that when As concentration is relatively high (5 mole/h), its solid–gaseous transformation temperature decreased by 400 °C because the Ni contained becomes less than the limit to interact with As, and hence captures 100% of the As. Additionally, As_2Ni_5 (solid) and AsN (gaseous) are the dominant species of As.

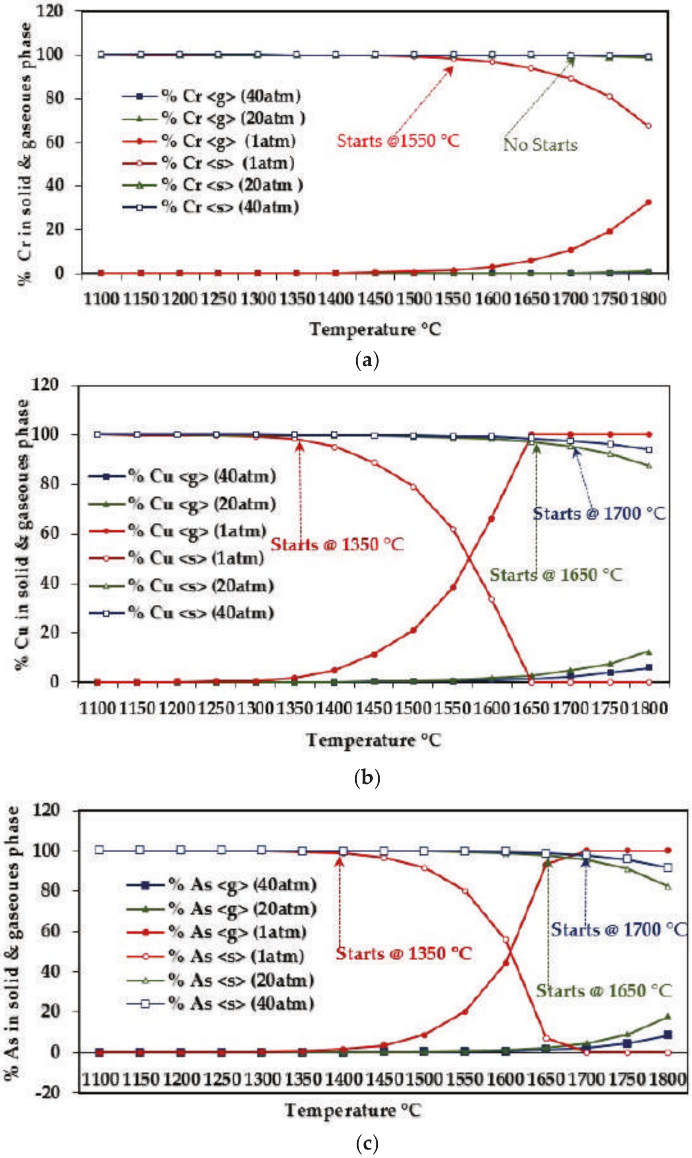

Figure 6. Cu, Cr, and As (CCA-elements) solid/gaseous transitions under 1, 20, and 40 atm: (**a**) chromium; (**b**) copper; (**c**) arsenic.

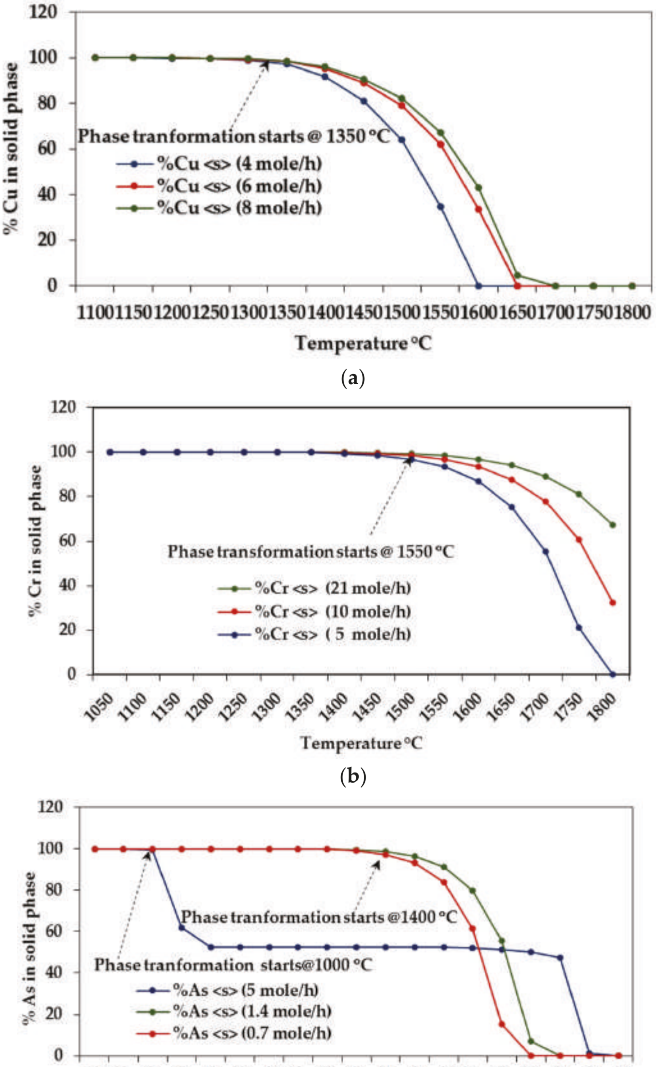

(**a**)

(**b**)

(**c**)

Figure 7. Resulting phase transformations of CCA-elements by changing the concentrations of each element individually: (**a**) copper; (**b**) chromium; (**c**) arsenic.

Influences of Ca, Na, S, Cl, Fe, and Ni on CCA-element

An illustration of the occurred interactions and interferences between CCA-elements and individual presence/absence of each of the elements Ca, Na, S, Cl, Fe and Ni are given in Figure 8. Note that, in all the simulations, the CCA-elements concentrations were kept fixed (as listed in Table 2) while the concentrations of other minor elements were considered as in Table 3.

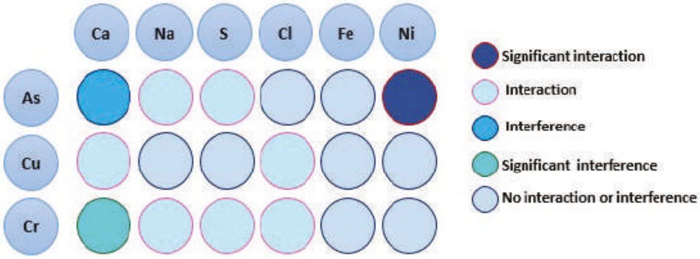

Figure 8. Interactions and interferences between the CCA-elements and each of Ca, Na, S, Cl, Fe, and Ni.

1. Copper

As presented in Figure 8, Cu interacts with Ca and Cl; however, all Cl-Cu interactions release only a single gaseous species—ClCu. The solid and gaseous species formed by Ca-Cu interactions are listed in Table 5. The analysis shows that the dominant species in solid phase are CaCu, CaCu and $CaCu_5$, and CaCu when Ca is present, respectively at concentrations of 250, 500, and 1000 mole/h. On the other hand, the presence of Ca at low concentrations would not be sufficient to interact with Cu; alternatively, it interacts with O and Cr, forming $CaCr_2O_4$ and CaO, respectively. Further, it is noted that the volatilization of Cu is not affected by the various concentrations of Ca, which is similar to Cl-Cu interactions.

Table 5. Calcium-copper interactions during PCR.

Ca Concentration (mole/h)	Species	Temperature Range (°C)
100	Cu <s>	0–800
	Cu <s>, Cu <g>, CuH <g>	850–950
	Cu <s>, ClCu <g>, Cu <g>, CuH <g>	1000–1800
250	CaCu <s>	0–800
	Cu <g>, CuH <g>, CaCu <s>	850–1150
	ClCu <g>, Cu <g>, Cu_2 <g>, CuH <g>, CaCu <s>	1350–1800
500	CaCu <s>, $CaCu_5$ <s>	0–800
	Cu, Cu <g>, CuH <g>	850–950
	Cu <g>, CuH <g>, CaCu <s>	1000–1150
	ClCu <g>, Cu <g>, Cu2 <g>, CuH <g>, CaCu <s>	1250–1800
1000	CaCu <s>	0–800
	Cu <g>, CuH <g>, CaCu <s>	850–950
	Cu <g>, CuH <g>, CaCu <s>	1000–1150
	ClCu <g>, Cu <g>, Cu_2 <g>, CuH <g>, CaCu <s>	1250–1800

2. Chromium

The analysis reveals that Ca plays an important role in Cr distribution across the solid and gaseous phases (Figure 9 and Table 6). That is, Na and Cr interact only when the concentration of Ca is ≤100 mole/h, leading to the formation of instable solid specie $Cr_2Na_2O_4$ between 1100 and 1550 °C. $CaCr_2O_4$ (solid) is the most likely to be generated by Ca-Cr interactions when Ca is present at 100 mole/h, thereby about 100% of Cr remains in solid phase at temperatures ≤1550 °C. As the Ca content increases (> 100 mole/h), Ca-Cr interferences and C-Cr interactions take place simultaneously, forming C_2Cr_3 and C_3Cr_7 in solid phase at temperatures up to 1550 °C. A most apparent observation in this case is the concentration shift in gaseous phase of Cr.

Other interactions, specifically, S-Cr and Cl-Cr interactions, exhibit no influence on Cr volatilization and solely yield gaseous species CrS, ClCr and Cl_2Cr, respectively.

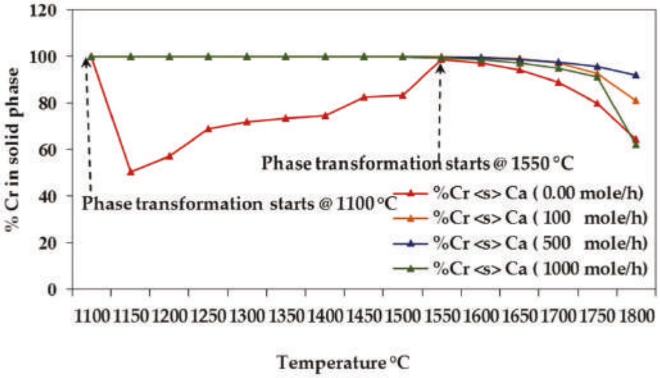

Figure 9. Effects of Ca on Cr phase formation.

Table 6. Chromium-calcium interactions.

Ca Concentration (mole/h)	Species	Temperature Range (°C)
0	$Cr_2Na_2O_4$ <s> C_2Cr_3 <s>, $Cr_2Na_2O_4$ <s> $Cr_2Na_2O_4$ <s> Cr <g>, C_2Cr_3 <s>, $Cr_2Na_2O_4$ <s> ClCr <g>, Cl_2Cr <g>, Cr <g>, CrHO <g>, CrS <g>, C_2Cr_3 <s>, Cr <s>, C_3Cr_7 <s>, C_6Cr_{23} <s>	0–300 350–400 450–600 650–1200 1250–1800
100	C_2Cr_3 <s>, $CaCr_2O_4$ <s>, CrN <s>, $Cr_2Na_2O_4$ <s> C_2Cr_3 <s>, $Cr_2Na_2O_4$ <s> C_2Cr_3 <s>, $CaCr_2O_4$ <s> ClCr <g>, Cr <g>, C_2Cr_3 <s>, $CaCr_2O_4$ <s> ClCr <g>, Cl_2Cr <g>, Cr<g>, C_2Cr_3 <s>	0–300 350–400 450–600 650–1200 1250–1800
250–500	C_2Cr_3 <s> C_2Cr_3 <s>, C_3Cr_7 <s> C_3Cr_7 <s> C_2Cr_3 <s>, ClCr <g>, Cl_2Cr <g>, Cr <g>, CrH <g>, C_3Cr_7 <s>, CrO <g>, CrS <g>, CrN <g>	0–300 350–600 650–1200 1250–1800
10000	C_3Cr_7 <s> Cr <g>, C_3Cr_7 <s> ClCr <g>, Cl_2Cr <g>, Cr <g>, CrH <g>, CrO <g>, CrS <g>, CrN <g>, C_3Cr_7 <s>	0–600 650–1200 1250–1800

3. Arsenic

When Ni content is present at various concentrations, all Ni-As interactions generate solid specie As_2Ni_5, by which the phase transformation temperature of As (Figure 10) increases to about 450 °C. In contrast, the absence of Ni leads to the formation of As_2 (gaseous) and $AsNa_3$ (solid) as dominant species, as shown in Figure 11. Similarly, Na-As interactions yield $AsNa_3$. While the absence of Na shows no influence on the As phase formation; it enhances Ni to capture As, generating As_2Ni_5 (100–99.15%) up to 1400 °C, as illustrated in Figure 12. Also, S tends to interact with As, yielding, at very low mass percentage, gaseous specie AsS between 1750 and 1800 °C.

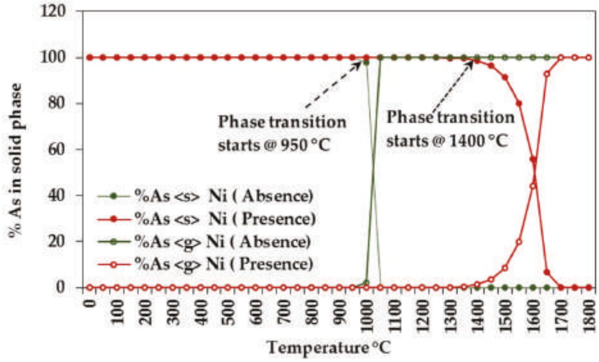

Figure 10. Arsenic distribution according to the presence/absence of Ni.

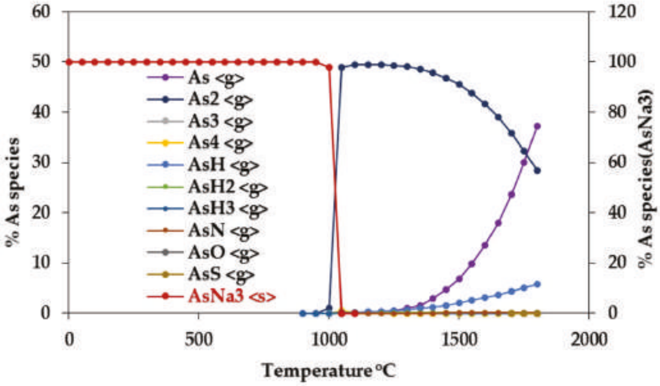

Figure 11. Arsenic speciation in the absence of Ni.

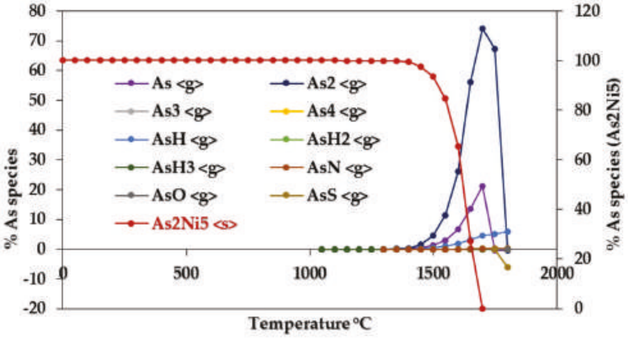

Figure 12. Arsenic speciation in the absence of Na.

Assessing CCA-elements Reactivity

All the minor elements were introduced to the model at the same concentration (0.25 mole/h) to assess the reactivity of the CCA-elements. In this case, the resulted speciation of CCA-elements are demonstrated in Figure 13a–c.

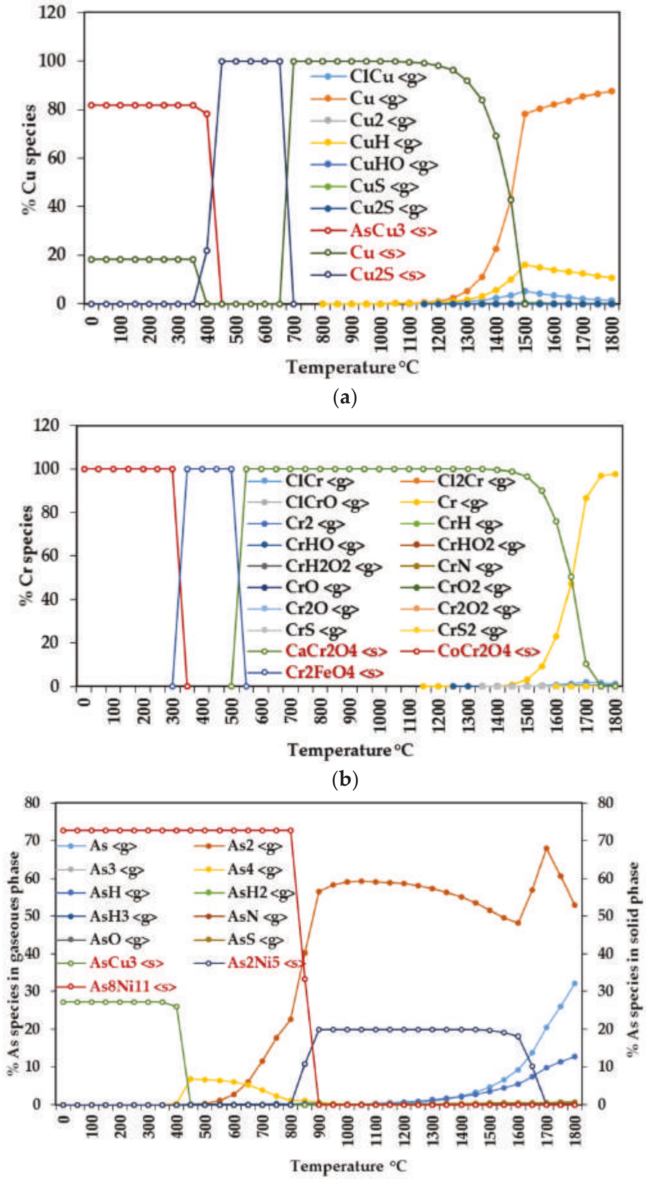

(**a**)

(**b**)

(**c**)

Figure 13. Speciation of CCA-elements when all minor elements are present at the same concentrations: (**a**) copper; (**b**) chromium; (**c**) arsenic.

As can be seen in Figure 13a, the behavior of Cu between 0 and 700 °C indicates that Cu interacts favorably with As and S, forming the solid species $AsCu_3$ (81.89–78.24%) and Cu_2S (100%), respectively. At temperatures above 700 °C, Cu is redistributed as elemental and a set of gaseous species, and its phase transformation temperature becomes 1200 °C, which is less than about 11% of that obtained with equilibrium composition (Figure 3). The predictive calculations, as shown in

Figure 13b, originate the Cr solid species $CoCr_2O_4$ (100% between 0–300 °C), Cr_2FeO_4 (100% between 350–500 °C), and $CaCr_2O_4$ (100% between 550–1450 °C) to the Co-O-Cr, Fe-O-Cr, and Ca-O-Cr interactions, respectively. Figure 13c shows As species formation. Intuitively, $AsCu_3$ (27.27% between 0–400 °C) and As_8Ni_{11} (72.73% between 0–800°C) are the most probable solid species from Cu-As and Ni-As interactions, respectively.

In this view, the distribution profiles of CCA-elements during gasification offer important trend towards their emissions control. More specifically, the presence of Ni and S enhances As and Cu capture in ash, respectively. Also, Cu and As interactions cause both of them to remain in solid phase, and the elements Ca, Co, and Fe are favored to Cr retention.

3.2. Under Boudouard Reaction (BR)

The modelling of BR was carried out using the composition data and BR process parameters, respectively, as reported in Tables 2 and 4. The simulation scenarios were considered similar to those for the case of PCR. On the whole, the obtained results were similar to those observed with the PCR model, except that at equilibrium partitioning, about 99.99% of the CCA-elements remained in solid phase at temperatures less than 1300 °C; also no gaseous species were formed under pressure conditions of 20 and 40 atm. Table 7 demonstrates the phase and species formation of CCA-elements at equilibrium composition under 1 atm.

Table 7. Phase transformations and speciation of the CCA-elements.

Elements	Solid Phase	Temperature (°C)	Gaseous Phase	Temperature (°C)
Cr	C_3Cr_7	0–1300	Cr CrCl CrH	1000–1300 1250–1300 1300
Cu	CaCu	0–1300	Cu, CuH Cu_2, ClCu	900–1300 1150–1300
As	$AsNa_3$ As_2Ni_5	0–800 850–1300	As, As_2, AsH, AsH_2 AsH_3	1150–1300 1150–1300

4. Conclusion

This paper introduces two predictive models for PCR and BR to understand the behavior of CCA-elements in terms of interactions and interferences during the gasification of contaminated WW. The refinement of the predicated results from PCR modelling indicates that most of the occurred Ni-As interactions led to about 100% of As remaining in solid phase at temperatures less than 1400 °C. It also indicates that Ca-Cr interferences form solid specie C_3Cr_7, but the absence of Ca causes instability in Cr distribution at temperatures from 1100 to 1550 °C. Whereas Co-O-Cr, Fe-O-Cr, and Ca-O-Cr interactions reduced the Cr volatilization as consequence of the generated solid species $CoCr_2O_4$, Cr_2FeO_4, and $CaCr_2O_4$, respectively. Most importantly, in both PCR and BR, the presence of Na and or Ni played a vital role for As remaining in solid phase at temperatures $\leq$800 °C. Eventually, these modellings are valuable for mitigating the negative impacts of toxicity emissions associated with CCA-elements; particularly, by systematically blending different types of contaminated WW prior to gasification.

Author Contributions: All authors contributed to this work. S.B.A.: Writing—Original Draft Preparation; S.T.W. and Y.J.: Supervision and Guidance.

Acknowledgments: The authors would like to thank Cranfield University for the facilities provided to carry out this work.

Conflicts of Interest: The authors declare no conflict of interest.

References

1. Edo, M.; Björn, E.; Persson, P.E.; Jansson, S. Assessment of chemical and material contamination in waste wood fuels-A case study ranging over nine years. *Waste Manag.* **2016**, *49*, 311–319. [CrossRef] [PubMed]
2. Brown, M.; Kearley, V. Role of wood waste as source of biomass fuel in the UK. *Energy Mater.* **2009**, *4*, 162–165. [CrossRef]
3. Department for Environment, Food and Rural Affairs. *Wood Waste: A Short Review of Recent Research*; Department for Environment, Food and Rural Affairs: London, UK, 2012.
4. Vassilev, S.V.; Baxter, D.; Andersen, L.K.; Vassileva, C.G. An overview of the chemical composition of biomass. *Fuel* **2010**, *89*, 913–933. [CrossRef]
5. Kamińska-Pietrzak, N.; Smoliński, A. Selected Environmental Aspects of Gasification and Co-Gasification of Various Types of Waste. *J. Sustain. Min.* **2013**, *12*, 6–13. [CrossRef]
6. Couto, N.; Rouboa, A.; Silva, V.; Monteiro, E.; Bouziane, K. Influence of the biomass gasification processes on the final composition of syngas. *Energy Procedia* **2013**, *36*, 596–606. [CrossRef]
7. Pandey, A.; Bhaskar, T.; Stöcker, M.; Sukumaran, R. *Recent Advances in ThermoChemical Conversion of Biomass*; Elsevier: New York, NY, USA, 2015.
8. Gomez-Barea, A.; Leckner, B. Modeling of biomass gasification in fluidized bed. *Prog. Energy Combust. Sci.* **2010**, *36*, 444–509. [CrossRef]
9. James, R.; Arthur, M.; Yuan, W.; Boyette, M.D. The effect of biomass physical properties on top-lit updraft gasification of woodchips. *Energies* **2016**, *9*, 283. [CrossRef]
10. González-Vázquez, M.P.; García, R.; Pevida, C.; Rubiera, F. Optimization of a bubbling fluidized bed plant for low-temperature gasification of biomass. *Energies* **2017**, *10*, 306. [CrossRef]
11. Tanger, P.; Field, J.L.; Jahn, C.E.; DeFoort, M.W.; Leach, J.E. Biomass for thermochemical conversion: targets and challenges. *Front. Plant Sci.* **2013**, *4*, 218. [CrossRef] [PubMed]
12. Tripathi, M.; Sahu, J.N.; Ganesan, P. Effect of process parameters on production of biochar from biomass waste through pyrolysis: A review. *Renew. Sustain. Energy Rev.* **2016**, *55*, 467–481. [CrossRef]
13. Vervaeke, P.; Tack, F.M.G.; Navez, F.; Martin, J.; Verloo, M.G.; Lust, N. Fate of heavy metals during fixed bed downdraft gasification of willow wood harvested from contaminated sites. *Biomass Bioenergy* **2006**, *30*, 58–65. [CrossRef]
14. Šyc, M.; Pohořelý, M.; Jeremiáš, M.; Vosecký, M.; Kameníková, P.; Skoblia, S.; Svoboda, K.; Punčochář, M. Behavior of heavy metals in steam fluidized bed gasification of contaminated biomass. *Energy Fuels* **2011**, *25*, 2284–2291. [CrossRef]
15. Tafur-Marinos, J.A.; Ginepro, M.; Pastero, L.; Torazzo, A.; Paschetta, E.; Fabbri, D.; Zelano, V. Comparison of inorganic constituents in bottom and fly residues from pelletised wood pyro-gasification. *Fuel* **2014**, *119*, 157–162. [CrossRef]
16. Zhou, X.; Liu, W.; Zhang, P.; Wu, W. Study on Heavy Metals Conversion Characteristics During Refused Derived Fuel Gasification Process. *Procedia Environ. Sci.* **2016**, *31*, 514–519. [CrossRef]
17. Wu, M.H.; Lin, C.L.; Zeng, W.Y. Effect of waste incineration and gasification processes on heavy metal distribution. *Fuel Process. Technol.* **2014**, *125*, 67–72. [CrossRef]
18. Jiang, Y.; Ameh, A.; Lei, M.; Duan, L.; Longhurst, P. Solid–gaseous phase transformation of elemental contaminants during the gasification of biomass. *Sci. Total Environ.* **2016**, *563–564*, 724–730. [CrossRef] [PubMed]
19. Froment, K.; Defoort, F.; Bertrand, C.; Seiler, J.M.; Berjonneau, J.; Poirier, J. Thermodynamic equilibrium calculations of the volatilization and condensation of inorganics during wood gasification. *Fuel* **2013**, *107*, 269–281. [CrossRef]
20. Kramb, J.; Konttinen, J.; Backman, R.; Salo, K.; Roberts, M. Elimination of arsenic-containing emissions from gasification of chromated copper arsenate wood. *Fuel* **2016**, *181*, 319–324. [CrossRef]
21. Thompson, D.; Argent, B.B. Prediction of the distribution of trace elements between the product streams of the Prenflo gasifier and comparison with reported data. *Fuel* **2002**, *81*, 555–570. [CrossRef]
22. Kilgallon, P.J.; Simms, N.J.; Oakey, J.E. Fate of trace contaminants from biomass fuels in gasification systems. *Mater. Adv. Power Eng.* **2002**, *21*, 903–912.
23. Reed, G.P.; Dugwell, D.R.; Kandiyoti, R. Control of trace elements in a gasifier hot gas filter: A comparison with predictions from a thermodynamic equilibrium model. *Energy Fuels* **2001**, *15*, 1480–1487. [CrossRef]

24. Liu, S.; Wang, Y.; Yu, L.; Oakey, J. Thermodynamic equilibrium study of trace element transformation during underground coal gasification. *Fuel Process. Technol.* **2006**, *87*, 209–215. [CrossRef]
25. Bradshaw, A.; Simms, N.J.; Nicholls, J.R. Passage of trace metal contaminants through hot gas paths of gas turbines burning biomass and waste-fuels. *Fuel* **2008**, *87*, 3529–3536. [CrossRef]
26. Svoboda, K.; Leitner, J.; Havlica, J.; Hartman, M.; Pohořelý, M.; Brynda, J.; Šyc, M.; Chyou, Y.P.; Chen, P.C. Thermodynamic aspects of gasification derived syngas desulfurization, removal of hydrogen halides and regeneration of spent sorbents based on La2O3/La2O2CO3 and cerium oxides. *Fuel* **2017**, *197*, 277–289. [CrossRef]
27. Contreras, M.L.; Arostegui, J.M.; Armesto, L. Arsenic interactions during co-combustion processes based on thermodynamic equilibrium calculations. *Fuel* **2009**, *88*, 539–546. [CrossRef]
28. Yan, R.; Gauthier, D.; Flamant, G. Possible interactions between As, Se, and Hg during coal combustion. *Combust. Flame* **2000**, *120*, 49–60. [CrossRef]
29. Energy Research Centre of the Netherlands. Available online: https://www.ecn.nl/phyllis2/ (accessed on 20 March 2017).
30. Prabir, B. *Biomass Gasification, Pyrolysis, and Torrefaction Practical Design and Theory*, 2nd ed; Academic Press: Cambridge, MA, USA, 30 July 2013.

energies

MDPI

Article

Investigation of the Olive Mill Solid Wastes Pellets Combustion in a Counter-Current Fixed Bed Reactor

Mohamed Ali Mami [1], Hartmut Mätzing [2], Hans-Joachim Gehrmann [2], Dieter Stapf [2], Rainer Bolduan [3] and Marzouk Lajili [1,*]

[1] Ionized and Reactive Media Studies Research Unit (EMIR), Preparatory Institute of Engineering Studies of Monastir (IPEIM), University of Monastir, 15 Avenue Ibn El Jazar Monastir 5019, Tunisia; Mohamedali.Mami@ipeim.rnu.tn

[2] Institute for Technical Chemistry (ITC), Karlsruhe Institute of Technology (KIT), Hermann-von-Helmholtz-Platz 1, 76344 Eggenstein-Leopoldshafen, Germany; hartmut.maetzing@kit.edu (H.M.); hans-joachim.gehrmann@kit.edu (H.-J.G.); dieter.stapf@kit.edu (D.S.)

[3] European Institute for Energy Research (EIFER), Karlsruhe Institute of Technology (KIT), Emmy-Noether-Str. 11, 76131 Karlsruhe, Germany; Rainer.Bolduan@eifer.uni-karlsruhe.de

* Corresponding: marzouk.lajili@ipeim.rnu.tn; Tel.: +216-73500277 or +216-97369126

Received: 28 June 2018; Accepted: 23 July 2018; Published: 28 July 2018

Abstract: Combustion tests and gaseous emissions of olive mill solid wastes pellets (olive pomace (OP), and olive pits (OP_i)) were carried out in an updraft counter-current fixed bed reactor. Along the combustion chamber axis and under a constant primary air flow rate, the bed temperatures and the mass loss rate were measured as functions of time. Moreover, the gas mixture components such as O_2, organic carbon (C_{org}), CO, CO_2, H_2O, H_2, SO_2, and NO_x (NO + NO_2) were analyzed and measured. The reaction front positions were determined as well as the ignition rate and the reaction front velocity. We have found that the exhaust gases are emitted in acceptable concentrations compared to the combustion of standard wood pellets reported in the literature (EN 303-5). It is shown that the bed temperature increased from the ambient value to a maximum value ranging from 750 to 1000 °C as previously reported in the literature. The results demonstrate the promise of using olive mill solid waste pellets as an alternative biofuel for heat and/or electricity production.

Keywords: olive mill solid wastes (OMSWs); fixed bed combustor; pellets; combustion parameters; gaseous emissions

---

1. Introduction

Agro-industrial by-products are viable alternatives to fossil fuels to reduce greenhouse gases emissions such as CO_2 and NO_x [1–3]. Among these by-products, olive mill solid wastes (OMSWs) are generated in large quantities in the leading producers in the olive oil industry, including Spain, Italy, Greece, and Tunisia. However, these by-products can present serious environmental problems affecting soil, air, and water when stockpiled and left untreated. However, these lignocellulosic biomasses can be considered as a promising source of renewable energy [4,5]. Indeed, these residues can be separated as olive pomace (OP) and olive pits (OP_i). Olive pits (OP_i) are a major bio-fuel in Spain [6], which is used in combustion processes to produce heat [7] owing to its low moisture content, high heating value, uniform size, and relatively high bulk density [8]. Using this material as a biofuel can be considered as an economically viable alternative to fossil fuels [9]. Despite this potential, only a few studies have been dedicated to characterizing this biofuel for the purpose of energy conversion [5]. Nevertheless, the value of the utilization of olive pomace as a biofuel is widely recognized [10,11]. Moreover, both OP and OP_i can be processed into cylindrical pellets (up to 40 mm length, at standard diameter from 6 to 10 mm, typically 6 mm). This process increases the energy density of these pellets [12,13].

Although the pelletization is a very complicated technique, with the potential for technical problems to arise, we concluded that when using the olive mill solid wastes with moisture content in the vicinity of 15%, and at the optimal conditions of frequency and temperature as we mention below, no problems will be encountered. The reason for this is that the lignocellulosic biomass contains its own binder (abrasive matter). However, it should be mentioned that in the case of this study, pelletization was successful without any additive binder and with the appropriate individual die. The samples of about 1 mm in size needed neither milling nor moisture adjustment and could directly be pelletized after homogenization.

The combustion behavior of pellets, either mixed with other residues or only derived from the OMSWs, has been studied in small powered pellets boilers (<50 kW). These investigations have shown that olive solid residue pellets are ecologically beneficial and are an environmentally friendly energy source for producing heat and/or electricity [14–16]. Nevertheless, the combustion of such biofuels in fixed/fluidized beds is rarely reported in the literature. Moreover, these high calorific pellets have not been commonly used in large-scale combustion systems. Indeed, except for the high quality woody pellets like DIN-plus which is commercialized in European markets, pellets like those considered in our work have not yet been investigated which may be because of the additional cost of transport and pelletization. For this reason, countries like Spain and Italy are still using raw olive mill by-products which have been dried and exhausted without pelletization. However, the pelletization has proven to be very suitable for heat production (domestic use for household boilers and stoves) [14,15]. Due to the higher ash volume (≈5%) of olive residues in comparison with woody biomass for DIN plus (<1%) filtering/ash management/burner suitability, as well as standardized industrial pellet requirement, must be considered for large-scale application. Further, their combustion produces more emissions than high quality woody pellets.

González et al. [14] have studied the combustion of different pellets made from olive stones (OP_i), tomato residues, and cardoon, respectively, in a mural boiler used for domestic heating (11.6 kW). The results were compared with forest wood pellets which are recommended as standard fuels. The authors showed that when using OP_i pellets, characterized by lower percentages of sulfur and nitrogen contents, they obtained a significant decrease in NO_x and SO_2 emissions. These biofuels represented the most favorable and attractive fuels from an environmental point of view by comparison to the tomato, cardoon, and forest wood pellets.

In the same context, Miranda et al. [17] conducted combustion tests on OMSWs (OP_i and OP) in their raw state (not pelletized). They used a prototype furnace to analyze the main combustion emissions: CO, CO_2, NO_x, N_2O, SO_2, and O_2. The tests resulted in a good combustion efficiency with relatively low emissions.

Several groups are currently focusing on the modeling of the combustion of pellets in reactors such as pilot fixed bed/fluidized bed, before expanding these studies to large scales (industrial plants) [18]. The choice of the fixed bed reactor for our study is based on its relative simplicity, which will be easier to eventually model. At the same time, our study allows the determination of the independent characteristic numbers needed to scale our results to an industrial scale [19–21].

To the best of our knowledge, the combustion of olive solid residues, such as OP and OP_i, in a counter-current fixed bed reactor has not been reported in the literature. In this study, the combustion pellets tests were carried out in the 40 kW fixed bed reactor "KLEAA" at Karlsruhe Institute of Technology (KIT) (Germany) [22,23]. To determine the combustion characteristics of these samples, the axial temperature evolution was measured. This permits the determination of the reaction front positions in terms of time during the combustion process. In addition, the mass loss is continuously measured during the test. Further, gaseous emission such as CO, CO_2, H_2, H_2O, O_2, and organic carbon (C_{org}) were analyzed and measured as well as other pollutants: SO_2 and NO_x (NO + NO_2). Consequently, some scale independent characteristic numbers such as the reaction front velocity u_{RF}, the ignition rate (*IR*), the mass conversion rate (*MCR*) and the specific heat release rate (*HR*) were derived. These specific numbers can serve to quantify and to assess the combustion quality.

All obtained results are compared to those of similar studies in literature and to standard wood pellets (EN-303-5).

2. Materials and Methods

2.1. Samples Preparation

Olive pomace (OP) and olive pits (OP_i) used in this study were obtained from the Zouila Oil Press Company located in the Sahel region of Tunisia (Mahdia-Tunisia). About 6 kg of pellets were prepared from the biofuels at EIFER (European Institute for Energy Research, Karlsruhe, Germany): 100% OP with a die compaction rate of 1:5 (conical pressing) and 100% OP_i with a compaction rate of 1:4 at 24 mm press channel length for both. The pellet press used is a Kahl lab scale flat matrix press 14–175 (with a maximum olive pellet production in the range 15–20 kg/h). The specific optimum rotation frequency was determined to be 85 Hz, and the optimum temperature for stable pellets in literature was 75 °C. The produced pellets were in compliance with the German and European standards (EN 303-5, EN 17225-6). After pelletization and air-cooling, the pellets were stored for minimum 24 h under room conditions to equalize any moisture differences as shown in Table 1.

Table 1. Operating pelletization condition.

Pelletizer Performance	100% Olive Pomace (OP)	100% Olive Pits (OP_i)
Pelletizing temperature (°C)	60	51
Biomass moisture (% w.b.)	14.7 ± 0.5	15.3 ± 0.3
Pellet moisture (% w.b.)	12.4 ± 0.4	13.7 ± 0.2

(% w.b. is the percentage on wet basis).

Table 1 indicates that the moisture content decreases after pelletization. This decrease is due to the evaporation associated with the rising temperature during the pelletization process. Finally, the obtained products were moisture-balanced cylindrical pellets of 6 mm diameter and 20–30 mm in length. As it is notable, the two OMSWs were pelletized under two different temperatures 60 and 51 °C for OP and OP_i, respectively. Indeed, because of its oil content and lubricity, pelletizing of olive pomace caused higher resistance (see compaction rate), and the higher friction, subsequently, raised the temperature to evaporate more water than during olive pits pelletizing. Hence, final moisture contents should be different because pelletization started with different initial moistures under different temperatures and calculations were done on wet basis. It can be observed that the difference between final moisture content on wet basis does not exceed 1.3%. Thereby, even though the moisture directly affects the low heating value (*LHV*), the difference between the two fuel types will be small.

2.2. Samples Characterizations

2.2.1. Raw Samples Characterizations

Ultimate and proximate analysis of the raw samples as olive pomace (OP), olive pits (OP_i) and sawdust (S) are summarized in Table 2.

Tables 2 and 3 show the ultimate and proximate analyses and the energy characteristics of the used raw materials. These characteristics are compared with those found in the literature for different agro-industrial wastes. All analyses were carried out at the Chemical and Microbiological Institute UEG GmbH (Germany). Ultimate, proximate and energy contents were realized according to the standards analytical methods for solid fuels. High heating value (*HHV*) is measured using a calorimetric bomb, and the *LHV* is then calculated using:

$$LHV = HHV - L_v\left(\frac{9\%\,\mathrm{H} + \%\,M}{100}\right) \tag{1}$$

where, *LHV* is the low heating value, *HHV* is the high heating value, % H is the hydrogen content and % *M* is the moisture content.

The energy density (*ED*) is obtained when multiplying the bulk density ρ_{BD} by the *LHV*:

$$ED = \rho_{BD} \times LHV \tag{2}$$

where, *ED* is the energy density and ρ_{BD} is the bulk density.

Table 2. Raw materials characteristics.

Samples	Equivalent Formula d.b.a.f. ^{a}	Ultimate Analysis (% d.b.)					Proximate Analysis (% d.b.)		
		% C	% H	% O	% N	% S	% ash	% FC	% VM
Olive pomace (OP)	$CH_{1.54}O_{0.56}N_{0.024}$	52.2 ± 0.8	6.70 ± 0.3	39.6 ± 0.6	1.50 ± 0.1	0.08 ± 0.01	5.10 ± 0.10	18.90 * ± 0.3	76.0 ± 1.0
Olive pits (OP$_i$)	$CH_{1.97}O_{0.92}N_{0.018}$	41.4 ± 0.4	5.20 ± 0.2	52.5 ± 0.9	0.91 ± 0.1	<0.2	0.80 ± 0.1	15.20 * ± 0.2	84.0 ± 0.8
Sawdust (S)	$CH_{1.49}O_{0.6}N_{0.0035}$	51.5 ± 0.5	6.40 ± 0.3	41.9 ± 0.5	0.20 ± 0.1	<0.1	0.5 ± 0.1	24.50 * ± 0.10	75.0 ± 1.0
Spruce wood [24,25]	$CH_{1.41}O_{0.59}N_{0.0033}$	51.9	6.10	40.9	0.30	0.30	1.70	18.10	80.2
Wood [26,27]	$CH_{1.46}O_{0.6}N_{0.0016}$	51.6	6.3 ^{b}	41.5	0.10	0.10 ^{b}	1.0	17.0	82.0
Palm Kernels [3,27]	$CH_{1.52}O_{0.58}N_{0.038}$	51.0	6.50	39.5	2.30	0.27	5.20	17.50	77.30
OP (Turkish) [28]	$CH_{1.36}O_{0.53}N_{0.021}$	51.3	5.85	36.9	1.27	0.08	4.51	17.90	71.17
OP (Italy) [29]	$CH_{1.57}O_{0.91}N_{0.034}$	44.2	5.80	48.2	1.80	-	5.40	29.60	65.0
OP$_i$ (Spain) [17]	$CH_{1.71}O_{0.57}N_{0.0009}$	52.2	7.48	40.0	0.06	<0.1	0.56	18.50	80.94
OP$_i$ (Spain) [30]	$CH_{1.6}O_{0.82}N_{0.0019}$	44.8	6.0	49.1	0.10	0.01	1.40	13.80	74.40

% d.b. is the percentage on dry basis; * Calculated by difference: % O = 100 − (% H + % C + % N), % FC = 100 − (% ash + % VM), ^{a} dry basis ash free, ^{b} Average value, $^-$ Not determined.

Table 3. Energy contents in the raw materials.

Samples	*LHV* (MJ/kg)	ρ_{BD} (kg/m^3)	*ED* (GJ/m^3)
Olive pomace (OP)	17.90 ± 0.40	539 ± 10	9.60 ± 0.50
Olive pits (OP$_i$)	17.29 ± 0.20	764 ± 12	13.20 ± 0.36
Sawdust (S)	16.30 ±0.10	103 ± 3	1.60 ± 0.06
Spruce wood [24,25]	18.10	105	1.90
Palm Kernels [26,27]	17.00	500	8.50
OC (Turkish) [31]	19.60	591	11.58
OC (Jordan) [32]	23.056	558	12.86
OP$_i$ (Spain) [8]	14.70 **	651.90 **	9.85
Oke (Greece) [33]	19.36	573	11.09
Rice Husks [34]	14.90	200	2.820

OC: Olive cake, Oke: Olive kernels, ** As received.

Furthermore, Table 2 shows high Nitrogen contents for OP and OP$_i$ in comparison with the sawdust (0.2%) and wood (0.1%). This fact will explain why nitrogen oxide emissions were relatively high.

As can be seen from Table 2, the ash content in the two samples (OP and OP$_i$) is high (3% and 4.7%) compared with 0.5% value for sawdust. For the two samples, the Energy density is higher than many biomass types in Table 3. Hence, the pelletization process is a compulsory process to increase the energy density of pellets and to make their transport and storage easier, ensuring a high hardness and long durability [35,36].

2.2.2. Pellets Samples Characterizations

Two pellets samples types were prepared: 100% olive pomace (OP) and 100% olive pits (OP$_i$). It needs to be clarified that the number of pellets used depends on the nature of characterization test we realize. For example, in the case of measuring the average length, diameter, and unit density (mass of the pellet divided by its volume) at least a 100 pellets are required to decrease the error according to the central limit theorem ($\varepsilon \sim \frac{1}{\sqrt{N}}$), where ε is the error and N is the number of samples. For the bulk density determination, the volume of the container (100 cm^3 in our case) ensured a large number of pellets was achieved. For the moisture content determination, the volume of the stove allowed a maximum of 10 crucibles containing one 1 pellet each to be used. The same process was undertaken when determining the ash content with a muffle furnace. However, for measuring the *HHV* via a calometric bomb, we used about 1 g of pellet and we repeated the test 5 times to attain the average value (this test is delicate and costly). In addition, during the pyrolysis tests to determine the volatile matter in a thermogravimetric balance, tests were repeated 3 times because this test type is time and cost intensive. Nevertheless, it was found that relative uncertainties were smaller than 5% of the mean value.

The main chemical characteristics of the produced pellets based on ultimate and proximate analysis are summarized in Table 4. These analyses are compared to the standard wood pellets and to other pellets presented in the literature. We observe that our prepared pellets show typical compositions when compared to other biomasses available in the literature [16,17,37].

The ash content was determined using a muffle furnace for which the temperature was fixed at 815 °C. The resulting values were lower than those fixed by the European normalization (<5%). In addition, the nitrogen content was 1.26% for OP and 0.61% for OP_i, respectively. These values were relatively higher than 0.11% obtained for wood pellets. The sulphur content was <0.1% for both samples. Therefore, SO_x emissions are expected to be insignificant.

Table 4. Pellets characteristics.

Samples	Equivalent Formula d.b.a.f.	Ultimate Analysis (% d.b.)					Proximate Analysis (% d.b.)		
		% C	% H	% O	% N	% S	% ash	% FC	% VM
100% OP	$CH_{1.3}O_{0.57}N_{0.021}$	49.50 ± 0.50	5.4 ± 0.5	43.70 * ± 1.80	1.3 ± 0.6	<0.10	2.90 ± 0.10	17.70 * ± 0.10	79.40 ± 0.20
100% OP_i	$CH_{1.65}O_{0.74}N_{0.011}$	46.50 ± 0.80	6.3 ± 0.1	46.60 * ± 0.90	0.5 ± 0.1	<0.10	1.90 ± 0.10	15.70 * ± 0.20	82.40 ± 1.00
wood pellets	$CH_{1.4}O_{0.63}N_{0.002}$	46.30 ± 0.20	5.4 ± 0.2	48.19 * ± 1.00	0.11	<0.10	0.30 ± 0.02	24.30 ± 0.90	75.40 ± 0.70
OP (Spain) [16]	$CH_{1.52}O_{0.49}N_{0.032}$	54.75	6.17	37.00	1.98	<0.10	5.55	17.28	77.17
OP (Spain) [17]	$CH_{1.65}O_{0.47}N_{0.007}$	58.20	6.00	35.40	0.40	0	2.50	17.69	79.81

* Calculated by difference.

In Table 5 the *LHV* values range between 17.45 and 20.36 MJ/kg. The energy density values of our samples were reasonably good (14.42 GJ/m^3 for OP_i and 15.59 GJ/m^3 for OP). However, the effect of pelletization was much more notable with OP than with OP_i. This is because of the difference in the bulk density between the two raw materials attributable to the better compressibility of the pomace (along with higher pressing energy needs) compared to the pits. On the other hand, the durability (*Du*), which is determined as a function of the percentage of fine particles leaving the pellets after appropriate mechanical tests, showed acceptable percentages with high regression factor ($R^2 = 0.985$) [38]. Indeed, after pelletization the pellets can be stored for longer before its use. During this period fine particles can leave the pellets so that the mass and, thereby, the energy of the fuel decreases. By using a centrifugation system based in a gyratory motor under standard normalizations (ISO 17831-1), the mechanical durability can be determined by weighing the mass before starting the experiment and subsequently. Thereafter, a percentage of material which is remaining in the fuel can be calculated: This is the so-called durability. The durability provides a reasonable assessment in regard to the transport and storage of a given solid biofuel [39]. Values of durability for both prepared samples (OP and OP_i) were in the same range of standard wood pellets. In addition, obtained durability (88–89%) for the peanut hull pellets agreed with our results [38].

Table 5. Energy contents in the pellets samples.

Samples	*LHV* (MJ/kg)	ρ_{BD} $\left(kg/m^3\right)$	*ED* (GJ/m^3)	*Du* (% w.b.)
OP pellets	19.02 ± 0.40	820 ± 15	15.59 ± 0.62	88 ± 2
OP_i pellets	18.38 ± 0.10	785 ± 10	14.42 ± 0.25	85 ± 2
wood pellets	17.45 ± 0.30	660 ± 8	11.51 ± 0.33	89 ± 2
OP (Spain) [16]	20.36	780	15.80	-
OP (Tunisia) [37]	19.23	920	17.69	-

3. Combustion Test

The experimental studies were carried out in a batch fixed bed reactor (KLEAA) characterized by a nominal power of 40 kW. This device is located at the Institute for Technical Chemistry (ITC) at the Karlsruhe Institute of Technology (KIT) in Germany.

The counter-current fixed bed reactor KLEAA has three main components: The combustion chamber composed by a fixed bed and a heated furnace, the post (or secondary) combustion chamber, and the flue gas cleaning system, which is equipped with a heat exchanger, a bag filter, and a carbon absorber.

The facility is suited to perform limited tests of solid fuel samples (about 3 kg for each test). The fuel bed has a total volume of 10 L. The furnace, and the secondary combustion chamber can be heated electrically up to a temperature of 1100 °C. The major components of the installation are represented schematically in Figure 1. A more detailed description of the facility is available elsewhere [21–23].

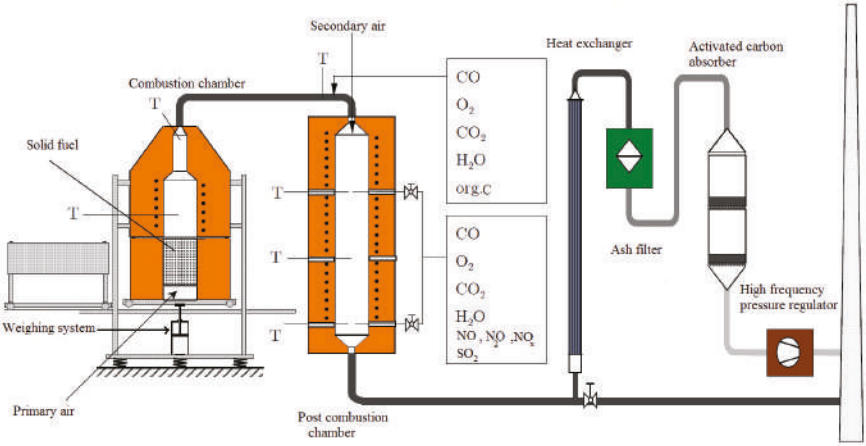

Figure 1. Sketch of the counter-current fixed bed reactor (KLEAA) facility at ITC, Karlsruhe, Germany.

The fixed bed has a height, h, of 250 mm and a diameter, d, of 230 mm. It is equipped with thirteen K-type thermocouples which are arranged in 20 mm intervals along the chamber's axis to measure the central bed temperature as it is shown in Figure 2.

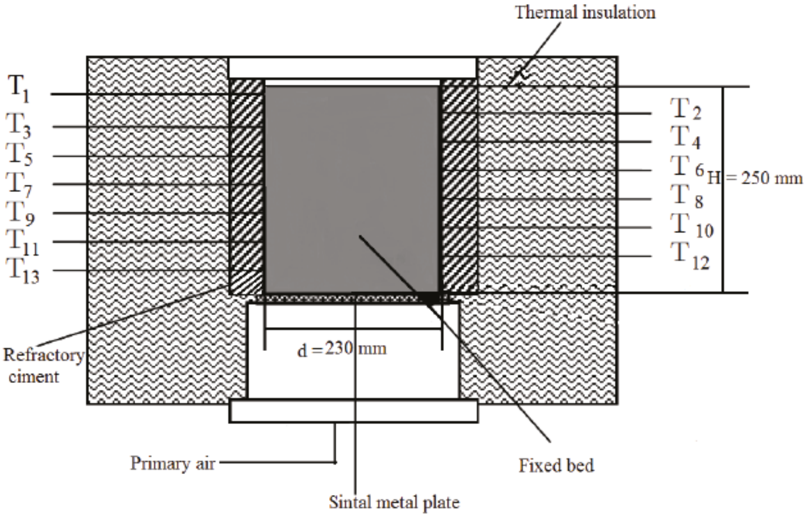

Figure 2. The fixed bed reactor and the thermocouples disposition.

Two experimental tests were performed with the biofuel pellets:

- 3.5 kg of 100% olive pomace (OP).
- 3.75 kg of 100% olive pits (OP_i).

The pellet samples were introduced into the combustion chamber. Then, the pellet samples were moved to the hot furnace, so that the fixed bed will be heated by radiation from the hot furnace wall (900 °C). The primary air was supplied at the bottom of the fixed bed via a sintered metal plate. The flow rate of the primary air was fixed at 10 Nm^3/h. The temperatures of the primary and the secondary air (25 Nm^3/h) were about 25 °C. Gaseous emissions were analyzed based on physical phenomena. Respectively CO, CO_2, and H_2O were analyzed by infrared techniques, C_{org} by flame ionization detector, O_2 by a paramagnetic system, and H_2 by heat conductivity. Trace gases, such as NO, NO_x, N_2O, and SO_2 were followed and also measured at the outlet of the post-combustion chamber. Thus, CO_2, CO, H_2O, and SO_2 were measured at the outlet of the post-combustion chamber. A heat exchanger has served for the heating of the water recovery system. After the combustion, the fly ash was emitted and collected in a special box under the grate via an ash filter. A pressure regulator ensured a pressure drop across the plant of about 50 Pa.

As stated earlier, there are limited studies on the types of biofuels in this study. Therefore, our results are compared to the results of some previous experiments conducted with conventional wood pellets under almost similar conditions [21–23,40,41].

4. Results and Discussion

4.1. Temperature Evolution in the Fuel Bed

Figure 3 shows the evolution of the bed temperature as a function of time at various bed heights from the bottom during the combustion process of olive pomace (OP), olive pits (OP_i), and the standard wood pellets. The thermocouple-based temperature measurements were collected at time intervals of 5 s.

Starting from the bed top to the bottom, the temperature profiles of the pellets samples show three distinct stages: (1) the ignition delay time, (2) the main combustion phase, and (3) the final char combustion.

During the ignition delay time, the bed surface is heated slowly. Hence, it dries and ignites by the radiation heat coming from the hot furnace wall. Then the ignition front propagates from the top of the bed downwards opposite to the gas flow [42]. The ignition delay time was measured by thermocouples T_2 and/or T_3 (blue and pink). It was determined to be equal to 3.5 min, 3.2 min, and 5.1 min, respectively (Figures 3 and 4).

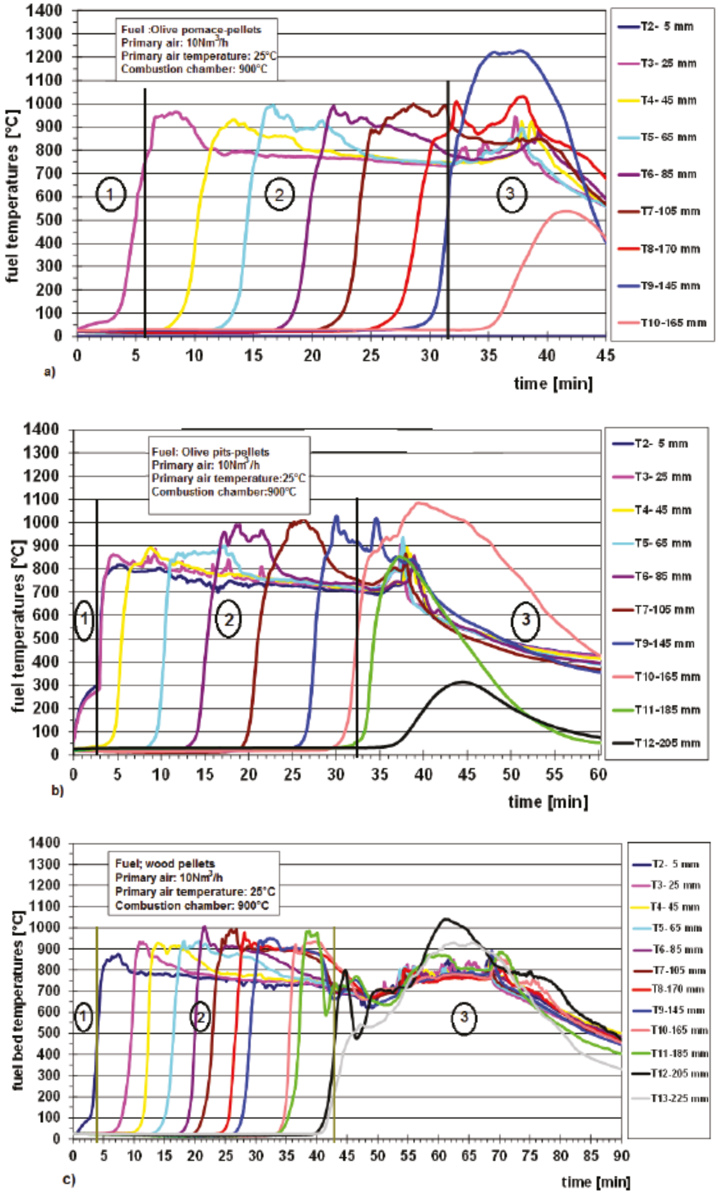

Figure 3. Thermocouples' readings during the passage of the flame front. (**a**) 100% olive pomace (OP); (**b**) 100% olive pits; (**c**) standard biofuel wood pellets.

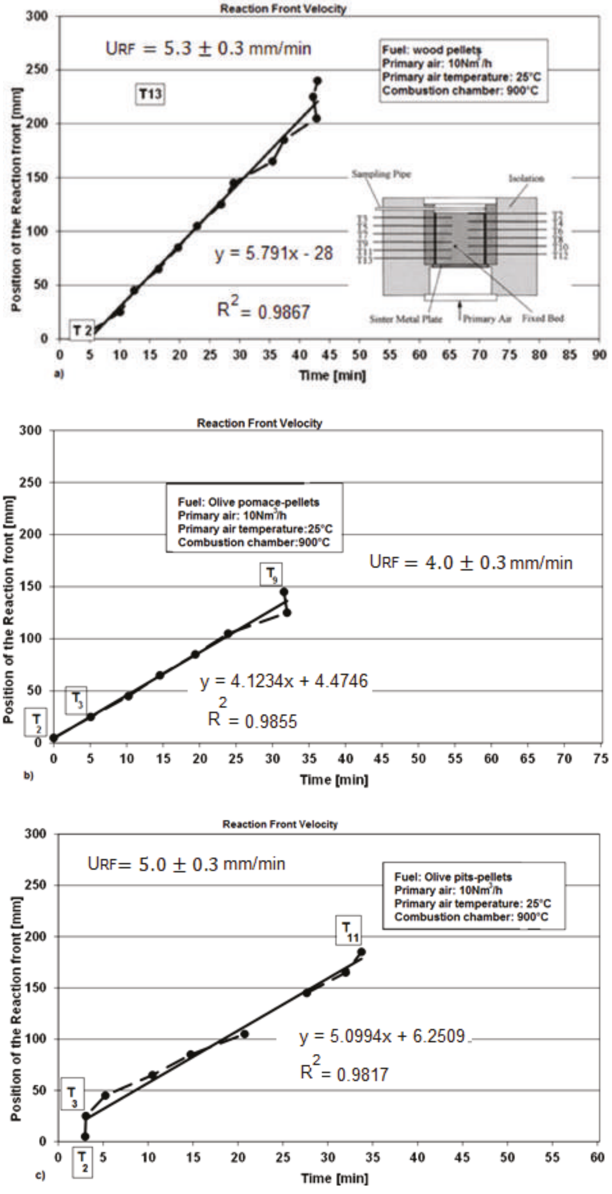

Figure 4. Reaction front positions derived from experimental pellets tests: (**a**) standard wood pellets; (**b**) 100% olive pomace (OP); (**c**) 100% olive pits (OP_i). Experimental conditions: Primary air 10 Nm^3/h; primary air temperature 25 °C and combustion chamber temperature 900 °C.

Thereafter, the main combustion phase starts when the flame front reaches and passes the thermocouples successively, and the temperature increases rapidly from ambient to almost 1000 °C. We observed that the temperatures rise from the initial values (25–30 °C) to reach about 880 °C for wood pellets, 800–875 °C for OP_i, and approximately 975 °C for OP. The observed overshoots of temperature can be explained by the highly exothermic combustion of a small amount of carbon (coke). The arrival time and the position of the reaction front are derived from the inflection point of the temperature curves. After the passage of the reaction front, the thermocouples recorded the temperature of the hot combustion gas.

For the time interval between 30 min and 45 min (Figures 3 and 4), the reaction front reaches the bottom of the bed, and the fuel bed temperature rises again due to the heat generated by the residual char oxidation with air (T_9, T_{10}, T_{12}, and T_{13}). In this stage, some of the thermocouples may have lower temperatures than others. This resulted in a faster convective cooling [43]. A second difference appears in the maximum value of the temperature, especially during the residual carbon combustion. The OP generated a higher flame front temperature reaching 1200 °C by comparison with 1090 °C and 1050 °C for the OP_i and the wood pellets, respectively. The high temperature observed in the case of olive pomace pellets can be attributed to its high heating value (22.03 MJ/kg on a dry basis). Indeed, this characteristic is strongly related to the carbon content in this sample type (49.5%) [37,44], by comparison with the 46.5% carbon content and 19.4 MJ/kg (*HHV* on a dry basis) for OP_i [14], and also to the 46.3% carbon content and 18.5 MJ/kg (on a dry basis) for the wood pellets [45].

During the main combustion phase characterized by the combustion of the pyrolysis gases, no effect on heat release is observed. Thus, the temperatures profiles are quite similar for the different biofuel pellets. However, during the burning of char, the heat release (*HR*) appears quite different due to different amounts of residual carbon (Table 6). Consequently, the maximum of temperature differs significantly for each sample.

4.2. Mass Loss History in the Fuel Bed and Reaction Front Velocity

Further analysis of experimental results leads to the determination of some combustion parameters, such as:

The reaction front velocity:

$$u_{RF} = \frac{dh}{dt} \tag{3}$$

where u_{RF} is the reaction front velocity, h is the bed height, and dt is the time increment.

The mass conversion rate:

$$MCR = \frac{\dot{m}}{A(1 - Y_{ash})} \tag{4}$$

where *MCR* is the mass conversion rate, $\dot{m}$ is the mass loss rate, A is the fuel bed cross section, and Y_{ash} is the ash mass fraction.

The ignition rate:

$$IR = u_{RF} \times \rho_{BD} \tag{5}$$

IR is the ignition rate, and other variables are defined in the above equations.

The specific heat release rate:

$$HR = MCR \times HHV \tag{6}$$

where *HR* is the heat release, and the two other variables are defined in the above equations.

These characteristic numbers are useful to predict and understand quantitatively the combustion process in the fixed bed. Moreover, these parameters are independent and good indicators of the combustion behavior in large industrial facilities. They are determined in similar ways as described in the literature [22,23,46–48].

4.2.1. Reaction Front Velocity

The position of the reaction front is obtained based on the inflection point in the temperature profiles shown above. In Figure 4a–c, the reaction front position is plotted as a function of the elapsed time, and almost linear curves are obtained. This result indicates a steady and uniform propagation of the flame front. For both samples (OP and OP_i), the reaction front velocities were equal to 3.50 mm/min and 4.00 mm/min respectively (Figure 4b,c); whereas, in the case of wood pellets the reaction front velocity is almost 4.40 mm/min (Figure 4a). The regression factor (R^2) exceeds 0.90 for all reported regressions.

4.2.2. Mass Loss History

The mass conversion rate (*MCR*) is defined as the mass loss per unit area and per unit time. It is obtained directly from the measured mass of the fixed bed, and thereafter, corrected by considering the ash content of the fuel.

The ignition rate (*IR*) defines the quantity of fuel ignited per unit area and per unit time due to the reaction front. This ignition rate is a crucial parameter used to estimate the grate position, where the reaction front reaches its limit at the bottom of the bed, indicating the end of the fuel combustion. Moreover, the heat release rate (*HR*) is determined by multiplying the *HHV* value and the mass conversion rate (Equation (6)).

However, the specific heat release in the main combustion zone (*HR I*) is calculated using *MCR I* and the *HHV* of the fuel. In the char residual oxidation phase, this value (*HR II*) is obtained from values of *MCR II* and *HHV*, respectively of the residual coke. It should be noted that the *HHV* of residual coke is calculated according to [49,50]:

$$HHV_{coke} = 19.6\, Y_{coke} + 14.119 \tag{7}$$

where Y_{coke} is the mass fraction of carbon in the coke, which is approximately 0.85 for lignocellulosic biomass coke [51,52]. HHV_{coke} then is approximately 30.80 MJ/kg.

Figure 5 shows the mass loss of OP, OP_i, and the standard wood pellets as a function of time. During the ignition interval from 0 to 3 min, the mass decreases slightly. This zone corresponds to the moisture evaporation and to the start of devolatilization. Thereafter, in the main combustion phase, the mass decreases steadily and almost linearly. In this important zone, it is possible to determine the two combustion parameters described above: The mass conversion rate (*MCR I*) and the specific heat release *HR I*. Finally, in the char oxidation zone, the decrease of the mass slows down again. *MCR II* (Figure 5) and *HR II* (Table 6) confirm this observation. The *HR* parameter should be below 1 MW/m^2 in the bottom of the bed [23].

The decrease of the heat release rate (*HR II*) in the third zone can be explained by the small oxidation rate of carbon. Moreover, the ignition rates (*IR*) for OP and OP_i are 0.05 $(kg/m^2)/s$ and 0.06 $(kg/m^2)/s$, respectively. These values are of the same order of magnitude of the standard wood pellets (0.05 $(kg/m^2)/s$).

Table 6. Specification Heat Release in the fuel bed.

Heat Release	100% OP	100% OP_i	Wood Pellets
HR I (MW/m^2)	0.96 ± 0.06	0.98 ± 0.08	1.01 ± 0.06
HR II (MW/m^2)	0.12 ± 0.01	0.12 ± 0.02	0.070 ± 0.005

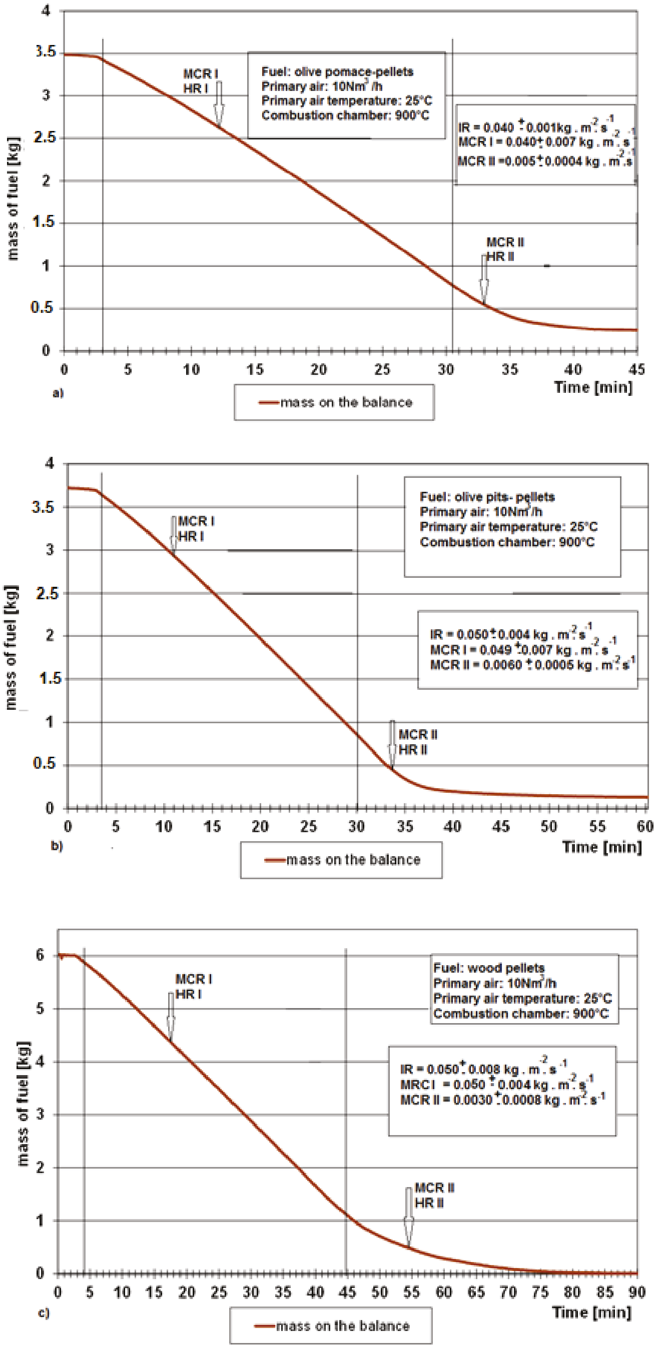

Figure 5. Mass loss curves in the fuel bed: (**a**) 100% OP; (**b**) 100% OP$_i$; (**c**) standard wood pellets. Experimental conditions: Primary air 10 Nm^3/h; primary air temperature 25 °C, and combustion chamber temperature 900 °C.

4.3. Gaseous Emissions

4.3.1. Gaseous Emissions Analysis above the Bed

Figure 6 shows the temporal evolution of the gas concentrations measured directly above the fixed bed (freeboard zone) versus the time during the combustion tests of the different samples. The considered gaseous emissions are respectively; O_2, CO_2, H_2O (steam), H_2, and C_{org} (organic carbon). All components are expressed in % vol. wet basis. Moreover, the local constant of air (λ) is plotted on the right axis.

At the beginning of all experimental tests, only the O_2 concentration in the flue gases is detected in the freeboard due to the primary air supply, and then it decays quickly from the ambient level of 21% to zero percent. In contrast, the H_2O mass flow increases due to the fuel bed drying process. After 4 to 5 min, the fuel ignites. Consequently, the concentrations of CO and CO_2 increases rapidly, while, H_2, C_{org}, and H_2O are released. Hence, the concentration of O_2 is significantly decreased. In addition, we observe that the gaseous emissions remain at a roughly constant level during the combustion process. This period is called: The main combustion zone or the quasi-stationary combustion zone [23]. During the time interval [37 min, 56 min], the reaction front reaches the bottom of the bed. Consequently, we observe a rise in the O_2 concentration again, while the concentrations of H_2 and C_{org} are decreased to their minimum levels. During this period, the char residue burning is enhanced exhibiting a little increase of CO_2. In contrast, CO rises also steeply with the decrease in CO_2 and stabilizes between 20% and 28%. This observation can be attributed to the gasification process for which the residual char is exposed, especially in the presence of CO_2 in the medium [21] according to the following reaction:

$$C + CO_2 \rightarrow 2CO \tag{8}$$

In this zone, the OP pellets are characterized by a high emission of CO which rises to 23% by comparison to 20.2% for the OP_i. But, this concentration remains quietly smaller than the 24.5% for the wood pellets. However, during the combustion process, these values remain still higher than those of CO_2 emissions. This growth may be attributed to the gasification process of the residual char in the presence of the water/steam (H_2O) according to the following reaction:

$$C + H_2O \rightarrow CO + H_2 \tag{9}$$

Indeed, this reaction yields an increase in CO and H_2 at the same time [21,53]. Moreover, Figure 6a shows that OP results in the highest percentage of CO_2 ($\approx$13%) compared to the 11% for OP_i. This result can be attributed to the high percentage of carbon content (about 49.5%) against only 46.5% of the OP_i. After a combustion time within the interval from 43 to 70 min, all gaseous emissions tend to zero, indicating the end of fuel conversion process.

Therefore, the comparison of the different samples shows that the wood pellets (Figure 6c) have the most stable emissions compared to OP and OP_i. Such behavior may be attributed first, to the lower moisture content (about 6.5%) compared with other samples, and second, to the chemical complexity of OMSWs samples when compared with wood pellets. Indeed, the chemical composition of the olive mill solid wastes is more complex with polyphenols, pectin, and fatty acids. In addition, this difference of behavior between woody pellets and OMSWs pellets can be attributed to the fact that the used reactor was designed to be fed by woody biomass rather than by olive mill by-products. Hence, modifications concerning primary air and secondary air positions and flow rates should be undertaken to increase the reactor efficiency when using OMSWs pellets.

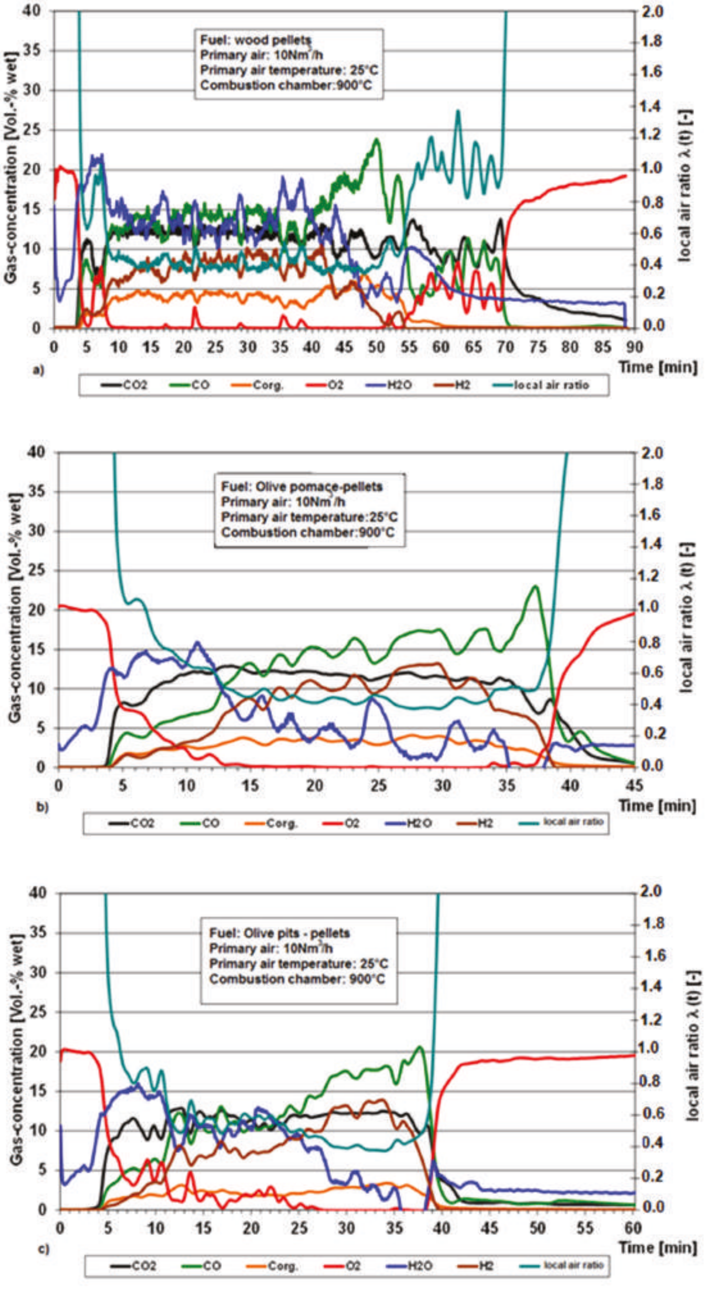

Figure 6. Concentrations of gaseous emissions analysis above the fixed bed (in the freeboard): (**a**) 100% standard wood pellets, (**b**) OP and (**c**) 100% OP_i. Experimental conditions: Primary air 10 Nm^3/h; primary air temperature 25 °C and combustion chamber temperature 900 °C.

4.3.2. Gaseous Emissions Analysis in the Post-Combustion Chamber

Figure 7 shows the temporal distribution of the traces of gas concentrations versus time in the flame front, especially, at the outlet of the post-combustion chamber. More specifically, we focus in this section on NO_x (nitrogen oxides), N_2O (nitrous oxide), and SO_2 (sulphur dioxide), expressed in mg/Nm^3, dry at normal temperature (25 °C) and pressure. Meanwhile, O_2, CO_2, and CO concentrations are also considered.

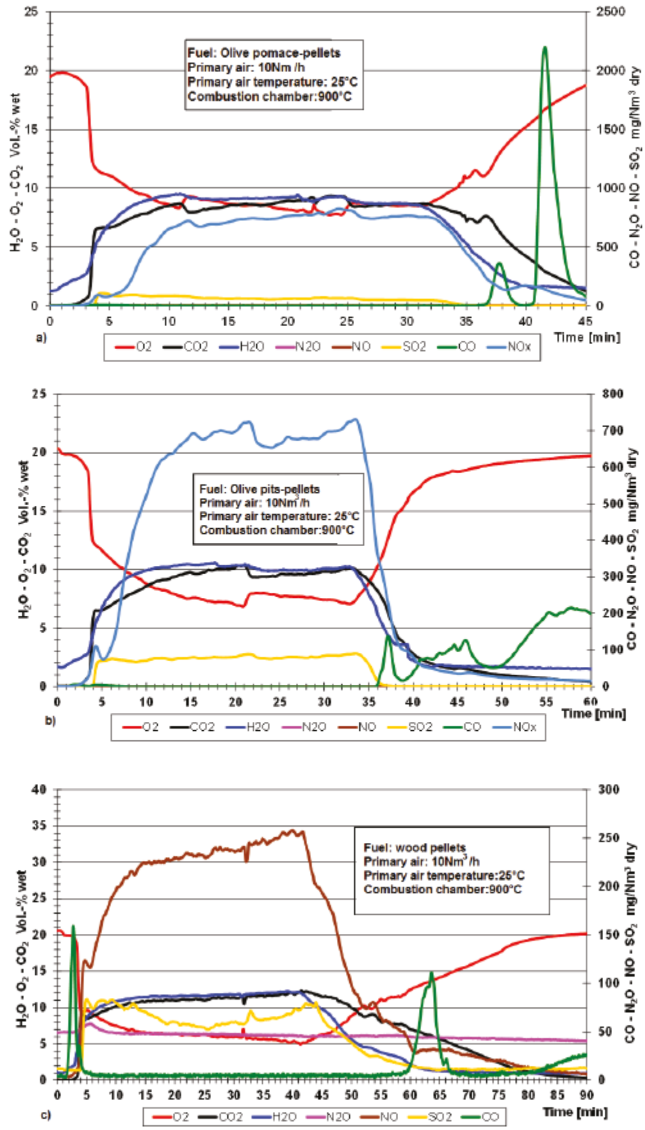

Figure 7. Traces of gases measured at the outlet of the post-combustion chamber (**a**) 100% OP; (**b**) 100% OP_i and (**c**) wood pellets.

When examining Figure 7, we observe that the emissions of NO_x at the secondary combustion chamber are relatively high when compared to the SO_2 emission. This increase may be attributed to the fuel-N combustion occurring in the post-combustion especially in the presence of a high flow of injected secondary air. Hence, a notable increase of the temperature in the medium results in NO formation (or thermal NO), and the corresponding mechanism is the so-called Zel'dovich mechanism. This mechanism consists of molecules dissociation at high temperature so that each molecule of oxygen and nitrogen in lean flame condition (Equivalence ratio less than 1.0) is dissociated into two atoms. Hence, the pair of reactions was first proposed by Y.B. Zel'dovich [54]:

$$O + N_2 \rightarrow NO + N \tag{10}$$

$$N + O_2 \rightarrow NO + O \tag{11}$$

Furthermore, the reduction of CO is consistent with the increase of the excess air in the secondary combustion chamber [55]. In contrast, Garijo et al. [56] and Staiger et al. [57] indicate that an increase in the CO concentration or another carbonaceous compound can inhibit the formation of NO_x. This is mainly due to a reduction of the temperature by heat absorption in the medium. On the other hand, the emissions of NO_x (Figure 7a) of the OP showed the highest value with about 895 mg/Nm^3 compared to 720 mg/Nm^3 (Figure 7b) of the OP_i and to almost 255 mg/Nm^3 (Figure 7c) of the wood pellets. In fact, this result is expected because the nitrogen content in olive pomace (1.26%) is higher than that of wood pellets (0.11%) and also than that of olive pits (0.61%) [58,59]. Moreover, this NO_x concentration growth can also be justified by the abundance of O_2 supplied to the post-combustion chamber [28]. In contrast, the emissions of SO_2 during the combustion tests of the pellets samples (OP and OP_i) exhibit only small traces of this compared to standards biofuels (ex. wood pellets). This may be attributed to the low sulphur contents ($\leq$0.1) for the different samples.

4.3.3. Conversion Unit of Gaseous Emissions

The gaseous emissions that we obtained were corrected and converted at 10% and 13% O_2 according to the following formula:

$$X_{O_2,ref} = X_{O_2,meas} \frac{21 - [O_2]_{ref}}{21 - [O_2]_{meas}} \tag{12}$$

The purpose of this conversion is to allow comparison between our results and those found by authors working under same conditions (10% O_2 and 13% O_2) and for which gaseous concentrations were expressed either in ppm or in mg/Nm^3as it is summarized in Table 7.

where X is the gas concentration, the subscript "O_2, ref" refers to the fixed oxygen concentration under which we want calculate X, and the subscript "O_2, meas" is related to the measured X value under the fixed oxygen value during the experiment.

We notice that gaseous emissions obtained in our study, with a fixed bed of 40 kW, are in the same range as other lignocellulosic materials. However, the concentrations of nitrogen oxides (NO_2 + NO) obtained at the post-combustion chamber were equal to 142 ppm and 116 ppm, at 10% O_2 for OP and OP_i, respectively. These values are of the same magnitude than 113 ppm NO_x obtained for the standard wood pellets. However, these values are higher than value obtained with the DIN plus (54 ppm at 10% O_2) [60]. In fact, the concentrations of NO_x were comparatively smaller (<30 ppm at 13% O_2), during the combustion of commercial pine pellets in a domestic pellets boiler (22 kW) [61]. Moreover, these values are close to those found in the literature for various pellets such as exhausted olive mill solid wastes (EOMSW) (115 ppm at 10% O_2), and olive pruning pellets (340 ppm at 10% O_2) [62]. Furthermore, the values of SO_2 varied between 14 and 22 ppm at 10% O_2 and between 10 and 16 ppm at 13% O_2 according to the obtained results. Nevertheless, these values remain lower than 36 ppm at 10% O_2 obtained for Sunflower shells [63]. Mohon et al. [64] showed that the combustion of grass pellet and three different types of wood pellets, when tested in a prototype pellet furnace (7–32 kW), emit between 0 and 7 ppm of SO_2 at 10% O_2.

Table 7. Emissions values corrected at respectively; (a) 10% O_2 and (b) 13% O_2.

Samples	O_2%	CO_2%	CO [1] %	H_2O%	H_2%	CO [2] (ppm)	NO_x (ppm)	SO_2 (ppm)
100 OP	11	6.84	11.58	8	7.63	(a) 1446 (b) 1054	(a) 142 (b) 104	(a) 22 (b) 16
100 OP_i	10.37	5.85	10.64	8	7.72	(a) 133 (b) 97	(a) 116 (b)84	(a) 17 (b) 12
Wood pellets	9.94	7	12.62	11.57	5.26	(a) 46 (b) 34	(a) 13 for N_2O; 100 for NO (b) 11 for N_2O; 73 for NO	(a) 14 (b) 10
Spent coffee ground (SCG) [65]	4	5	-	-	-	(a) 2456 (b) 1785	(a) 245 for NO; 39 for N_2O (b) 178 for NO; 28 for N_2O	-
Wood DIN plus [60]	12	6	-	-	-	(b) 153	(b) 19	-
EOMSW [36]	12	8	-	-	-	(a) 795 (b) 578	(a) 115 (b) 85	-
Sawdust (S) [36]	12	6	-	-	-	(a) 277 (b) 202	(a) 36 (b) 26	-
Sunflower shells [61]	13	-	-	-	-	(a) 252	(a) 55	(a) 36
French Wood pellets [61]	15	6	-	-	-	(a) 277	(a) 36	(a) 7
Pine pellets [62]	13.22	4.5	-	-	-	(b) 470	(b) 50	-

OMSW: olive mill solid waste, EOMSW: exhaust olive mill solid waste; [1] At the primary combustion chamber; [2] At the post-combustion chamber.

5. Conclusions

In this paper, olive pomace OP and olive pits OP_i have been investigated as renewable and environmentally friendly energy sources. More precisely, we focused on the combustion of the pelletized biofuels in a 40 kW counter-current fixed bed reactor. The temperature inside the bed and the mass loss were measured. Three distinct phases for the progress of the combustion process were observed: The ignition delay time, the main combustion phase, and the char oxidation phase. Moreover, some crucial combustion parameters were evaluated: The reaction front velocity, the ignition rate, the heat release rate, and the mass conversion rate.

We have found that the results are quite similar to results of the standard wood pellets which are used currently in European markets. Moreover, we have observed that the gaseous emissions are produced in acceptable concentrations compared to Germany and European standards. Hence, these results motivate future investigations to reuse the olive mill solid wastes for producing alternative biofuels which can be used for heat and/or electricity production, either in domestic or in industrial plants.

Author Contributions: Funding acquisition, H.-J.G. and M.L.; Investigation, H.M. and M.L.; Methodology, H.M., D.S. and M.L.; Project administration, H.-J.G.; Resources, R.B.; Supervision, H.M. and M.L., Writing-original draft, M.A.M. and M.L.; Writing-review and editing, H.M., H.-J.G., D.S. and R.B.

Funding: This research received no external funding.

Acknowledgments: Mohamed Ali Mami would like to thank the Doctoral School of Monastir University for the Financial Support of this project. In addition, the author is grateful to Zouila Company (Mahdia-Tunisia) for providing him the raw biomass. In addition, the author expresses deep thanks to A. Gerig and other technical team members of KIT for their assistance during the experimental tests. Marzouk Lajili would like to address special thanks to Professor T. Echekki (N.C.U.) for his precious comments and for his help with English.

Conflicts of Interest: The authors declare no conflict of interest.

Nomenclature

A	Fuel bed cross-section (m^2)
HHV	Higher heating value (MJ·kg^{-1})
HR	Heat release rate (MW·m^{-2})
IR	Ignition rate (kg·m^{-2}·s^{-1})
MCR	Mass conversion rate (kg·m^{-2}·s^{-1})
h	Bed height (mm)
$\dot{m}$	Mass loss rate (kg·s^{-1})
u	Velocity (mm·min^{-1})
y	Mass fraction (-)
ρ	Density (kg·m^{-3})
L	Latent heat (kJ·kg^{-1})

Subscripts and Superscripts

ash	ash
RF	Reaction front
C_{coke}	Carbon in coke
BD	Bulk density
v	vaporization

References

1. Demirbas, A. Combustion characteristics of different biomass fuels. *Prog. Energy Combust. Sci.* **2004**, *30*, 219–230. [CrossRef]
2. Heschel, W.; Rweyemamu, L.; Scheibner, T.; Meyer, B. Abatement of emission in small-scale combustors through utilization ofblended pellet fuels. *Fuel Process. Technol.* **1999**, *61*, 223–242. [CrossRef]
3. Saidur, R.; Abdelaziz, E.A.; Demirbas, A.; Hossain, M.S.; Mekhilef, S. A review on biomass as a fuel for boilers. *Renew. Sustain. Energy Rev.* **2011**, *15*, 2262–2289. [CrossRef]
4. Christoforou, E.; Fokaides, P.A. A review of olive mill solid wastes to energy utilisation techniques. *Waste Manag.* **2016**, *49*, 346–363. [CrossRef] [PubMed]
5. Rodríguez, G.; Lama, A.; Rodríguez, R.; Jiménez, A.; Guillén, R.; Fernández-Bolaños, J. Olive stone an attractive source of bioactive and valuable compounds. *Bioresour. Technol.* **2008**, *99*, 5261–5269. [CrossRef] [PubMed]
6. Lopez, F.J.; Pinzi, S.; Ruiz, J.J.; Lopez, A.; Dorado, M.P. Economic viability of the use of olive tree pruning as fuel for heating systems in public institutions in South Spain. *Fuel* **2010**, *89*, 1386–1391. [CrossRef]
7. Moya López, A.J.; Mateo Quero, S. Aprovechamiento de los residuos del olivar. Available online: https://www.researchgate.net/publication/259228577_Aprovechamiento_de_los_residuos_del_olivar (accessed on 20 June 2018).
8. Mata-Sánchez, J.; Pérez-Jimenéz, J.A.; Díaz-Villanueva, M.J.; Serrano, A.; Núñez-Sánchez, N.; López-Giménez, F.J. Development of Olive stones quality system based on biofuel energetic parameters study. *Renew. Energy* **2014**, *66*, 251–256. [CrossRef]
9. Pattara, C.; Cappelletti, G.M.; Cichelli, A. Recovery and use of olive stones: commodity, environmental and economic assessment. *Renew. Sustain. Energy Rev.* **2010**, *14*, 1484–1489. [CrossRef]
10. Alkhamis, T.M.; Kablan, M.M. Olive cake as an energy source and catalyst for oil shale production of energy and its impacton the environmental. *Energy Convers. Manag.* **1999**, *40*, 1863–1870. [CrossRef]
11. Ramachandran, S.; Singh, S.K.; Larroche, C.; Soccol, C.R.; Pandey, A. Oil cakes and their biotechnological applications—A reviews. *Bioresour. Technol.* **2007**, *98*, 2000–2009. [CrossRef] [PubMed]
12. Brlek, T.; Pezo, L.; Voća, N.; Krička, T.; Vukmirović, Đ.; Čolović, R.; Bodroža-Solarov, M. Chemometric appraoch for assessing the quality of olive cake pellets. *Fuel Process. Technol.* **2013**, *116*, 250–256. [CrossRef]
13. Christoforou, E.; Kylili, A.; Fokaides, P.A. Technical and economical evaluation of olive mills solid waste pellets. *Renew. Energy* **2016**, *96*, 33–41. [CrossRef]
14. González, J.F.; González-García, C.M.; Ramiro, A.; González, J.; Sabio, E.; Gañán, J.; Rodríguez, M.A. Combustion optimisation of biomass residue pellets for domestic heating with a mural boiler. *Biomass Bioenergy* **2004**, *27*, 145–154. [CrossRef]

15. Lajili, M.; Jeguirim, M.; Kraiem, N.; Limousy, L. Performance of a household boiler fed with agropellets blended from olive mill solid waste and pine sawdust. *Fuel* **2015**, *153*, 431–436. [CrossRef]
16. Miranda, T.; Arranz, J.I.; Montero, I.; Román, S.; Rojas, C.V.; Nogales, S. Characterization and combustion of olive pomace and forest residue pellets. *Fuel Process. Technol.* **2012**, *103*, 91–96. [CrossRef]
17. Miranda, M.T.; Cabanillas, A.; Rojas, S.; Montero, I.; Ruiz, A. Combined combustion of various phases of olive wastes in a conventional combustor. *Fuel* **2007**, *86*, 367–372. [CrossRef]
18. Khodaei, H.; Al-Abdeli, Y.M.; Guzzomi, F.; Yeoh, G.H. An overview of processes and considerations in the modelling of fixed-bed biomass combustion. *Energy* **2015**, *88*, 946–972. [CrossRef]
19. Yang, Y.B.; Sharifi, V.N.; Swithenbank, J. Effect of air flow rate and fuel moisture on the burning behaviours of biomass and simulated municipal solid wastes in packed beds. *Fuel* **2004**, *83*, 1553–1562. [CrossRef]
20. Porteiro, J.; Patiño, D.; Collazo, J.; Granada, E.; Moran, J.; Miguez, J.L. Experimental analysis of the ignition front propagation of several biomass fuels in a fixed-bed combustor. *Fuel* **2010**, *89*, 26–35. [CrossRef]
21. Ménard, Y. Modélisation de L'incinération sur Grille D'ordures Ménagères et Approche Thermodynamique du Comportement des Métaux Lourds. Ph.D. Thesis, National Polytechnic Institute of Lorraine, Nancy, France, July 2008.
22. Mätzing, H.; Germann, H.-J.; Kolb, T.; Seifert, H. Experimental and numerical investigation of wood particle combustion in fixed bed reactors. *Environ. Eng. Sci.* **2012**, *29*, 907–914. [CrossRef]
23. Baris, D.; Gehrmann, H.-J.; Mätzing, H.; Stapf, D.; Seifert, H.; McGowan, T. Characterization of the combustion behavior of "DMC fuel$^{\text{TM}}$". In Proceedings of the 34th International Conference on Thermal Treatment Technologies and Hazardous Waste Combustors, Houston, TX, USA, 20–22 October 2015.
24. Demirbas, A. Potential applications of renewable energy sources, biomass combustion problems in boiler power systems and combustion related environmental issues. *Prog. Energy Combust. Sci.* **2005**, *31*, 171–192. [CrossRef]
25. Demirbas, A. Calculation of higher heating values of biomass fuels. *Fuel* **1997**, *76*, 431–434. [CrossRef]
26. McKendry, P. Energy production from biomass (part 1): Overview of biomass. *Bioresour. Technol.* **2002**, *83*, 37–46. [CrossRef]
27. Vassilev, S.V.; Baxter, D.; Andersen, L.K.; Vassileva, C.G. An overview of the chemical composition of biomass. *Fuel* **2010**, *89*, 913–933. [CrossRef]
28. Varol, M.; Atimtay, A.T. Combustion of olive cake and coal in a bubbling fluidized bed with secondary air injection. *Fuel* **2007**, *86*, 1430–1438. [CrossRef]
29. Borello, D.; De Caprariis, B.; DeFilippis, P.; Di Carlo, A.; Marchegiani, A.; Marco Pantaleo, A.; Shah, N.; Venturini, P. Thermo-economic Assessment of a olive pomace Gasifier for Cogeneration Applications. *Energy Procedia* **2015**, *75*, 252–258. [CrossRef]
30. González, J.F.; Román, S.; Encinar, J.M.; Martínez, G. Pyrolysis of various biomass residues and char utilization for the production of activated carbons. *J. Anal. Appl. Pyrolysis* **2009**, *85*, 134–141. [CrossRef]
31. Atimay, A.T. Combustion of agro-waste with coal in fluidized bed. *Clean Technol. Environ. Policy* **2010**, *12*, 43–52. [CrossRef]
32. Abu-Qudais, M. Fluidized bed combustion for energy production from olive cake. *Energy* **1996**, *21*, 173–178. [CrossRef]
33. Skoulou, V.; Koufodimos, G.; Samaras, Z.; Zabaniotou, A. Low temperature gasification of olive kernels in a 5-kW fluidized bed reactor for H_2-rich producer gas. *Int. J. Hydrogen Energy* **2008**, *33*, 6515–6524. [CrossRef]
34. Chiang, K.-Y.; Chien, K.-L.; Lu, C.-H. Characterization and comparison of biomass produced from various sources: suggestions for selection of pretreatment technologies in biomass-to-energy. *Appl. Energy* **2012**, *100*, 164–171. [CrossRef]
35. Nunes, L.J.R.; Matias, J.C.O.; Catalão, J.P.S. Mixed biomass pellets for thermal energy production: a review of combustion models. *Appl. Energy* **2014**, *127*, 135–140. [CrossRef]
36. Karkania, V.; Fanara, E.; Zabaniotou, A. Review of sustainable biomass pellets production—A study for agricultural residues pellets' market in greece. *Renew. Sustain. Energy Rev.* **2012**, *16*, 1426–1436. [CrossRef]
37. Lajili, M.; Limousy, L.; Jeguirim, M. Physico-chemical properties and thermal degradation characteristics of agropellets from olive mill by-products/sawdust blends. *Fuel Process. Technol.* **2014**, *126*, 215–221. [CrossRef]
38. Fasina, O.O. Physical properties of peanut hull pellets. *Bioresour. Technol* **2008**, *99*, 1259–1266. [CrossRef] [PubMed]

39. Lehtikangas, P. Quality properties of pelletised sawdust, logging residues and bark. *Biomass Bioenergy* **2001**, *20*, 351–360. [CrossRef]
40. Markovic, M.; Bramer, E.A.; Brem, G. Experimental investigation of wood combustion in a fixed bed with hot air. *Waste Manag.* **2014**, *34*, 49–62. [CrossRef] [PubMed]
41. Kolb, T.; Bleckwehl, S.; Gehrmann, H.-J.; Seifert, H. Characterisation of combustion behaviour of refuse derived fuel. *J. Energy Inst.* **2008**, *81*, 1–6. [CrossRef]
42. Thunman, H.; Leckner, B. Co-current and counter-current fixed bed Combustion of biofuel: A comparison. *Fuel* **2003**, *82*, 275–283. [CrossRef]
43. Porteiro, J.; Patiño, D.; Miguez, J.L.; Granada, E.; Moran, J.; Collazo, J. Study of the reaction front thickness in a counter-current fixed-bed combustor of a pelletised biomass. *Combust. Flame* **2012**, *159*, 1296–1302. [CrossRef]
44. Meranda, T.; Montero, I.; José Sepúlveda, F.; Arranz, J.I.; Rojas, C.V.; Nogales, S. A review of pellets from different sources. *Materials* **2015**, *8*, 1413–1427. [CrossRef] [PubMed]
45. Magelli, F.; Boucher, K.; Bi, H.T.; Melin, S.; Bonoli, A. An environmental impact assessment of exported wood pellets from canada to europe. *Biomass Bioenergy* **2009**, *33*, 434–441. [CrossRef]
46. Ryu, C.; Phan, A.N.; Yang, Y.; Sharifi, V.N.; Swithenbank, J. Ignition and burning rates of segregated waste combustion in packed beds. *Waste Manag.* **2007**, *27*, 802–810. [CrossRef] [PubMed]
47. Gehrmann, H.-J.; Kolb, T.; Seifert, H.; Mark, F.E.; Frankenhaeuser, M.; Schanssema, A.; Wittstock, K.; Kolb, J.J. Synergies between biomass and solid recovered fuel in energy conversion processes. *Environ. Eng. Sci.* **2010**, *27*, 557–567. [CrossRef]
48. Shin, D.; Choi, S. The combustion of simulated waste in a fixed bed. *Combust. Flame* **2000**, *180*, 121–167. [CrossRef]
49. Ahmaruzzaman, M. Proximate analyses and predicting hhv of chars obtained from cocracking of petroleum vacuum residue with coal, plastics and biomass. *Bioresour. Technol.* **2008**, *99*, 5043–5050. [CrossRef] [PubMed]
50. Vargas-Moreno, J.M.; Callejón-Ferre, A.J.; Pérez-Alonso, J.; Velázquez-Martí, B. A review of the mathematical models for predicting the heating value of biomass materials. *Renew. Sustain. Energy Rev.* **2012**, *16*, 3065–3083. [CrossRef]
51. Kawakami, M.; Karato, T.; Takenaka, T.; Yokoyama, S. Structure analysis of coke, wood charcoal and bamboocharcoal by Raman spectroscopy and the irreaction rate with CO_2. *ISIJ Int.* **2005**, *45*, 1027–1034. [CrossRef]
52. Mueller, A.; Haustein, H.D.; Stoesser, P.; Kreitzberg, T.; Kneer, R.; Kolb, T. Gasification kinetics of biomass- and fossil-based fuels: Comparison study using fluidized bed and thermogravimetric analysis. *Energy Fuels* **2015**, *29*, 6717–6723. [CrossRef]
53. Imen, G.; Mejdi, J.; Uta, S.; Lionel, L.; Simona, B.; Eckhard, D.; Christof, A.; Roman, L.; Frank, S.; Abedlmottaleb, O. The Potential of Activated Carbone Made From Agro-Industrial Residues in NO_x Immessions. *Energies* **2017**, *10*, 1508. [CrossRef]
54. Anetor, L.; Odetunde, C.; Osakue, E.E. Computational Analysis of Extended Zel'dovich Mechanism. *Arab. J. Sci. Eng.* **2014**, *39*, 8287–8305. [CrossRef]
55. Atimtay, A.T.; Varol, M. Investigations of co-combustion of coal and olive cake in a bubbling fluidized bed with secondary air injection. *Fuel* **2009**, *88*, 1000–1008. [CrossRef]
56. Garijo, E.G.; Jensen, A.D.; Glarborg, P. Kinetic Study of NO Reduction over Biomass Char under Dynamic Conditions. *Energy Fuels* **2003**, *17*, 1429–1436. [CrossRef]
57. Staiger, B.; Unterberger, S.; Berger, R.; Hein, K.R.G. Development of an air staging technology to reduce NOx emissions in grate-fired boilers. *Energy* **2005**, *30*, 1429–1438. [CrossRef]
58. Nussbaumer, T. Combustion and co-combustion of biomass: Fundamentals, Technologies and Primary measures for Emission Reduction. *Energy Fuels* **2003**, *15*, 10–21. [CrossRef]
59. Stubenberger, G.; Scharler, R.; Zahirovic, S.; Obernberger, I. Experimental investigation of nitrogen species release from different solid biomass fuels as basis for release models. *Fuel* **2008**, *87*, 793–806. [CrossRef]
60. Kraiem, N.; Lajili, M.; Limousy, L.; Said, R.; Jeguirim, M. Energy recovery from Tunisian agri-food wastes: Evaluation of combustion performance and emissions characteristics of green pellets prepared from tomato residues and grape marc. *Energy* **2016**, *107*, 409–418. [CrossRef]

61. Fernandes, U.; Costa, M. Particle emissions from a domestic pellets-fired boiler. In Proceedings of the 4th International Congress on Energy and Environment Engineering and Management, Mérida, Spain, 26–27 May 2011.
62. Garcia-Maraver, A.; Zamorano, M.; Fernandes, U.; Rabaçal, M.; Costa, M. Relationship between fuel quality and gaseous and particulate matter emission in a domestic pellet-fired boiler. *Fuel* **2014**, *119*, 141–152. [CrossRef]
63. Cardozo, E.; Erlich, C.; Alejo, L.; Fransson, T.H. Combustion of agriculture residues: An experimental study for small-scale applications. *Fuel* **2014**, *115*, 778–787. [CrossRef]
64. Roy, M.M.; Dutta, A.; Corscadden, K. An experimental study of combustion and emissions of biomass pellets in a prototype pellet furnace. *Appl. Energy* **2013**, *108*, 298–307. [CrossRef]
65. Limousy, L.; Jeguirim, M.; Dutournié, P.; Kraiem, N.; Lajili, M.; Said, R. Gaseous products and particulate matter emissions of biomass residual boiler fired with spent coffee ground pellets. *Fuel* **2013**, *107*, 323–329. [CrossRef]

energies

MDPI

Article

Preparation and Evaluation of a Coconut Shell-Based Activated Carbon for CO_2/CH_4 Separation

Amna Abdeljaoued [1,2,*], Nausika Querejeta [3], Inés Durán [3], Noelia Álvarez-Gutiérrez [3], Covadonga Pevida [3] and Mohamed Hachemi Chahbani [1,4]

[1] LR11ES54-Laboratory of "Chemical Processes and Industrials Systems", University of Gabes, Gabès 6029, Tunisia; chahbani.med_hachemi@yahoo.com
[2] National School of Engineers of Gabes (ENIG), University of Gabes, Omar Ibn Elkhattab Street, Zrig, Gabès 6029, Tunisia
[3] Instituto Nacional del Carbón, INCAR-CSIC, c/Francisco Pintado Fe 26, 33011 Oviedo, Spain; n.querejeta@incar.csic.es (N.Q.); i.duran@incar.csic.es (I.D.); noeag0591@gmail.com (N.Á.-G.); cpevida@incar.csic.es (C.P.)
[4] Higher Institute of Applied Sciences and Technology of Gabes, University of Gabes, Omar Ibn Elkhattab Street, Zrig, Gabes 6029, Tunisia
* Correspondence: amna.abdeljawad.2009@gmail.com

Received: 7 June 2018; Accepted: 29 June 2018; Published: 3 July 2018

Abstract: Biomass is a widely distributed and renewable source of carbon. The main objective of this work is to produce an activated carbon from coconut shells with suitable characteristics to separate CO_2 from biogas. The textural characterization of the adsorbent has been determined. Pure component adsorption isotherms of CO_2 and CH_4 at 30, 50 and 70 °C have been measured. The results reveal that the activated carbon had high CO_2 adsorption capacity. Equilibrium of adsorption of CO_2 and CH_4 adsorption on the produced activated carbon reached 8.36 mmol/g and 4.63 mmol/g, respectively, at 30 °C and 10 bars. Moreover, the performance of the produced activated carbon, as a potential adsorbent for CO_2 capture from a CO_2/CH_4 gas mixture, has been evaluated under dynamic conditions in a dedicated fixed-bed setup. The CO_2 and CH_4 adsorption capacities of the produced activated carbon are estimated to be 1.86 and 0.52 mol/kg, respectively, at 30 °C and 1 bar.

Keywords: biogas purification; coconut shells; biomass valorization; textural characterization; adsorption isotherms; breakthrough curves

---

1. Introduction

Biogas is a biofuel that is naturally produced by the decomposition of various types of organic matter. Upgrading of biogas has gained important attention due to the steady growth in global energy demand, coupled with the depletion of fossil fuel resources, their unaffordable prices, and the environmental damage they cause [1–3].

Methane and carbon dioxide are the main components of biogas. The energy value of biogas is much lower than natural gas due to the presence of carbon dioxide. Thus, to increase its heating value, the carbon dioxide content must be reduced. From the economic side, the CO_2 removal is the most important step in biogas upgrading.

Capture and storage of CO_2 has gained an important place in efforts to reduce greenhouse gas emissions [4,5].

Key economic and environmental factors promote the development of energy-efficient CO_2 separation technologies [6].

Among the various processes proposed to remove CO_2 from biogas, namely adsorption, absorption, membrane and cryogenic separation, pressure swing adsorption (PSA) processes are often used [7–13].

The selection of the adsorbent is a key factor for the efficient operation of a PSA unit. The properties of the adsorbents are one of the most important aspects of unit performance for a determined cycle configuration [14]. Many solid adsorbents have been investigated for the separation of CO_2 from gas effluents, such as zeolites, calcium oxides, activated carbons, hydrotalcites, metal–organic framework (MOF) materials and supported amines [15–20]. Over the past few decades, the use of biomass to prepare carbon-based materials to reduce greenhouse gas emissions has attracted special attention [21–26].

In general, activated carbons can be synthesized from a wide range of biomass materials given that they present low levels of inorganic compounds (ash content) and high carbon content. Many carbon-based materials such as peat, wood, lignite, coal and nut shells are being used in the production of commercial activated carbons. The (CNS) is characterized with high lignin, high carbon content and low ash content; these properties make the material suitable for the production of microporous activated carbons [27,28].

Two conventional methods for biomass activation have been reported: physical and chemical activation procedure [29,30].

Chemical activation is considered an ineffective environmental procedure as it uses solvents to dissolve reagents, extract and wash products, separate mixtures, clean reaction apparatus and disperse products for practical applications. On the contrary, physical activation is ecological in relation to chemical activation. In the present work, a physical activation method using a single step was selected.

The activated carbon produced can be found in pellet, powder or granular form [31–33]. The main purpose of this work is to produce an activated carbon from dry CNS utilizing a physical activation procedure and to evaluate the textural characteristics and the performance of the produced adsorbent for CO_2 separation from biogas effluents.

2. Material and Methods

2.1. Precursor Material

CNS was selected as carbon-based material for the production of the activated carbon. The carbon material was ground and sieved and particles between 1 and 3 mm were selected. The UNE 32-004-84 standard was adopted to conduct the proximate analysis using a thermogravimetric analyser TAG24 Ultimate analyses were carried out in a LECO VTF-900 and in a LECO CHNS-932, respectively.

The non-isothermal mass-loss profile of the precursor material in carbon dioxide atmosphere was determined using a thermogravimetric analyzer Setaram TGA92 (France) in order to elucidate optimal activation time and temperature.

The raw CNS was introduced in a platinum crucible (70 μL) and was dried for one hour at 100 °C in nitrogen flow; then a carbon dioxide (activating agent) flow (50 mL/min) was used to heat up the sample up to 1000 °C using a heating rate of 15 °C/min and kept at this final temperature during 30 min.

2.2. Activated Carbon Production

Once the activation conditions were selected, the production of the activated carbon was initiated. A vertical tubular kiln was used for that purpose. The raw CNS was introduced in a quartz jacketed reactor and then placed in the vertical tubular kiln. The experimental set-up has been described elsewhere [34].

After a drying step, the reactor was cleaned with N_2 flow for 30 min at ambient temperature and a CO_2 gas flow rate of 100 mL/min was used to heat up the system up to 900 °C at a heating rate of 10 °C/min. A thermocouple was placed in the reactor to control the temperature variation. The sample was kept at this temperature in carbon dioxide atmosphere for 73 min. Then the gas was shifted to nitrogen and the sample was cooled down to ambient temperature.

The adsorption capacity of CO_2 of the synthetized activated carbon was tested in a TGA 92 thermogravimetric analyzer from Setaram following the procedure described elsewhere [35].

The produced activated carbon particles between 1 and 2 mm were selected for this study. A Micromeritics ASAP 2010 was used for the characterization of the adsorbent by N_2 physical adsorption at −196 °C. A Micromeritics TriStar 3000 volumetric apparatus was used to assess the CO_2 adsorption at 0 °C.

Before gas adsorption experiments, the sample was purged overnight at 100 °C under vacuum. The N_2 adsorbed quantity, at a relative pressure of 0.99, was used to calculate the total pore volume (V_p). The Brunauer–Emmett–Teller (BET) equation was used to estimate the apparent surface area using the N_2 adsorption isotherms at −196 °C [36]. The helium density was determined using an Accupyc 1330 equipment at 35 °C. The micropore volume (W_0) was calculated using Dubinin–Radushkevich (DR) and Dubinin–Astakhov (DA) equations [37] .The average micropore width was estimated by means of the Stoeckli–Ballerini relation [38]. A Micromeritics Autopore IV 9500 mercury porosimeter was used to calculate the apparent density at 0.1 MPa.

2.3. Adsorption Isotherms

To evaluate the performance of the prepared adsorbent for biogas upgrading, adsorption isotherms of pure CO_2 and CH_4 experiments were conducted using a high-pressure magnetic suspension balance, Rubotherm-VTI.

Three temperatures (30, 50 and 70 °C) and pressure up to 10 bars were selected for the study. Before the adsorption experiment, the sample (approximately 1 g) was placed in the measuring cell, which was dried at 100 °C for 120 min under vacuum. The temperature was then decreased to the desired temperature, and pressurized with pure CO_2 or CH_4 gas. When equilibrium was achieved, the weight variation of the sample, the pressure and temperature were collected. Experiments with helium were performed to account for the buoyancy correction. CO_2 and CH_4 absolute quantity adsorbed at pressures up to 10 bars were calculated based on the procedure mentioned in a precedent work [39].

2.4. Breakthrough Measurements

To study the performance of the synthesized activated carbon for CO_2/CH_4 separation under dynamic conditions, breakthrough measurements of an equimolar gas mixture were performed in a lab-scale fixed-column packed with 5.914 g of adsorbent material. The experimental set-up is described in detail elsewhere [40].

The amount of gas flow at the exit of the fixed bed was measured using a mini CORIFLOW meter from Bronkhorst. The concentration of the outlet gas was assessed using a dual-channel micro-gas chromatograph, Varian CP-4900, fitted with a thermal conductivity detector (TCD).

The column was filled with the CNS adsorbent to evaluate the CO_2/CH_4 adsorption under dynamic conditions. An equimolar biogas CO_2/CH_4 gas mixture was fed (30 mL/min STP) to the column and the performance of the sample was evaluated under isothermal conditions (30 °C) at 1 bar. The adsorbed gases were completely desorbed by flowing 50 mL/min STP of He and increasing the column temperature to 180 °C at 1 bar.

Adsorption–desorption cycles were carried out to explore the reproducibility of the system, where adsorption was maintained until saturation was achieved and desorption was carried out until the adsorbent bed was totally regenerated. For the adsorption step, the concentrations of CO_2 and CH_4 in the bed effluent gas were incessantly controlled as a time-depending function (breakthrough curve), and for dynamic equilibrium, the capacity of adsorption of adsorbent was determined when the concentration of CO_2 is equal to that of the feed.

Breakthrough time, t_b, defined as the time required for the detection of CO_2 at the exit of the column, and the adsorption capacity of CO_2 at equilibrium, were calculated as the average of the values obtained from the six successive cycles [34].

3. Results and Discussion

3.1. Precursor Material

The data obtained from the proximate and ultimate analyses of CNS are summarized in Table 1. Proximate analysis shows that CNS are characterized by low ash content (0.42 wt.%), which is a desirable feature for activated carbon production. Ultimate analysis shows that the raw material possesses a high carbon content (i.e., 51.6 wt.%) and low hydrogen and oxygen contents. In addition, the absence of sulfur in the raw material eliminates the possibility of sulfur dioxide emission during the production process. These data make CNS a promising material to be utilized as an activated carbon precursor.

Table 1. Proximate and ultimate analyses of the raw (CNS).

	Proximate Analysis (wt.%)		**Ultimate Analysis (wt.%, daf)**				
Sample	**Moisture**	**Ash (db)**	**C**	**H**	**N**	**S**	**O**
CNS	12.55	0.42	51.6	5.6	0.1	0	42.7

db: dry basis; daf: dry ash free basis.

Weight loss of the CNS during heat treatment under carbon dioxide is presented in Figure 1. This figure indicates that the greater weight losses for (CCS) mainly occur between 27 and 627 °C. The first mass loss at 100 °C corresponds to humidity and other guest molecules adsorbed on the material. Waste agricultural biomass commonly consists of cellulose, hemi-cellulose and lignin. The second and third peaks in the derivative of the thermogravimetric (TG) curve (DTG curve) represent the fragmentation of hemi-cellulose and that of cellulose, respectively.

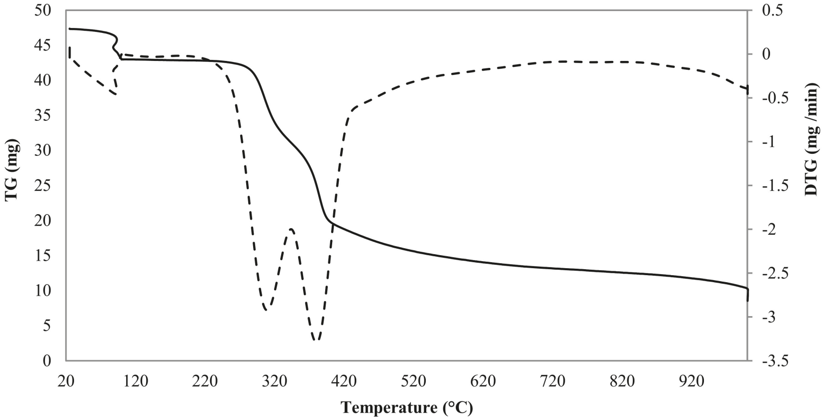

Figure 1. Mass loss and rate of mass loss profiles for CNS. The solid line corresponds to the thermogravimetric (TG) curve and the dashed line represents the derivative of the curve (DTG).

According to the experimental results of the weight-loss profile, the activation temperature was set at 900 °C and three activation times were selected, 35, 73 and 115 min, which correspond to the following yields, as estimated from Equation (1): 21.51, 16.92, and 10.47%, respectively.

$$Yield\ (\%) = \left(\frac{mass \text{ of the sample after activation (g)}}{initial\ mass \text{ of dried sample (g)}}\right) \times 100 \quad (1)$$

3.2. (CNS)Activated Carbon Characterization and Evaluation

3.2.1. Textural Characterization

Figures 2 and 3 represent the N_2 and CO_2 adsorption isotherms at −196 and 0 °C, respectively, on the activated carbon produced from CNS.

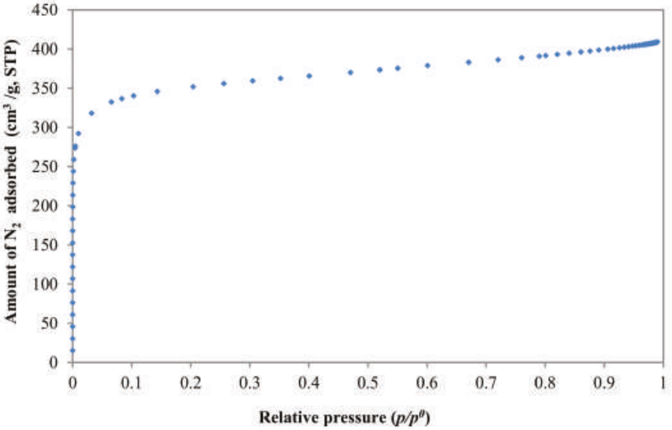

Figure 2. Adsorption isotherm of N_2 at −196 °C for the synthetized adsorbent.

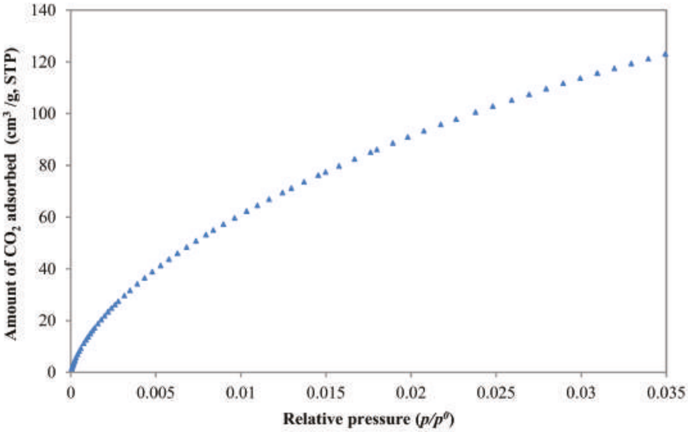

Figure 3. Adsorption isotherms of CO_2 at 0 °C for the synthetized adsorbent.

According to the International Union of Pure and Applied Chemistry (IUPAC) classification, the N_2 adsorption isotherm is of type I; this indicates that the produced activated carbon is strictly microporous. As can be noted from Figure 2, the nitrogen uptake is high at low relative pressure ($p/p^0 < 0.1$) and can be explained by micropores filling. As expected, the use of CO_2 as activating agent in a single step physical activation method mainly develops microporosity in biomass activated carbons [41].

CO_2 adsorption in Figure 3 assesses the narrower microporosity (<1 nm). A wide narrow micropore size distribution characterizes the shape of the CO_2 isotherm.

As can be noted from Table 2, the BET surface area estimated, 1378 m^2/g is considerably high and it is on the range of a commercial biomass-based carbon (500–1500 m^2/g). Micropores (W_0) represent more than 85% of the whole volume of pores (V_p). It is also observed that average narrow micropore size, L_0 as estimated from CO_2 adsorption, is close to the average micropore size, L_0 as estimated from N_2 adsorption.

Table 2. Main textural characteristics of the produced CNS-activated carbon.

Adsorbate	**V_p (cm^3/g)**	**S_{BET} (m^2/g)**	**Dubinin**				
			n	**S_{mic} (m^2/g)**	**L_0 (nm)**	**E_0 (kJ/mol)**	**W_0 (cm^3/g)**
N_2	0.63	1378	2	1043	1.04	21.76	0.54
CO_2	-	-	1.77	1126	0.84	24.22	0.47

3.2.2. Adsorption Isotherms

The experimental adsorption isotherm data collected at 30, 50 and 70 °C were fit to three different models to account for the equilibrium of adsorption, namely Sips, Toth and Dual-Site Langmuir (D-S), (Equations (2)–(8)).

The first isotherm model used for the representation of the experimental data is the Sips model whose equation is given as follow [42]:

$$q = \frac{q_s (bP)^{\frac{1}{n}}}{1 + (bP)^{\frac{1}{n}}} \tag{2}$$

where q (mol/g) refers to the gas adsorbed quantity and q_s (mol/g) the adsorbed quantity at equilibrium, P (Pa) the adsorption pressure and b the affinity constant. The parameter n indicates the heterogeneity of the system. Generally, n value is greater than unity; thus, the higher the value of n, the more heterogeneous the system that is obtained.

q_s (mol/g) was considered temperature independent whereas n and b (Pa^{-1}) were considered temperature dependent as shown in Equations (3) and (4) [42].

$$b = b_0 \exp\left[\frac{Q}{RT_0}\left(\frac{T_0}{T} - 1\right)\right] \tag{3}$$

$$\frac{1}{n} = \frac{1}{n_0} + \alpha\left(1 - \frac{T_0}{T}\right) \tag{4}$$

In the equations above, b_0, n_0 and α are the constants related to the temperature-dependent correlations; R (J/(mol.k)) is the ideal gas constant and T (K) is the temperature. Q is the isosteric heat of adsorption at a fractional loading of 0.5 and T_0 (K) is the reference temperature (30 °C).

The Toth model is used as the second isotherm model for fitting the experimental results which is represented by Equation (5) [42]:

$$q^* = q^*{}_s \frac{b^* P}{\left[1 + (b^* P)^t\right]^{\frac{1}{t}}} \tag{5}$$

where q^* (mol/g) is the adsorbed quantity, $q^*{}_s$ (mol/g) is adsorbed quantity at equilibrium and P (Pa) is the adsorption pressure. b^* (Pa^{-1}) and t are characteristic of the adsorbate–adsorbent couple. Thus, as n in the Sips relation, t characterizes the heterogeneity of the system. However, t is generally less than unity.

As in the Sips relation, the dependence of the equilibrium parameters with temperature in the Toth equation must also be taken into account [42].

$$t = t_0 + \alpha^* \left(1 - \frac{T}{T_0}\right) \tag{6}$$

In Equation (6), t_0 and α^* are the constants related to the temperature dependency of t. The variation of b^* (Pa^{-1}) with temperature is analogue to the dependence of b (Pa^{-1}) in the Sips equation, but in this case, Q accounts for the isosteric heat of adsorption at a nil fractional loading.

Finally, the third isotherm model selected for the prediction of the experimental results is the Dual-Site Langmuir model (D-S) (Equation (7)). This model accounts for the heterogeneity of adsorption of a pure component on the adsorbent which is composed of two homogeneous but different energy sites [43–45]. All assumptions of the Langmuir model are applicable to each site, with an absence of interactions between the two.

$$q = \frac{q_{s1} b_1 P}{1 + b_1 P} + \frac{q_{s2} b_2 P}{1 + b_2 P} \tag{7}$$

where q_{s1} (mol/g) and q_{s2} (mol/g) are respectively the equilibrium adsorbed quantity at sites 1 and 2, so the adittion of those quantities define the total capacity of saturation ($q_s = q_{s1} + q_{s2}$) (mol/kg); b_1 (Pa^{-1}) and b_2 (Pa^{-1}) represent free energy parameters for sites 1 and 2 respectively, or affinity , which depend on temperature as shown in Equation (8), where the subscript j refers to free energy sites (1 or 2), $b_{0,j}$ are the pre-exponential factors or entropies of adsorption, and E_j (J/mol) are their energies of adsorption [42].

$$b_j = b_{0,j} \exp\left(\frac{E_j}{RT}\right) j = 1,2 \tag{8}$$

The comparison between experimental and fitted data of adsorption of pure CO_2 and CH_4 on the CNS-activated carbon is shown in Figures 4 and 5. The experimental pure CO_2 and CH_4 adsorption isotherms of the CNS adsorbent at 30, 50 and 70 °C are represented by symbols. Sips, Toth and Dual-Site Langmuir (D-S) model fitting are represented by dashed lines with symbols.

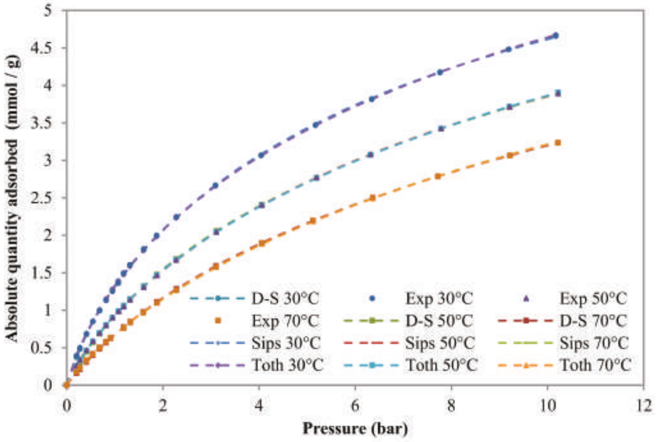

Figure 4. CH_4 isotherm at different temperatures (dashed line with symbols for Sips, Dual-Site Langmuir and Toth models predictions and symbols for experimental data).

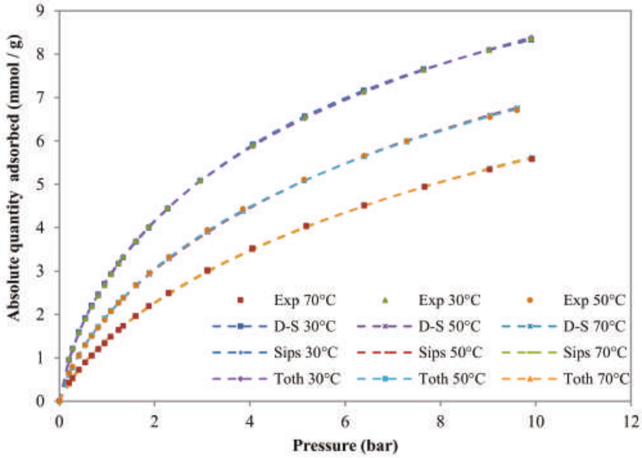

Figure 5. CO_2 isotherm at different temperatures (dashed line with symbols for Sips, Dual-Site Langmuir and Toth models fitting and symbols for experimental results).

Capacity of adsorption is an important factor to estimate the gas separation aptitude of an adsorbent. As can be noted, the CO_2 uptake capacities of CO_2 and CH_4 increased by increasing the pressure but decreased when the temperature increased. This is the expected behaviour for a physical adsorption-based process. The activated carbon produced presents a high CO_2 adsorption capacity compared to that of CH_4 over the studied pressure and temperature range.

The Excel tool Solver was used to fit the experimental results to the different models, and the different values of the parameters were calculated by minimizing the minimum residual sum of squares (SSR) i.e., by reducing the gap between the model predictions and empirical amounts adsorbed at the evaluated temperatures for a specific adsorbate–adsorbent system. Equation 9 shows the objective function used in Solver.

$$\text{SSR } (\%) = \sum_{T_1}^{T_3} \frac{\sum\limits_{i=1}^{N} (q_{\text{exp},i} - q_{\text{mod},i})^2}{N} \times 100 \tag{9}$$

where $q_{exp,i}$ (mol/g) and $q_{mod,i}$ (mol/g) are the empirical and prediction models of the amounts adsorbed, respectively, and N is the number of experimental points.

Figures 4 and 5 show the results for the three models. The optimal fitting parameters and the values of the minimum residual sum of squares (SSR) are reported in Table 3.

As can be noted in Table 3, the maximum adsorption capacities predicted by the three models for CO_2 are always much higher than those for CH_4. Such a difference in adsorption capacity is advantageous for separation via adsorption. The Toth's predictions of the adsorbed amounts at saturation are higher than those estimated by Sips and Dual-Site Langmuir, respectively. This difference can be justified by the fact that experimental data only correspond to fractional loadings of up to about 0.5 [46].

It is clearly observed that values of b^*, b_1, b_2 and b are reduced with temperature increase. This supposes that, at high temperature, the attraction of molecules to the surface is weaker.

The n constant in the Sips model and the t constant in the Toth model reflect the degree of heterogeneity of the system. As can be noted in Table 3, the heterogeneity of the system remains practically unchanged with the temperature increase.

Table 3. Sips, Dual-Site Langmuir, and Toth-fitting parameters models to CO_2 and CH_4 pure component adsorption isotherms for the CNS-activated carbon.

Model	Component	T (°C)	q_{s1}, q_{s2}, q_s and q_s*(mol/kg)	b_1, b_2, b and b* (kPa)	n (Sips) t(Toth)	ff ff*	SSR (%)
Dual-site	CH_4	30	1.00 6.63	0.0137 0.0012	-	-	0.04
		50		0.0078 0.0008	-	-	
		70		0.0049 0.0006	-	-	
	CO_2	30	1.86 10.50	0.0235 0.0017	-	-	0.20
		50		0.0133 0.0010	-	-	
		70		0.0078 0.0006	-	-	
Sips	CH_4	30	8.32	0.0013	1.21	0.25	0.03
		50		0.0008	1.20		
		70		0.0006	1.18		
	CO_2	30	14.25	0.0016	1.30	0.22	0.12
		50		0.0009	1.31		
		70		0.0006	1.29		
Toth	CH_4	30	11.64	0.0022	0.54	0.21	0.03
		50		0.0013	0.56		
		70		0.0008	0.57		
	CO_2	30	20.73	0.0039	0.47	0.12	0.13
		50		0.0022	0.47		
		70		0.0013	0.48		

3.2.3. Breakthrough Curves

In Figure 6, it can also be noted that the CNS adsorbent bed presents a stable performance in consecutive cycling under fixed-bed operations.

Figure 7 shows an example of six-consecutive adsorption and desorption experiments for an equimolar CO_2/CH_4 gas mixture fed to the adsorption fixed-bed at 1 bar. It was used as carrier gas during the preconditioning and regeneration steps. It is observed that during the initial period preceding the saturation of the bed, both components in the feed gas, CO_2 and CH_4, are completely adsorbed on the CNS activated carbon bed. Then, as expected according to the data from the adsorption isotherms (see Figures 4 and 5), CH_4 breaks through first.

The CH_4 breakthrough curve presents a so-called roll-up (see Figure 7). This is because the CH_4 adsorbed is displaced by CO_2 adsorption. This phenomenon has been previously reported for a similar separation in [47]. The strong adsorption of CO_2 over CH_4 can be justified by the fact that the molecules have different adsorption strength.

From Figure 7, it has to be noted that consecutive breakthrough curves overlap showing that the adsorbent was totally regenerated in each cycle and maintained a stable adsorption performance over the six successive sorption cycles. Based on the timing noted in the concentration fronts of CH_4 and CO_2, the CO_2/CH_4 gas separation is technically possible on the CNS-based activated carbon. The required time for the CO_2 front to reach the column outlet is approximately 18 min, whereas CH_4 need a much shorter time to breaks the column (6 min).

The adsorption capacities of CO_2 and CH_4 of the produced activated carbon are estimated to be 1.86 and 0.52 mol/kg, respectively, at 30 °C and 1 bar.

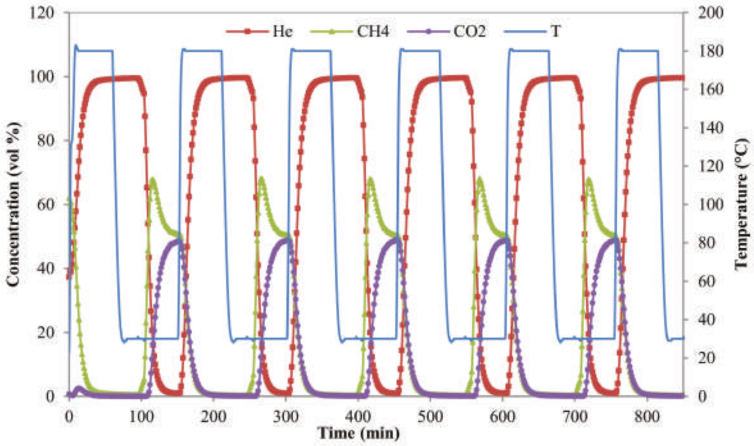

Figure 6. Breakthrough experiments composed of six successive sorption cycles for an equimolar CO_2/CH_4 gas mixture at 1 bar. (Solid lines with symbols represent the concentration profiles of CH_4, CO_2 and He. The blue solid line represents the temperature).

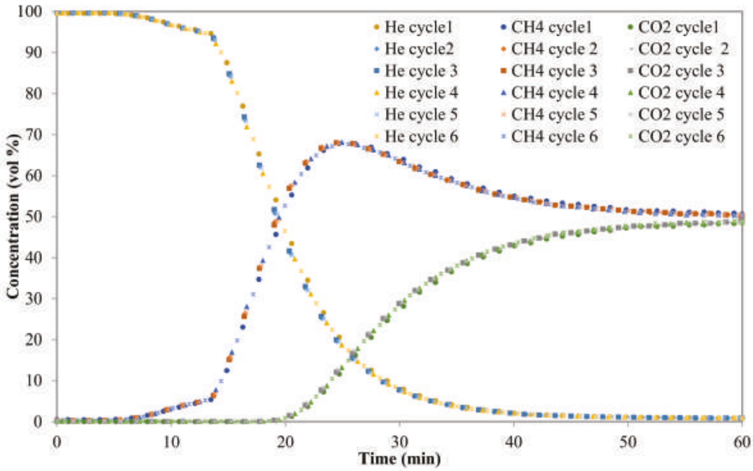

Figure 7. Breakthrough curves for a 50/50 vol % CO_2/CH_4 binary gas mixture at 1 bar. (Symbols represent CO_2 and CH_4 concentrations for different cycles).

For the design of the PSA, it is essential to determine precisely the breakthrough time of CO_2 at the adsorption pressure chosen. This could be done experimentally or using a simulation tool with a model already validated. CH_4, separated from CO_2, has to be collected from the bed exit during the period preceding the breakthrough of CO_2. Just before CO_2 breaks through, the collection of CH_4 should be stopped and the bed undergoes the next step according to the retained PSA cycle design (equalization, depressurization, regeneration, etc.).

3.2.4. Adsorption Selectivity

Aiming to assess the efficiency of the produced activated carbon for CO_2/CH_4 separation, the adsorption selectivity ($S_{CO2/CH4}$) was calculated using Equation (10) [48]

$$S_{CO_2/CH_4} = \frac{x_{CO_2}}{x_{CH_4}} \frac{y_{CH_4}}{y_{CO_2}} \quad (10)$$

where x refers to the molar fraction in the adsorbed phase and y refers to the molar fraction in the gas.

The selectivity of CO_2 over CH_4 for the CNS at 1 bar and 30 °C was approximately 3.6. It was found that the value of selectivity was comparable to that of carbon-based adsorbents [49].

Many works reported that (MOF) possess high CO_2 selectivity and high CO_2 working capacities compared to zeolites and carbon-based adsorbents [50–52]. In general, the separation of CO_2/ CH_4 can be affected by many parameters such as temperature and pressure.

4. Conclusions

In this work an activated carbon from dry CNS using one-pot activation procedure was produced. The results of this study showed that the activated carbon presented good development and high BET surface area. The characterization of the CNS-based activated carbon indicated that the adsorbent is basically microporous with a BET surface of 1378 m^2/g. CNS can be utilized as a suitable precursor to prepare a microporous activated carbon for CO_2 adsorption from biogas streams.

Pure component CO_2 and CH_4 adsorption isotherms were carried out at three different temperatures. As expected, CO_2 is the strongest adsorbate. Afterwards, breakthrough tests consisting of six successive sorption cycles were run in a lab-scale fixed-column. The CNS based activated carbon maintains its activity during the experiments which reflect a perfect cyclability and regenerability under the evaluated conditions.

Based on the timing observed in the concentration fronts of CH_4 and CO_2, the gas separation of CO_2/CH_4 is technically feasible using the CNS-based activated carbon. For instance, the CO_2 and CH_4 adsorption fronts reach the outlet of the column after approximately 18 min and 6 min, respectively.

The adsorption capacities of CO_2 and CH_4 of the produced activated carbon are estimated to be 1.86 and 0.52 mol/kg, respectively, at 30 °C and 1 bar.

The collected preliminary data report that the synthesized CNS-adsorbent shows suitable characteristics for the CO_2/CH_4 separation.

Author Contributions: A.A. conducted the experimental work with the assistance of N.Q. in the sample preparation and characterization and I.D. and N.Á.-G. in the fixed-bed experiments and data processing. C.P. and M.H.C. supervised the work. All authors contributed to the writing and/or revision of the paper.

Funding: This research was funded by The Tunisian Ministry of Higher Education and Scientific Research.

Conflicts of Interest: The authors declare no conflicts of interest.

References

1. Zheng, B.; Xu, J. Carbon Capture and Storage Development Trends from a Techno-Paradigm Perspective. *Energies* **2014**, *7*, 5221–5250. [CrossRef]
2. Rodrigues, C.F.A.; Dinis, M.A.P.; Lemos de Sousa, M.J. Review of European energy policies regarding the recent "carbon capture, utilization and storage" technologies scenario and the role of coal seams. *Environ. Earth Sci.* **2015**, 74–2553. [CrossRef]
3. Yoro, K.O.; Sekoai, P.T. The Potential of CO_2 Capture and Storage Technology in South Africa's Coal-Fired Thermal Power Plants. *Environments* **2016**, *3*, 24. [CrossRef]
4. Lackner, K.S.; Park, A.H.A.; Miller, B.G. Eliminating CO_2 emissions from coal-fired power plants. In *Generating Electricity in a Carbon-Constrained World*; Academic Press: Cambridge, MA, USA, 2010; pp. 127–173.

5. Pires, J.C.M.; Martins, F.G.; Alvim-Ferraz, M.C.M.; Simões, M. Recent developments on carbon capture and storage: An overview. *Chem. Eng. Res. Des.* **2011**, *89*, 1446–1460. [CrossRef]
6. Zhou, K.; Chaemchuen, S.; Verpoort, F. Alternative materials in technologies for Biogas upgrading via CO_2 capture. *Renew. Sustain. Energy Rev.* **2017**, *79*, 1414–1441. [CrossRef]
7. Sarkar, S.C.; Bose, A. Role of activated carbon pellets in carbon dioxide removal. *Energy Convers. Manag.* **1997**, *38*, S105–S110. [CrossRef]
8. Horikawa, M.S.; Rossi, F.; Gimenes, M.L.; Costa, C.M.M.; Da Silva, M.G.C. Chemical absorption of H_2S for biogas purification. *Braz. J. Chem. Eng.* **2004**, *21*, 415–422. [CrossRef]
9. Yeo, Z.Y.; Chew, T.L.; Zhu, P.W.; Mohamed, A.R.; Chai, S.P. Conventional processes and membrane technology for carbon dioxide removal from natural gas: A review. *J. Natl. Gas Chem.* **2012**, *21*, 282–298. [CrossRef]
10. Tuinier, M.J.; van Sint Annaland, M. Biogas Purification Using Cryogenic Packed-Bed Technology. *Ind. Eng. Chem. Res.* **2012**, *51*, 5552–5558. [CrossRef]
11. Shigaki, N.; Mogi, Y.; Haraoka, T.; Sumi, I. Reduction of Electric Power Consumption in CO_2-PSA with Zeolite 13X Adsorbent. *Energies* **2018**, *11*, 900. [CrossRef]
12. Xu, G.; Liang, F.; Yang, Y.; Hu, Y.; Zhang, K.; Liu, W. An Improved CO_2 Separation and Purification System Based on Cryogenic Separation and Distillation Theory. *Energies* **2014**, *7*, 3484–3502. [CrossRef]
13. Abdeljaoued, A.; Relvas, F.; Mendes, A.; Chahbani, M.H. Simulation and experimental results of a PSA process for production of hydrogen used in fuel cells. *J. Environ. Chem. Eng.* **2018**, *6*, 338–355. [CrossRef]
14. Maring, B.J.; Webley, P.A. A new simplified pressure/vacuum swing adsorption model for rapid adsorbent screening for CO_2 capture applications. *Int. J. Greenh. Gas Control* **2013**, *15*, 16–31. [CrossRef]
15. Ghouma, I.; Jeguirim, M.; Sager, U.; Limousy, L.; Bennici, S.; Däuber, E.; Asbach, C.; Ligotski, R.; Schmidt, F.; Ouederni, A. The Potential of Activated Carbon Made of Agro-Industrial Residues in NOx Immissions Abatement. *Energies* **2017**, *10*, 1508. [CrossRef]
16. Ferella, F.; Puca, A.; Taglieri, G.; Rossi, L.; Gallucci, K. Separation of carbon dioxide for biogas upgrading to biomethane. *J. Clean. Prod.* **2017**, *164*, 1205–1218. [CrossRef]
17. Siriwardane, R.V.; Shen, M.-S.; Fisher, E.P.; Poston, J.A. Adsorption of CO_2 on Molecular Sieves and Activated Carbon. *Energy Fuels* **2001**, *15*, 279–284. [CrossRef]
18. Li, G.; Xiao, P.; Webley, P.; Zhang, J.; Singh, R.; Marshall, M. Capture of CO_2 from high humidity flue gas by vacuum swing adsorption with zeolite-13X. *Adsorption* **2008**, *14*, 415–422. [CrossRef]
19. Millward, A.R.; Yaghi, O.M. Metal-Organic Frameworks with Exceptionally High Capacity for Storage of Carbon Dioxide at Room Temperature. *J. Am. Chem. Soc.* **2005**, *127*, 17998–17999. [CrossRef] [PubMed]
20. Furukawa, H.; Ko, N.; Go, Y.B.; Aratani, N.; Choi, S.B.; Choi, E.; Yazaydin, A.O.; Snurr, R.Q.; O'Keeffe, M.; Kim, J.; et al. Ultrahigh Porosity in Metal-Organic Frameworks. *Science* **2010**, *329*, 424–428. [CrossRef] [PubMed]
21. Choi, S.; Drese, J.H.; Jones, C.W. Adsorbent materials for carbon dioxide capture from large anthropogenic point sources. *ChemSusChem* **2009**, *2*, 796–854. [CrossRef] [PubMed]
22. Wei, H.; Deng, S.; Hu, B.; Chen, Z.; Wang, B.; Huang, J.; Yu, G. Granular Bamboo-Derived Activated Carbon for High CO_2 Adsorption:The Dominant Role of Narrow Micropores. *ChemSusChem* **2012**, *5*, 2354–2360. [CrossRef] [PubMed]
23. Samanta, A.; Zhao, A.; Shimizu, G.K.H.; Sarkar, P.; Gupta, R. Post-Combustion CO_2 Capture Using Solid Sorbents: A Review. *Ind. Eng. Chem. Res.* **2012**, *51*, 1438–1463. [CrossRef]
24. Jeguirim, M.; Limousy, L. Biomass Chars: Elaboration, Characterization and Applications. *Energies* **2017**, *10*, 2040. [CrossRef]
25. Álvarez-Gutiérrez, N.; Gil, M.V.; Martínez, M.; Rubiera, F.; Pevida, C. Phenol-Formaldehyde Resin-Based Carbons for CO_2 Separation at sub-atmospheric pressures. *Energies* **2016**, *9*, 189. [CrossRef]
26. Guizani, C.; Jeguirim, M.; Valin, S.; Limousy, L.; Salvador, S. Biomass Chars: The Effects of Pyrolysis Conditions on Their Morphology, Structure, Chemical Properties and Reactivity. *Energies* **2017**, *10*, 796. [CrossRef]
27. Heschel, W.; Klose, E. On the suitability of agricultural by-products for the manufacture of granular activated carbon. *Fuel* **1995**, 1786–1791. [CrossRef]
28. Kirubakaran, C.J.; Krishnaiah, K.; Seshadri, S.K. Experimental Study of the Production of Activated Carbon from Coconut Shells in a Fluidized Bed Reactor. *Ind. Eng. Chem. Res.* **1991**, *30*, 2411–2416. [CrossRef]

29. Prauchner, M.J.; Rodríguez-Reinoso, F. Chemical versus physical activation of coconut shell: A comparative study. *Microporous Mesoporous Mater.* **2012**, *152*, 163–171. [CrossRef]
30. Juárez-Galán, J.M.; Silvestre-Albero, A.; Silvestre-Albero, J.; Rodríguez-Reinoso, F. Synthesis of activated carbon with highly developed "mesoporosity". *Microporous Mesoporous Mater.* **2009**, *117*, 519–521. [CrossRef]
31. Bartocci, P.; Bidini, G.; Saputo, P.; Fantozzi, F. Biochar pellet carbon footprint. *Chem. Eng. Trans.* **2016**, *50*, 217–222. [CrossRef]
32. Orrego-Romero, A.F.; Arbeláez-Pérez, O.F.; Bustamante-Londoño, F.; Villa-Holguín, A.L. Pelletization of catalysts supported on activated carbon. A Case Study: Clean synthesis of dimethyl carbonate from methanol and CO_2. *Revista Facultad de Ingeniería Universidad de Antioquia* **2016**, 38–47. [CrossRef]
33. Chen, T.; Gu, W.; Li, G.; Wang, Q.; Liang, P.; Zhang, X.; Huang, X. Significant enhancement in catalytic ozonation efficacy: From granular to super-fine powdered activated carbon. *Front. Environ. Sci. Eng.* **2018**, *12*, 6. [CrossRef]
34. Gil, M.V.; Álvarez-Gutiérrez, N.; Martínez, M.; Rubiera, F.; Pevida, C.; Morán, A. Carbon adsorbents for CO_2 capture from bio-hydrogen and biogas streams: Breakthrough adsorption study. *Chem. Eng. J.* **2015**, *269*, 148–158. [CrossRef]
35. Plaza, M.G.; González, A.S.; Pis, J.J.; Rubiera, F.; Pevida, C. Production of microporous biochars by single-step oxidation:Effect of activation conditions on CO_2 capture. *Appl. Energy* **2014**, *114*, 551–562. [CrossRef]
36. Brunauer, S.; Emmett, P.H.; Teller, E. Adsorption of gases in multimolecular layers. *J. Am. Chem. Soc.* **1938**, *60*, 309–319. [CrossRef]
37. Dubinin, M.M. Porous structure and adsorption properties of active carbons. In *Chemistry and Physics of Carbon*; Walker, P.L., Ed.; Marcel Dekker Inc.: New York, NY, USA, 1966; pp. 51–119.
38. Stoeckli, F.; Ballerini, L. Evolution of microporosity during activation of carbon. *Fuel* **1991**, *70*, 557–559. [CrossRef]
39. García, S.; Pis, J.J.; Rubiera, F.; Pevida, C. Predicting mixed-gas adsorption equilibria on activated carbon for precombustion CO_2 capture. *Langmuir* **2013**, *29*, 6042–6052. [CrossRef] [PubMed]
40. García, S.; Gil, M.V.; Martín, C.F.; Pis, J.J.; Rubiera, F.; Pevida, C. Breakthrough adsorption study of a commercial activated carbon for pre-combustion CO_2 capture. *Chem. Eng. J.* **2011**, *171*, 549–556. [CrossRef]
41. Rodríguez-Reinoso, F.; Molina-Sabio, M.; González, M.T. The use of steam and CO_2 as activating agents in the preparation of activated carbons. *Carbon* **1995**, *33*, 15–23. [CrossRef]
42. Do, D.D. *Adsorption Analysis: Equilibria and Kinetics*; Imperial College Press: London, UK, 1998.
43. Langmuir, I. The adsorption of gases on plane surfaces of glass, mica and platinum. *J. Am. Chem. Soc.* **1918**, *40*, 1361–1403. [CrossRef]
44. Ritter, J.A.; Bhadra, S.J.; Ebner, A.D. On the use of the dual process Langmuir model for correlating unary equilibria and predicting mixed-gas adsorption equilibria. *Langmuir* **2011**, *27*, 4700–4712. [CrossRef] [PubMed]
45. Bhadra, S.J.; Ebner, A.D.; Ritter, J.A. On the use of the dual process Langmuir model for predicting unary and binary isosteric heats of adsorption. *Langmuir* **2012**, *28*, 6935–6941. [CrossRef] [PubMed]
46. Esteves, I.A.; Lopes, M.S.; Nunes, P.M.; Mota, J.P. Adsorption of natural gas and biogas components on activated carbon. *Sep. Purif. Technol.* **2008**, *62*, 281–296. [CrossRef]
47. Álvarez-Gutiérrez, N.; García, S.; Gil, M.V.; Rubiera, F.; Pevida, C. Dynamic performance of biomass-based carbons for CO_2/CH_4 separation. Approximation to a pressure swing adsorption process for biogas upgrading. *Energy Fuels* **2016**, *30*, 5005–5015. [CrossRef]
48. Ruthven, D.M.; Farooq, S.; Knaebel, K.S. *Pressure Swing Adsorption*; VCH Publishers: New York, NY, USA, 1994.
49. Álvarez-Gutiérrez, N.; Gil, M.V.; Rubiera, F.; Pevida, C. Adsorption performance indicators for the CO_2/CH_4 separation: Application to biomass-based activated carbons. *Fuel Proc. Technol.* **2016**, *142*, 361–369. [CrossRef]
50. Ben-Mansour, R.; Habib, M.; Bamidele, O.; Basha, M.; Qasem, N.; Peedikakkal, A.; Laoui, T.; Ali, M. Carbon Capture by Physical Adsorption: Materials, Experimental Investigations and Numerical Modeling and Simulations—A Review. *Appl. Energy* **2016**, *161*, 225–255. [CrossRef]

51. Xu, X.; Zhao, X.; Sun, L.; Liu, X. Adsorption separation of carbon dioxide, methane, and nitrogen on Hβ and Na-exchanged β-zeolite. *J. Natl. Gas Chem.* **2008**, *17*, 391–396. [CrossRef]
52. Altintas, C.; Avci, G.; Daglar, H.; Azar, A.N.V.; Velioglu, S.; Erucar, I.; Keskin, S. A database for CO_2 Separation Performances of MOFs based on Computational Materials Screening. *ACS Appl. Mater. Interfaces* **2018**. [CrossRef] [PubMed]

energies

Article

Value-Added Performance and Thermal Decomposition Characteristics of Dumped Food Waste Compost by Pyrolysis

Ye-Eun Lee [1,2], Jun-Ho Jo [1], I-Tae Kim [1] and Yeong-Seok Yoo [1,2,*]

[1] Division of Environment and Plant Engineering, Korea Institute of Civil Engineering and Building Technology, 283, Goyang-daero, Ilsanseo-gu, Goyang-si 10223, Gyeonggi-do, Korea; yeeunlee@kict.re.kr (Y.-E.L.); junkr@kict.re.kr (J.-H.J.); itkim@kict.re.kr (I.-T.K.)

[2] Department of Construction environment Engineering, University of Science and Technology, 217, Gajeong-ro, Yuseong-gu, Daejeon KS015, Korea

* Correspondence: ysyoo@kict.re.kr; Tel.: +82-31-910-0298; Fax: +82-31-910-0288

Received: 6 March 2018; Accepted: 20 April 2018; Published: 25 April 2018

Abstract: Food waste compost has a high Na content, which interferes with plant growth when used as a soil enhancer and therefore makes it difficult to use. And, compared to the amount of compost produced every day, the amount of consumption required in farms is smaller, and the rest is buried underground, which releases greenhouse gases and pollutes underground water. This research compared and analyzed thermal degradation behavior, calorific value, and gas spectrometry during the pyrolysis between food waste compost and sawdust to suggest producing food waste compost biochar by pyrolysis as a new alternative solution to utilize the massive amount of food waste compost. Biochar from pyrolysis of food waste compost had a high carbon content of 51% at 300 °C, and the carbon content decreased as the pyrolysis temperature increased. According to the thermogravimetric analysis (TGA) and derivative thermo-gravimetric (DTG) analysis results, compost showed the largest weight reduction from 240 °C to 365 °C. The weight reduction temperature ranges for compost and sawdust were quite similar. This occurred because food waste of the compost was degraded, but sawdust of compost remained nearly during the composting process. A gas chromatography and mass spectrometry (GC-MS) analysis found that the gases were fragments of fatty acids, protein, and hemi-cellulose. These results could also have been caused by degradation of microorganisms involved in the composting process, sawdust, and small fragments of food waste. In the calorific value of biochar, the highest value (24.33 kJ/g) was obtained 300 °C. At a low pyrolysis temperature, carbon fixation occurred easily since the food waste in compost was degraded by microorganism, and the volatilization of sawdust, which plays an important role in determining the calorific value, was also small. That is why the highest calorific value was shown at 300 °C, not 400 °C or 500 °C. Hence, it seems that food waste compost can be used as a promising alternative fuel at a low pyrolysis temperature, as other lignocellulosic refuse-derived fuels (RDF).

Keywords: food waste compost; sawdust; pyrolysis; biochar; thermogravimetric analysis (TGA); calorific value

1. Introduction

Even though food waste, which has a high content of organic matter, contains much potential energy, it is not used frequently. It takes compost produced from the composting process, which is mainly applied for food waste treatment and recycling, a lot of time to fully mature, and it is difficult to produce compost with consistent quality. In addition, when the compost has high Na content, it interferes with plant growth, which makes it difficult to use [1,2]. The salt content in food waste in Korea is high because of its unique food culture, and it is difficult to use food waste as compost [3]. As of 2015, 33.9% of the

13,546.9 tons/day of the food waste generated in Korea is treated via composting, and only 6.49% is recycled for farms [4]. This amount accounts for just 2.1% of the total food waste, and it shows that the recycling rate is very low. Furthermore, compared to the amount of compost produced every day, the amount of consumption required in farms is smaller, and the rest is not consumed and has to be used as landfill, which releases greenhouse gases, pollutes underground water [5], and causes other environmental problems. Accordingly, a new solution is needed to utilize the excess food waste compost that is not used for its original production purposes and requires treatment.

Pyrolysis is a process that breakdown of large complex molecules into several smaller molecules [6]. Gases, such as carbon dioxide and carbon monoxide, liquids such as bio-oil, or solid chars such as charcoal are generated during this process [6]. Pyrolysis reduces the large volume of biomass which is difficult to recycle and converts it into the material which has an economic value, such as bio-oil and biochar [7]. In fact, many studies have been conducted on the recycling of organic waste using pyrolysis. Iman and Capareda [8] analyzed the characteristics of synthetic gases and biochar produced by pyrolysis on dry grass, at temperatures ranging from 400 °C to 600 °C and demonstrated that biofuel can be produced through pyrolysis. Jahiru reviewed the previous studies that used pyrolysis and produced biofuels, but most were limited to botanical waste such as rice, straw, nut shells, and sugarcane [9].

There have also been studies that used compost as biomass. Agustin [10] performed a study using the gases generated from the composting process, including a study on compost degradation to produce hydrogen gases, but it did not utilize the compost itself. Ghorbel et al. [5] performed pyrolysis on farm breeding compost and cardboard, compared them, and revealed that the value of compost as a biofuel was not good enough, as cardboard had a much higher calorific value than compost. Ryu et al. [11] performed a study that combined mushroom compost with coal tailings and recycled it as a pellet-type fuel, but compost was only used to play a supporting role for coal tailings. In addition, the main source of compost used in these studies was vegetable waste, and no study performed pyrolysis of food waste compost to produce solid fuels. This is because there was a lack of awareness about the necessity of re-treating the waste that had been previously treated, or they were not convinced of the possibility of converting it into valuable matter. A new study is required to explore the scope of fuels other than those researched previously.

Lee et al. [12] researched the possibility of turning food waste containing grain, vegetables, or meat into a fuel. Pyrolysis at temperatures ranging from 200 °C to 400 °C produced a product with calorific value ranging from 23.7 to 29.7 kJ/g, whose energy content did not lag behind Ghorbel [5] calorific value from cardboard pyrolysis of 22.8 to 26.8 kJ/g, Phan et al. [13] calorific value from waste wood char pyrolysis of 27.1 to 31.4 kJ/g, and Ryu et al. [14] calorific value from pine wood pyrolysis of 31.7 to 32.5 kJ/g. In other words, it is possible to recycle food waste compost into a solid fuel, unlike compost containing vegetable matter only.

Hence, after performing pyrolysis of food waste compost, this study aims to compare and analyze the calorific values and thermal degradation of biochar produced at pyrolysis temperatures in the range 300–500 °C. Gas chromatography and mass spectrometry (GC-MS) of gases generated from food waste and sawdust contained in compost will also be used to examine the value of biochar as an energy-storing fuel.

2. Materials and Methods

2.1. Materials

Food waste compost was collected from the Un-Jeong Environment Management Center, Paju-si, Gyeonggi-do, Korea. To remove large foreign matter, this study used food waste compost sieved through a 1.18 mm sieve.

The Un-Jeong Environment Management Center receives 20 tons of food waste from the region each day and washes it with water to remove salt. 10 tons of solid matter is obtained from the dehydrating process and is converted into compost in an aerobic composting tank. 1.1 tons of sawdust is added each day as a bulking agent. The aerobic composting tank goes through two stages. The 1st stage involves 14 days of accelerated degradation, and the 2nd stage involves 20 days of maturation. The process produces 3 tons of compost every day.

2.2. Experimental Method

The experiment was carried out in four steps, including sample homogenization, pyrolysis, washing, and dehydration. Food waste compost was placed in a pyrolysis furnace at 300 °C, 400 °C, and 500 °C for 2 h. Nitrogen gas was added at 5 L/min to prevent oxidation. The 200 g of food waste compost sample was put in an open container with a width, length, and height of 5 cm, 20 cm, and 4.5 cm, and was then placed into the pyrolysis furnace. Figure 1 shows the reactor design.

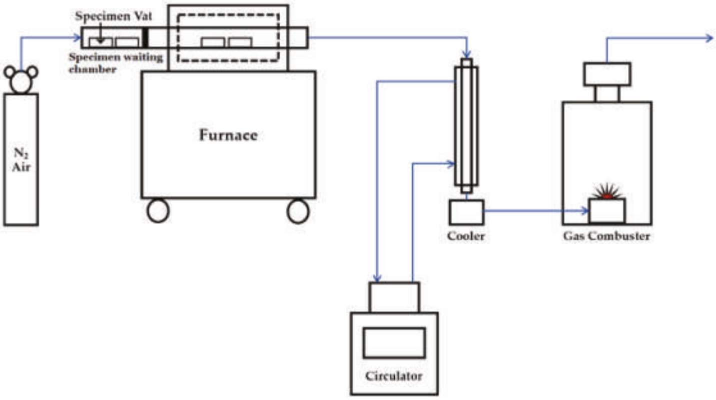

Figure 1. The pyrolysis reactor design diagram.

After the sample completed pyrolysis, it was cooled down to room temperature. Some portion of the sample was washed in distilled water at a 1:10 ratio for 30 min to remove any remaining salt, which is characteristic of Korean food waste. Biochar in the washed sample was separated using a 47 mm glass microfiber filters (Whatman, Maidstone, UK), and was dried again at 100 °C. Samples from each pyrolysis temperature were analyzed for chemical composition, thermal degradation behavior, calorific value, and gases released during pyrolysis. Whole experiment proceeded three times, and analysis results represent average values. This process allowed the food waste compost pyrolysis characteristics to be examined as a potential solid fuel. Sawdust was added to the food waste composting process as a bulking agent. Sawdust is not degraded well by microorganisms and is likely to remain in the compost. This study also compared sawdust with a compost samples when analyzing the characteristics of compost and pyrolysis biochar.

2.3. Analysis Method

To obtain the elemental composition of food waste compost and biochar after pyrolysis, this study used the CHNS analyser (2400 Series II CHNS, Perkin Elmer, Boston, MA, USA). The raw compost and sawdust were analyzed only once as it is considered homogeneous as it was made using a specimen in the form of fully blended and sieved powder. All the biochar samples obtained from the three times of experiments were analyzed, and average values are stated. This study measured the Cl content using the combustion ion chromatography (AQF-2100H, Mitsubishi Chemical Analytech, Chigasaki, Japan) to determine the salt content in food waste compost, as well as the amount of salt removed from the biochar. An atomic absorption photometer (AAnalyst400, PerkinElmer, Boston, MA, USA) was used to measure the Na content.

To measure the energy amount of the biochar, this study measured the calorific value using a calorimeter (6400Automatic Isoperibol Calorimeter, Parr, Moline, IL, USA). The thermal degradation behavior was investigated with a thermogravimetric analyser (TGA), and the heating rate was set at 10 °C/min and 20 °C/min in different experiments. The balance purge and sample purge was nitrogen gas 40 mL/min, 20 mL/min each. GC injection temperature is 320 °C, and 520 °C. Gases generated during pyrolysis were analyzed using thermogravimetric analysis (TGA)—gas chromatography (GC)—mass spectrometry (MS), and based on TGA results, this study analyzed released gases during the highest weight loss period.

3. Results and Discussion

3.1. Characterization of Raw Material and Biochar

The chemical composition of the sawdust, food waste compost, and food waste is shown in Table 1. This study referenced other papers for data on food waste. Jo et al. [15] used mixed food produced according to the average composition of Korean food waste. Similar to this study, Zhang, Ruihong, et al. [16] were provided with food waste from a waste management company in Northern California. Kwon and Lee et al. [17] were provided with food waste from a university cafeteria in Seoul.

Table 1. Physical-chemical characterization of food waste compost and sawdust.

Sample	C	H	N	Moisture	Dry Basis			Reference
					Ash	Volatile	Fixed Carbon	
Food waste compost	29.7	4.3	2.9	21.6 ± 4.4	9.8	78.3	11.9	This study
Sawdust	24.4	2.9	-	28.6 ± 3.1	0.6	83.3	16.14	
Mixed food	47.5	12.2	2.9	85.7 ± 2.9	3.8 ± 0.1	79.0 ± 2.7	17.25	Jo et al. [15]
Food waste	46.8	-	3.2	-	-	85.3 ± 0.7	4.54	Zhang, Ruihong, et al. [16]
Cafeteria food waste	-	-	-	80.0 ± 2.3	1.3 ± 0.3	93.6 ± 1.9	-	Kwon and Lee et al. [17]

Carbon and volatile content in food waste compost were found to be lower than that of food waste in other studies because organic matter contained in food waste was degraded and volatilized by microorganisms through the composting process [18]. While the carbon content in food waste was greatly decreased, its nitrogen content did not change very much because nitrogen is a nutrient necessary for the growth of microorganisms and is absorbed into microorganisms to form their cells, while some nitrogen is degraded and volatilized into ammonia.

The carbon content in food waste compost decreased by about 40% compared with food waste down to 29.7%, which is twice as high as the 14.8% content in farm breeding compost from Ghorbel study [5]. Unlike Ghorbel's finding that farm breeding compost has little value as a fuel, food waste compost is more promising as a source of energy.

Food waste compost showed higher carbon and ash content than sawdust, but a lower moisture content. Notably, the amount of ash produced from sawdust was small, whereas, the ash content in food waste compost was more than 50 times higher. It was also higher than the content of food waste. The high ash content in food waste compost is due to the composting process, where the remaining inorganic matter that was not degraded after the organic matter is degraded and volatilized are concentrated. Table 2 shows the C, H, N, and S content in biochar produced after pyrolysis of food waste compost and the salt content analysis results:

Table 2. Element and salt content analysis of biochar at various pyrolysis temperatures.

(wt %)	C	H	N	S	Cl	Na
Compost	29.73	4.27	2.90	-	0.66	0.77
300 [1]	51.04 ± 0.11	5.53 ± 0.09	4.55 ± 0.09	-	0.18 ± 0.03	0.64 ± 0.02
300 [2]	51.83 ± 0.16	5.39 ± 0.10	4.68 ± 0.22	-	1.13 ± 0.14	1.57 ± 0.12
400 [1]	48.67 ± 0.46	4.28 ± 0.09	3.74 ± 0.05	-	0.30 ± 0.03	1.11 ± 0.08
400 [2]	47.58 ± 0.45	3.75 ± 0.74	3.25 ± 0.88	-	1.73 ± 0.03	1.91 ± 0.05
500 [1]	51.72 ± 1.31	2.24 ± 0.21	3.39 ± 0.31	-	1.03 ± 0.24	1.52 ± 0.01
500 [2]	48.42 ± 0.55	1.94 ± 0.07	3.61 ± 0.39	-	2.52 ± 0.02	2.64 ± 0.00

[1] Washed biochar. [2] Unwashed biochar.

According to the salt content of compost before pyrolysis, around 1.4% of the salt content remained, despite the fact it was washed to remove salt from the food waste before the composting process. It shows that washing raw food waste cannot completely remove salt content, even though some salt on the surface can be washed away, and additional treatment is required. In addition, salt remaining after washing is one of the primary factors that decreases its value as compost.

The Cl and Na content of biochar after pyrolysis of food waste compost increased as the pyrolysis temperature increased, which demonstrated that salt was not volatilized but concentrated during pyrolysis, while the organic matter was reduced in weight and volatile substances were released as gases. Na and Cl did not exist independently. Instead, they existed as solid NaCl. Therefore, salt was not volatilized during pyrolysis [19]. After washing, the Cl and Na content decreased rapidly, demonstrating that they were removed through washing after carbonization. The Na content after washing was relatively higher than the Cl content because some Na ions from washing water were absorbed due to biochar's cation exchange capacity (CEC) [17]. When the Cl content is high in combustion fuel, it can cause corrosion and boiler slagging, and it is regulated as it can produce hazardous substances such as hydrochloric acid (HCl) and polychlorinated dibenzodioxins (PCDD). The British-adopted European Standard (BS EN 15359: 2011) [20] for solid recovery fuel defines Grade 1 fuel as having a Cl content less than 0.2%, Grade 2 as less than 0.6%, and Grade 3 as less than 0.8%. The Cl content in biochar washed after pyrolysis at 300 °C to 400 °C was 0.18% and 0.3%, which put them into Grade 1 and Grade 2, respectively.

Another characteristic found in the table is the carbon content in biochar more than doubled compared to raw food waste compost. That content level is similar to or higher than that of food waste, which means that its possibility as a fuel is further increased. Its carbon, nitrogen, and hydrogen content all tended to decrease as the pyrolysis temperature increased because volatile substances were released as gases, and degradation and weight reduction occurred during pyrolysis.

Differences were also observed before and after washing. There were few differences at 300 °C, and differences increased as pyrolysis temperature increased. It seems that each element content per unit weight increased relatively as concentrated NaCl was removed during washing.

3.2. Thermogravimetric Analysis

To examine the thermal degradation behavior of food waste compost, sawdust and compost were analyzed with a TGA.

Figure 2a,b show TGA and DTG results for sawdust. The weight is reduced as moisture is evaporated at temperatures below 100 °C. If this range is excluded, there are two decomposition ranges: one from 275 °C to 360 °C, and another from 500 °C to 550 °C. Weight reduction in the range of 275 °C to 360 °C seems to be the result of hemi-cellulose decomposition [5,21] and lignin decomposition, which takes place gradually over temperatures ranging from 160 °C to 900 °C [22]. According to the thermal degradation behavior of pine sawdust in Ningbo Gao [23], hemi-cellulose decomposition took place at temperatures ranging from 225 °C to 375 °C, similar to the results found in this study. In the range of 500 °C to 550 °C, like the findings of Ulloa et al. [24], TGA-DTG results from coal and in radiated pine sawdust blend, weight reduction could be explained by the transition into aliphatic or aromatic compounds due to char decomposition and lignin volatilization.

According to the food waste kinetic study by Jo et al. [15], the key differential thermogravimetric (DTG) peaks in food waste were reached from 325 °C (10 °C/min) to 366 °C (20 °C/min) due to carbohydrate decomposition, and from 336 °C to 376 °C and from 399 °C to 446 °C due to protein and fat decomposition, and from 330 °C to 360 °C and from 200 °C to 500 °C due to cellulose and lignin decomposition. According to the DTG peaks in Figure 3 for food waste compost, there were two decomposition ranges of 250 °C to 370 °C and 500 °C to 560 °C, which were different from the results presented by Jo et al. The 250 °C to 370 °C temperature range was similar to the hemi-cellulose decomposition range (240 °C to 365 °C) described by Vamvukaa [21] and Ghorbel [5], whereas the 500 °C to 560 °C range was similar to the saturated fatty acid degradation range (480 °C to 550 °C) stated by Souza et al. [25] and the polypeptide decomposition range (500 °C or higher) described by Bihari-Varga et al. [26].

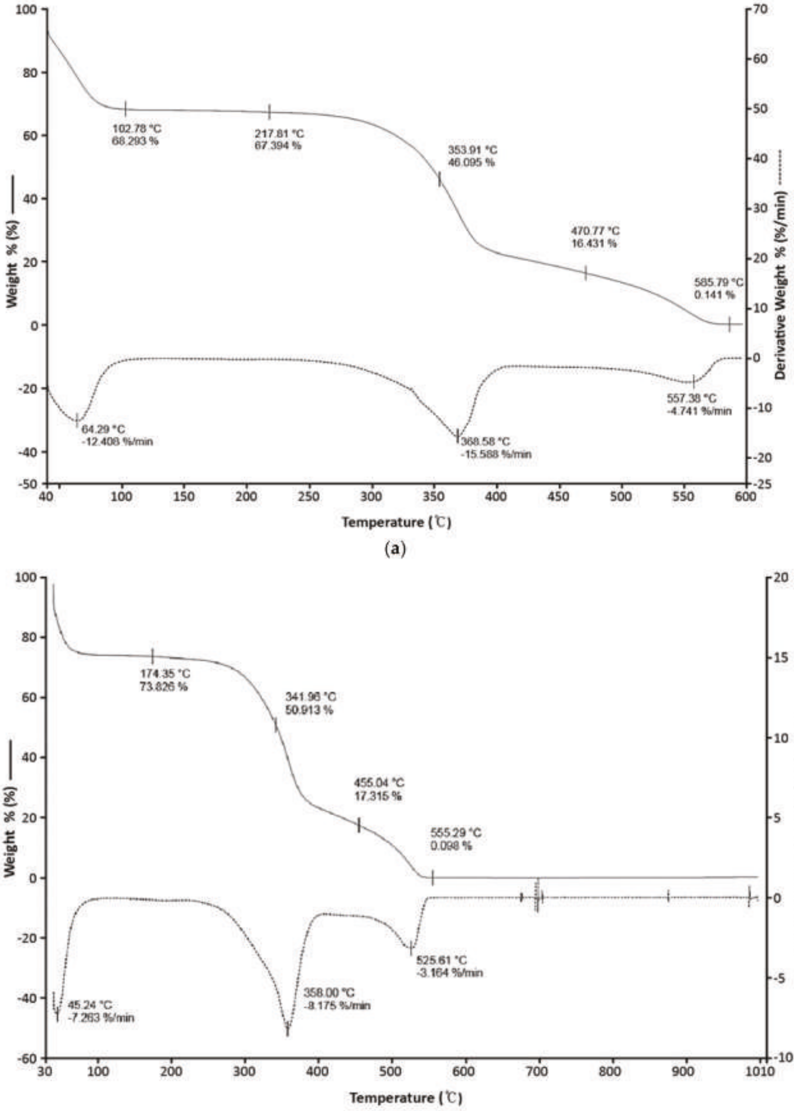

Figure 2. (**a**) Sawdust at 600 °C, 20 °C/min; (**b**) Sawdust 1000 °C, 10 °C/min.

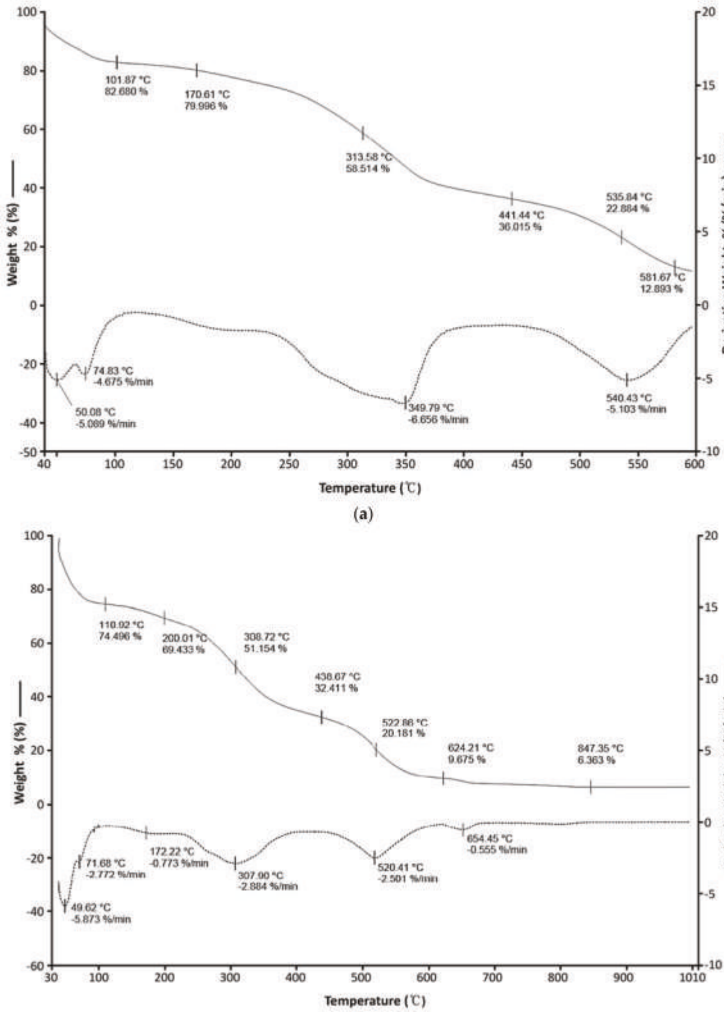

Figure 3. (**a**) Compost at 600 °C, 20 °C/min; (**b**) Compost at 1000 °C, 10 °C/min.

As mentioned earlier, these differences could be interpreted as a phenomenon that occurred as compost was degraded by microorganisms beforehand, even though the raw material properties were similar. Carbohydrates, proteins, and fat in food waste are digested by microorganisms during the composting process and are degraded into glucose, polypeptide, and fatty acids, or most of them convert into carbon dioxide or ammonia. In the end, small fractions of food waste remain in the final compost [18].

When the thermal degradation tendencies of sawdust and compost were compared, their decomposition took place in nearly the same temperature ranges. This happens when most of the food in food waste compost is degraded, and sawdust, which is not degraded, accounts for most of the compost. Their hemi-cellulose decomposition ranges of 275 °C to 360 °C and 250 °C and 370 °C were nearly identical. When their second decomposition ranges were compared, it was found that compost tended to be degraded more than sawdust. According to James [18], fat in food waste composting was degraded more slowly than protein or carbohydrate, and after 412 h of composting, protein fractions were very low while fat fractions remained high. Hence, one can see that decomposition in compost is greater than sawdust because the decomposition of fatty acids, a byproduct of fat decomposition, and the decomposition of char, which also occurred in sawdust, took place simultaneously in the second decomposition range in food waste compost.

3.3. Mass Spectrometry Analysis

To analyze the gases released during the pyrolysis of sawdust and compost, this study performed a TGA-GC-MS analysis within the largest decomposition temperature range. Figure 4 show GC-MS peak results for gases released from the TGA process of compost and sawdust, and each peak is described in Tables 3 and 4. Since Si-C compounds found in sawdust and compost TGA-GC-MS results around 12~36 (min) in Figure 4 are influenced by moisture which is one of the emitted gases (H_2O, CH_4, CO_2, etc.) during the decomposition process into several smaller molecules [27], it was excluded from the interpretation. The Si-C compounds are not produced by the degradation of food waste compost. But the detection was inevitable since it is a GC column substance measured by the moisture generated by the food waste compost's decomposition affects the GC column.

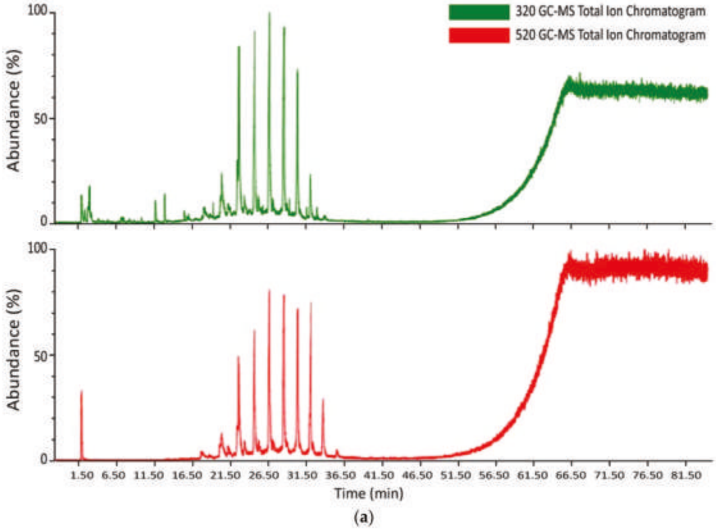

Figure 4. *Cont.*

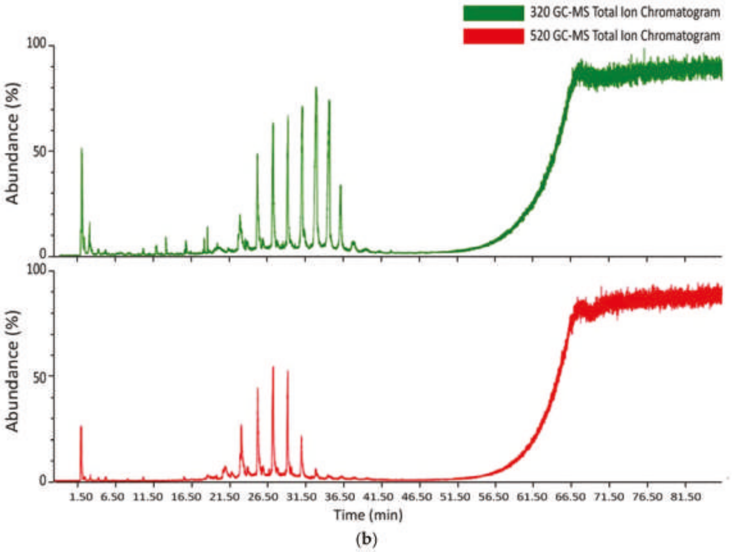

Figure 4. (**a**) Sawdust TGA-GC-MS results; (**b**) Compost TGA-GC-MS results.

Table 3. TGA-GC-MS analysis results for sawdust.

Temperature	Time (min)	MW	Compound Name	Formula
320 °C	1.973	130	thiocyanic acid, methylene ester	$C_3H_2N_2S_2$
	2.279	122	Butanoic acid, 4-chloro	$C_4H_7O_2Cl$
	6.617	96	furfural	$C_5H_4O_2$
	7.21	98	furanmethanol	$C_5H_6O_2$
	8.503	84	2(5H)-furanone	$C_4H_4O_2$

Table 4. TGA-GC-MS analysis results for compost.

Temperature	Time (min)	MW	Compound Name	Formula
320 °C	1.962	285	fumaric Acid 2-dimethylaminoethyl-heptyl ester (N-contain)	$C_{15}H_{27}O_4N$
	2.296	88	Thiophene, Tetrahydro	C_4H_8S
	6.634	96	1H-pyrazole, 3,4-dimethyl(C)	$C_5H_8N_2$
	7.213	88	methylene cyclo propane carboxylic acid	$C_5H_6O_2$
	8.497	84	2(5H)-furanone(C,P)	$C_4H_4O_2$
	9.694	106	Benzaldehyde	C_7H_{6O}
	9.892	157	Glycine, N-Cyclopropylcarbonyl-methyl ester	$C_7H_{11}O_3N$
520 °C	2.356	202	1,3-propanediol, 2-methyl-dipropanoate(Fatty acids, aliphatic compounds)	$C_{10}H_{18}O_4$
	2.866	78	Benzene	C_6H_6
	3.334	258	oxalic acid butyl 2-Ethylhexyl ester(Fatty acids, aliphatic compounds)	$C_{14}H_{26}O_4$
	5.764	214	pentanoic acid 2-Ethylhexyl ester	$C_{13}H_{26}O_2$
	8.384	214	propanoic acid, 2,2-Dimethyl-,2-Ethylhexyl ester	$C_{13}H_{26}O_2$

Based on the TGA results, the TGA-GC-MS analysis was conducted at the biggest weight reduction range around 320 °C and around 520 °C. Sawdust analysis result in Table 3 shows most of the substances are emitted is furan groups. Furans organics were produced by hemi-cellulose decomposition [23,27]. Compared with TGA-GC-MS analysis result and sawdust TGA result at a 320 °C, detecting of furan groups at 320 °C is reasonable because a large weight loss at 320 °C is caused by the decomposition of hemi-cellulose. On the other hand, sawdust GC-MS results at 520 °C show that only Si-C compounds are detected. As in the TGA results, most weight loss is done at around 320 °C, so the amount of emission gases at around 520 °C appears to be small. Si-C compounds detected in this section indicates that the substances slight decomposition occurs, and moisture from the light gas (H_2O, CH_4, CO_2, etc.) produced during the decomposition process seems to have affected the GC-MS results.

Food waste compost analysis result at 320 °C shows that furan groups are detected as in sawdust. This indicates that the sawdust contained in the compost is broken down and discharged. Fatty acids, which are generated from thermo-chemolysis of fat during the composting process, are detected in the form of methyl esters in pyrolysis gases, and include propanoic acids and 2,2-dimethyl-,2-ethylhexyl esters. In addition, C12–C19 polymeric carbon compounds are also found as products of fatty acid degradation [28]. In particular, while C12–C19 carbon compounds could have simply come from fat fractions in food waste, they also could have originated from degradation by microorganisms. As compost includes many microorganisms in the final product, both of those possibilities are considered.

Smidt, Ena, et al. [29] detected m/z 202, 258 compounds as the decomposition products of fatty acids, or aliphatic compounds. Oxalic acid butyl 2-ethylhexyl esters, 1,3-propanediol, and 2-methyl-dipropanoate were detected in the TGA-GC-MS results. This confirmed that the second decomposition of food waste compost yielded fatty acids and aliphatic compounds, as mentioned in the TGA-DTG results. Nitrogen compounds, which are released by protein decomposition, were detected in the form of glycine and fumaric acid 2-dimethylaminoethyl-heptyl esters. Proteins in food waste, however, were not present with a high content in compost, and it seems that proteins were absorbed as elements essential for bacteria and microorganisms. In other words, they had been discharged by microorganism decomposition. In addition, low molecular weight compounds, such as benzene and benzaldehyde, are produced by microorganism pyrolysis [30], but they are also generated by lignin and hemi-cellulose decomposition. Therefore, it is difficult to track their exact origin.

3.4. Biochar Production

Table 5 shows biochar mass yield results. They were calculated by dividing the weight of the residue after pyrolysis by that of the input at each temperature.

Table 5. Food waste compost biochar yield.

Temperature (°C)	Before Pyrolysis (g)	After Pyrolysis (g)	Yield (%)
300	200.52 ± 0.38	88.52 ± 2.07	44.14 ± 0.95
400	200.32 ± 0.16	60.57 ± 0.04	30.24 0.05
500	200.31 ± 0.12	45.09 ± 3.20	22.51 ± 1.61

As the pyrolysis temperature increased, the yield decreased by 14% from 300 °C to 400 °C, which was higher than the 8% decrease observed between 400 °C to 500 °C. The weight reduction was greatest from 300 °C to 400 °C as demonstrated in TGA results in Section 3.2.

Figure 5 compares the calorific values of food waste compost biochar, pre-pyrolysis raw material compost, and the food waste calorific values of Lee et al. [12] and Jo et al. [15]. Food waste compost showed 17.85 kJ/g, a lower calorific value than raw food waste 19.46 kJ/g, because the organic matter in food waste was degraded. As a result, the substances that increase the calorific value (e.g., carbon) was relatively lower. After pyrolysis, food waste compost has increased in the calorific value compared with raw food waste compost as the pyrolysis temperature changes from 300 °C to 500 °C. Considering a large amount of organic matter was degraded by microorganisms, the calorific value did not show a large decrease; sawdust played a supporting role. In fact, Chen and Leung [31] showed that sawdust had a calorific value of 18.064 kJ/g.

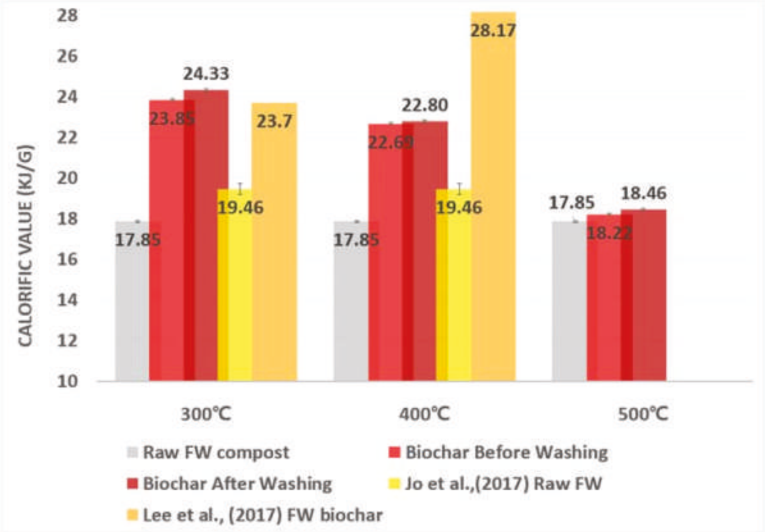

Figure 5. Calorific values of food waste compost biochar and raw material.

The calorific value of biochar, which was produced after pyrolysis of food waste compost, tended to decrease from 24.33 kJ/g to 18.46 kJ/g as the pyrolysis temperature increased. This tendency was also found in Ghorbel's study [5], in which the calorific value fell from 25.3 kJ/g to 22.8 kJ/g when the pyrolysis temperature increased from 250 °C to 350 °C and pyrolysis was performed for 2 h. By contrast, Lee et al. [12], who performed pyrolysis of food waste, found that the calorific value increased from 23.7 kJ/g to 28.17 kJ/g when the pyrolysis temperature rose from 200 °C to 400 °C. This occurs because Lee et al. [12] used food waste as a raw material, while this study used food waste compost. When raw food waste is used for pyrolysis, the carbon content increases as volatile substances and containing moistures are removed by supplied energy, and key components are carbonized [32]. Demirbas [33] interpreted the char generation process from biomass through pyrolysis with the following scheme:

$$\text{1st stage: Biomass} \rightarrow \text{Water} + \text{Unreacted residue} \tag{1}$$

$$\text{2nd stage: Unreacted residue} \rightarrow (\text{Volatile} + \text{Gases})\ 1 + (\text{Char})\ 1 \tag{2}$$

$$\text{3rd stage: } (\text{Char})\ 1 \rightarrow (\text{Volatile} + \text{Gases})\ 2 + (\text{Char})\ 2 \tag{3}$$

In other words, while the raw food waste requires much energy for the 1st, 2nd, and 3rd stages, food waste compost has a lower moisture content and has already been degraded fracture by microorganisms. Therefore, the reaction at the 1st and 2nd stage can take place with lower energy. At 300 °C, Char 1 is produced and increases the calorific value. Since the compost has low volatile matter and water content, 300 °C is enough to conduct 1st and 2nd stage. But when the pyrolysis temperature increases, volatilization occurs in Char 1 and decreases the carbon content, the yield, and the calorific value.

In addition, in food waste compost, sawdust plays an important role in producing a calorific value. This is in contrast to raw food waste. As described in the TGA results, hemi-cellulose, a major component in sawdust, is degraded rapidly from 300 °C to 400 °C, and lignin and other components continue to be degraded at 400 °C or higher. Therefore, food waste compost shows a lower calorific value when the pyrolysis temperature increases from 300 °C to 500 °C.

Consequently, food waste compost already degraded by microorganisms has carbon fixation at a low pyrolysis temperature and produces a high calorific value. Sawdust, which plays an important role in producing the calorific value, shows little volatilization, and it shows a higher calorific value than food waste at 300 °C pyrolysis temperature.

4. Conclusions

This study intended to examine the value of biochar produced from pyrolysis of food waste compost as an energy storing fuel. Food waste compost had a lower carbon and higher ash content than food waste because the organic matter was degraded. This decreased the carbon content during the composting process, while the ash content increased relatively. Biochar from pyrolysis of food waste compost had a high carbon content of 51% at 300 °C, and the carbon content decreased as the pyrolysis temperature increased. According to the TGA-DTG analysis results, compost showed the largest weight reduction from 240 °C to 365 °C. The weight reduction temperature ranges for compost and sawdust were quite similar. This occurred because organic matter in food waste was degraded, and sawdust, which showed relatively lower degradation, remained during the composting process. A GC-MS analysis on gases released in these ranges found that the gases were fragments of fatty acids, protein, carbohydrate, and hemi-cellulose. These results could also have been caused by degradation of microorganisms and sawdust involved in the composting process or small fragments of food waste. This study measured the calorific value of biochar and found that biochar showed the highest calorific value of 24.33 kJ/g at 300 °C in proportion to the carbon content. At a low pyrolysis temperature, carbon fixation occurred easily since the food waste in compost was degraded by microorganisms, and the volatilization of sawdust, which plays an important role in determining the calorific value, was also small. That is why it showed a higher calorific value than food waste at 300 °C. Hence, it seems that food waste compost can be used as a promising alternative fuel compared with other refuse-derived fuels (RDF) since food waste compost is able to convert into a fuel that shows similar calorific values to other fuels with a smaller energy supply.

Author Contributions: J.-H.J. and Y.-S.Y. designed the experiment devices; Y.-S.Y., I.-T.K., and Y.-E.L. contributed to the analysis of experimental results; Y.-E.L. performed the experiments, analyzed the data, and wrote the paper.

Funding: This research was funded by the major project (2018-0063) of the Korea Institute of Civil engineering and building Technology (KICT).

Acknowledgments: This study was supported by the major project (2018-0063) of the Korea Institute of Civil engineering and building Technology (KICT).

Conflicts of Interest: The authors declare no conflict of interest.

References

1. Lee, S.E.; Ahn, H.J.; Youn, S.K.; Kim, S.M.; Jung, K.W. Application effect of food waste compost abundant in NaCl on the growth and cationic balance of rice plant in paddy soil. *Kor. J. Soil Sci. Fertil.* **2000**, *33*, 100–108.
2. Zhao, S.-X.; Ta, N.; Wang, X.-D. Effect of Temperature on the Structural and Physicochemical Properties of Biochar with Apple Tree Branches as Feedstock Material. *Energies* **2017**, *10*, 1293.
3. Lee, J.J.; Park, R.D.; Kim, Y.W.; Shim, J.H.; Chae, D.H.; Rim, Y.S.; Sohn, B.K.; Kim, T.H; Kim, K.Y. Effect of food waste compost on microbial population, soil enzyme activity and lettuce growth. *Bioresour. Technol.* **2004**, *93*, 21–28. [CrossRef] [PubMed]
4. Ministry of Environment. *2015 Food Waste Treatment Facility Installation and Operation Status (Nationwide)*; Ministry of Environment: Sejong City, Korea, 2015.
5. Ghorbel, L.; Rouissi, T.; Brar, S.K.; López-González, D.; Ramirez, A.A.; Godbout, S. Value-added performance of processed cardboard and farm breeding compost by pyrolysis. *Waste Manag.* **2015**, *38*, 164–173. [CrossRef] [PubMed]
6. Williams, P.T. *Waste Treatment and Disposal*; John Wiley & Sons: New York, NY, USA, 2005.
7. Brassard, P.; Godbout, S.; Raghavan, V.; Palacios, J.H.; Grenier, M.; Zegan, D. The Production of Engineered Biochars in a Vertical Auger Pyrolysis Reactor for Carbon Sequestration. *Energies* **2017**, *10*, 288. [CrossRef]

8. Imam, T.; Capareda, S. Characterization of bio-oil, syn-gas and bio-char from switchgrass pyrolysis at various temperatures. *J. Anal. Appl. Pyrolysis* **2012**, *93*, 170–177. [CrossRef]
9. Jahirul, M.I.; Rasul, M.G.; Chowdhury, A.A.; Ashwath, N. Biofuels production through biomass pyrolysis—A technological review. *Energies* **2012**, *5*, 4952–5001. [CrossRef]
10. Barneto, A.G.; Carmona, J.A.; Conesa Ferrer, J.A.; Díaz Blanco, M.G. Kinetic study on the thermal degradation of a biomass and its compost: Composting effect on hydrogen production. *Fuel* **2010**, *89*, 462–473. [CrossRef]
11. Ryu, C.; Finney, K.; Sharifi, V.N.; Swithenbank, J. Pelletised fuel production from coal tailings and spent mushroom compost—Part I: Identification of pelletisation parameters. *Fuel Process. Technol.* **2008**, *89*, 269–275. [CrossRef]
12. Lee, Y.-E.; Jo, J.-H.; Kim, S.-M.; Yoo, Y.-S. Recycling Possibility of the Salty Food Waste by Pyrolysis and Water Scrubbing. *Energies* **2017**, *10*, 210. [CrossRef]
13. Phan, A.N.; Ryu, C.; Sharifi, V.N.; Swithenbank, J. Characterisation of slow pyrolysis products from segregated wastes for energy production. *J. Anal. Appl. Pyrolysis* **2008**, *81*, 65–71. [CrossRef]
14. Ryu, C.; Sharifi, V.N.; Swithenbank, J. Waste pyrolysis and generation of storable char. *Int. J. Energy Res.* **2007**, *31*, 177–191. [CrossRef]
15. Jo, J.-H.; Kim, S.-S.; Shim, J.-W.; Lee, Y.-E.; Yoo, Y.-S. Pyrolysis Characteristics and Kinetics of Food Wastes. *Energies* **2017**, *10*, 1191. [CrossRef]
16. Zhang, R.; El-Mashad, H.M.; Hartman, K.; Wang, F.; Liu, G.; Choate, C.; Gamble, P. Characterization of food waste as feedstock for anaerobic digestion. *Bioresour. Technol.* **2007**, *98*, 929–935. [CrossRef] [PubMed]
17. Kwon, S.-H.; Lee, D.-H. Evaluation of Korean food waste composting with fed-batch operations I: Using water extractable total organic carbon contents (TOCw). *Process Biochem.* **2004**, *39*, 1183–1194. [CrossRef]
18. Chang, I.J.; Hsu, T. Effects of compositions on food waste composting. *Bioresour. Technol.* **2008**, *99*, 8068–8074. [CrossRef] [PubMed]
19. Lee, Y.-E.; Jo, J.-H.; Kim, I.-T.; Yoo, Y.-S. Chemical Characteristics and NaCl Component Behavior of Biochar Derived from the Salty Food Waste by Water Flushing. *Energies* **2017**, *10*, 1555. [CrossRef]
20. *EN, BS. 15359: 2011 Solid Recovered Fuels. Specifications and Classes*; BSI: London, UK, 2011; p. 30.
21. Vamvuka, D.; Kakaras, E.; Kastanaki, E.; Grammelis, P. Pyrolysis characteristics and kinetics of biomass residuals mixtures with lignite ☆. *Fuel* **2003**, *82*, 1949–1960. [CrossRef]
22. Yang, H.; Yan, R.; Chen, H.; Lee, D.H.; Zheng, C. Characteristics of hemicellulose, cellulose and lignin pyrolysis. *Fuel* **2007**, *86*, 1781–1788. [CrossRef]
23. Gao, N.; Li, A.; Quan, C.; Du, L.; Duan, Y. TG–FTIR and Py–GC/MS analysis on pyrolysis and combustion of pine sawdust. *J. Anal. Appl. Pyrolysis* **2013**, *100*, 26–32. [CrossRef]
24. Ulloa, C.A.; Gordon, A.L.; García, X.A. Thermogravimetric study of interactions in the pyrolysis of blends of coal with radiata pine sawdust. *Fuel Process. Technol.* **2009**, *90*, 583–590. [CrossRef]
25. De Souza, A.G.; Santos, J.C.O.; Conceição, M.M.; Silva1, M.C.D.; Prasad, S. A thermoanalytic and kinetic study of sunflower oil. *Braz. J. Chem. Eng.* **2004**, *21*, 265–273. [CrossRef]
26. Bihari-Varga, M.; Sepulchre, C.; Moczár, E. Thermoanalytical studies on protein-polysaccharide complexes of connective tissues. *J. Therm. Anal. Calorim.* **1975**, *7*, 675–683. [CrossRef]
27. Gu, X.; Ma, X.; Li, L.; Liu, C.; Cheng, K.; Li, Z. Pyrolysis of poplar wood sawdust by TG-FTIR and Py–GC/MS. *J. Anal. Appl. Pyrolysis* **2013**, *102*, 16–23. [CrossRef]
28. Som, M.-P.; Lemée, L.; Amblès, A. Stability and maturity of a green waste and biowaste compost assessed on the basis of a molecular study using spectroscopy, thermal analysis, thermodesorption and thermochemolysis. *Bioresour. Technol.* **2009**, *100*, 4404–4416. [CrossRef] [PubMed]
29. Smidt, E.; Eckhardt, K.U.; Lechner, P.; Schulten, H.R.; Leinweber, P. Characterization of different decomposition stages of biowaste using FT-IR spectroscopy and pyrolysis-field ionization mass spectrometry. *Biodegradation* **2005**, *16*, 67–79. [CrossRef] [PubMed]
30. Simmonds, P.G. Whole microorganisms studied by pyrolysis-gas chromatography-mass spectrometry: Significance for extraterrestrial life detection experiments. *Appl. Microbiol.* **1970**, *20*, 567–572. [PubMed]
31. Chen, G.; Leung, D.Y.C. Experimental investigation of biomass waste, (rice straw, cotton stalk, and pine sawdust), pyrolysis characteristics. *Energy Sources* **2003**, *25*, 331–337. [CrossRef]

32. Kim, K.-S.; Choi, E.-A.; Ryu, J.-S.; Lee, Y.P.; Park, J.-Y.; Choi, S.-H.; Park, S.-J. A study on pyrolysis characterization and heating value of semi-carbonized wood chip. *Appl. Chem. Eng.* **2012**, *23*, 440–444.
33. Demirbas, A. Effects of temperature and particle size on bio-char yield from pyrolysis of agricultural residues. *J. Anal. Appl. Pyrolysis* **2004**, *72*, 243–248. [CrossRef]

energies

MDPI

Article

Advanced One-Dimensional Entrained-Flow Gasifier Model Considering Melting Phenomenon of Ash

Jinsu Kim [1], Hyunmin Oh [2], Seokyoung Lee [1] and Young-Seek Yoon [2,*]

[1] Department of Chemical Engineering, Pohang University of Science and Technology (POSTECH), Pohang 37673, Korea; jinsukim1102@postech.ac.kr (J.K.); lsylove0626@postech.ac.kr (S.L.)

[2] Graduate Institute of Ferrous Technology, Pohang University of Science and Technology (POSTECH), Pohang 37673, Korea; min0808@postech.ac.kr

* Correspondence: ysyoon@postech.ac.kr; Tel.: +82-54-279-0149; Fax: +82-54-279-0138

Received: 3 March 2018; Accepted: 17 April 2018; Published: 21 April 2018

Abstract: A one-dimensional model is developed to represent the ash-melting phenomenon, which was not considered in the previous one-dimensional (1-D) entrained-flow gasifier model. We include sensible heat of slag and the fusion heat of ash in the heat balance equation. To consider the melting of ash, we propose an algorithm that calculates the energy balance for three scenarios based on temperature. We also use the composition and the thermal properties of anorthite mineral to express ash. gPROMS for differential equations is used to solve this algorithm in a simulation; the results include coal conversion, gas composition, and temperature profile. Based on the Texaco pilot plant gasifier, we validate our model. Our results show good agreement with previous experimental data. We conclude that the sensible heat of slag and the fusion heat of ash must be included in the entrained flow gasifier model.

Keywords: Texaco pilot plant; reactor modelling; ash fusion temperature (AFT); melting phenomenon

---

1. Introduction

Generally, an entrained flow gasifier (EFG) uses finely pulverized coal with steam and oxygen co-current to make syngas. This design forms a uniform internal temperature, and has a residence time of only a few seconds [1]. The coal conversion reaches approximately 100%, because the gasifiers use pulverized coal at high temperature. An EFG is not affected by the rank of the coal [2]. Currently many commercial EFGs are operated by enterprises such as (General Electric) GE, Shell, Siemens, CB&I, MHI and ThyssenKrupp [3]. These types of gasifiers are operated at a temperature higher than the AFT. The ash, which is a coal residue, is discharged in the form of molten slag. The slag that is discharged to the bottom has a considerable amount of sensible heat. The design of the gasifier should consider this heat, because it affects the internal maximum temperature.

Existing EFG models [4–6] focus on calculating the composition of the gas. To improve the model, representations of the reaction mechanism of coal have been improved. Previous models have proposed various reaction kinetic models, such as random pore model [7], shrinking core model [8,9], and shrinking sphere model [10]. In addition, equilibrium models have been suggested calculating the reaction between gases [11–14]. Most of the studies [7–13,15] have focused on developing reaction models and adjusting parameters. The energy balance is not considered sufficiently to find the optimal gasifier design. They have developed heat balance with two variables: (i) input and output heat flow; and, (ii) reaction heat.

The Texaco pilot plant is a typical EFG. Several studies (Table 1) [4–6,16,17] have attempted to model it based on experimental data [18] acquired from the Electric Power Research Institute (EPRI). Wen et al. (1979) proposed a model that uses three reaction zones: (i) pyrolysis and volatile combustion zone; (ii) combustion and gasification zone; and, (iii) only gasification zone; the model applies a

Stokes' law approximation instead of momentum balance [16]. Govind and Shah (1984) used the same kinetics as those of Wen et al., but neglected the momentum balance [17]. Vamvuka et al. (1995) used thermogravimetric analysis data to develop the kinetics based on bituminous coal, but does not consider the momentum balance [4,5]. Hwang et al. (2015) expressed two reaction zones without considering the 'pyrolysis and volatile combustion' zone; this model applies the Stokes' law approximation, and adjust parameters, such as outer wall temperature and the reaction rate constant [6].

Table 1. Texaco pilot plant entrained flow gasifier (EFG) model based on the Electric Power Research Institute (EPRI) data.

Researcher	Kinetics	Momentum	Energy Balance
Wen et al.	3 reaction zones	Stokes' law approximation	Thermal
Govind and Shah	3 reaction zones	Not considered	Thermal
Vamvuka et al.	Parameter based on thermogravimetric analysis	Not considered	Thermal
Hwang et al.	2 reaction zones	Stokes' law approximation	Thermal

All of these models of the EFG have limitations. For energy balance, they all consider only input and output heat flow, and reaction enthalpy; they neglect energy that is absorbed by the melting of ash, and therefore do not accurately represent the inside of the gasifier in the real world. As a result, the calculated temperature is too high. For this purpose, previous papers introduce an additional term that represents heat loss to the outer wall. This calculation of heat loss requires assumptions about variables such as wall temperature, overall heat transfer coefficient, and thermal conductivity. These assumptions decrease the accuracy of the models.

The objective of this study is to improve the existing one-dimensional EFG model by including the ash-melting phenomenon instead of approximating it as heat loss at the outer wall. We propose a model to increase the accuracy of the temperature profile. The resulting model can predict the composition change of the product gas. We apply a shrinking sphere model to consider the combustion reaction, and then suggest reaction kinetics to calculate the amount of ash. We also design a new algorithm to consider the melting phenomenon of ash to improve the accuracy of the predicted temperature profile. We discuss the energy balance equation in three cases, according to the temperature: (i) temperature is lower than AFT; (ii) temperature in the first cell is higher than AFT; and, (iii) temperature in the second cell is higher than AFT. Finally, we compare the simulation results with the experimental results.

2. EFG Model

2.1. Basic Assumptions

To build the model, we assumed that:

- The inside of the gasifier is cylindrical; this assumption is suitable for modeling the Texaco EFG [17].
- Coal and gas mass flow rates are constant.
- Temperature and gas concentration are uniform in the radial direction.
- Each cell is perfectly mixed.
- The reactor consists of equally divided cells (Figure 1). The reaction rate depends on each cell's conditions.
- Spherical coal particles react from the outer surface while moving through the cell from front to end. As the reaction of the coal progresses, the size of the particles decreases.
- All of the coal grains in the same cell are uniform.

- Ash changes to slag after temperature exceed an AFT.
- Ashes are inert.

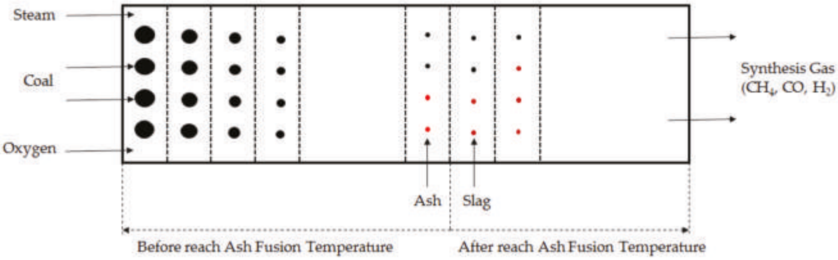

Figure 1. Gasifier internal scheme that considers melting of ash. Red dot: ash; brown dot: slag.

2.2. Reaction Kinetics

The reaction type can be divided into a heterogeneous reaction and a homogeneous reaction. The heterogeneous reaction indicates that the coal particles react with the gas. Coal reacts with oxygen, carbon dioxide, steam, and hydrogen (Table 2). The water gas shift reaction (WGS) and CO oxidation were considered as major reactions. The WGS reaction proceeds rapidly at a high temperature, and was therefore considered to be at equilibrium. CO oxidation was regarded as irreversible; as a consequence, gasification and combustion reaction could be expressed without dividing the reaction zone. Therefore, we solved reaction kinetics based on the single reaction zone; i.e., the six reaction schemes that are presented below were considered equally from the first cell to the last cells. The EFG does not produce much methane [19], so the methane-steam reforming reaction was not considered in this model.

Table 2. Homogeneous and heterogeneous reaction list used in this study.

Reaction Type	Reaction	Description
Heterogeneous	$R_1:\ C_aH_bO_cN_dS_eA_f + \left(\frac{a}{\phi^*} + \frac{b}{4} - \frac{c}{2} - \frac{e}{2}\right)O_2 \rightarrow \left(\frac{2}{\varnothing} - 1\right)aCO_2 + 2\left(1 - \frac{1}{\varnothing}\right)aCO + \left(\frac{b}{2} - e\right)H_2O + eH_2S + \frac{d}{2}N_2 + fA$	Coal↔O_2
	$R_2:\ C_aH_bO_cN_dS_eA_f + aCO_2 \rightarrow 2aCO + cH_2O + (\frac{b}{2} - c - e)H_2 + eH_2S + \frac{d}{2}N_2 + fA$	Coal↔CO_2
	$R_3:\ C_aH_bO_cN_dS_eA_f + (a - c)H_2O \rightarrow aCO + \left(a + \frac{b}{2} - c - e\right)H_2 + eH_2S + \frac{d}{2}N_2 + fA$	Coal↔H_2O
	$R_4:\ C_aH_bO_cN_dS_eA_f + \left(2a - \frac{b}{2} + c - e\right)H_2 \rightarrow aCH_4 + cH_2O + eH_2S + \frac{d}{2}N_2 + fA$	Coal↔H_2
Homogeneous	$R_5:\ CO + H_2O \leftrightarrow CO_2 + H_2$ $R_6:\ CO + \frac{1}{2}O_2 \rightarrow CO_2$	WGS CO oxidation

* ϕ is a function of absolute temperature T, and adjusts the ratio of complete and incomplete combustion. $\varnothing = \frac{2w+2}{w+2}$, $w = 2500 \cdot \exp\left(-\frac{6249}{T}\right)$. [4].

To incorporate the coal components in reaction kinetics, the ultimate analysis was applied. The reaction kinetics (Table 3) of coal used in this study was based on Hwang et al.'s work. One difference is that we have attempted to quantify ash. We introduce subscript *f*, which means that the ash component contained in 1 g of coal, and is the result of the proximate analysis. The subscripts *a* through *e* represent elements contained in 1g of coal. For heterogeneous reactions, the reaction rate of coal was proportional to both the surface area of the coal particles and the partial pressure of each gas. In homogeneous reactions, all of the gases were assumed to be ideal.

Table 3. Reaction kinetics and parameters that were used in this study.

action Type	Reaction Rate (g/s)	k (g/(m^2·atm·s))	Reference
Heterogeneous	$k_1 \pi {d_c}^2 P_{O_2}$	$6180 \cdot e^{\left(-\frac{10,233.9}{T}\right)}$	[5,6]
	$k_2 \pi {d_c}^2 P_{CO_2}$	$198,100 \cdot e^{\left(-\frac{10,233.9}{T}\right)}$	
	$k_3 \pi {d_c}^2 P_{H_2O}$	$198,100 \cdot e^{\left(-\frac{10,233.9}{T}\right)}$	
	$k_4 \pi {d_c}^2 P_{H_2}$	$385 \cdot e^{\left(-\frac{17,451.7}{T}\right)}$	
Homogeneous	**Equilibrium**	**Equilibrium Constant**	**Reference**
	$\mathrm{K} = \frac{P_{CO_2} P_{H_2}}{P_{CO} P_{H_2O}}$	$-2.4198 + 0.003855 \cdot \mathrm{T} + \frac{2180.6}{T}$	[20]
	Reaction Rate (mole/s)	**k (m^3/(mole·s))**	**Reference**
	$k_6 C_{CO} C_{CO_2}$	$3.09 \cdot e^{\left(-\frac{11,199}{T}\right)}$	[21]

3. Solving Procedure

3.1. Mass Balance

For mass balance, only production and consumption due to the reaction were calculated. The kinetics of the coal reaction was based on one coal grain. The number of coal particles per unit volume came from the following Equation (1):

$$N_v = \frac{W_{c,0}}{m_c v_c A} \tag{1}$$

The four coal reactions caused the coal conversion when the coal particles passed through the unit cell. Δz is unit cell length. The change of coal mass was calculated as

$$\Delta W_c = -N_v \cdot A \sum_{i=1}^{4} R_i \cdot \Delta z \tag{2}$$

Mass balance of the ash could be expressed in the same way as that of coal. The only difference is that the stoichiometric coefficients f are added. The stoichiometric coefficients that correspond to ashes were all equal to f (Equation (3)). For slag, the mass balance was not considered separately. When the temperature was higher than AFT, ash was regarded as slag.

$$\Delta W_a = -N_v \cdot A \sum_{i=1}^{4} R_i \cdot f \cdot \Delta z \tag{3}$$

For gas mass balance, R_5 and R_6 were also included. R_6 is irreversible, so it was applied in the same manner as the heterogeneous reactions. α means the degree of deviation from equilibrium. To calculate α, we used Equation (4)

$$\mathrm{K} = \frac{\left(F_{CO_2} - \alpha\right) \cdot \left(F_{H_2} - \alpha\right)}{\left(F_{CO} + \alpha\right) \cdot \left(F_{H_2O} + \alpha\right)} \tag{4}$$

After converting this to an explicit form, we took a small root of the quadratic equation. The reason was that large roots make the mole flow negative.

Equation (5) is the mass balance of gases where ξ_i is a stoichiometric coefficient for each component. Heterogeneous and homogeneous reactions were considered in different forms. The terms on the right side of the equation mean in order: (i) initial value; (ii) heterogeneous reactions; (iii) CO oxidation; and, (iv) each cell reaches equilibrium.

$$F_i = F_{i,0} - \left(N_v \cdot A \cdot \Delta z \cdot \sum_{j=1}^{4} \xi_{i,j} \cdot \frac{R_j}{MW_i} \right) + (R_5 \cdot \xi_{i,5}) \pm \alpha \tag{5}$$

3.2. Energy Balance

Heat flow of input and output and reaction enthalpy were considered equally in all cells. In some existing models [5,6,16,17], oxygen, steam, and coal temperature were set differently. When the temperatures of coal and gas are separately calculated, the temperature difference between them is generally ~10 K [22]. In this study, we simplified the problem by assuming that the gas temperature was the same as the coal temperature.

Coal residue is ash or slag depending on temperature condition (Figure 1). To consider ash melting, energy balance was calculated by dividing it into three cases. At temperature <AFT, Equation (6) was applied. It did not incorporate the fusion heat of ash.

$$\Delta \left\{ \left(W_c \cdot c_{p,c} + W_a \cdot c_{p,a} + W_s \cdot c_{p,s} + \sum_i F_i \cdot c_{p,i} \right) \mathrm{T} \right\} = -N_v \cdot A \cdot \sum_{j=1}^{6} R_j \cdot \Delta H_j - H_{loss} \tag{6}$$

Cells with temperature >AFT were considered using Equations (7) and (8). Equation (7) was applied only to the first cell, which has temperature >AFT. This equation calculates all of the latent heat of the accumulated ashes.

$$\Delta \left\{ \left(W_c \cdot c_{p,c} + W_a \cdot c_{p,a} \cdot W_s \cdot c_{p,s} + \sum_i F_i \cdot c_{p,i} \right) T \right\} = -N_v \cdot A \cdot \sum_{j=1}^{6} R_j \cdot \Delta H_j + W_a \cdot \Delta H_{ash} - H_{loss} \tag{7}$$

Equation (8) was applied to the remaining cells. It considers the heat of fusion of ash that occurs as it passes through each cell.

$$\Delta \left\{ \left(W_c \cdot c_{p,c} + W_a \cdot c_{p,a} \cdot W_s \cdot c_{p,s} + \sum_i F_i \cdot c_{p,i} \right) T \right\} = -N_v \cdot A \cdot \sum_{j=1}^{6} R_j \cdot \Delta H_j + \triangle W_a \cdot \Delta H_{ash} - H_{loss} \tag{8}$$

Calculation of the heat loss must consider radiation, convection, and conduction. In addition, the thermal conductivity varies depending on the material of the refractory. If these cannot be reasonably estimated, the overall heat transfer coefficient will produce large errors. In a previous study, the heat transfer coefficient was indirectly estimated instead of calculating the heat loss [6,16,17]; the authors claimed that 30% of the reaction heat was lost to the outer wall, and that the corresponding calorific value is about 7–10% of the heating value of coal. However, heat losses typically considered in an EFG range from 1 to 4% [23,24]. This value is dependent on the gasifier scale. When compared with industrial gasifiers, pilot-scale gasifiers have higher heat losses. Therefore, we assumed a heat loss of 4%.

3.3. Solving Algorithm

The length of the gasifier was divided into 1650 cells (500 parts/m). Each cell was a system. Mass and energy balance were calculated sequentially. The computational algorithm was terminated when it reached the end of the reactor, and we obtain a sufficiently smooth curve in the simulation result. The information calculated in each cell was as follows:

- Information about coal: coal conversion, coal mass flow rate.
- Molar flow rate of product gas.
- Temperature profile.

The proposed algorithm (Figure 2) was designed to apply the energy balance of three cases according to temperature. gPROMS simulation software (Process Systems Enterprise Ltd., London, UK) was used to perform the algorithm. The DASolver was applied; it could be used to solve differential equations in the steady state. Both the relative tolerance and absolute tolerance were fixed as 1.0×10^{-5}.

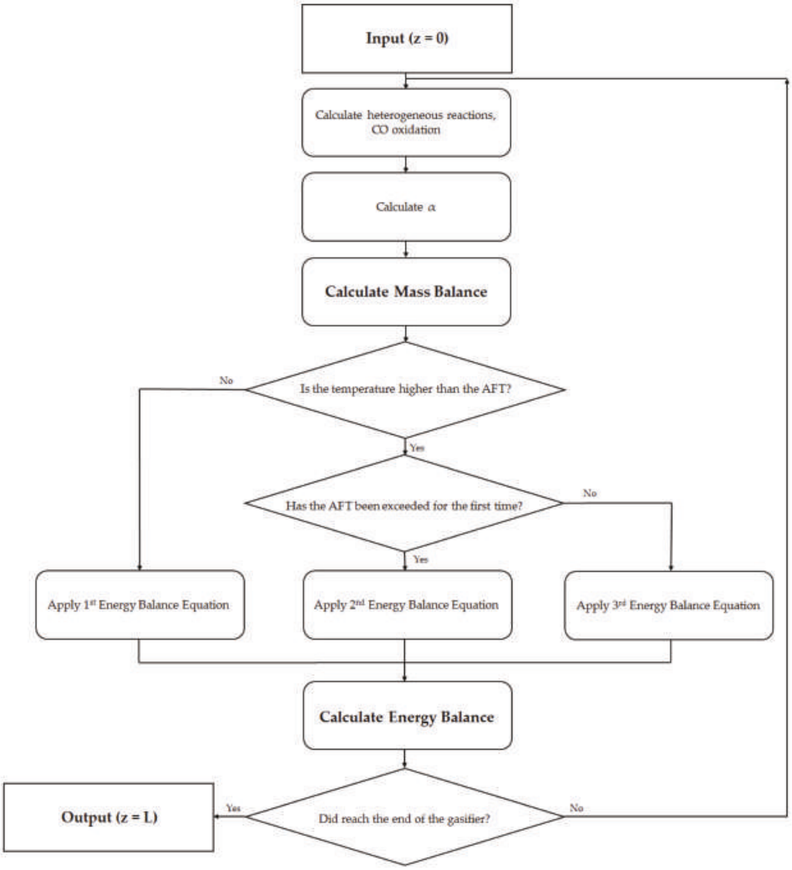

Figure 2. Algorithm that includes the melting of ash.

4. Required Information for Simulation

4.1. Operating Variables and Reactor Size

Required inputs, including operating variables and particle sizes (Table 4), were those of the existing pilot gasifier. These results were compared with those of previous studies. The experimental conditions were presented in the work of Govind and Shah, which is the same as for their simulation conditions. Experimental information on the outer wall temperature of the gasifier was not provided. The existing model assumed that the temperature of the outer wall started at 2100 K, and then decreased linearly [16,17]. We indirectly estimated the amount of heat loss from the coal heating value, instead of assigning an initial outer wall temperature.

Table 4. Comparison of operating variables and gasifier size between this and previous studies.

Operating Variables	This Work	Wen	Govind
Coal feed rate (g/s)	50	75	77
Steam to coal ratio (-)	0.24	0.24	0.241
Oxygen to coal ratio (-)	0.86	0.86	0.86
Feed coal temperature (K)	900	900	505
Feed gas temperature (K)	900	900	697(H_2O), 298(O_2)
Gasifier pressure (MPa)	2.0	2.0	2.4
Gasifier wall temperature (K)	Not considered	2100–600(Z/L)	2100–600(Z/L)
Gasifier Size	**This Work**	**Wen**	**Govind**
Gasifier length (cm)	330	330	330
Inner diameter (cm)	152	152	152

4.2. Coal Properties

This study considered Illinois no. 6 coal, which is the same type using previous modeling studies. The results (Table 5) of coal elemental analysis were acquired from the EPRI [18]. Density and specific heat capacity of the coal were the same as in previous work [16,17]. We considered a smaller particle size (41 µm) of coal than did previous work, for two reasons. First, 41 µm is closer to the size of the particles that were used in the EFG in real industry; particularly, when entering a dry feed, the particle size is $<$ 100 µm [25]. Second, the reaction of coal is directly related to particle size and kinetic parameters, so particle size is an important factor in kinetics. Therefore, the kinetic parameter and particle size must be taken from the same reference. We used the same kinetics parameters and the coal particle size as Hwang's model [6].

Table 5. Element analysis (wt %), coal properties, and feed conditions that were used in this study.

Element	Measurement
C	74.05
H	6.25
O	1.32
N	0.71
S	1.77
Ash	15.33
Coal Properties	**Assumed**
Density (g/cm^3)	1.80
Specific heat capacity (cal/(g·K))	0.45
Feed Conditions	**Set**
Feed particle size (µm.)	41
Velocity (cm/s)	50

4.3. Ash and Slag Properties

The EPRI provided only the coal analysis data; it does not provide information about ash. One of way to remedy this lack of information is to assume the ash component. However, the physical properties differ depending on the ash component. Calculate of thermal properties that consider its components is a difficult task. In some documents [26,27], a formula for predicting thermal properties according to the temperature have been proposed. However, they were out of the range of gasifier operating temperature.

In this study, different approaches were used. Coal ashes are composed of minerals (Figure 3). About 70–90% of the constituents are CaO, Al_2O_3, and SiO_2. They also include such as Fe_2O_3 and MgO [28,29]. In this work, we adopt the thermal properties of gehlenite (Figure 3) to represent ash.

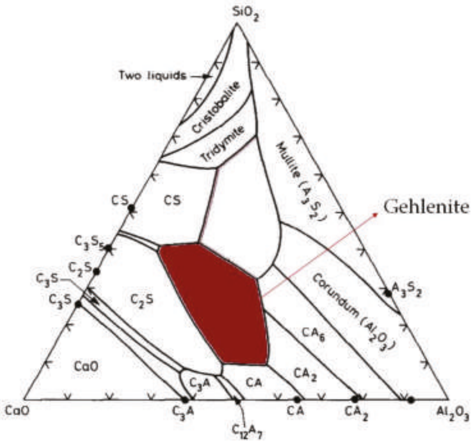

Figure 3. Ternary phase diagram of Al_2O_3-CaO-SiO_2. Brown: gehlenite.

The properties (Table 6) of ash and slag used in this study were obtained from the literature because the ash was considered to be a well-known mineral, and its thermal properties were set accordingly.

Table 6. Thermal properties of ash and slag used in this study.

Thermal Properties	Value	Reference
Fusion heat of ash (J/g)	627.6	[30]
Ash fusion temperature (K)	1863	[30]
Specific heat capacity of ash (J/(g·K))	$-0.976 + \ln T + \frac{279}{T} - \frac{1.094 \cdot 10^5}{T^2} + \frac{1.169 \cdot 10^7}{T^3}$	[31]
Specific heat capacity of slag (J/(g·K))	1.15	[32]

5. Results and Discussion

5.1. Model Valdation

To validate the model, several main variables were selected: final coal conversion rate; major product gas composition at exit; and, the hydrogen-to-carbon monoxide ratio (H_2/CO). The results (Table 7) of this simulation are presented together with the results of the previous researchers and experimental data. We did not arbitrarily adjust the kinetic parameters that were used in this study. We applied the same reactor size and operating conditions of the existing pilot gasifier. For this reason, results of this work were similar to results of previous studies. In addition, we considered the melting phenomenon of ash that was not considered in the existing one-dimensional (1-D) model and reduced the estimated heat loss in the previous model. As a result, the modeling results are improved.

Table 7. Simulation results and comparison of previous models with experimental data (Dry based).

Major Variables	This Work	Wen [16]	Govind [17]	Experiment [17]
Conversion (%)	98.8	98.9	98.1	98.6
H_2 (mole %)	38.6	39.8	40.0	39.1
CO (mole %)	57.7	56.6	55.5	57.6
H_2/CO ratio	0.668	0.703	0.721	0.679
CO_2 (mole %)	2.56	2.92	3.95	2.95

5.2. Simulation Results

5.2.1. Coal Conversion

Most of the reaction proceeded rapidly at the front of the gasifier (Figure 4). Only 10% of coal was reacted at around 0.15 m of the gasifier, but 80% had reacted at 0.24 m. This increase occurred because the combustion reactions were accelerated. The reaction rate of coal decreased as the size of coal particles decreased. Especially after oxygen was completely consumed, the reaction rates were very slow. This trend is characteristic of typical EFGs; it is consistent with the results in past research [5,6,16]. The final coal conversion was 98.8%.

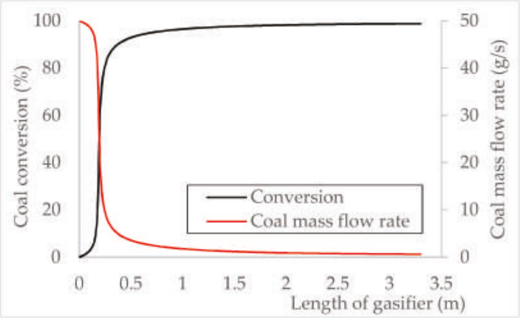

Figure 4. The profile of the coal conversion and coal mass flow rate.

5.2.2. Gas Composition

The mole fractions of the major gases changed over the reactor length (Figure 5). Oxygen was abruptly consumed near 0.25 m; this change is the result of rapid combustion. Syngas was generated in an oxygen-free environment. Steam was slightly generated in the front of the gasifier; afterwards, the proportion of steam was controlled by WGS equilibrium. After all of the oxygen was consumed, the gas composition did not change significantly. CH_4, H_2S, and N_2 were < 1% of the product; they are not represented in Figure 5. Trends in the graph agreed with trends that were reported in previous research [5,6,16]. The exit gas consists mainly (mole fraction 98.9%) of carbon dioxide, hydrogen, steam, and carbon monoxide. All of these compositions are determined by WGS equilibrium, which is a function of temperature and is closely related to the outlet temperature of the gasifier. The attempt to calculate the temperature is the first step in predicting the composition of the gas, and this study is significant in that respect.

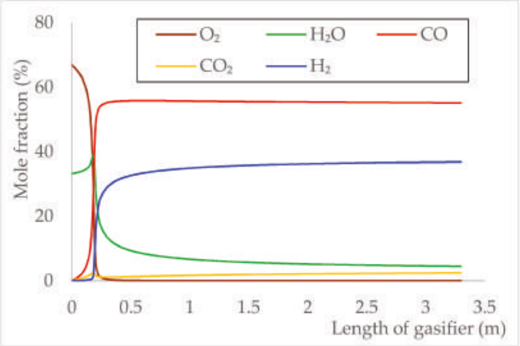

Figure 5. The profile of the major product gas mole fraction.

5.2.3. Temperature and Heat Flow

Simulations were used to calculate two temperature profiles (Figure 6). The heat balance of the first case (Figure 6, blue line) considered the sensible heat of the slag and the latent heat of the ash. The second case (Figure 6, red line) neglected these phenomena; both were set to 0. Below AFT, the temperatures of the two cases were the same, but the peak and outlet temperatures differed between the two cases. The same results were obtained in the temperature range below AFT; they are acceptable because the melting of ash had not yet been considered. The maximum temperature was calculated as 2112 K when sensible heat of the slag and the latent heat of the ash were considered, but 2155 K when they were neglected. The exit temperatures were 1464 K when the sensible heat of the slag and the latent heat of the ash were considered, and 1521 K when they were neglected; the difference between the two outlet temperatures was 57 K. The difference can be explained, as follows. The heat capacity of ash and slag is not taken into account in the system, and the corresponding energy was transferred to the gas, so the calculated temperature increased. Previous models have released heat to outside. EFGs generally use thick refractories. The assumption that a significant amount of heat escapes to the outside must be modified: these two temperature profiles show that the ash melting phenomenon must be considered when the internal temperature of the gasifier is calculated. This is a reasonable conclusion, given the fact that the internal peak temperature of the gasifier is higher than the AFT.

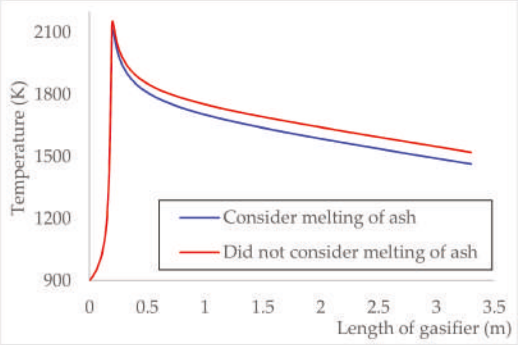

Figure 6. Differences in temperature profile depending on whether melting of ash is considered or not.

In this study, ash accounted for 15% of the mass of the coal and 7% of the total mass. The effect of sensible heat of slag is evident when the heat flows are divided into the solid and gas (Figure 7). Solids include coal, ash, and slag. After most of the reaction has proceeded, the solids are mainly in slag form. Especially at the exit condition, >99% of the solid was slag, which accounted for 5.0% of the total heat. In the coal that was used in this study, the ash was not negligible. As a result, our new attempt was meaningful. This phenomenon must be considered, especially for coal that has high ash content.

5.3. Consideration of Ash Melting Effect

The melting of ash has a similar effect on energy balance, as does heat loss from the outer wall. Because the ash melts and absorbs energy, the temperature of the system is lowered. In contrast, the loss to the outer wall lowers the temperature because heat escapes from of the system. These are different phenomena that occurred inside the gasifier, and were considered independently.

We quantitatively calculated the melting effect. This approach used the same method that was used to consider the heat loss. Based on the coal heating value, the latent heat of the ash and the sensible heat of the slag were calculated. The melting effect at the outlet was ~1%. This is not negligible given that heat loss is assumed to be 4% in this study. We calculated the melting effect at the exit as

$$\frac{Slag\ Sensible\ Heat + Ash\ Fusion\ Heat}{Coal\ Heating\ Value(HHV)} = \frac{W_{s,L} \cdot c_{P,s,L} \cdot T_L + W_{a,L} \cdot X_L \cdot \Delta H_{ash}}{W_{c,0}\ \cdot HHV\ of\ Illinois\ No.6} \quad (9)$$

In this way, we corrected the overestimate of heat loss that occurred in previous studies. In addition, we could explain some of the uncertainty of heat loss.

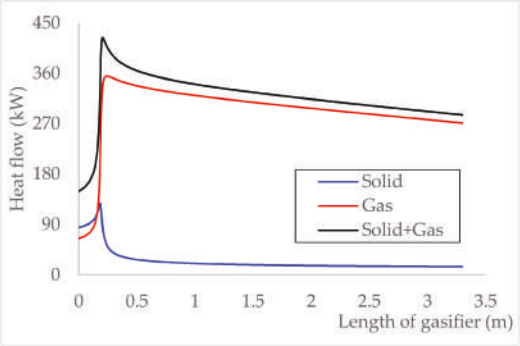

Figure 7. Heat flow of solid and gas.

5.4. Applicability of High Ash Content Coal and Limitations

Coal containing a large amount of ash can be applied in the same manner. If information about the ash component is available, then it can be used to calculate the slag properties and incorporate thermal properties in the heat balance. When the ash content is high, modeling errors can be reduced by considering the fusion heat of ash and the sensible heat of the slag.

However, the reaction kinetic parameters that are cited in this study represent only coal combustion and gasification, so the model is only applicable to the entrained coal gasifier. In addition, lab-scale or pilot-scale data of other coal that has high ash content should be used to further assess applicability of this model.

6. Conclusions

This study suggests that a heat-balance model of an EFG must consider the effects of melting of ash. We attempted modeling based on kinetic models similar to those of previous researchers. Our proposed 1-D model is the only one that includes ash in the heat-balance and temperature-calculation algorithm. Gas production and coal conversion trends were similar to those of existing ones, and the results at the exit were mostly consistent with the experiments.

This result is meaningful in that it reflects actual phenomena occurring inside the EFG. Ash melts in any slagging-type gasifier. We can expect to calculate the internal temperature more accurately based on this study. These results can be used to guide the choice of design elements of EFG, such as material and thickness of the refractory wall.

One limitation of this model is that information on the ash component was not available. We used minerals to express ash components. This demerit must be eliminated. For further research, advanced modelling should use thermal properties based on ash analysis data. This model can be extended to account for radial direction temperature distribution.

Acknowledgments: This work was financially supported by the Pohang Iron & Steel Company Limited in South Korea (No. 2017Y005).

Author Contributions: Jinsu Kim programmed the gasifier model and wrote draft paper. Hyunmin Oh checked the coding results, analyzed the simulation results, and corrected minor errors. Seokyoung Lee did the validation work and wrote the figure. Young-Seek Yoon proposed idea, supervised research based on literature review and finished the paper.

Conflicts of Interest: The authors declare no conflict of interest.

Nomenclature

A	cross section area of gasifier (m^2)
C	molar concentration (mole/m^3)
c_p	specific heat capacity (J/g·K for solid, J/mole·K for gas)
d_c	coal particle size (m)
F	molar flow rate of gas (mole/s)
H	enthalpy (J)
H_{loss}	heat loss to outer wall (J/s)
HHV	high heating value of coal (J/g)
K	equilibrium constant of water gas shift reaction (-)
k_i	rate constant of ith reaction
L	reactor length (m)
m_c	mass of one coal particle (g/#)
MW	molecular weight (g/gmole)
N_v	number of particles contained in coal (#/m^3)
P_i	partial pressure of gas i (atm)
R_j	reaction rate of j (g/s for heterogeneous reaction, mole/s for homogeneous reaction)
T	temperature (K)
v_c	coal velocity (m/s)
W_a	ash mass flow rate (g/s)
W_c	coal mass flow rate (g/s)
W_s	slag mass flow rate (g/s)
w	phi control function according to temperature (-)
X	Coal conversion (-)
Z	the coordinates of the axis of the gasifier in the previous model (m)
z	the coordinates of the axis of the gasifier in this model (m)
Greek Characters	
α	degree of deviation from equilibrium (mole/s)
ϕ	the stoichiometric coefficient to adjust the complete, incomplete combustion
ξ	stoichiometric coefficient
Subscripts	
a	the weight of C contained in 1 g of coal
b	the weight of H contained in 1 g of coal
c	the weight of O contained in 1 g of coal
d	the weight of N contained in 1 g of coal
e	the weight of S contained in 1 g of coal
f	the weight of ash contained in 1 g of coal
i	gas species
j	reaction
L	value at the reactor exit
0	value at the reactor inlet

References

1. Phillips, J. Different types of gasifiers and their integration with gas turbines. In *The Gas Turbine Handbook*; 2006; Volume 1. Available online: https://www.netl.doe.gov/File%20Library/Research/Coal/energy%20systems/turbines/handbook/1-2-1.pdf (accessed on 2 January 2018).
2. Guo, X.; Dai, Z.; Gong, X.; Chen, X.; Liu, H.; Wang, F.; Yu, Z. Performance of an entrained-flow gasification technology of pulverized coal in pilot-scale plant. *Fuel Process. Technol.* **2007**, *88*, 451–459. [CrossRef]
3. Wang, T.; Stiegel, G.J. *Integrated Gasification Combined Cycle (IGCC) Technologies*; Woodhead Publishing: Cambridge, UK, 2016; ISBN 978-0-08-100185-1.
4. Vamvuka, D.; Woodburn, E.T.; Senior, P.R. Modelling of an entrained flow coal gasifier. 2. Effect of operating conditions on reactor performance. *Fuel* **1995**, *74*, 1461–1465. [CrossRef]
5. Vamvuka, D.; Woodburn, E.T.; Senior, P.R. Modelling of an entrained flow coal gasifier. 1. Development of the model and general predictions. *Fuel* **1995**, *74*, 1452–1460. [CrossRef]
6. Hwang, M.; Song, E.; Song, J. One-Dimensional Modeling of an Entrained Coal Gasification Process Using Kinetic Parameters. *Energies* **2016**, *9*, 99. [CrossRef]
7. Bhatia, S.K.; Perlmutter, D.D. A random pore model for fluid-solid reactions: II. Diffusion and transport effects. *AIChE J.* **1981**, *27*, 247–254. [CrossRef]
8. Ishida, M.; Wen, C.Y. Comparison of kinetic and diffusional models for solid-gas reactions. *AIChE J.* **1968**, *14*, 311–317. [CrossRef]
9. Sadhukhan, A.K.; Gupta, P.; Saha, R.K. Modelling of combustion characteristics of high ash coal char particles at high pressure: Shrinking reactive core model. *Fuel* **2010**, *89*, 162–169. [CrossRef]
10. Gupta, P.; Sadhukhan, A.K.; Saha, R.K. Analysis of the combustion reaction of carbon and lignite char with ignition and extinction phenomena: Shrinking sphere model. *Int. J. Chem. Kinet.* **2007**, *39*, 307–319. [CrossRef]
11. Kong, X.; Zhong, W.; Du, W.; Qian, F. Three Stage Equilibrium Model for Coal Gasification in Entrained Flow Gasifiers Based on Aspen Plus. *Chin. J. Chem. Eng.* **2013**, *21*, 79–84. [CrossRef]
12. Biagini, E.; Bardi, A.; Pannocchia, G.; Tognotti, L. Development of an Entrained Flow Gasifier Model for Process Optimization Study. *Ind. Eng. Chem. Res.* **2009**, *48*, 9028–9033. [CrossRef]
13. Chen, C.; Horio, M.; Kojima, T. Numerical simulation of entrained flow coal gasifiers. Part I: Modeling of coal gasification in an entrained flow gasifier. *Chem. Eng. Sci.* **2000**, *55*, 3861–3874. [CrossRef]
14. Eri, Q.; Wu, W.; Zhao, X. Numerical Investigation of the Air-Steam Biomass Gasification Process Based on Thermodynamic Equilibrium Model. *Energies* **2017**, *10*, 2163. [CrossRef]
15. Liu, X.; Wei, J.; Huo, W.; Yu, G. Gasification under CO_2–Steam Mixture: Kinetic Model Study Based on Shared Active Sites. *Energies* **2017**, *10*, 1890. [CrossRef]
16. Wen, C.Y.; Chaung, T.Z. Entrainment Coal Gasification Modeling. *Ind. Eng. Chem. Process Des. Dev.* **1979**, *18*, 684–695. [CrossRef]
17. Govind, R.; Shah, J. Modeling and simulation of an entrained flow coal gasifier. *AIChE J.* **1984**, *30*, 79–92. [CrossRef]
18. Robin, A.M. *Hydrogen Production from Coal Liquefaction Residues*; Final Report; Montebello Research Lab, Texaco, Inc.: Montebello, CA, USA, 1976.
19. Basu, P. *Biomass Gasification and Pyrolysis: Practical Design and Theory*; Academic Press: New York, NY, USA, 2010; ISBN 978-0-08-096162-0.
20. Callaghan, C.A. Kinetics and Catalysis of the Water-Gas-Shift Reaction: A Microkinetic and Graph Theoretic Approach. Ph.D Dissertation, Worcester Polytechnic Institute, Worcester, MA, USA, 2006.
21. Deng, Z.; Xiao, R.; Jin, B.; Huang, H.; Shen, L.; Song, Q.; Li, Q. Computational Fluid Dynamics Modeling of Coal Gasification in a Pressurized Spout-Fluid Bed. *Energy Fuels* **2008**, *22*, 1560–1569. [CrossRef]
22. Breault, R.W. Gasification Processes Old and New: A Basic Review of the Major Technologies. *Energies* **2010**, *3*, 216–240. [CrossRef]
23. Gazzani, M.; Manzolini, G.; Macchi, E.; Ghoniem, A.F. Reduced order modeling of the Shell–Prenflo entrained flow gasifier. *Fuel* **2013**, *104*, 822–837. [CrossRef]
24. Tremel, A.; Becherer, D.; Fendt, S.; Gaderer, M.; Spliethoff, H. Performance of entrained flow and fluidised bed biomass gasifiers on different scales. *Energy Convers. Manag.* **2013**, *69*, 95–106. [CrossRef]

25. Krishnamoorthy, V.; Pisupati, S.V. A Critical Review of Mineral Matter Related Issues during Gasification of Coal in Fixed, Fluidized, and Entrained Flow Gasifiers. *Energies* **2015**, *8*, 10430–10463. [CrossRef]
26. Richardson, M.J. The specific heats of coals, cokes and their ashes. *Fuel* **1993**, *72*, 1047–1053. [CrossRef]
27. Rezaei, H.R.; Gupta, R.P.; Bryant, G.W.; Hart, J.T.; Liu, G.S.; Bailey, C.W.; Wall, T.F.; Miyamae, S.; Makino, K.; Endo, Y. Thermal conductivity of coal ash and slags and models used. *Fuel* **2000**, *79*, 1697–1710. [CrossRef]
28. Mills, K.C.; Rhine, J.M. The measurement and estimation of the physical properties of slags formed during coal gasification: 1. Properties relevant to fluid flow. *Fuel* **1989**, *68*, 193–200. [CrossRef]
29. Blissett, R.S.; Rowson, N.A. A review of the multi-component utilisation of coal fly ash. *Fuel* **2012**, *97*, 1–23. [CrossRef]
30. Žigo, O.; Adamkovičová, K.; Kosa, L.; Nerád, I.; Proks, I. Determination of the heat of fusion of $2CaOAl_2O_3$ SiO_2 (gehlenite). *Chem. Pap.* **1987**, *41*, 171–181.
31. Richet, P.; Fiquet, G. High-Temperature Heat Capacity and Premelting of Minerals in the System MgO-CaO-Al_2O_3-SiO_2. *J. Geophys. Res.* **1991**, *96*, 445–456. [CrossRef]
32. Berman, R.G.; Brown, T.H. Heat capacity of minerals in the system Na_2O-K_2O-CaO-MgO-FeO -Fe_2O_3-$Al_2O_3SiO_2$-TiO_2-H_2O-CO_2: Representation, estimation, and high temperature extrapolation. *Contrib. Mineral. Petrol.* **1985**, *89*, 168–183. [CrossRef]